This electronic thesis or dissertation has been downloaded from the King's Research Portal at https://kclpure.kcl.ac.uk/portal/

Exploring Pretargeted PET Imaging Strategies for Liposomal Nanomedicines

Mishra, Aishwarya

Awarding institution:
King's College London

The copyright of this thesis rests with the author and no quotation from it or information derived from it may be published without proper acknowledgement.

END USER LICENCE AGREEMENT

Unless another licence is stated on the immediately following page this work is licensed under a Creative Commons Attribution-NonCommercial-NoDerivatives 4.0 International licence. https://creativecommons.org/licenses/by-nc-nd/4.0/

You are free to copy, distribute and transmit the work

Under the following conditions:

- Attribution: You must attribute the work in the manner specified by the author (but not in any way that suggests that they endorse you or your use of the work).
- Non Commercial: You may not use this work for commercial purposes.
- No Derivative Works - You may not alter, transform, or build upon this work.

Any of these conditions can be waived if you receive permission from the author. Your fair dealings and other rights are in no way affected by the above.

Take down policy

If you believe that this document breaches copyright please contact librarypure@kcl.ac.uk providing details, and we will remove access to the work immediately and investigate your claim.

Download date: 13. Jan. 2025

Exploring Pretargeted PET Imaging Strategies for Liposomal Nanomedicines

Thesis submitted for the degree of Doctor of Philosophy in Imaging Sciences

Aishwarya Mishra

Department of Imaging Chemistry and Biology
School of Biomedical Engineering and Imaging Sciences
Faculty of Life Sciences and Medicine
King's College London
October 2022

ACKNOWLEDGEMENTS

First and foremost, I want to thank my supervisor, Dr Rafael T. M. de Rosales for your support and guidance over the last 5 years. You have not only been my thesis supervisor but also been mentor and a friend supporting me throughout my time in London away from family. Without your support and understanding attitude, it would have been very difficult to keep myself motivated through my PhD. You have helped me develop my research skills, supported my ideas, provided me liberty to be creative with ideas and encouraged me to pursue my different passions: teaching and public engagement alongside my research career.

I also want to thank my second supervisor, Dr James Choi for all your guidance, expert advice and mentoring over the years. Your guidance has been instrumental in fulfilling the interdisciplinary nature of my research and I have learned a lot from you on the topic of focussed ultrasound.

Thank you to past and present members of our group: Francis, Peter, Azalea, George, Juan, Amaia, Jill, Laura, Ana, Aitor and Tia for always making me feel comfortable, resolving my queries and lending an ear to all my research problems and frustrations. Thanks to members of the Non-invasive surgery and biopsy lab group (Dr Choi's group), especially Sophie Morse and Tiffany Chan for collaboratively bringing focussed ultrasound mediated liposome delivery project to completion.

I am very grateful to other supervisors within the department especially Phil and Michelle for their specialist advice and discussions around Ga radiochemistry. I want to thank all the members of my Thesis Progression Committee: Michelle Ma, Maya Thanou and Ran Yan — for their valuable advice and encouragement during multiple TPC sessions.

I want to thank Fred, Charlotte, Truc, Oskar, Rich, Aidan, Sophie, Ivan, Helio, Jordan, Filipa, Afnan, Elise, Will, Tom and everyone else in Department of the Imaging Chemistry and Biology Department for their support in the lab as well as making this journey within the department comfortable and enjoyable.

Amongst the amazing people in the department, I would like to extend a special thanks to the "dinner" group members Peter, Joanna, George Firth, Alex, Ines and Hannah for

not only helping me in the labs but also feeding me amazing food regularly. Thanks for being the amazing group of people who I could always depend on during my five years and spending all the time on long zoom calls during the COVID lockdowns. Additional thanks to Alex for helping with purification of my compounds on the ancient HPLC in the synthetic chemistry.

Thank you to all the technical staff: David, Steve, Max, Matt, Kavitha, Jana, Lisa, and Floyd — for smooth running of the labs and, of course, the BSU. I am grateful to Mr Paul Simpson from the Electron Microscopy Centre at Imperial College London for acquiring the cryo-EM images. Thank you to Jana, George Firth, Fahad, Amaia, Peter, and George Keeling for being with me during the long *in vivo* days; thanks to Hannah, Truc, Arshiya for help with injections. Thank you to Mark Wyatt from the EPSRC National Mass Spectrometry Facility and Anna Caldwell, Francesca Mazzacuva from the King's Mass Spectrometry Facility. Also, thank you to James Mason from FWB NMR facility for training of the NMR spectrometer. I am hugely grateful to Fred for training in cryosectioning techniques and Azalea and Gilbert for training on the microscopy equipment. Thank you to Jana again for training me in all the *in vivo* and imaging procedures, *in vivo* study planning and guidance, and meaningful conversations about research and life.

My PhD journey would be incomplete without mentioning the Cohort 4 and the CDT who have been an instrumental support system during this journey. Thank you to Vassilis, Federico, Alex, George, Jonny, Sam, Caitlin, Ines who have shared up and downs of this PhD journey together and some of them already defended their thesis with flying colours who I am hoping to join on the other side of this thesis. Special thanks to CDT and PE support staff past and present: Valeria, Andrea, Rob, Alice, Deanne and Bella for making this ride smooth and helping me get the best out of it.

I want to thank Jyoti, Fahad, Rebecca, and Raul for their unwavering support and helping me get through the pandemic. Thank you for all those cycling trips, holidays, dinners, shows, and endless adventures. Thank you, Jyoti, for motivating me to do better each day and always having time to talk. Also, I want to thank Sanam and Vignesh who made me feel at "home away from home" through NISAU.

I would like to mention my undergraduate friends especially Rohit, Sangeeth, and many more who motivated me to do a PhD, pursued their PhDs alongside me around the world and paid me a visit in London and brought a piece of home with them to me. I also want to thank my mentor Dr Swapan Kumar Ghosh for his guidance and encouraging me to pursue a research career since the first year of undergraduate studies.

I am forever indebted to my parents, my brother, and my sister-in-law for their blessings and for always being there by my side, understanding the challenges of my PhD and being supportive of all my decisions.

LAY SUMMARY

Little balls of fatty shells called liposomes can be used to deliver enclosed medicines to different diseased targets within the body. These balls can be tailor made to directly deliver high concentration of medicine to tumours and inflammatory cells of different types. However, some patients and some types of cancers are difficult to treat with liposomes, in particular brain cancers.

To find the reason behind these difficulties, we can label liposomes with radiation emitting particles (special type of light) which allow us to follow them inside the body and report on their whereabouts at different time points. Using this technology, we have been able to show that one of the reasons brain cancers are difficult to treat with liposomes are due to their large size preventing them infiltrating the brain. To overcome this issue, we have used sound waves and air bubbles to open the brain barrier and allow for the delivery of these medicine balls. Labelling liposomes with radiation has allowed us to observe the opening of the brain barrier and allowed the delivery of liposomes to the brain without damage and with high efficiency.

In conclusion, these methods to track and deliver liposomes carrying medicines have been explored to improve their impact on treatment of diseases in humans.

ABSTRACT

Liposomal nanomedicines have emerged as efficient drug carriers. These nanomedicines can passively accumulate in tumours/inflammation through the enhanced permeation and retention (EPR) phenomenon while reducing off-site drug toxicity. However, tumoral targeting can be variable, leading to heterogeneous uptake among tumour types and fluctuating clinical efficacies in patients. While nuclear imaging (e.g., PET and SPECT) provides valuable spatiotemporal (whole-body biodistribution) information and informed clinical management, it requires long-lived radionuclides and produces high radiation doses. Therefore, pretargeted nuclear imaging could improve our ability to study nanomedicine with the advantage of lower radiation doses and allow the use of short-lived radionuclides that would not otherwise be compatible with the long half-life of PEGylated liposomes.

In this thesis we have explored two strategies for pretargeted imaging of liposomal nanomedicines. **Chapter 2** reports a novel metal chelation pretargeting system based on tris(hydroxypyridinone)(THP). The THP chelator can be radiolabelled at low concentrations with the generator-produced radionuclide gallium-68 ($t_{1/2}$ = 68 min) at room temperature and physiological conditions with high efficiency, and it could be used to create a novel pretargeted nuclear imaging system for PEGylated liposomes. The bifunctional chelator THP-NCS was conjugated to a DSPE-PEG2000 amine phospholipid and incorporated into the bilayer of the PEGylated liposomes to give THP-PL-liposomes. Pretargeting experiments were performed *in vitro* under high dilution conditions in serum, showing high THP-PL-liposomes radiolabelling. *In vivo* imaging experiments were performed in healthy BalB/c mice at multiple time points. Pretargeting group (administration of THP-PL-liposomes, followed either after 5 h or 27 h by neutralised $^{68}Ga^{3+}$(^{68}Ga-acetate)) was compared with positive control (administration of directly radiolabelled PEGylated liposomes (^{67}Ga-THP-PL-liposomes)) and negative control (administration of ^{68}Ga-only). At earlier time point, when the liposomes were majorly circulating in the blood,

pretargeting was observed, showing radioactive accumulation in the blood pool, heart, liver, and spleen. No difference between the *in vivo* biodistribution of directly labelled liposomes (positive control) and the pretargeting group was observed, indicating an effective pretargeting. However, lower pretargeting was observed at the later time point, with a slight difference between the pretargeting group and the negative control. These findings suggests that pretargeting via metal chelation is not feasible at the later time point possible due to the inability of the ^{68}Ga to reach the THP-PL-liposomes accumulated in the liver and spleen.

This metal chelation pretargeting was also examined for the bone targeting bisphosphonate THP-Pam, to examine the ability of pretargeting in targets other than the liver and spleen. Imaging experiments were performed in healthy BalB/c mice at multiple time points (5 and 27 hours). The pretargeting group (administration of THP-Pam followed either after 5 h or 27 h by neutralised ^{68}Ga^{3+} (^{68}Ga-acetate)) was compared with both a directly radiolabelled THP-Pam (^{68}Ga-THP-Pam) and a ^{68}Ga-only (negative control). Moderate pretargeting was observed at both time points showing higher observed uptake in the target tissues of bones compared to the negative control ($p<0.05$), but lower than directly labelled THP-Pam. While this metal chelation pretargeting method did not work for the liver and spleen localised agents, it worked effectively for tracking agents in the blood, heart, and bones.

In **chapter 3**, a biorthogonal pretargeted nuclear imaging system that has shown promise with antibodies was examined for PEGylated liposomes. We hypothesised that IEDDA biorthogonal reaction between tetrazine and transcyclooctene known to take place in physiological conditions with high reaction rates, could be used to create a pretargeted nuclear imaging system for PEGylated liposomes. To this end, we made two components of this pretargeting system: TCO-PL-liposomes (PEGylated liposomes with a transcycloctene containing phospholipid embedded into the bilayer) and THP-tetrazine (TCO reactive THP bioconjugate with high affinity for ^{68}Ga). *In vitro* pretargeting experiments performed in high dilution conditions in PBS and serum showed high biorthogonal reaction rates between TCO-PL-liposomes and ^{68}Ga-THP-tetrazine. Imaging experiments were performed in healthy BalB/c mice at 4 h and 26 h post-injection. Pretargeting TCO-PL-liposomes followed either by neutralised ^{68}Ga-THP-tetrazine with both a directly radiolabelled PEGylated liposomes (^{67}Ga-TCO-PL-liposomes) and a ^{68}Ga-THP-tetrazine (negative control) were compared. At both time points, pretargeting was observed, showing a higher accumulation of radioactivity in the blood pool, heart, liver and spleen (target organs for PEGylated liposomes) compared to the negative control ($p<0.05$). These results were also confirmed in a fibrosarcoma tumour model in mice ($p<0.05$). However, no pretargeting was observed within the tumours. The radioactivity uptake observed in tumours in pretargeting group showed no significant difference to uptake observed in negative control and was low compared to directly labelled TCO-PL-liposomes.

In **Chapter 4,** we aim to tackle another significant disadvantage faced by liposomal nanomedicines, which is their inability to cross the blood brain barrier (BBB) and reach the brain, as well as the areas of interest (e.g., inflammation, tumours, and neurodegeneration). However, new methods to disrupt the BBB can make brain targets accessible to liposomes. Therefore, we examined whether rapid short pulse (RaSP) can deliver liposomes to the murine brain *in vivo*. Fluorescent DiD-PEGylated liposomes were synthesised and injected intravenously alongside microbubbles and applied focussed ultrasound at different pressures. The delivery and biodistribution were assessed by fluorescence imaging of the brain sections, and the safety profile of the sonicated brains was evaluated by histological staining. RaSP was shown to deliver liposomes locally across the BBB at 0.53 MPa with a more diffused and safer profile compared to the long pulse ultrasound sequence. Cellular uptake of liposomes was observed in neurons and microglia, while no uptake within astrocytes was observed in both RaSP and long pulse-treated brains.

FUNDING STATEMENTS

This work was funded by the EPSRC Centre for Doctoral Training in Medical Imaging [EP/L015226/1], the Wellcome/EPSRC Centre for Medical Engineering [WT/203148/Z/16/Z], and the EPSRC programme for next generation molecular imaging and therapy with radionuclides [EP/S032789/1]. Further support comes from a Wellcome Trust Multiuser Equipment Grant: A multiuser radioanalytical facility for molecular imaging and radionuclide therapy research and the National Institute for Health Research (NIHR) Biomedical Research Centre based at Guy's and St Thomas' NHS Foundation Trust and KCL [grant number IS-BRC-1215-20006]. PET and SPECT scanning equipment at KCL was funded by an equipment grant from the Wellcome Trust under grant number WT 084052/Z/07/Z. We acknowledge the Electron Microscopy Centre at the Centre of Structural Biology, Imperial College (funded by the Science Research Investment Fund in June 2007) and EPSRC UK National Mass Spectrometry Facility (NMSF), Swansea for the analysis of mass spectrometry sample. The views expressed are those of the author and not necessarily those of the NHS, the NIHR or the Department of Health.

DECLARATION

I, Aishwarya Mishra, confirm that no part of this thesis has been submitted in support of any other application for a degree or qualification of King’s College London, or any other university or institute of learning. I confirm that this work is my own. Where information has been derived from other sources it has been indicated in this thesis.

CONTENTS

ACKNOWLEDGEMENTS III

LAY SUMMARY VI

ABSTRACT VII

FUNDING STATEMENTS X

DECLARATION XI

CONTENTS XII

LIST OF FIGURES XXIV

LIST OF TABLES XXXVII

1 INTRODUCTION 39

1.1 Nanomedicines: Efficient drug delivery systems 40

- 1.1.1 Liposomes 44
  - 1.1.1.1 Structure of liposomes 45
- 1.1.2 Passive targeting and the enhanced permeation and retention (EPR) phenomenon 50
- 1.1.3 EPR heterogeneity challenges: the need for imaging 53

1.2 Imaging liposomes: Applications 55

- 1.2.1 Imaging of liposomes 56
  - 1.2.1.1 MRI 56
  - 1.2.1.2 Computed Tomography 56
  - 1.2.1.3 Ultrasound Imaging 57
  - 1.2.1.4 Optical imaging 60
  - 1.2.1.5 Nuclear Imaging 60
- 1.2.2 Why nuclear imaging to track liposomal nanomedicines? 63
  - 1.2.2.1 Rationale 63
  - 1.2.2.2 PET imaging 65
  - 1.2.2.3 SPECT imaging 66
  - 1.2.2.4 PET vs SPECT 67

1.2.2.5 Nuclear imaging for non-invasive tracking of nanomedicines........... 68
1.2.2.6 Multimodality imaging 68
1.2.2.7 Radionuclide nanotheranostics 69
1.2.2.2.1 Alpha-particle radiation. 69
1.2.2.2.2 Beta-particle radiation 70
1.2.2.2.3 Auger electron radiation 70
1.2.2.2.4 Nanoradiotherapeutics 71
1.3 Radiolabelling liposomes: How? 72
1.3.1 List of PET/SPECT radionuclides 73
1.3.1.1 PET radionuclides: relevant examples 74
1.3.1.2 SPECT radionuclides: relevant examples 75
1.3.2 Strategies for radiolabelling: 77
1.3.2.1 Surface labelling 77
1.3.2.2 Core labelling 79
1.3.2.2.1 Ionophore binding method 79
1.3.2.2.2 Remote loading 80
1.3.2.2.3 Unassisted loading 81
1.3.3 Limitations of current liposome radiolabelling methods 82
1.4 The concept of pretargeting 84
1.4.1 Introduction to pretargeting 84
1.4.2 Types of pretargeting 85
1.4.2.1 Non-covalent interaction approach 85
1.4.2.1.1 Bispecific antibody-hapten binding 85
1.4.2.1.2 Avidin/Streptavidin-Biotin binding 86
1.4.2.1.3 Complementary oligonucleotide binding 87
1.4.2.2 Covalent interaction approach 87
1.4.3 Role of pretargeted imaging in nanomedicine 88
1.4.4 Limitations of pretargeted imaging in nanomedicine 89

1.5 Hypothesis and aims of the thesis 91

2 METAL CHELATION BASED PRETARGETING OF LIPOSOMAL NANOMEDICINES 96

2.1 Introduction: Trishydroxypyridinone and Ga: A promising pair for metal chelation-based pretargeted imaging 97

2.1.1 Ga isotopes: PET and SPECT pair 98

2.1.2 Tris(hydroxypyrdinone): an ideal chelator for Ga, but also Fe 101

2.1.3 Aims and hypothesis 102

2.2 Results and discussion 105

2.2.1 Synthesis and characterisation of THP-Phospholipid 105

2.2.2 Synthesis and characterisation of THP-PL-PEG(2k)-liposomes 110

2.2.2.1 Dynamic light scattering (DLS) 111

2.2.2.2 Nanoparticle tracking analysis 112

2.2.2.3 Cryo-electron microscopy 114

2.2.3 Radiochemistry 116

2.2.3.1 Radiolabelling of THP-PL 116

2.2.3.2 Radiolabelling of THP-PL-liposomes 120

2.2.4 *In vitro* stability of ^{68}Ga-THP-PL-liposomes and ^{67}Ga-THP-PL-liposomes 121

2.2.5 *In vitro* pretargeting validation 122

2.2.6 *In vivo* evaluation of pretargeting of THP-PL-PEG(2k)-liposomes in healthy mice 125

2.2.7 *In vivo* evaluation of pretargeting of THP-Pam in healthy mice 133

2.3 Conclusion 138

3 BIORTHOGONAL CHEMISTRY BASED PRETARGETING OF LIPOSOMAL NANOMEDICINES 139

3.1 Introduction: Biorthogonal chemistry for pretargeting of nanomedicines .. 140

3.1.1 Biorthogonal Chemistry: inverse electron demand Diels Alder reaction and strain-promoted azide-alkyne reaction 140

3.1.2 SPAAC and its application in nanoparticle pretargeting 142

3.1.3 Preclinical pretargeted imaging of nanoparticles using SPAAC 142

3.1.4 IEDDA and its application in pretargeted nuclear imaging 144

3.1.5 Preclinical pretargeted imaging of nanoparticles using IEDDA 145

3.1.6 Aims and Motivations 150

3.2 Results and discussion 151

3.2.1 Synthesis of TCO-DSPE-PEG(2000) amine (TCO-PL) 151

3.2.1.1 Synthesis and Purification 151

3.2.2.2 Characterization 154

3.2.2 Synthesis of 6-methyl tetrazine-THP 157

3.2.2.1 Synthesis and Purification 157

3.2.2.2 Radiolabelling 160

3.2.3 Synthesis of TCO-liposomes 163

3.2.3.1 Synthesis and purification 163

3.2.3.2 Dynamic light scattering (DLS) 164

3.2.3.3 Nanoparticle tracking analysis 165

3.2.3.4 Cryo-electron microscopy 166

3.2.4 *In vitro* evaluation of TCO-PL liposomes 168

3.2.4.1 Serum stability 168

3.2.4.2 *In vitro* pretargeting 169

3.2.5 *In vivo* evaluation of pretargeting of TCO-PL liposomes in healthy mice 171

3.2.6 *In vivo* evaluation of pretargeting of TCO-PL liposomes in a syngeneic mouse cancer model 178

3.3 Conclusion 189

4 RASP FOCUSED ULTRASOUND MEDIATED DELIVERY OF LIPOSOMAL NANOMEDICINES TO THE BRAIN 190

4.1 Introduction: Nanomedicines delivery to the brain 191

4.1.1 Drug delivery to the brain 191

4.1.2 Transport across the blood-brain barrier (BBB) 192

4.1.2.1 Blood-brain barrier (BBB) 192

4.1.2.2 Disruption of the blood-brain barrier 194

4.1.2.2.1 Osmotic disruption: 194

4.1.2.2.2 Chemical disruption: 195

4.1.2.2.3 Physical disruption: 195

4.1.3 Focussed ultrasound 196

4.1.3.1 Rapid short pulse (RaSP) sequence for FUS-mediated BBB opening 198

4.1.4 Liposome delivery with focussed ultrasound 199

4.1.5 Aims and objectives 200

4.2 Results and discussion 202

4.2.1 Synthesis and characterization of fluorescent DiD-liposomes 202

4.2.2 *In vitro* validation of fluorescent DiD-liposomes 203

4.2.3 *In vivo* delivery of fluorescent liposomes using focused ultrasound in mice model 204

4.2.3.1 Detected delivery and dose 204

4.2.3.2 Delivery distribution 209

4.2.3.3 Subcellular localisation 213

4.2.3.4 Cellular uptake 215

4.2.3.5 Safety profile 221

4.2.4 *In vivo* delivery of THP-PL liposomes using focused ultrasound in mice model 225

4.2.5.1 Synthesis of THP-PL liposomes 226

4.2.5.2 Delivery quantification by *ex vivo* pretargeting 226

4.3 Conclusion 229

5 METHODS 234

5.1 Chapter 2 234

5.1.1 Materials 234

5.1.1.1 Equipment and Instrumentation 234

5.1.1.2 Reagents 235

5.1.2 Synthesis and characterisation of THP-Phospholipid 235

5.1.3 Synthesis and characterisation of THP-PL-liposomes 237

5.1.4 Nanoparticle Tracking Analysis (NTA) **238**
5.1.5 Cryo-Electron Microscopy **238**
5.1.6 Radiochemistry **239**
  5.1.6.1 Buffering of ^{68} GaCl$_3$ used for labelling and purification. **239**
  5.1.6.2 Radiolabelling of THP-Phospholipid **239**
  5.1.6.3 Radiolabelling of THP-PL-PEG (2k)-liposomes **240**
  5.1.6.4 Synthesis of ^{67}Ga-THP-PL-liposomes **240**
5.1.7 *In vitro* stability **241**
5.1.8 *In vitro* pretargeting methods **241**
  5.1.8.1 *In vitro* ^{68}Ga complexation tests -1 .... **241**
  5.1.8.2 *In vitro* ^{68}Ga complexation tests -2 .... **241**
5.1.9 *In vivo* PET imaging **242**
  5.1.9.1 Animals **242**
  5.1.9.2 Preclinical PET/CT and SPECT/CT scanners **242**
  5.1.9.3 Pretargeting of THP-PL-liposomes in healthy animals **243**
  5.1.9.4 Pretargeting of bone targeting THP-Pam in healthy animals **244**
5.1.10 Analysis **245**
5.2 Chapter 3 .... **246**
5.2.1 Materials **246**
  5.2.1.1 Equipment and Instrumentation **246**
  5.2.1.2 Reagents **247**
5.2.2 Purification methods **248**
  5.2.2.1 HPLC methods **248**
5.2.3 Synthesis and characterisation of TCO-phospholipid **251**
5.2.4 Synthesis and characterisation of THP-tetrazines **252**
5.2.5 Synthesis of TCO-PL-liposomes **253**
5.2.6 Nanoparticle Tracking Analysis **254**
5.2.7 Cryo-Electron Microscopy **254**
5.2.8 Radiochemistry **255**

5.2.9 Log P and Log D measurements 257
5.2.10 Serum stability 257
5.2.11 *In vitro* pretargeting methods 257
5.2.12 *In vivo* pretargeting methods 258
5.2.12.1 Animals 258
5.2.12.2 Preclinical PET/CT and SPECT/CT scanners 259
5.2.12.3 Pretargeting of TCO-PL-liposomes in healthy animals 260
5.2.12.4 Pretargeting of TCO-PL-liposomes in tumoured animals 261
5.2.13 Analysis 264
5.3 Chapter 4 264
5.3.1 Materials 264
5.3.5 Animals 268
5.3.6 Microbubbles 270
5.3.7 Sonication experimental workflow 270
5.3.7 Brain sectioning 271
5.3.8 Histological staining 272
5.3.9 Microscopy 273
5.3.10 Analysis 273
5.3.11 Statistical analysis 275
5.3.12 Autoradiography via ^{68}Ga based pretargeting 275
6 CONCLUSIONS AND FUTURE OUTLOOK 277
7 APPENDIX 277
8 REFERENCES 285

Table of Abbreviations

AAV	Adeno-associated virus
ACN	Acetonitrile
ANOVA	Analysis of variance
ATCC	American type culture collection
BALB	Bagg and albino mice
BBB	Blood brain barrier
BFC	Bifunctional chelator
BMEDA	2,2'-{[2-(Diethylamino)ethyl]imino}diethanethiol
BSU	Biological services unit
CDC	Centre for Disease control
CED	Convection enhanced delivery
CMC	Critical micelle concentration
CNS	Centre nervous system
COV	Coefficient of variance
CT	Computed tomography
DAPI	4′,6-diamidino-2-phenylindole
DBCO	Dibenzo cyclooctene
DCE	Dynamic contrast enhanced
DCTB	trans-2-[3-(4-tert-Butylphenyl)-2-methyl-2-propenylidene]malononitrile
DFO	Desferrioxamine
DHP	Dihydropyrimidinase
DIBAC	Aza-dibenzocyclooctynes
DIBO	4-dibenzocyclooctynol
DIPEA	Diisopropyl ethyl amine
DISIDA	Diisopropyl iminodiacetic acid
DLS	Dynamic light scattering
DMSO	Dimethly Sulphoxide
DNA	Deoxy ribonucleic acid
DOTA	2,2′,2”,2”'-(1,4,7,10-tetraazacyclododecane-1,4,7,10-tetrayl)tetraacetic acid
DOTAP	1,2-dioleoyl-3-trimethylammonium-propane
DOTATOC	DOTA-(Tyrosine)-octreotate

DOX	Anthracycline doxorubicin
DOXIL	Liposomal doxorubicin
DPEG	Discrete polyethylene glycol
DPL	DiD-PEGylated liposomes
DSPE	1,2-Distearoyl-sn-glycero-3-phosphorylethanolamine
DTPA	Diethylenetriamine pentaacetate
EDG	Electron donating group
EDTA	Ethylenediaminetetraacetic acid
EGFR	Epidermal growth factor receptor
EMA	European medicines agenct
EPR	Enhanced permeation and retention effect
ESI	Electrospray ionisation
ETPN	European nanomedicine technolgy platform
EWG	Electron withdrawing group
FDA	Food and drug adminsitration
FITC	Fluorescein isothiocyanate
FL	Fluorescence intenstiy
FPLC	Foast protein liquid chromatography
FUS	Focused ultrasound
FWHM	Full width half maximum
GE	General Electric
GFP	Green fluorescent protein
GMP	Good manufacturing practices
HIV	Human immunodeficiency virus
HMPA	Hexamethylpropyleneamine
HMPAO	Hexamethylpropyleneamine oxime
HOMO	Highest ocuupied molecular orbital
HPLC	High performance liquid chromatography
HPMA	N-(2-Hydroxypropyl)methacrylamide
HSPC	L-α-phosphatidylcholine,hydrogenated
HYNIC	Hydrazinonicotinic acid
ICAM	Intercellular Adhesion Molecule
IEDDA	Inverse electron demand Diels Alder
ITLC	Instant thin layer chromatography
IV	Intravenous
LC	Liquid chromatography
LCMS	Liquid chromatography mass spectrometry

LF	Liposome fraction
LNP	Lipid nanoparticles
LUMO	Lowest unoccupied molecular orbital
MALDI	Matrix assited laser desorption ionisation
MB	Microbubbles
MIRD	Medical internal radiation dose
MO	Molecular orbital
MORF	Morpholino oligomers
MPS	Mononuclear phagocytic system
MR	Magnetic resonance
MRI	Mangetic resonance imaging
MW	Molecular weight
MWCO	Molecular weight cutoff
NCS	Isothiocyanata
NHS	N-hydroxysuccinimide
NIR	Near-infrared
NMR	Nuclear magnetic resonance
NMSF	National mass spectroemtry facility
NOD	Normalised optical density
NODAGA	1,4,7-triazacyclononane,1-glutaric acid-4,7-acetic acid
NOTA	2,2′,2”-(1,4,7-triazacyclononane-1,4,7-triyl)triacetic acid
NP	Nanoparticle
NSB	Non-invasive surgery and biopsy lab
NTA	Nanoparticle tracking analysis
OCT	Optimal cutting temperature compound
PBS	Phosphate buffered saline
PCD	Passive cavitation detector
PCR	Polymerase chain reaction
PDI	Polydispersity index
PEG	Polyethylene glycol
PET	Positron emission tomography
PK	Pharmacokinetics
PL	Phospholipid
PLA	Polylactic acid
PMT	Photon multiplier tubw
PSMA	Prostrate specific membrane antigen
RBC	Red blood cells

RES	Reticulo-endothelial system
RGD	Arginylglycylaspartic acid
RLY	Radiolabelling yield
RMP	Synthetic bradykinin analogue
RNA	Ribonucleic acid
ROI	Region of interest
ROS	Reactive oxygen species
RPMI	Rosewell park memorial institute media
RT	Romm temperature
SD	Standard deviation
SEC	Size exclusion chromatography
SMANCS	Styrene Maleic Acid Neocarzinostatin
SNP	Supramolecular nanoparticle
SNR	Signal to noise ration
SPAAC	Strain promoted azide alkyne cycloaddition
SPE	Solid phase extraction
SPECT	Single photon emission computed tomography
SST	Somatostatin
TCO	Transcyclooctene
TEM	Transmission electron microscope
TFA	Trifluoroacetic acid
THF	Tetrahydrofuran
THP	Tris(hydroxypyridinone)
TIFP	Tumour interstitial fluid pressure
TLC	Thin layer chromatography
TOF	Time of flight
UV	Ultraviolet
VEGF	Vascular epidermal growth factor
WEHI	Mouse BALB/c fibrosarcoma cell line
WT	Wild type
ZP	Zeta potential
ZS	Zeta scattering

LIST OF FIGURES

Figure 1.1 Nanomedicines: Different nanoparticle types with drug-carrying/therapeutic potential in a clinical or preclinical setting including metallic nanoparticles, lipid-based nanoparticles, polymeric nanoparticles and biological nano therapeutic vectors 41

Figure 1.2. Versatility of liposomal nanomedicines as a drug-delivery vehicle: Conventional liposomes possess the ability to carry hydrophilic, hydrophobic and genetic material-based drugs; Stealth PEGylated liposomes with PEG modification for passive targeting with long blood circulation half-life; Active targeting liposomes for different targeting vectors on the surface for targeted accumulation on different biological targets; and Theranostic liposomes for imaging as well as drug delivery applications using different modalities. 44

Figure 1.3. Components of a liposome: cross-section of an empty PEGylated liposome (right); Structure of a phospholipid bilayer, cholesterol, and a phospholipid molecule. 45

Figure 1.4 Enhanced permeation and retention effect: Comparison of normal and tumour vasculature. The increased leaky vasculature, tumour-associated macrophages and decreased lymphatic drainage assist the EPR effect. 52

Figure 1.5. Image-assisted development of drug delivery methods: Imaging methods have found various applications in drug-delivery as well as diagnostic development. This schematic representation depicts these applications including prediction of drug response, drug efficacy, biodistribution, pharmacokinetics assessment and a better understanding of various aspects of nanotherapeutics to provide a valuable field of nanotheranostics. Various advantageous aspects of this field of nanotheranostics can be seen above. Image reproduced.[85] 55

Figure 1.6. Iodinated liposomes used as a CT contrast agent formed from modified lipids containing ((E)-10,11-diiodoundec-10-enoic acid). [95] 57

Figure 1.7. Applications of different imaging modalities in the tracking of liposomal nanomedicine: MRI: MRI imaging of magnetic fluid loaded liposomes post 4-h exposure to a magnetic field gradient showing a high concentration of MFLs into human U87 glioblastoma implanted in the striatum of mice.[88] , Ultrasound/Optical: (A) Therapeutic MB-Lipo particles containing both doxorubicin and siRNA (siSTAT3) were imaged using US imaging showing target-specific labelling of tumours;(B) Ex vivo optical imaging of tumour tissue showed delivery of high concentrations of Dox (red fluorescence). (C) The delivery of siSTAT3 was confirmed by performing PCR on tissue extract. [107] , CT: Computed tomography of rat with breast tumour in left flank (A) before, and (B) 5 minutes after i.v. administration of liposomal contrast agent (2 g of iodine per kg), C) Accumulation of the contrast agent within tumour vasculature.[107] , PET: PET imaging of Zr89 labelled liposomes in mouse tumour model (maximum intensity projection and other views).[109] , SPECT: Whole-body gamma camera images over 7 days of a patient with Kaposi's sarcoma administered In-111-labeled liposomes. Areas of liposome uptake in the left foot and leg, right arm, and face corresponded with typical Kaposi's sarcoma lesions. Prolonged retention of the radiolabel is seen despite significant

clearance of circulating liposomes, as demonstrated by disappearance of the cardiac blood pool image.[110] 62

Figure 1.8. Applications of nuclear imaging in nanomedicine: (A) Nuclear imaging in early nanomedicine development for validation of various formulations in small animal disease models with non-invasive tracking followed by further validation using ex vivo tissue collection. (B) The pharmacokinetics and biodistribution of ^{124}I-labeled liposomes in the murine model were monitored over 3 days by PET imaging.[116] (C) For screening of formulations: Three pegylated porphyrin nanocomplexes radiolabelled with ^{64}Cu and their biodistribution was monitored longitudinally over 24 h using PET revealing the best formulation and size for tumour targeting to be chosen for further evaluation and development.[117] (D) Evaluation of targeting efficiency: The effect of incorporation of targeting ligands on the doxorubicin-loaded iron oxide nanoparticles was studied by PET imaging of ^{64}Cu labelled particles.[118] (E) Dose quantification of target accumulation: The dose of therapeutic delivered to the tumours can be estimated using companion PET/SPECT imaging. ^{89}Zr-labelled liposomes were used as companion imaging for Doxil to obtain the intratumoural doxorubicin delivered dose from the quantified ^{89}Zr PET signal.[119] Image adapted and reproduced from Medina et al[120] 64

Figure 1.9. Schematics of the working of a PET scanner: The emitted positron from the PET radiotracer annihilates in the presence of an electron to produce two diametrically opposite y-ray photons. 65

Figure 1.10. Schematics of the working a SPECT scanner: The emitted gamma photons from the SPECT radiotracer is collected by a collimator which is detected by the array of detectors. 66

Figure 1.11. Schematic illustration of the different methods for radiolabelling liposomes: Surface radiolabelling: the radionuclide (A), with a chelator (B) or an organic radionuclide compound (C), can be linked to the liposomal surface. Core radiolabelling: the radionuclide is encapsulated within the aqueous core. Ionophores can be used to transport radionuclides across the bilayer where they can be bound by chelators or drugs inside the liposomes, or radioactive compounds/complexes can passively cross the bilayer and become trapped. 82

Figure 1.12. General scheme of Pretargeting imaging concept used for imaging of antibodies. Image reproduced from reference. [239] 84

Figure 1.13. Types of pretargeting: The library of different approaches of pretargeting available for imaging of antibodies: (a) Streptavidin-biotin; (b) Complimentary oligonucleotide binding; (c) Bispecific antibody-hapten; (d) Strain promoted alkyne-azide cycloaddition (SPAAC): alkyne-azide; (e) Inverse electron demand Diels-Alder reaction (IEDDA). 88

Figure 1.14. Different nuclear imaging methods for nanomedicines: (A) Conventional Imaging (B) Pretargeted Imaging (C) Pretargeted Imaging with clearing agent. Image reproduced. [260] 89

Figure 1.15. Graphical abstract of Chapter 2: Metal chelation based pretargeted PET imaging of PEGylated liposomes using the high chelating affinity of tris(hydroxypyridinone) towards Ga. 93

Figure 1.16. Graphical abstract of Chapter 3: Biorthogonal IEDDA reaction based pretargeted PET imaging of PEGylated liposomes exploiting the fast and efficient reaction kinetics between tetrazine and transcyclooctene. 94

Figure 1.17. Graphical abstract of Chapter 4: Focussed ultrasound and microbubble assisted delivery of fluorescent PEGylated liposomes to the brain followed by quantification and safety assessment. 95

Figure 2.1 Structure of Trishydroxypyridinone (THP): A tripodal framework of 3,4-hydroxypyridinones was formed to give this hexadentate chelator. THP can be derivatised for bioconjugation from the root of three arms, away from the binding groups minimising the impact of the chelation ability. Two different variants of THP are available for use as chelators: THP^{Me} and THP^{H}. 97

Figure 2.2. Metal chelation pretargeting of antibodies: (Top) Schematic representation of the experiment worklflow of the reported metal chelation pretargeting of antibodies. (Bottom) The Representative PET images of nude mice bearing SW1222 xenografts. (A) Mouse treated with directly labelled 89Zr-DFO-NCS-huA33 (Positive control group, 25 hours p.i.); (B) Mouse pretreated with THP^{Me}-NCS-huA33 (Test group) followed at 24 h by ^{68}Ga acetate (imaged at 2 h p.i.); (C) Mouse injected with ^{68}Ga acetate only (2 h 30 min p.i., Negative control). White arrows indicate location of the tumour. Image reproduced from Imberti et al. [305] 103

Figure 2.3. Graphical abstract of the metal chelation based pretargeting of PEGylated liposomes in a murine model. 104

Figure 2.4. Scheme of the reaction between an isothiocyanate and amine: The reactants forming a stable thiourea bond in mild basic conditions where R^1 is Trishydroxypyridinone and R^2 is DSPE-PEG2000 (phospholipid) in this chapter. 105

Figure 2.5 Impact of PEG2000 on chelator availability: Accessibility of the THP chelators on the surface depending on the different formulation of liposomes/PEGylated liposomes and THP-phospholipid with a PEG chain. The addition of a PEG2000 chain to THP-phospholipid allows them to be accessible to Ga for chelation. 106

Figure 2.6. Comparative ^{1}H-NMR of THP-PL and DSPE-PEG2000 amine using 400 MHz NMR in $CDCl_3$ (1024 scans): THP-PL is characterised by the presence of broad THP peaks (highlighted using red circles) and absence of NH_2 peak unlike the NMR of DSPE-PEG2000-amine (highlighted using black circle). 108

Figure 2.7. Mass spectra recorded with MALDI-TOF High Resolution Mass spectrometry: The envelope like nature is a characteristic of the mass spectra of PEGylated molecules due to the polydispersity in MW of PEG chains attached to the phospholipid: (A) DSPE-PEG2000-amine: z=1 species 2500-3000 (Exact mass: 2790); z=2 species 1250-1650 (Exact mass: 1395); z=3 species 800-1100 (Exact mass: 930), (B) THP-PL: z=2 species 1700-2100 (Exact mass: 1866); z=3 species 1140-1360 (Exact mass: 1244); Z=4 species 840-1060 (Exact mass: 933). Base peak in both the spectra is at 607.5 due to formation of stable phospholipid fragment on ionisation. 109

Figure 2.8. Synthesis of THP-PL-liposomes: Insertion of THP-PL into PEGylated liposomes by co-incubation of THP-PL and PEG-2k liposomes. 111

Figure 2.9. Characterisation of THP-PL-liposomes using dynamic light scattering and Nanoparticle Tracking Analysis: (A) The hydrodynamic size of THP-PL-liposomes and PEG(2k)-liposomes was recorded showing no effect on size (Z-average) due to insertion of THP-PL into the liposomes; the surface charge was measured as zeta potential (ZP) of the liposome samples showing minimal change in the magnitude of surface charge with no change in the polarity post-insertion of THP-PL in the liposomal bilayer; the polydispersity index (PDI) was determined showing small increase in the polydispersity of THP-PL-liposomes compared to unmodified PEG(2k)-liposomes. (B) Nanoparticle Tracking Analysis (NTA) results: PEG(2k)-liposomes (concentration: 9.01 x 10^{14} ± 7.15 x 10^{13} particles/mL, mode:80 nm, mean: 102.4 nm); THP-PL-liposomes (concentration: 4.20 x 10^{12} ± 1.05 x 10^{11} particles/mL, mode: 106.2 nm, mean: 131.6 nm)................113

Figure 2.10. Cryo-electron microscopy of liposomes pre- and surface post-modification with THP-PL: (A) showing THP-PL-liposomes have retained their spherical nature and the size distribution is not altered by insertion of THP-PL into the bilayer of liposomes and bilayer nature is also retained; (B) showing PEG(2k)-liposomes spherical morphology and bilayer structure. Size quantification of liposomes from analysis of cryoEM images showing frequency distribution of diameter of liposomes: (A) Unmodified PEG(2k)-liposomes; (B) THP-PL liposomes. The scale shown in the cryoEM image is 100 nm. 115

Figure 2.11. Radiolabelling of THP-PL: (A) RadioTLC trace for the radiolabelling of the THP-PL conjugate with ^{68}Ga compared to controls: (left) TLC Mobile phase A system (Chloroform:Methanol:Water in the ratio 75:36:6) and (right) TLC mobile phase B system (Citrate buffer); (B) Quantification of radiolabelling yield of THP-PL was performed using size exclusion chromatography..118

Figure 2.12. Purification of ^{68}Ga: The colloids generated after neutralisation of gallium generator eluate are removed and the different gallium samples pre and post purification are characterised using ITLC (A) Generator eluate; (B) Neutralised ^{68}Ga pre-purification and (C)Neutralised ^{68}Ga post-purification 119

Figure 2.13. Radiolabelling of THP-PL-liposomes: Elution from the size exclusion column confirmed the incorporation of THP chelators on the surface of liposomes. THP-PL and unmodified PEG(2k)-liposomes were labelled as controls showing less than 5% radioactivity eluted in liposome fraction of a size-exclusion chromatography system while the THP-PL-liposomes showed % radiolabelling of 94.6 ± 1.9 % 120

Figure 2.14. Serum stability assessment of ^{68}Ga-THP-PL-liposomes using AKTA system: (A) UV profile shows three UV active species: liposomes, albumin protein from serum and transferrin protein from serum; (B) Radioactivity profile shows all the radioactivity associated with liposomes; (C) Serum stability of THP-PL-liposomes in human serum over 180 minutes: 90.9±0.6% of the ^{68}Ga is attached to the liposomes after 180 minutes showing minimal transchelation to serum proteins..124

Figure 2.15. *In vitro* pretargeting of THP-PL-liposomes: (A) Pretargeting in commercially obtained human serum (containing citrate) with ^{68}Ga. The radiolabelling yield was determined after 15, 30, and 45 minutes of incubation showing less than 59 % labelling after 45 minutes; (B) Pretargeting of THP-PL-liposomes with ^{68}Ga incubated in

citrate free human serum after 30 minutes; (C) Pretargeting of THP-PL-liposomes incubated in citrate free human serum with ^{68}Ga after 15 minutes 124

Figure 2.16. Scheme of *in vivo* pretargeting PET experients: Negative control: Group 1; THP-PL liposome pretargeting group: Group 2; Positive control group: Group 3 126

Figure 2.17. Positive control group: (A) Schematics of the positive control group of *in vivo* experiment; (B) *In vivo* SPECT image for positive control group i.e.,^{67}Ga-THP-PL-liposome at t = 2 h and t = 24 h; (C) Biodistribution at t = 25 h (n=4), (D) Blood *kinetic in vivo* study to determine the circulation characteristics of THP-PL-liposomes: ^{67}Ga-THP-PL-liposomes are injected intravenously followed by sampling of blood liposomes concentration at different intervals (n=4). 127

Figure 2.18. Negative control group: (A) Schematics of the negative control group of *in vivo* experiment; (B) *In vivo* PET image for negative control group t = 2 h; (C) Biodistribution at t = 3 h (n=3) 128

Figure 2.19. Pretargeting group: (A) Schematics of the pretargeting group of *in vivo* experiment; (B) *In vivo* PET pretargeted imaging of THP-PL liposome at t=2 h and t=24 h; (C) Biodistribution at t = 25 h (n=4) 129

Figure 2.20. Comparison of the images and radioactivity uptake values quantified from images: THP-PL-liposome pretargeting PET/SPECT scans at two different time points of interest (A) at t = 2 h and (B) at t = 24 h; Image quantification performed on the THP-PL-liposome pretargeting PET/SPECT scans by drawing ROIs using vivoquant (n=4) at two different time points of interest (C) at t = 2 h and (D) at t = 24 h. 131

Figure 2.21 Comparison heat map showing radioactivity uptake in different organs among different experimental groups (in % ID/g): (A) Negative control vs Pretargeting – 2 h; (B) Pretargeting – 2 h vs Positive control- 2 h; (C) Negative control vs Positive control- 2 h; (D) Negative control vs Pretargeting group- 25 h; (E) Pretargeting group- 25 h vs Positive control- 25 h; (F) Negative control vs Positive control- 25 h. A, B, and C heat map are created from image analysis data and D, E, and F heat map are created from biodistribution data. 132

Figure 2.22. Scheme of *in vivo* pretargeting PET experients: Negative control: Group 1; THP-Pam pretargeting group: Group 2; Positive control group: Group 3 134

Figure 2.23. Positive control group: (A) Schematic of the positive control *in vivo* experiment of THP-Pam pretargeting; (B) *In vivo* PET imaging of ^{68}Ga-THP-Pam at 1 h p.i.; and (C) Biodistribution performed at 2 h p.i. 135

Figure 2.24. Pretargeting group: (A) Schematics of the pretargeting group of *in vivo* experiment; (B) *In vivo* PET pretargeted imaging of THP-Pam at t=2 h and t=24 h; (C) Biodistribution at t = 25 h (n=4). 136

Figure 2.25. Biodistribution and image quantification performed on the THP-Pam pretargeting PET/SPECT scans by drawing ROIs using vivoquant (n=4) at two different time points of interest: (A) Ex vivo biodistribution comparison of Positive control i.e. directly labelled THP-palmidronate (^{68}Ga-THP-Pam) vs Pretargeting at t = 24 h (27 h post THP-Pam injection) vs Negative control (neutralised ^{68}Ga); (B) Image quantification

comparison of Pretargeting at two time points and negative control: Pretargeting at t = 2 h vs pretargeting at t = 24 h vs Negative control; (C) Heat map comparison between three experimental groups at t= 24 h time point; and (D) Heat map comparison between three experimental groups at t = 2 h time point. 137

Figure 3.1. The components of an two main biorthogonal reactions used for pretargeting: (A) Azide attached to a targeting molecule R_1 reacts with DBCO (dibenzocycloocotene) attached to an imaging molecule R_2 in physiological conditions to provide a conjugate (B) Transcyclooctene attached to a targeting molecule R_1 reacts with tetrazine attached to an imaging molecule R_2 in physiological conditions to provide a conjugate. 141

Figure 3.2 Pretargeting PET imaging study by iorthogonal covalent ^{18}F-labeling: (A) The procedure of the biorthogonal SPAAC reaction for the DBCO-PEG-MSN-pretargeting PET-imaging study; (B) Negative control: PET-CT images of non-pretargeted ^{18}F-labeled azide in a U87 MG tumour-bearing mouse; (C) Pretargeting group: Mouse given DBCO-PEG-MSNs 24 h earlier in a U87 MG tumour-bearing mouse recorded at 15, 30, 60, and 120 min after injection of before ^{18}F-labeled azide. T=tumour, K=kidneys.[332] 144

Figure 3.3 Timeline of the injection protocol employed for (a) pretargeted, (b) SNP positive control group (^{64}Cu-DHP⊂SNPs), and (c) negative control group Cu-Tz. Preclinical *in vivo*-PET/CT images of the mice for each group at 24 h p.i. Labels T, L, K, and B refer to the tumour, liver, kidney, and bladder, respectively. Image reproduced.[354] 148

Figure 3.4. Scheme of the pretargeted nuclear imaging experiment for tumour targeting nanomedicine using IEDDA reaction compared to conventional nuclear imaging: The primary targeting agent is Peptobrush modified with trans-cyclooctene (TCO), and the secondary imaging agent is a ^{111}In labelled tetrazine (Tz). Top: Conventional nuclear imaging involving administration of the radiolabelled nanomedicine, administered, and allowed to circulate for days to achieve tumour accumulation up to 72 h. Bottom: Pretargeted nuclear imaging involving the TCO-modified Peptobrush (blue box) is administered and allowed to circulate until tumour accumulation followed by administration of radiolabelled Tz. Imaging is performed with the first few hours of the administration of Tz. Image reproduced.[355] 149

Figure 3.5. Schematic of the biorthogonal pretargeted imaging of PEGylated liposomes experiment: The pretargeted imaging involves administration of TCO modified PEGylated liposomes (TCO-PL-liposomes) in either healthy or tumour mice and allowing them to circulate and accumulate in organs of interest. This is followed by administration of small molecule imaging agent ^{68}Ga-THP-tetrazine followed by imaging of the mice after allowing enough time for interaction of the TCO-PL-liposomes and tetrazine *in vivo*. 151

Figure 3.6. Structure of the TCO-phospholipid conjugate (TCO-PL): The synthesised TCO-PL has three major components: TCO (biorthogonal reactive moiety), PEG2000 linker (allows for the TCO to available on the surface of the PEGylated liposomes), the phospholipid chain (gets embedded into the bilayer of the PEGylated liposomes)...... 152

Figure 3.7. Different combinations of surface modifications of liposomes: TCO-PEG2000 represents the TCO-PL synthesised in this chapter which has a PEG2000 chain.

The images above show how PEGylation of liposomes provide a brush like exterior to the liposomes and presence of PEG2000 in the TCO-PL allows TCO to be available at the surface for interactions with tetrazine imaging agent. 152

Figure 3.8. NMR spectra of TCO-PL: The synthesised TCO-PL is characterised by the presence of characteristic peaks of TCO incorporated in the phospholipid: δ 2.5 -CH; 5.5 =CH in cyclooctene. The integration of the peaks accounts for 283 out of 293 protons. The integration is not quantitative due to the relative high intensity of protons from ethylene peak of the PEG2000 chain which decrease the resolution of other peaks. ... 155

Figure 3.9. The mass spectrum of the TCO-PL (A) and DSPE-PEG2000 amine (B): The envelope nature observed in both spectra is due to the polydispersity of the PEG2000 chain which is characterised by a difference of 44 between each peak within the envelope. The TCO-PL is characterised by the higher m/z=2700-3700 compared to the lower m/z for DSPE-PEG2000 amine m/z=2400-3200. 156

Figure 3.10. Structure of the THP-tetrazine: the synthesised THP-tetrazine has two important components: Trishydroxypyridinone which is an excellent chelator for Ga as well as Fe, and Tetrazine (in the highlighted circle) which has high reactivity towards transcyclooctene (TCO). 157

Figure 3.11. Purification of THP-tetrazine: (A) HPLC chromatogram of the semi-prep HPLC method used for isolation of THP-tetrazine from the reaction mixture. Fraction collected between t_r =29 min-33 min contained the THP-tetrazine; (B) Mass spectra of the THP-tetrazine crude reaction mixture showing the THP-tetrazine as the major product alongside unreacted Methyl-tetrazine amine and hydrolysed THP; and (C) Mass spectra of the THP-tetrazine fraction collected after semi-prep HPLC showing the pure isolated THP-tetrazine. 158

Figure 3.12. NMR spectra of the THP-tetrazine: The synthesised THP-tetrazine was characterised by the presence of the above peaks. The spectrum was recorded in CD_3CN/D_2O due to low solubility in $CDCl_3$. ^1H NMR (400 MHz) δ 8.43-8.41(m, 2H Ar-H from tetrazine), 7.25-7.58(6H from N-H), 6.96 (m, 6H from Ar-H from tetrazine), 4.89(s, 3H from Ar-H from THP), 4.54 (s, 2H), 3.79-3.82 (m, 9H from CH_3-N, 8H from CH_2-N), 3.01(s, 2H) 2.48(s, 3H), 2-42-2.44 (m, 2H), 2.11-2.15 (m, 4H), 1.95 (m, 9H), 1.85 (s, 2H), 1.25 (d, 4H). Non-deuterated solvent H_2O and CD_3CN impurity peaks are also observed in the spectrum. 160

Figure 3.13. Radiolabelling of THP-tetrazine: (A-D) radioTLC chromatogram: (A) ^{68}GaCl3 (R_f=0) in citrate buffer; (B) ^{68}Ga-THP-tetrazine(R_f=1) in citrate buffer; (C) ^{68}Ga-THP-tetrazine in 80% v/v ammonium acetate/methanol; (D) SEP-PAK purified ^{68}Ga-THP-tetrazine in 80% v/v ammonium acetate/methanol(R_f=0.8-1 for ^{68}Ga-THP-tetrazine and R_f=0 for lipophilic impurity); (E-F) radioHPLC chromatogram: (E) ^{68}Ga-THP-tetrazine characterised using analytical radioHPLC method 3; (F) SEP-PAK purified ^{68}Ga-THP-tetrazine characterised by analytical radioHPLC method 3. 162

Figure 3.14. Characterisation of liposomes using Nanoparticle Tracking Analysis (NTA) to determine concentration and size distribution: (A) PEG(2k)-liposomes (concentration: $2.88 \times 10^{16} \pm 2.17 \times 10^{15}$ particles/mL, mode:97.8 nm, mean: 116.2 nm); (B) TCO-PL-

liposomes (concentration: $3.74 \times 10^{15} \pm 2.36 \times 10^{14}$ particles/mL, mode: 93.1 nm, mean: 110.6 nm) 166

Figure 3.15. Cryo-electron microscopy of liposomes pre- and surface post-modification with TCO-PL: (A) showing TCO-PL-liposomes have retained their spherical nature and the size distribution is not altered by insertion of TCO-PL into the bilayer of liposomes and bilayer nature is also retained; (B) showing PEG(2k)-liposomes spherical morphology and bilayer structure. Size quantification of liposomes from analysis of cryoEM images showing frequency distribution of diameter of liposomes: (A) Unmodified PEG(2k)-liposomes; (B) TCO-PL-liposomes........ 167

Figure 3.16. Serum stability assessment of ^{68}Ga-THP-tetrazine using HPLC SEC method 4: (A) RadioHPLC chromatogram of serum incubated ^{68}Ga-THP-tetrazine at t = 15 minutes; (B) RadioHPLC chromatogram of serum incubated ^{68}Ga-THP-tetrazine at t = 3 hours; RadioHPLC chromatogram species: serum bound ^{68}Ga (t_r= 9 min), ^{68}Ga-THP-tetrazine (t_r = 20 min). 169

Figure 3.17. Radiolabelling of TCO-PL-liposomes: *In vitro* biorthogonal pretargeting was performed to validate the TCO/tetrazine pretargeting system. Two different *in vitro* biorthogonal pretargeting experiments were performed where TCO-PL-liposomes were incubated in either PBS or serum followed by addition of ^{68}Ga-THP-tetrazine and incubation at 37°C for 30 minutes. The incubated samples were then purified via size exclusion chromatography and radioactivity attached to the TCO-PL-liposomes was determined. Unmodified PEG(2k)-liposomes were labelled as controls. The experiments showed showing % radiolabelling of 75 ± 2 % (n=3) and 61.7 ± 3.1 % (n=3) for PBS and serum incubated samples respectively. 170

Figure 3.18. Scheme of *in vivo* pretargeting PET experiments: Negative control: administration of ^{68}Ga-THP-tetrazine; pretargeting test group: administration of TCO-PL-liposomes followed ^{68}Ga-THP-tetrazine; Positive control group: administration of ^{67}Ga-TCO-PL-liposomes. 172

Figure 3.19. Negative control *in vivo* group (n=4): (A) Schematic of the negative control group (B) PET image of healthy animal administered with ^{68}Ga-THP-tetrazine at 1 h p.i.; (C) Biodistribution at 2 h p.i. after the PET scan; (D) Image quantification performed on the PET images acquired at 1 h p.i........ 174

Figure 3.20. Positive control *in vivo* group (n=4): (A) Schematic of the positive control group; (B) SPECT image of healthy animal administered with ^{67}Ga-TCO-PL-liposomes at t = 1 h and t = 24 h; (C) Biodistribution at 28 h p.i. (t = 25 h) after the SPECT scan; (D) Image quantification performed on the SPECT images acquired at both time points 175

Figure 3.21. Pretargeting test *in vivo* group(n=4): (A) Schematic of pretargeting test group (B) PET image of animal administered with TCO-PL-liposomes followed by administration of ^{68}Ga-THP-tetrazine at t = 0 h and PET scan at t = 1 h, and at t = 23h and PET scan at t = 24 h; (C) Biodistribution at t = 25 h after the PET scan; (D) Image quantification performed on the PET images acquired at both time points........ 177

Figure 3.22. Biorthogonal *in vivo* pretargeting experiments in fibrosarcoma tumour model: (A) shows tumour growth curve for the different animals against the number of days post inoculation with WEHI-164 cells. The tumour growth is plotted as tumour volume and calculated using the formula V= 0.5*l*b*h; (B) Scheme of *in vivo* pretargeting PET experiments: Negative control: administration of ^{68}Ga-THP-tetrazine; pretargeting test group: administration of TCO-PL-liposomes followed ^{68}Ga-THP-tetrazine; Positive control group: administration of ^{67}Ga-TCO-PL-liposomes. 179

Figure 3.23. Negative control *in vivo* group for tumoured animals(n=4): (A) Schematic of the negative control group; (B) PET image of mice administered with ^{68}Ga-THP-tetrazine at 1 h p.i. (dotted circle shows the tumour region); (C) Biodistribution at 2 h p.i. after the PET scan; (D) Image quantification performed on the PET images acquired at 1 h p.i.. 180

Figure 3.24. Positive control *in vivo* group for tumoured animals(n=4): (A) Schematic of the positive control group; (B) SPECT image of animal administered with ^{67}Ga-TCO-PL-liposomes at 4 h p.i.(t = 1 h), 27 h p.i.(t = 24 h), 51 h p.i.(t = 48 h), 75 h p.i.(t = 72 h)(S-spleen, L-liver, dotted circle-tumour); (C) Tranverse section of SPECT images showing tumour cross-section at different time points, tumour highlight within dotted circular lines (D) Biodistribution at 52 h p.i. (t = 49 h) after the SPECT scan.................................. 181

Figure 3.25 Image analysis of the positive control group SPECT images recorded at different time points: Tissue accumulation of radiolabelled liposomes ^{67}Ga-TCO-PL-liposomes in tumour, heart, liver, spleen and muscle at different time points (A) 4h, (B) 24 h, (C) 48 h, (D) 72 h; (E) Variation of observed uptake of liposomes in different organs with time; (F) Variation of T/M contrast over different time points of scanning. 182

Figure 3.26. Pretargeting test *in vivo* group for tumoured animals(n=4): (A) Schematic of the pretargeting test group; (B) PET image of animal administered with TCO-PL-liposomes followed by administration of ^{68}Ga-THP-tetrazine at t = 23h and PET scan at t = 24 h; (C) Biodistribution at t = 25 h after the PET scan; (D) Image quantification performed on the PET images acquired. 184

Figure 3.27. Comparative analysis among different groups of the pretargeting tumour study: (A) Comparison of the biodistribution of the different experimental groups. The uptake observed in the liver and spleen for the pretargeting test groups is higher compared to negative control group ($p<0.05$); (B) Comparison of the tumour uptake values observed for negative control and the pretargeting test group. Differences observed in tumour uptake values for the groups was non-significant; (C) Autoradiography of tumour obtained from pretargeting test group showing accumulation of radioactivity was observed on the margins and not spread all over the tumour; (D) Autoradiography of tumour obtained from the positive control group showing the accumulation of radioactivity all over the tissue. 186

Figure 4.1. Blood-brain barrier: Different components of the BBB vasculature including pericytes, astrocytes, basement membrane, tight junctions (left); Different mechanisms of transport of molecules across the blood-brain barrier: (A) Transcellular lipophilic pathway (lipid-soluble agents); (B) Paracellular aqueous pathway (water-soluble agents); (C) Transport proteins (Glucose, amino acids, nucleosides); (D) Receptor-mediated

transcytosis (Insulin, transferrin); (E) Adsorptive transcytosis (Albumin, plasma proteins); (F) Efflux pumps (PgP mediated)(right) 193

Figure 4.2. Focussed ultrasound and microbubbles: Top: Schematic of mechanism of blood brain barrier opening using focussed ultrasound and microbubbles: (a) Microbubbles (big sphere) and drug molecule (small sphere) injected into the bloodstream; (b & c) Blood brain barrier opening and releasing drugs due to contraction and expansion of microbubbles.[494] Bottom: Rapid short pulse overlayed and compared from conventional long pulse sequence.[424] 197

Figure 4.3. Graphical abstract of the chapter: Delivery of fluorescently labelled PEGylated liposomes to the brain using conventional long pulse and novel RaSP FUS sequence. 201

Figure 4.4. DiD-PEGylated liposomes (DPLs): (A) The carbocyanine dye DiD is incorporated in the phospholipid bilayer of the PEGylated liposome due to its hydrophobic nature. (B) The hydrodynamic size distribution polydispersity index (PDI, measure of size distribution), and zeta potential of the PEGylated liposomes show negligible changes (n = 4) before and after incorporation of the dye. (C) Size-exclusion chromatograms show the stability of the DPLs (fluorescent liposomes) post-incubation in human serum and 37 °C for up to 48 h and confirm high retention of the dye within the liposomes. Fractions 8–10 contained the liposomes and fractions 12–25 contained the serum proteins. The high fluorescence signal in fractions 8–10 at both time points confirmed the retention of DiD in the liposomes up to 48 h. (D) Serum stability curve shows % dye associated with the liposomes post-incubation in serum at time points 0, 3, 12, 18, 24, and 48 h. 203

Figure 4.5. DiD: The structure of lipophilic, fluorescent, and cationic dye DiD (1,1′-Dioctadecyl-3,3,3′,3′-tetramethylindodicarbocyanine, 4-Chlorobenzenesulfonate Salt) 203

Figure 4.6. Liposomal delivery with rapid short-pulse (RaSP) and long pulse sequences at 0.4 and 0.6 MPa, and at 0 and 2 h after ultrasound treatment: Fluorescence images (10x) show examples of liposomes delivered with (A, C, E, G) RaSP and (B, D, F, H) long pulse sequences at (A-D) 0.4 MPa and (E-H) 0.6 MPa, and at either (A-B, E-F) 0 h or (C-D, G-H) 2 h after the ultrasound treatment. Right hippocampus control regions are shown in white boxes in the bottom right corner of each image. (A, C) No delivery was observed at 0.4 MPa when brains were treated with a RaSP sequence. (E-H) At 0.6 MPa, delivery was observed in all brains. More spots of delivery were observed in long-pulse-treated brains compared to RaSP-treated brains. The scale bars indicate 50 µm. 206

Figure 4.7. Detected dose of liposomes delivered with rapid short-pulse (RaSP) and long pulse sequences at 0.4 and 0.6 MPa, and at 0 h or 2 h after the ultrasound treatment: The threshold for liposomal delivery with RaSP was found to be between 0.4 and 0.6 MPa. The detected dose, quantified with the normalised optical density (NOD), was higher at 0.6 MPa for both RaSP and long pulse sequences (P < 0.05). The detected dose was only found to be significantly different between 0 h (green) and 2 h (purple) in long-pulse-treated brains at 0.4 MPa (P < 0.05). Significance was also found between RaSP 0.4 MPa (0 h) and all higher pressures and long pulse brains; between RaSP 0.4 MPa (2 h) and all higher pressures and long pulses 0.4 MPa (2 h) brains; between long 0.4 MPa (0 h) and

both sequence types at 0.6 MPa (0 h) brains; and between long 0.4 MPa (2 h) and long 0.6 MPa (0 h) brains ($P < 0.05$). For clarity, significance bars were only shown between 0 h and 2 h results and not between different pressures or sequence types. 207

Figure 4.8. Distribution of liposomes delivered with rapid short-pulse (RaSP) and long pulse sequences at 0.4 and 0.6 MPa, and at 0 h or 2 h after the ultrasound treatment: A lower coefficient of variation (COV) was calculated in RaSP-treated brains compared to long-pulse-treated brains, which indicates less variation and therefore a more homogenous distribution. The COV was not found to be significantly different between 0 h (green) and 2 h (purple) recovery times ($P > 0.05$). However, significant differences in COV were found between long pulse brains at 0.4 MPa (0 h) and RaSP brains at 0.6 MPa (0 h); between RaSP brains at 0.6 MPa (0 h and 2 h), and long pulse brains at 0.6 MPa (0 h). The COV was not quantified for RaSP-treated brains at 0.4 MPa as no liposomal delivery was observed in these brains. For clarity, significance bars were not shown between different pressures or sequence types. 210

Figure 4.9. Number of areas with liposome delivery above 100 µm^2: The number of areas above 100 µm^2 with liposome delivery was found to be higher in long pulse compared to RaSP-treated brains with the same acoustic pressures. Increasing the acoustic pressure, increased the number of delivery regions. In addition, waiting for 2 h instead of 0 h, led to an increase in the number of delivery spots only in long-pulse-treated brains. Significant differences were found between RaSP 0.6 MPa brains and long 0.6 MPa 2 h brains ($P < 0.05$). The areas of delivery were not quantified for RaSP-treated brains at 0.4 MPa as no liposomal delivery was observed in these brains. For clarity, significance bars were not shown between different pressures or sequence types. 212

Figure 4.10. Number of areas with liposome delivery above 500 µm^2: The number of areas above 500 µm^2 with liposome delivery was found to be higher in long pulse compared to RaSP-treated brains. Increasing the acoustic pressure, also increased the number of delivery regions. In addition, waiting for 2 h instead of 0 h, led to an increase in the number of delivery spots only in long-pulse-treated brains ($P < 0.05$ at 0.4 MPa). Significant differences were found between long 0.4 MPa brains and all 2 h wait 0.6 MPa brains; between RaSP 0.6 MPa brains and long pulse 0.6 MPa brains at 2 h ($P < 0.05$). The areas of delivery were not quantified for RaSP-treated brains at 0.4 MPa as no liposomal delivery was observed in these brains. For clarity, significance bars were not shown between different pressures or sequence types. 213

Figure 4.11. Subcellular localisation of liposomes: A and B panel confocal images of different slices of brain with evidence of liposome delivery (20x) show details of the subcellular localisation of the liposomes within ultrasound-targeted regions. These specific examples are from long-pulse-treated brains at 0.6 MPa and two hours after the ultrasound treatment. Fluorescence was observed within cells, specifically within the cytoplasm and not in the nucleus (darker circular centre within cells). Morphologically these cells with uptake appear to be neuron-like cells. The scale bars indicate 50 µm. 214

Figure 4.12. Uptake of liposomes within neurons in RaSP and long pulse-treated brains: Fluorescence images (10x) show liposome uptake within neurons in (A,C) RaSP-treated brains and (B,D) long-pulse-treated brains. Uptake was higher in long-pulse-treated brains than in RaSP ones. White arrows highlight examples of liposome uptake within neurons. The scale bars indicate 50 µm. 218

Figure 4.13. Number of neurons with liposome uptake in brains treated with RaSP or long pulses at 0.4 or 0.6 MPa, and at 0 h or 2 h after the ultrasound treatment: Neuronal uptake was observed in all brains where delivery was observed. However, more so in long-pulse-treated brains at 0.6 MPa than at the lower pressure or in RaSP-treated brains. This plot displays the average number of neurons with uptake across the evaluated brain slices. No statistical analysis was performed as the sample size was too small. 219

Figure 4.14. Uptake of liposomes within microglia in RaSP and long pulse-treated brains: Fluorescence images (10x) show liposome uptake within microglia in a (A) RaSP-treated brain slice and a (B) long-pulse-treated brain slice. White arrows highlight examples of liposome uptake within microglia. The scale bars indicate 50 µm. 220

Figure 4.15. Number of microglia with liposome uptake in brains treated with RaSP or long pulses at 0.4 or 0.6 MPa, and at 0 h or 2 h after the ultrasound treatment: Microglial uptake was only observed in 0.6 MPa brains 2 h after ultrasound treatment. Higher uptake was observed in long-pulse-treated brains compared to RaSP ones. This plot displays the average number of microglia with uptake across the evaluated brain slices. No statistical analysis was performed as the sample size was too small. 220

Figure 4.16. Uptake of liposomes within astrocytes in RaSP and long pulse-treated brains: Fluorescence images (10x) show no liposome uptake within astrocytes in (A-B) RaSP-treated brains and (C-D) long pulse-treated brains. The scale bars indicate 50 µm. 221

Figure 4.17. H&E staining on RaSP-treated brains at 0.6 MPa to assess tissue damage: Microscopic examination of H&E stained (A-C) left (targeted) and (D-F) right (control) hippocampi of RaSP-treated brains show (C) a single site of red blood cell extravasation (arrows), but no histological damage in all other regions and brain slices. The black boxes show the enlarged regions in the middle and right columns respectively. The scale bars indicate 50 µm. 222

Figure 4.18. H&E staining on long-pulse-treated brains at 0.6 MPa to assess tissue damage: microscopic examination of H&E stained (A-C) left (targeted) and (D-F) right (control) hippocampi of long-pulse-treated brains show (B-C) histological damage at multiple sites within the ultrasound targeted hippocampus (arrows): red blood cell extravasation, microvacuolations and dark neurons. The black boxes show the enlarged regions in the middle and right columns respectively. The scale bars indicate 50 µm. 223

Figure 4.19. Number of sites with red blood cell extravasations, microvacuolations and dark neurons in RaSP and long pulse brains at 0.6 MPa: The average number of sites with more than five extravasated red blood cells (RBCs), microvacuolations and dark neurons is shown for (blue) RaSP and (orange) long-pulse-treated brains. This quantification was performed on nine H&E-stained slices per brain. In all RaSP brains, only one site with more than five extravasated RBCs and no sites with microvacuolations or dark neurons were observed. In long pulse brains, however, damaged sites were found in all brains. No significant differences were found between RaSP and long pulse brains ($P > 0.05$). .. 224

Figure 4.20. Autoradiography of the brain-stained tissue slices. 228

Figure 5.1. Synthesis of THP-PL: DSPE-PEG2000 amine was reacted with the isothiocyanate derivative of THP to give the THP-PEG-phospholipid (THP-PL) 237

Figure 5.2. Synthesis of THP-PL-liposomes: THP containing PEGylated liposomes are synthesised by insertion of THP-PL in preformed liposomes at mild heating below the phase transition temperature. The purified liposomes are radiolabelled to confirm the incorporation of THP on the liposomal surface as shown above. 238

Figure 5.3. Scheme of *in vivo* pretargeting experiment using metal chelation approach: Negative control: Group 1: $^{68}GaCl_3$; Pretargeting: Group 2: THP-PL-liposomes followed by introduction of $^{68}GaCl_3$; Positive control: Group 3: ^{67}Ga-THP-PL-liposomes 243

Figure 5.4. Scheme of blood kinetic study to determine the blood half-life of THP-PEG-PL liposomes 244

Figure 5.5. Scheme of pretargeting experiment of bone tracer THP-Pam using metal chelation approach: Negative control: Group 1: $^{68}GaCl_3$; Pretargeting: Group 2: THP-Pamidronate followed by introduction of $^{68}GaCl_3$; Positive control: Group 3: ^{67}Ga-Palmidronate 245

Figure 5.6. Procedure for purification of liposomes using size exclusion chromatography column. 251

Figure 5.7. Synthesis of TCO-PL: DSPE-PEG2000 amine was reacted with NHS ester derivative of TCO to give the Phospholipid-TCO conjugate (TCO-PL) 252

Figure 5.8. Synthesis of THP-tetrazine 253

Figure 5.9. Synthesis of TCO-PL-liposomes: Insertion of TCO-PL conjugate into the lipid bilayer of preformed PEGylated liposomes at mild heating below phase transition temperature 254

Figure 5.10. Scheme of *in vivo* pretargeting experiment of TCO liposomes using biorthogonal chemistry in healthy animal. 261

Figure 5.11. Scheme of *in vivo* pretargeting experiment of TCO liposomes using biorthogonal chemistry in tumoured animal. 263

Figure 5.12. Ultrasound experimental setup: Ultrasound was focused through the intact scalp and skull onto the left hippocampus of the mouse's brain while the right hippocampus was used as a control (no ultrasound). Ultrasound pulses were emitted from the therapeutic transducer (1 MHz) driven by one or two function generators through a 50-dB amplifier and an impedance matching network. A 7.5 MHz passive cavitation detector captured the acoustic emissions from the microbubbles, which were filtered by a band pass filter, amplified by a 28-dB pre-amplifier and recorded by an 8-bit oscilloscope. 268

Figure 5.13. DiD-PEGylated liposome structure. The liposomes consist of a phospholipid bilayer with PEG brushes attached to the surface for biocompatibility and the DiD fluorophore embedded within the lipid bilayer to enable ex vivo fluorescence detection of the liposomes. 270

LIST OF TABLES

Table 1.1 Different liposomal formulations approved for clinical use by FDA (Food and Drug administration, USA Regulatory body) and EMA (European Medicines Association, European pharmaceutical regulatory body) for different ailments 43

Table 1.2 shows the EPR heterogeneity: variability of radiolabelled liposome uptake in tumours: variability within the same stage (in red), variability within the same tumour type (in yellow); variability within different tumour types (in blue)[83] 54

Table 1.3 shows the comparison of different imaging modalities depending on parameters such as resolution, penetration depth and suitability for applications in nanomedicine 59

Table 1.4. Therapeutics radionuclides for applications radionuclide therapy 71

Table 1.5 Commonly used PET radionuclides for radiolabelling of liposomal nanomedicines 75

Table 1.6. Commonly used SPECT radionuclides for radiolabelling of liposomal nanomedicines 76

Table 1.7. Advantages and disadvantages of pretargeted imaging in nanomedicine over conventional imaging methods 91

Table 5.1. Summary of mice used in each study: Twenty-four mice were used to compare the delivery and distribution of liposomes with RaSP or long pulse sequences at 0.4 or 0.6 MPa either immediately or 2 h after the ultrasound treatment. Twelve mice were used to assess tissue damage with haematoxylin and eosin (H&E) staining at the two acoustic pressures and with the two sequence types at 0 h. 269

Table 5.2. Primary and secondary antibodies used to stain for neurons, microglia and astrocytes 272

Table 5.3. Excitation and emission filters for the fluorophores: Excitation and emission filters are given as the centre wavelength and the bandwidth. 273

Table 7.1. Biodistribution data from the THP-PL-liposomes pretargeting experiment on healthy animals 283

Table 7.2. Biodistribution data from the THP-PL-Pam pretargeting experiment on healthy animals 283

Table 7.3. Biodistribution data from the TCO-PL-liposomes pretargeting experiment on healthy animals 284

Table 7.4. Biodistribution data from the TCO-PL-liposomes pretargeting experiment on tumour animals 284

1 INTRODUCTION

1.1 Nanomedicines: Efficient drug delivery systems

More than a century ago, Nobel laureate Paul Ehrlich coined the term “magic bullet” in the Harben lectures in London.[1] The “magic bullet” is a unit that can identify a specific target and then deliver drugs to that identified target. The magic bullet theory encompasses three key components: *i*) a targeting molecule, *ii*) a drug molecule, and *iii*) a drug molecule carrier vehicle.[2] The nanomedicine concept embodies the principle of a magic bullet which has allowed their development as therapeutic delivery agents, diagnostic agents and recently for the design of personalised precision therapeutics.[3,4]

Nanomedicines are nanoparticles with varied applications in healthcare which can be characterised as nanosized units (ranging from 1–500 nm) for use in therapeutics, diagnostics, and disease prevention.[5,6] These nanomedicines can be produced in different forms (gold, iron oxide-based nanoparticles and contrast loaded drug delivery systems), and have found applications in the detection of multiple diseases, delivery of drug molecules to specific targets (actively and passively targeted liposomes, polymers, micelles), their controlled release at the site of action at high concentration and, more recently, as mRNA LNPs in the field of disease prevention in the form of vaccines.[7–10] With the increased interest in the field of precision medicine, nanomedicines have emerged as a key player in the form of precision nanomedicine because of their easily adaptable physicochemical properties to cater to personalised therapeutic needs.[4]

Nanomedicine research appeared on the drug delivery horizon around the 1990s with an ever-increasing interest during the last three decades. The field gained significant momentum due to increased funding in the United States followed by FDA approval of the first nanomedicine drug, Doxil/Caelyx for use in clinics.[11] This led to increased research in Europe with the formation of the European Technology Platform on Nanomedicine (ETPN) which defines “nanomedicine” as the application of nanotechnology to achieve breakthroughs in healthcare that exploits the improved and often novel physical, chemical and biological properties of materials at the nanometre scale".[9] Like the FDA, the European Medicines Agency (EMA) has approved multiple nanomedicines for clinical use with the first one being AmBisome, an amphotericin B containing liposomes for fungal infections.[12,13] EMA designates nanomedicines as a drug delivery system for clinical application involving nanoparticles as a component to provide improved targeting, therapeutic carrying capacity, and better modes of action.[14,15] The applications of nanomedicines have been mostly explored in the oncology field, mainly as diagnostics and therapeutics. They have been utilised either as encapsulated carriers (*e.g.,* liposomes) of chemotherapeutic molecules[16,17,18] or as therapeutics themselves like gold and iron oxide nanoparticles which act as thermal agents in photothermal therapy.[19,20] Recent developments include nanomedicines being used as radiosensitizers and in radiotherapy which has opened a new field of research.

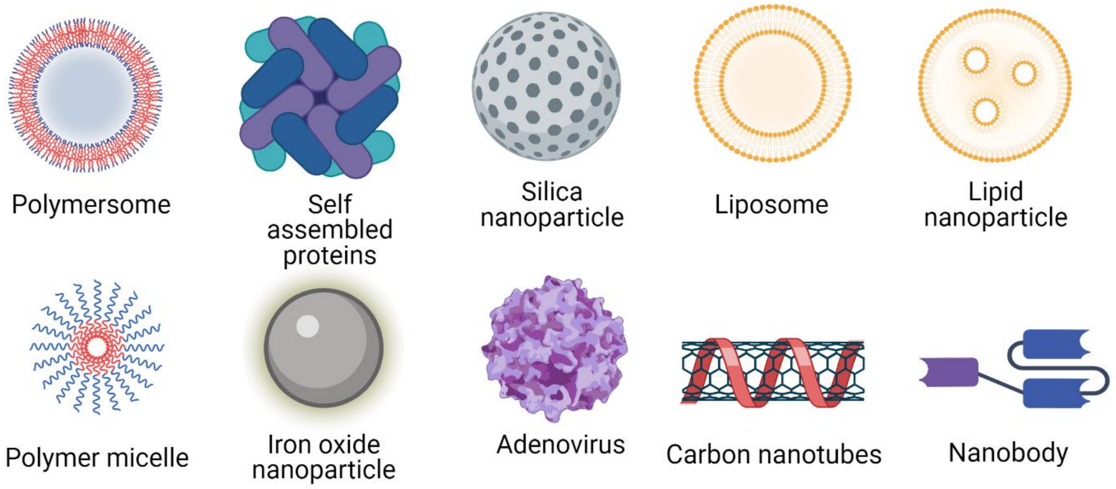

Figure 1.1 Nanomedicines: Different nanoparticle types with drug-carrying/therapeutic potential in a clinical or preclinical setting including metallic nanoparticles, lipid-based nanoparticles, polymeric nanoparticles and biological nano therapeutic vectors. Created with BioRender.com.

The first nanomedicine with clinical use approval in the US was Doxil®/Caelyx (Doxorubicin containing PEGylated liposomes) in 1995 for the treatment of Kaposi's sarcoma and ovarian cancer.[21] Next year, DaunoXome® (Nexstar Pharmaceuticals), daunorubicin containing liposomes, was approved by the US FDA for the treatment of advanced HIV-associated Kaposi sarcoma.[22] Following the success of these two drug delivery agents, multiple nanomedicines have made a clinical impact on the treatment of multiple diseases as summarised in Table 1.1.[23]

As evident in Table 1.1, liposomal nanomedicines have been a forerunner for inflammation and cancer therapeutics and have made a significant clinical impact. Specifically, the PEGylated liposomal version exhibiting steric stability has dominated the translational landscape by securing clinical approvals for different therapeutics.[24] Liposomes have been successful in the clinical setting and pushed towards precision nanomedicine due to their versatility in carrying both hydrophobic and hydrophilic drugs, their surface characteristics, targeting abilities and foremost their bilayer membrane structure which bears similarity to cell membrane structure.[25] In the next section, we will discuss liposomal nanomedicines in more detail.

Table 1.1 Different liposomal formulations approved for clinical use by FDA (Food and Drug administration, USA Regulatory body) and EMA (European Medicines Association, European pharmaceutical regulatory body) for different ailments

NAME OF THE NANOMEDICINE	AILMENT	LIPID COMPOSITION	DRUG/ACTIVE COMPOUND	SIZE (IN NM)	APPROVAL YEAR
DOXIL/CAELYX	Breast, ovarian cancer, and Kaposi sarcoma	HSPC, cholesterol, PEG 2000-DSPE (56:39:5)	Doxorubicin	100	FDA 1995 EMA 1996
AMBISOME	Fungal infections	HSPC, DSPG, cholesterol, amphotericin B (2:0.8:1:0.4)	Amphotericin B	45-80	FDA 1997 EMA 2006
DAUNOXOME	HIV-related Kaposi sarcoma	DSPC, cholesterol, daunorubicin (10:5:1)	Daunorubicin	45-80	FDA 1996 EMA 2004
MYOCET	Metastatic breast cancer	EPC, cholesterol (55:45)	Doxorubicin hydrochloride and anthracycline	190	FDA 2000 EMA 2000
DEPOCYT	Lymphomatous meningitis	Cholesterol, triolein, DOPC, DPPG (11:1:7:1)	Cytarabine	20	FDA 1999 EMA 2001
MARQIBO	Acute lymphoblastic leukaemia	Sphingomyelin, Cholesterol (60:40)	Vincristine	100	FDA 2012 EMA 2012
ONIVYDE	Pancreatic cancer	HSPC, cholesterol, PEG 2000-DSPE (56:39:5)	Irinotecan	80-140	FDA 2015 EMA 2011
ONPATTRO **PATISIRAN-LNP**	Hereditary transthyretin amyloidosis	DLin-MC3-DMA, Cholesterol, DSPC, PEG2000-C-DMG	Patisiran sodium (siRNA)	-	FDA 2018 EMA 2018
VISUDYNE	Ocular Histoplasmosis	EPG, DMPC (3:5)	Verteporphin	100	FDA 2000 EMA 2000
MODERNA COVID-19 VACCINE	Antibody production against SARS-CoV-2	SM-102, PEG2000-DMG, DSPC, Cholesterol	Synthetic mRNA-1273	70-100	FDA 2020 EMA 2020

1.1.1 Liposomes

Liposomes were discovered as lyotropic smectic mesophases by Alec D. Bangham in Cambridge, United Kingdom in 1964. They were obtained from phosphatidylcholine and cholesterol of varying concentrations dispersed in water and observed under an electron microscope post-staining using potassium phosphotungstate.[26,27] Thirty years later, liposomes were the first nanomedicines approved for cancer treatment. The variable favourable properties of liposomes as an efficient clinical drug carrier include biocompatibility, low toxicity, and high drug-carrying capacity.[28,29] Recently, liposomes have had a renewed interest as nucleic acid-based therapeutic delivery vehicles and made an immediate widespread clinical impact as RNA-based vaccines in the form of both the Pfizer BioNTech and Moderna CoVID19 vaccines.[30]

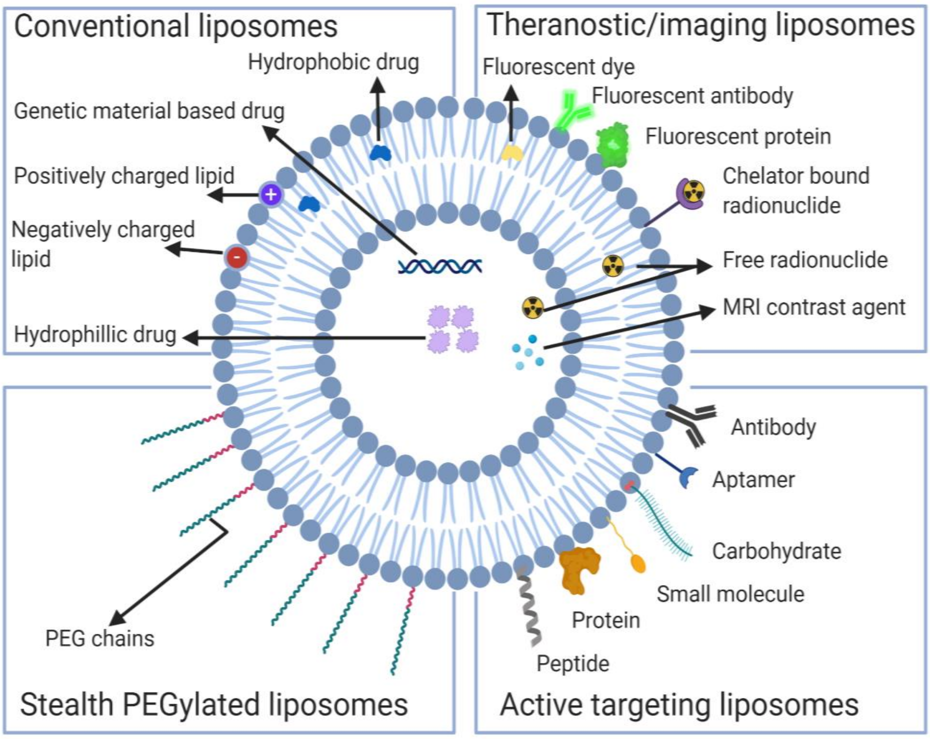

Figure 1.2. Versatility of liposomal nanomedicines as a drug-delivery vehicle: Conventional liposomes possess the ability to carry hydrophilic, hydrophobic and genetic material-based drugs; Stealth PEGylated liposomes with PEG modification for passive targeting with long blood circulation half-life; Active targeting liposomes for different targeting vectors on the surface for targeted accumulation on different biological targets; and Theranostic liposomes for imaging as well as drug delivery applications using different modalities. Created with BioRender.com.

1.1.1.1 Structure of liposomes

Liposomes are bilayered membranous round vesicles of varying compositions of amphiphilic phospholipids and cholesterol. They are formed by the dispersion of lipids in aqueous solvents with a hydrophilic (aqueous) core and a hydrophobic bilayer. This dual environment allows them to encapsulate both hydrophobic (*e.g.,* poorly water-soluble doxorubicin encapsulated in PEGylated liposomes: Doxil®) and hydrophilic (e.g., antifungal amphotericin B in liposomes: Ambisome®) therapeutics immersed in the phospholipid bilayer by Van der Waals forces.[31,32] (Figure 1.2, Figure 1.3).

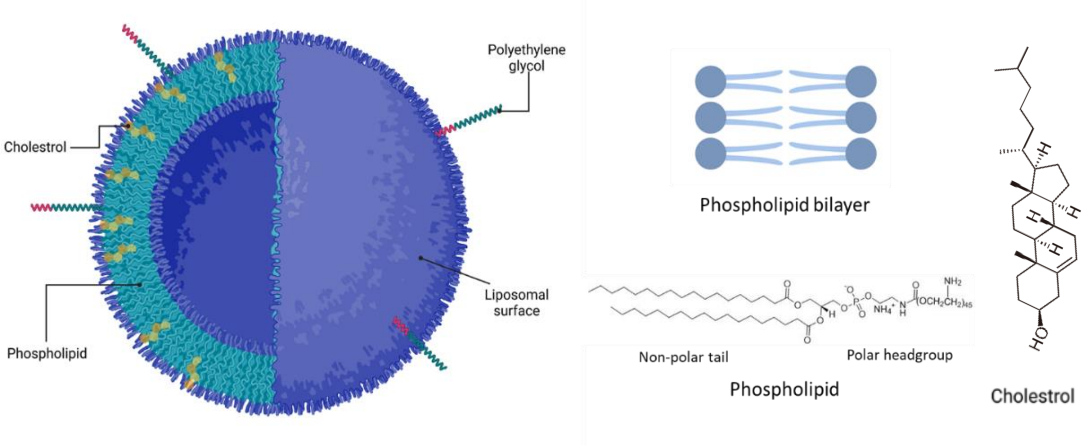

Figure 1.3. Components of a liposome: cross-section of an empty PEGylated liposome (right); Structure of a phospholipid bilayer, cholesterol, and a phospholipid molecule**.** Created with BioRender.com.

The resemblance of the amphiphilic phospholipid bilayer of liposomes to the eukaryotic cell membrane is the key characteristic that enables them to stand out as drug delivery vehicles. This bilayer allows for the interaction of liposomes with the cell membrane and utilizes efficient pathways for cellular uptake. The amphiphilic phospholipids that form bilayers consist of the following: a phosphate group, a glycerol molecule, saturated or unsaturated fatty acid chains attached to the glycerol molecule and finally the phosphate group modified with amino alcohol via an ester bond.[33,34] (Figure 1.3) The different components of phospholipids are key to providing specific characteristics to liposomes, including drug encapsulation, targeting, and entry into the mammalian cell. Since the mammalian cell membrane consists of various phospholipids that play an important role in cellular events, both liposomal and cell membranes coexist and dictate the drug release mechanism at target cells.[35]

The composition of the liposomes affects their size, surface charge, and lamellarity. The critical micelle concentration (CMC) is an important parameter affecting liposome formation and its properties. The ability of the mixture of the amphiphilic phospholipids to undergo self-aggregation to give lamellar vesicles such as liposomes is dependent on the CMC. A concentration of lipids below the CMC leads to monomeric dispersion of phospholipids rather than liposomes. However, at the CMC, the lipids show self-aggregation to produce micelles with characteristic physical properties different from the monomers. The CMC values are dependent on the structure and properties of the amphiphilic lipids including the hydrophobic end (fatty acids chains) and a hydrophilic end (phosphate group).[36]

In addition to the CMC, the other key property that affects the formation of the liposome and its membrane characteristics is the transition temperature (T_c) of phospholipids.[37] The transition temperature indicates the temperature at which there is a change in the physical state of the phospholipids from the solid gel phase (ordered), characterised by the tightly packed and extended hydrocarbon chains, to the liquid crystalline phase (disordered phase), characterised by the randomly oriented and fluid hydrocarbon chains. Several factors affect the transition temperature, including the length of the fatty acid chain, the degree of fatty acid chain unsaturation, the charge, and headgroup species.[38,39] The increase in the chain length increases the van der Waals interactions and thereby increasing the amount of energy required to disrupt the packing and thus, an increase in transition temperature. On the other hand, the presence of double bonds decreases the packing order and decreases the energy required to break the order.[34,38,40] The above-mentioned effect of transition temperature on the phospholipids translates to an impact on the fluidity and permeability of the liposomal lamellae. Liposomes exhibit low fluidity and permeability at temperatures lower than T_c whereas, at temperatures over T_c, liposomes exhibit greater fluidity and permeability due to the phospholipid being in the liquid crystalline phase.[34,39,41] However, liposomes are known to exhibit a mixture of gel and crystal phase also termed as ripple phase which provides the liposomes with their characteristic spherical curvature. Thus, the T_c is responsible for the fluidity of the membranes of different liposomal formulations and plays a vital role in key liposomal functions such as formation, loading and release, the curvature of membrane, lipid transfer in cells and temperature dependence of the size of liposomes.

Researchers have utilised different T_c lipid formulations to form stimuli-responsive liposomes providing targeted drug release at the site of stimuli. At the mammalian body temperature of 37 °C, the bilayer structures and physical properties of liposomes are expected to be preserved to work efficiently as drug vehicles.[42,43] Moreover, the modulation of permeability and fluidity of liposomes at higher temperatures is an excellent way to develop ways of loading drugs, probes, and surface modifications on preformed liposomes which have been utilised during this thesis. In particular, the modulation of permeability has been utilised to incorporate the phospholipid conjugates THP-PL and TCO-PL, respectively, into the bilayer of the liposomes in **Chapter 2** and **Chapter 3** whereas the fluorescent dye DiD has been incorporated into the lipid bilayer at a temperature close to transition temperature in **Chapter 4** (*vide infra*).

The other aspect of phospholipids that makes a major impact on liposomal properties is the presence of different polar and non-polar groups. As discussed above, the modification of the tail can vary the T_c of phospholipids and thereby the properties of the liposomal lamella. The phospholipid head group controls the surface charge of the liposomes, and it can be either negative, positive, or neutral.[44] The surface charge of the liposomes alters their pharmacokinetics, stability, mechanism of cell uptake, and *in vivo* biodistribution. Positively charged phospholipids such as DAP and DOTAP form liposomes with an overall positive charge attracting them towards the negatively charged cell membrane, thereby increasing their cell uptake via endocytosis. They also show a higher clearance rate by the liver, lung, and spleen due to their high binding affinity toward plasma protein. However, the positive charge of these lipids makes them excellent for interacting with RNA or DNA, which has led them to play a vital role in the formulation of both Pfizer and Moderna vaccines.[30]

Neutral phospholipids such as DSPE and HSPC, have longer circulation times and in conjunction with negative lipids form the bulk of drug delivery systems. These neutral phospholipids are essential for fusion with the cell membrane for the subsequent release of drugs. The negative lipids are responsible for increasing the electrostatic repulsive force and preventing the aggregation of liposomes and binding to serum proteins.[45,46] The negatively charged liposomes are easily detected by macrophages and shown to accumulate in sites of inflammation and infection. Therefore, liposomes with a negative surface charge form the bulk of clinically approved drug delivery systems.[47–49]

Another important building block of liposomes alongside phospholipids is cholesterol (Figure 1.3). This sterol lipid is embedded in the phospholipid bilayers with its hydroxyl group aligned to the hydrophilic head and aromatic rings aligned with the lipophilic tail (Figure 1.3). Cholesterol serves both a structural and functional role in liposomes. Cholesterol affects the phase transition of liposomes playing a vital role in modulating the fluidity, thickness, and curvature of the liposomal bilayer. The surface charge is also affected by the presence of cholesterol thereby affecting their cell uptake and circulation.[50] Therefore, due to the above reasons, most clinically approved formulations contain cholesterol (Table 1.1) which acts as a liposome stabilizer and limits their interaction with serum proteins including globulin, albumin, transferrins, and other lipoproteins.[23]

The size of liposomes is also largely responsible for their pharmacokinetics, route of excretion, tissue(tumour) and cell extravasation, and blood half-life.[49,51] The clinically translated liposomes are in the hydrodynamic diameter range of 40-150 nm, allowing them to enter leaky vasculature of the tumours and fenestrations formed due to inflammation/infection.[48,49] The liposomal nanomedicines in the above size range also exhibit smooth circulation in well-perfused organs such as lungs, heart and kidney and thereby limiting their accumulation in these tissues.[52] Furthermore, the blood circulation times can be modulated by limiting the reactivity of liposomes towards opsonins and serum proteins. The animal-based lipid formulations such as sphingomyelin/cholesterol-based liposomes (*e.g.,* Marqibo) show a blood circulation half-life of several hours. However, the rapid clearance of conventional liposomes from the bloodstream was a major hurdle.[52,53]

To overcome this hurdle of rapid clearance of liposomes from the blood, the modification of the liposomal surface with the hydrophilic, large molecular weight polymer Polyethylene glycol (PEG) has emerged as the key approach. The presence of PEG increases their blood half-life by more than 10 times[54,55]. PEG-modified liposomes are also called PEGylated or stealth liposomes and usually have a hydrodynamic size of 90-150 nm, showing reduced interaction with serum proteins such as opsonin and thereby reduced clearance by the reticuloendothelial system. The opsonisation process is prevented by the formation of a water corona around the oxyethylene unit in PEG, which significantly increases the apparent molecular weight of liposomes leading to increased solubility and decreased aggregation.[53,56–58] The success of the stealth technology *via* PEGylation of liposomes has been proven in the clinically-approved anticancer liposome DOXIL, leading to an increase in the blood half-life from a few hours to a few days.[59] The various formulations of liposomes with or without PEGylation and different lipid/cholesterol and their applications have been listed in Table 1.1. The long blood circulation half-life of PEGylated liposomes can also be exploited for the delivery of therapeutic levels of drugs to the brain, which is a challenging task with conventional small-molecule drugs. However, the large size of the liposomal nanomedicines prevents their entry into the brain. This can be resolved using surface modifications of the liposomes, as well as physical methods of blood-brain barrier disruption allowing their entry into the brain as will be discussed in **Chapter 4**.

To summarise this section, the *in vivo* properties of liposomes depend on their constituents and size. Their ability to manipulate these properties according to the requirements while maintaining the advantages of high drug-carrying capacity, low systemic toxicity and passive/active targeting have made them a trailblazer in the field of nanomedicines. They have become the most explored, used and clinically relevant drug delivery system for cancer, infection, and inflammation.[60–64] A ligand-based targeting strategy can be added to specifically and actively target tissues of interest to improve their ability to pass through target barriers and deliver therapeutics effectively.[65,66] However, passive targeting plays a significant role in active targeting.[67] It is responsible for the passive accumulation of long-circulating liposomes at the site of infection, inflammation, and cancer without generating any immunogenic response (absence of targeting ligands) and ensuring complete biocompatibility to effectively accumulate at the target tissue. In the next section, we will look at how passive targeting works due to the enhanced permeation and retention effect (EPR), and what are its associated challenges.

1.1.2 Passive targeting and the enhanced permeation and retention (EPR) phenomenon

Hiroshi Maeda and Matsumura discovered the enhanced permeation and retention (EPR) phenomenon in the 1980s and published their ground-breaking work in 1986 calling the EPR effect "a mechanism of tumoritropic accumulation of proteins and the antitumour agent SMANCS (styrene-maleic acid copolymer-conjugated neocarzinostatin)".[68] This discovery stimulated further dedicated research to develop an understanding of this concept and its impact on the development of drug delivery systems for tumour therapeutics.[69] Shortly after this discovery, the drug delivery carrier

Doxil©/ Caelyx© was successfully clinically translated working on the principle of passive targeting of tumours, with the EPR effect being a key part of its design.[70]

The EPR effect and its impact on the design of passively tumour-targeted nanomedicine have been widely studied in the past two decades. The rapid and abnormal angiogenesis of tumours leads to growth in the fenestration of the vessels, decreased lymphatic drainage, and the endothelium of the blood vessels becomes leaky (more permeable) than in the corresponding healthy vessels.[71] This leads to increased permeation of large drug-delivery macromolecules (>40 kDa) and nanomedicines to the tumour cells.[72,73] This passive targeting due to the EPR effect relies on the tumour characteristics (leakiness, hypoxia, core density, vascularity).[70] The intrinsic tumour characteristics which affect EPR include the rate of angiogenesis and lymphangiogenesis (also observed in inflammation and infection), vascularity of the tumour core, and intratumoural pressure.[74] Other factors which affect the EPR effect include vascular dilators such us angiotensin, bradykinin, VEGF, etc.[69] The abnormal decreased lymphatic drainage contributes to the retention of these nanomedicines in the tumours. Conventional small molecule drugs which have a fast washout from the tumours and fast blood circulation times are not retained selectively. However, these small molecule drugs encapsulated in drug delivery vehicles like nanomedicines prolong their blood circulation, selective tumour permeation, decreased tumour washout and systemic toxicity.[72,73] The phenomenon of the EPR effect and passive targeting is illustrated in figure 1.4.

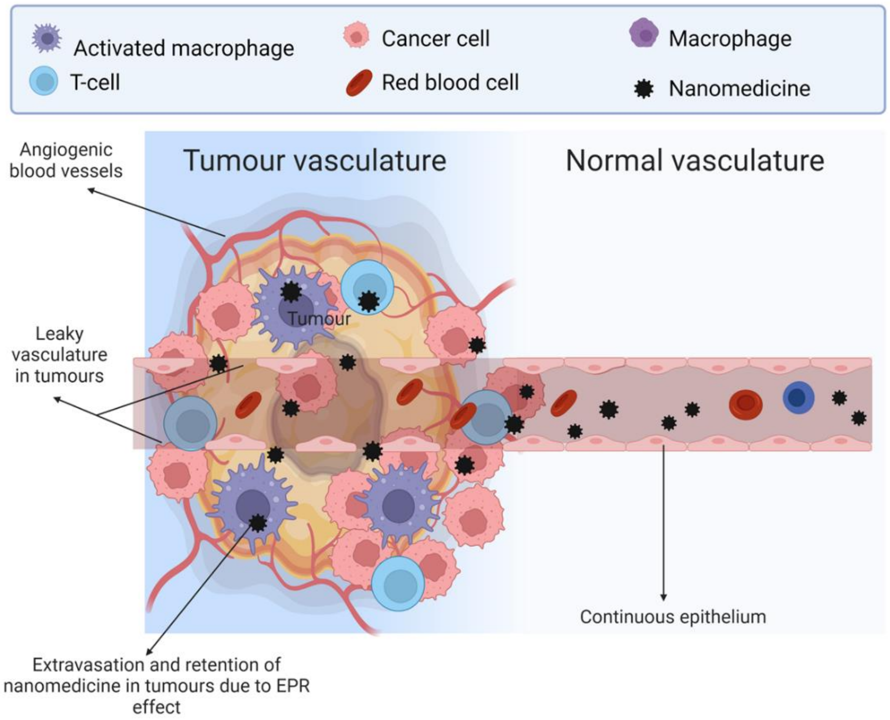

Figure 1.4 Enhanced permeation and retention effect: Comparison of normal and tumour vasculature. The increased leaky vasculature, tumour-associated macrophages and decreased lymphatic drainage assist the EPR effect. Created with BioRender.com.

For EPR-based passive targeting, the particle size, and surface charge of the nanoparticles extensively affect the circulation time, efficiency of delivery and the cellular uptake pathway for various nanomedicines, including liposomes[75], quantum dots[76], polymeric NPs[77,78], AuNPs[79] and silica NPs.[80] The particle size is especially important for the permeation and retention in the tumour vessels and is limited by the size of fenestrations (gaps in the endothelial walls) in the tumour vasculature (~200–800 nm).[71,75] Thus, the optimal size range for nanoparticles for drug delivery should be in the 30-200 nm range as particles smaller than 20 nm are quickly cleared by renal excretion and the particles bigger than 500 nm are cleared by the reticuloendothelial system (RES).[70]

In addition to particle size, the NP surface charge and the presence of surface-bound molecules also play a significant role in EPR-mediated passive targeting. Systems that are positively charged and highly lipophilic are rapidly detected and cleared by the mononuclear phagocytic systems (MPS) *via* opsonisation. However, particles with a slightly neutral or negative charge are preferred due to lower detection by phagocytic systems. Also, a hydrophilic NP surface is preferred, with most clinically approved liposomal nanomedicines (Table 1.1) having hydrophilic polymers added to the liposomal surface. The water-soluble polymer PEG present on the liposomal surface prevents aggregation and interaction with plasma proteins by modulating surface charge and hydration.[66,71,81] PEG has been used to modify all kinds of nanoparticles to provide passive targeting capabilities including liposomes, polymeric micelles, silica nanoparticles, and metallic nanoparticles.

1.1.3 EPR heterogeneity challenges: the need for imaging

Enhanced permeability and retention (EPR) effect is promoted by leaky vasculature caused by rapid angiogenesis in tumours, but this leakiness of the newly formed tumour vessels also contributes to the high tumour interstitial fluid pressure (TIFP). The high TIFP is responsible for the inhibition of the accumulation of therapeutic as well as therapeutic carriers in tumours.[82] Furthermore, the disproportionate angiogenic signalling in various parts of the tumour can be pro- or anti-angiogenesis. This leads to abnormal vessel growth with dilated, constricted, and disorganised patterns of branching which in turn leads to a heterogeneous blood supply. The heterogenous blood supply leads to irregular growth of tumour cells which proliferate faster in areas of higher blood supply and *vice versa* leading to the formation of necrotic core in advanced tumours due to low availability of oxygen and nutrients in these areas. The presence of the necrotic core and high tumour interstitial fluid pressure leads to non-leaky vasculature and decreased accumulation of the nanomedicines leading to drug delivery below therapeutic levels.[70,73]

Table 1.2 shows the EPR heterogeneity: variability of radiolabelled liposome uptake in tumours: variability within the same stage (in red), variability within the same tumour type (in yellow); variability within different tumour types (in blue)[83]

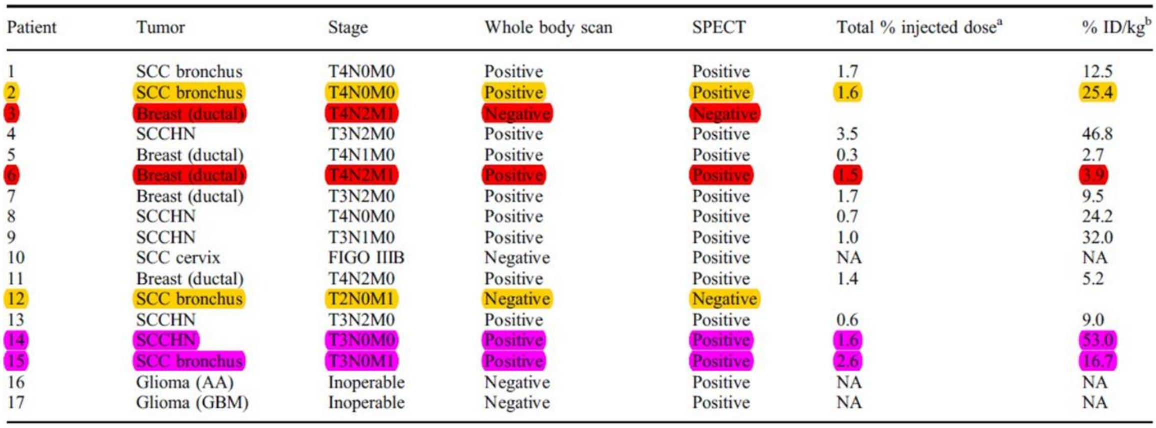

Patient	Tumor	Stage	Whole body scan	SPECT	Total % injected dose^a	% ID/kg^b
1	SCC bronchus	T4N0M0	Positive	Positive	1.7	12.5
2	SCC bronchus	T4N0M0	Positive	Positive	1.6	25.4
3	Breast (ductal)	T4N2M1	Negative	Negative		
4	SCCHN	T3N2M0	Positive	Positive	3.5	46.8
5	Breast (ductal)	T4N1M0	Positive	Positive	0.3	2.7
6	Breast (ductal)	T4N2M1	Positive	Positive	1.5	3.9
7	Breast (ductal)	T3N2M0	Positive	Positive	1.7	9.5
8	SCCHN	T4N0M0	Positive	Positive	0.7	24.2
9	SCCHN	T3N1M0	Positive	Positive	1.0	32.0
10	SCC cervix	FIGO IIIB	Negative	Positive	NA	NA
11	Breast (ductal)	T4N2M0	Positive	Positive	1.4	5.2
12	SCC bronchus	T2N0M1	Negative	Negative		
13	SCCHN	T3N2M0	Positive	Positive	0.6	9.0
14	SCCHN	T3N0M0	Positive	Positive	1.6	53.0
15	SCC bronchus	T3N0M1	Positive	Positive	2.6	16.7
16	Glioma (AA)	Inoperable	Negative	Positive	NA	NA
17	Glioma (GBM)	Inoperable	Negative	Positive	NA	NA

Due to the above factors, the EPR effect is highly heterogeneous in humans, leading to variable nanomedicine accumulation in tumours of different cancers, in various stages and in different patients (Table 1.2).[83]Therefore, the overall lack of success of cancer nanomedicines in humans can be majorly attributed to EPR heterogeneity.

Modulation of the EPR effect can be performed to increase tumour perfusion by either chemical or mechanical methods to increase the accumulation of nanomedicines. The chemical enhancers include vascular modulators and chemical compounds like nitric oxide and peroxynitrite.[72,73] The mechanical approaches include tumour-focused ultrasound, radiotherapy and phototherapy-assisted enhancement of the permeability of tumours towards nanomedicines.[70,73,82] These methods are either in the preclinical stage or cannot be universally applied to different cases. Imaging has been proposed as a tool to overcome and predict this EPR-mediated passive targeting variability (Figure 1.5).[83,84] The imaging of the liposomal nanomedicines allows us to track the delivery of these particles at target sites using different modalities including Optical, MRI and nuclear imaging, among others. The toolbox for imaging liposomes which is available to us in both clinical and preclinical settings and how it can help us resolve the issue of EPR heterogeneity is described in the next sections.

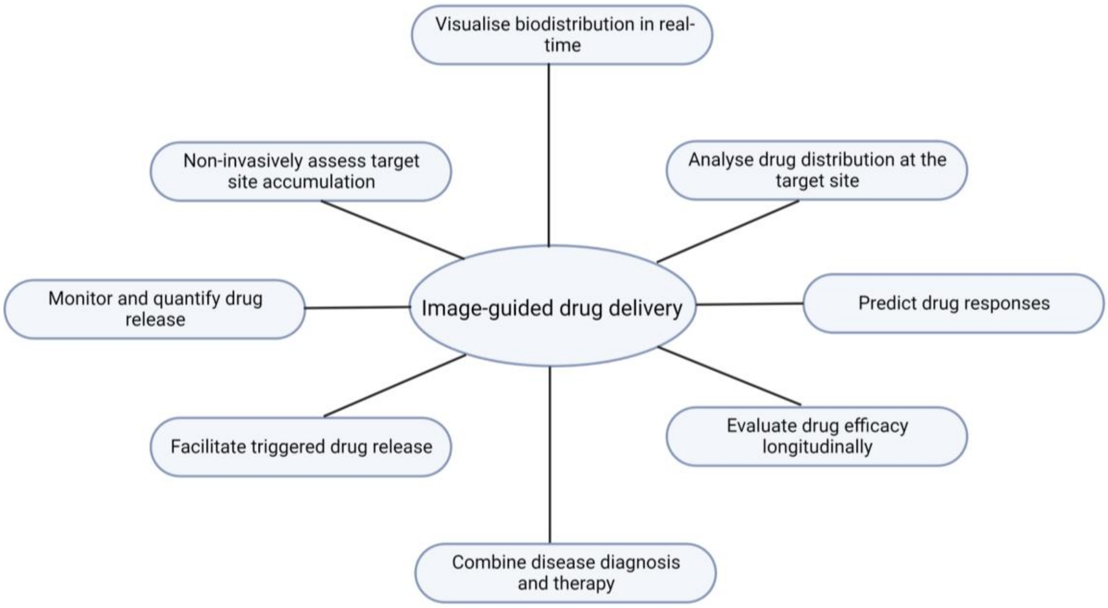

Figure 1.5. Image-assisted development of drug delivery methods: Imaging methods have found various applications in drug-delivery as well as diagnostic development. This schematic representation depicts these applications including prediction of drug response, drug efficacy, biodistribution, pharmacokinetics assessment and a better understanding of various aspects of nanotherapeutics to provide a valuable field of nanotheranostics. Various advantageous aspects of this field of nanotheranostics can be seen above. Created with BioRender.com.[85]

1.2 Imaging liposomes: Applications

The therapeutic efficacy of liposomal nanomedicines varies according to the tumour types, stages, and patients due to EPR-mediated passive targeting. This poses a challenge to the clinical applications of liposomal nanomedicines and consequently the development of liposomes as personalised nanomedicines.[86] Therefore, there is a need to better understand the pathways of liposomal delivery, hindrance due to the EPR effect and screening ability to stratify patients for treatment with liposomal nanomedicine. A non-invasive and effective method to study the biodistribution and pharmacokinetics of liposomes *in vivo* is using medical imaging techniques.

1.2.1 Imaging of liposomes

To track liposomes *in vivo*, various imaging methods can be used depending on the information needed, clinical or pre-clinical setting, benefits, and drawbacks. The key deciding factors include sensitivity (defined as the amount of contrast agent required to obtain an imaging signal), ease of quantification, tissue penetration, temporal and spatial resolution, and non-invasiveness (Table 1.3).

1.2.1.1 MRI

Magnetic resonance imaging is an excellent functional, anatomical, and molecular imaging tool based on the interaction of different atoms/ions with radio frequencies in the presence of a magnetic field.[87] MRI (Magnetic Resonance Imaging) can be used in the presence or absence of contrast agents but to track liposomal nanomedicines, the liposomes can be loaded with paramagnetic ions Gd^{3+}, Mn^{2+} or superparamagnetic iron oxide nanoparticles.[88–91] The non-ionizing nature of this modality and its high spatial resolution with increasing magnetic field strength of scanners make it an excellent candidate. However, the requirement of high concentrations of contrast agents per liposome due to its low sensitivity and the relative toxicity of one of these contrast ions (Gd^{3+}) is one of the major drawbacks of liposome imaging *in vivo.* [92] This risk, however, can be minimised through chelation of Gd to polydentate chelators. The other drawback of MRI includes the high magnetic field strengths required to obtain high SNR and accurate quantification.[87]

1.2.1.2 Computed Tomography

Computed tomography (CT) is based on X-ray imaging and collects information in 3D compared to standard X-ray imaging by using a higher number of detectors placed in a circular geometry. The CT modality has several advantages including high spatial resolution, short scan times, no penetration depth limit, and can be used with iodinated contrast agents.[87,93] The iodinated contrast agents have been either loaded in liposomes as hydrophobic (ethiodol), hydrophilic (iopamidol) molecules or covalently linked ((E)-10,11-diiodoundec-10-enoic acid) molecules (Figure 1.6).[94,95] Although it has shown success in preclinical imaging of liposomal nanomedicines in breast cancer models and atherosclerotic animals, it does have a few disadvantages.[96,97] Most importantly, like MRI, it suffers from low sensitivity and requires substantial amounts of contrast agents. Furthermore, it leads to high ionizing radiation doses in patients, particularly when imaging the whole body. [93,98]

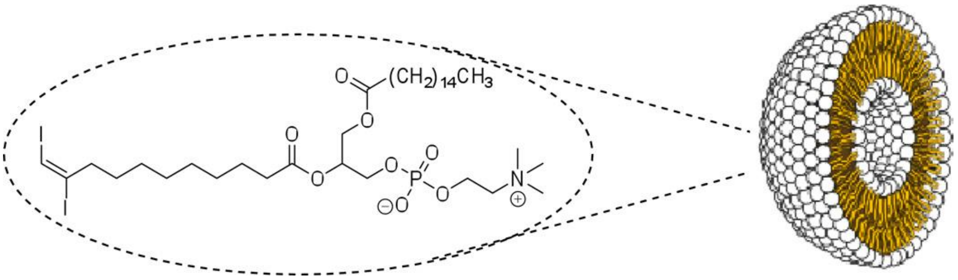

Figure 1.6. Iodinated liposomes used as a CT contrast agent formed from modified lipids containing ((E)-10,11-diiodoundec-10-enoic acid). [95]

1.2.1.3 Ultrasound Imaging

Ultrasound imaging (US) is an economical and reliable imaging modality that utilizes high-frequency sound waves to view inside the body. In US, a transducer emits a pulse of high-frequency sound waves aimed at the body and the reflected sound waves are detected by a transducer. The reflected sound waves collected are utilised to create a 2D image depending on the properties of sound waves including time of reflection, amplitude, and frequency. It has been used for a few decades for abdominal, foetal and breast ultrasounds with recently being used with microbubbles as a contrast agent for measuring blood flow with excellent spatial and temporal resolution.[87,99,100] For tracking liposomes, microbubbles can be conjugated to liposomes or echogenic liposomes can be used.[101] Ultrasound in addition to imaging has also been useful in the controlled release of drugs from the liposomes.[102] However, ultrasound suffers from some disadvantages which include the inability of whole-body imaging and limited tissue penetration depth (less than a few cm).[87]

Table 1.3 shows the comparison of different imaging modalities depending on parameters such as resolution, penetration depth and suitability for applications in nanomedicine

Modality	**Spatial resolution**	**Depth of penetration**	**Sensitivity**	**Multiplexing ability**	**Ionizing radiation**	**Cost**	**Comments**
Computed tomography (CT)	0.5 mm	No limit	~mM for iodine contrast agents	Yes, PET/CT, SPECT/CT	Yes	£	Can be used with and without contrast agents, High dose of radiation
Ultrasound (US)	0.1-2 mm	limited to few cms	~pM when using microbubbles	Yes, PETUS	No	£	Portable, Microbubble contrast enhance US provides very high resolution
Optical Imaging	1 um-10 mm	Limited to a few mms	~pM-nM	Yes	No	£-££	Severely limited by depth, Good for preclinical use and in vitro applications
Positron Emission Tomography (PET)	1 mm	No limit	~fM	Yes, PET/CT, PET-MRI	Yes	£££	Quantitative, Total body scanning capabilities
Single Photon Emission tomography (SPECT)	5 mm	No limit	~pM-nM	Yes, SPECT/CT, Multisotope SPECT	Yes	££	
Magnetic resonance imaging (MRI)	1 mm	No limit	~mM	Yes, PET-MRI	No	££	

1.2.1.4 Optical imaging

The tracking of liposomal nanomedicines can be performed using different types of optical imaging including fluorescence, NIR, Optical coherence tomography and Raman imaging. Different optical labels such as fluorophores and dyes can be loaded onto liposomes allowing their tracking for molecular imaging.[103–106] High sensitivity and precise quantification are the key advantages of optical imaging allowing us to precisely track and measure the amount of liposomal delivered to the target site, especially in animal models *in vivo* and *ex vivo*. The resolution of optical imaging at the cellular level is unparalleled compared to other imaging techniques. Therefore, it can be effectively utilised for the study of the cellular uptake of liposomes, and we have exploited these capabilities of optical imaging to study the uptake of the PEGylated liposomes in different types of neuronal cells which will be discussed in chapter 4. However, the applications to the clinical setting are severely limited due to low tissue penetration depth. Moreover, the different properties and varying *in vivo* stability of different optical probes used for labelling also pose some challenges.[87]

1.2.1.5 Nuclear Imaging

Nuclear imaging or radionuclide imaging is based on tracking radiolabelled probes *in vivo* in both animals and humans non-invasively. The nuclear imaging modality has properties that are advantageous for tracking drugs including high sensitivity, high temporal and spatial resolution, unlimited tissue depth penetration, and accurate quantification. The high sensitivity allows the use of small tracer quantities (*i.e.,* micrograms or less for one patient) to image the drug delivery with subtherapeutic doses hence minimising toxicity issues. This high sensitivity is a key advantage of nuclear imaging over other techniques such as CT and MRI which require large doses of contrast agents (*i.e.,* grams for a human patient). In the context of liposomal nanomedicines, the high sensitivity is a great asset for imaging as the use of subtherapeutic doses in the order of micrograms (μg) allows quantification of their biodistribution and therapeutic efficacy.

The main disadvantage of nuclear imaging is the exposure to ionizing radiation which is absent in other modalities like MRI and optical imaging. Moreover, the comparative spatial resolution of nuclear imaging is lower than MRI and optical imaging. Nuclear imaging methods have a spatial resolution in the range of 1-10 mm depending on the instrument and radionuclide used whereas MRI and optical imaging have sub-millimetre resolution to sub-micrometre resolution. Due to the above properties, we chose SPECT/PET as the imaging modality to further investigate the liposomal nanomedicines. In the next section, we will further look at different nuclear imaging techniques in the context of imaging liposomal nanomedicines.

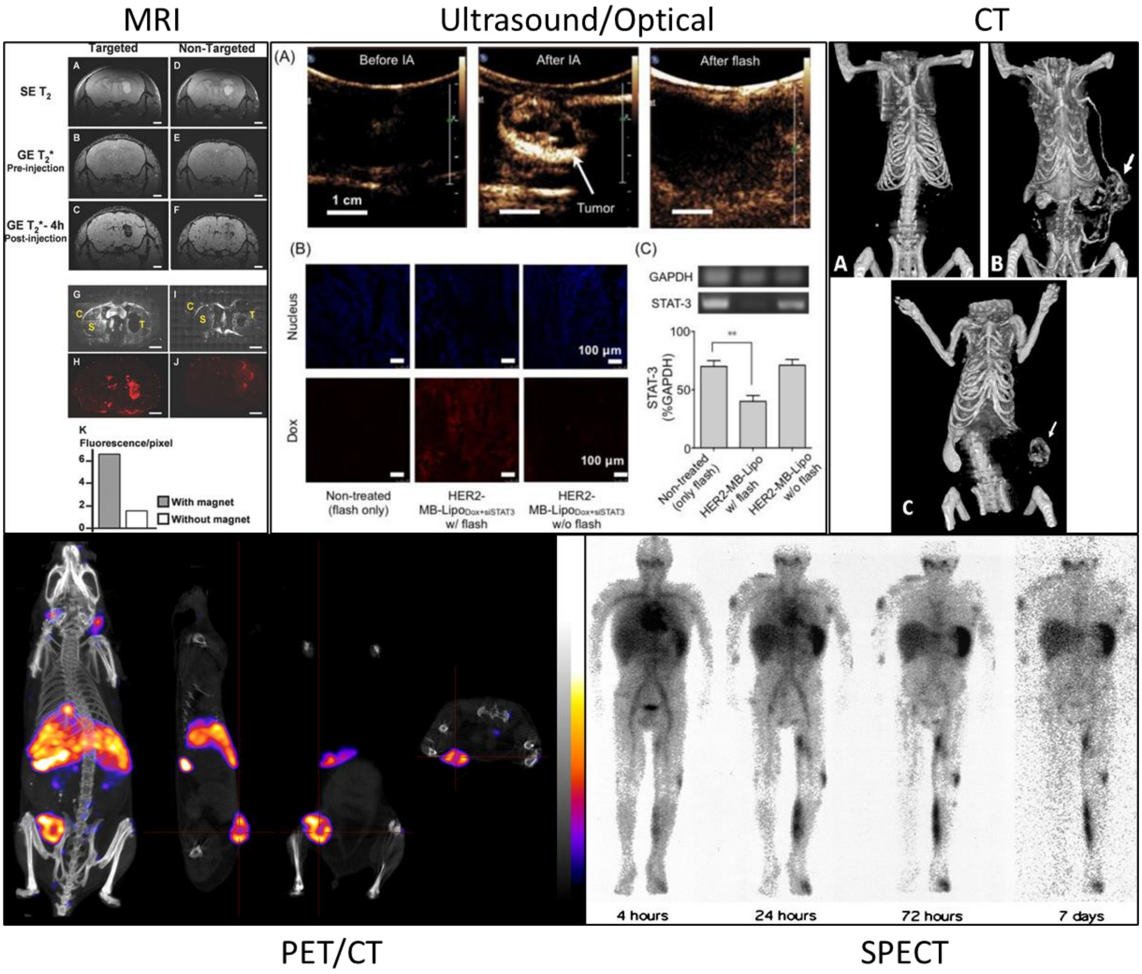

Figure 1.7. Applications of different imaging modalities in the tracking of liposomal nanomedicine: MRI: MRI imaging of magnetic fluid loaded liposomes post 4-h exposure to a magnetic field gradient showing a high concentration of MFLs into human U87 glioblastoma implanted in the striatum of mice.[88] , Ultrasound/Optical: (A) Therapeutic MB-Lipo particles containing both doxorubicin and siRNA (siSTAT3) were imaged using US imaging showing target-specific labelling of tumours;(B) Ex vivo optical imaging of tumour tissue showed delivery of high concentrations of Dox (red fluorescence). (C) The delivery of siSTAT3 was confirmed by performing PCR on tissue extract. [107] , CT: Computed tomography of rat with breast tumour in left flank (A) before, and (B) 5 minutes after i.v. administration of liposomal contrast agent (2 g of iodine per kg), C) Accumulation of the contrast agent within tumour vasculature.[107] , PET: PET imaging of Zr89 labelled liposomes in mouse tumour model (maximum intensity projection and other views).[109] , SPECT: Whole-body gamma camera images over 7 days of a patient with Kaposi's sarcoma administered In-111-labeled liposomes. Areas of liposome uptake in the left foot and leg, right arm, and face corresponded with typical Kaposi's sarcoma lesions. Prolonged retention of the radiolabel is seen despite significant clearance of circulating liposomes, as demonstrated by disappearance of the cardiac blood pool image.[110]

1.2.2 Why nuclear imaging to track liposomal nanomedicines?

1.2.2.1 Rationale

Imaging modalities based on nuclear imaging have been used in the past for personalised medicine for their sensitivity, and quantitative and isotropic detection. [111,112] Both single-photon emission computed tomography (SPECT) and positron emission tomography (PET) are highly suitable to quantify the EPR effect due to these properties and thereby assist in selecting patient groups likely to be responsive to nanomedicine treatment. Moreover, nuclear imaging can also assist in the process of drug development in terms of providing information on nanomedicine biodistribution, therapeutic efficiency assessment and drug release quantification.[83,111,113] Nuclear imaging has been widely used to study liposome circulation time and drug delivery potential.[114] The biodistribution studies can also be used to predict toxicological effects and prevent further expensive trials and harmful effects. For example, a phase I/II clinical trial study of an N-HMPA copolymer-bound doxorubicin nanomedicine (PK2) biodistribution in patients with liver cancer found that efficacy was low. A retrospective imaging analysis revealed that nanomedicine PK2 targeted healthy liver tissue.[115] An imaging study at an earlier stage could have averted both expensive trials and harmful effects on patients.

The two main nuclear imaging techniques available are SPECT and PET. Depending on the radionuclide used for labelling nanomedicines for tracking, either of the two techniques is used. This allows *in vivo* clinical and preclinical non-invasive imaging via the radioactive decay emissions from the radionuclides. Both techniques are discussed below and compared in terms of their benefits and pitfalls.

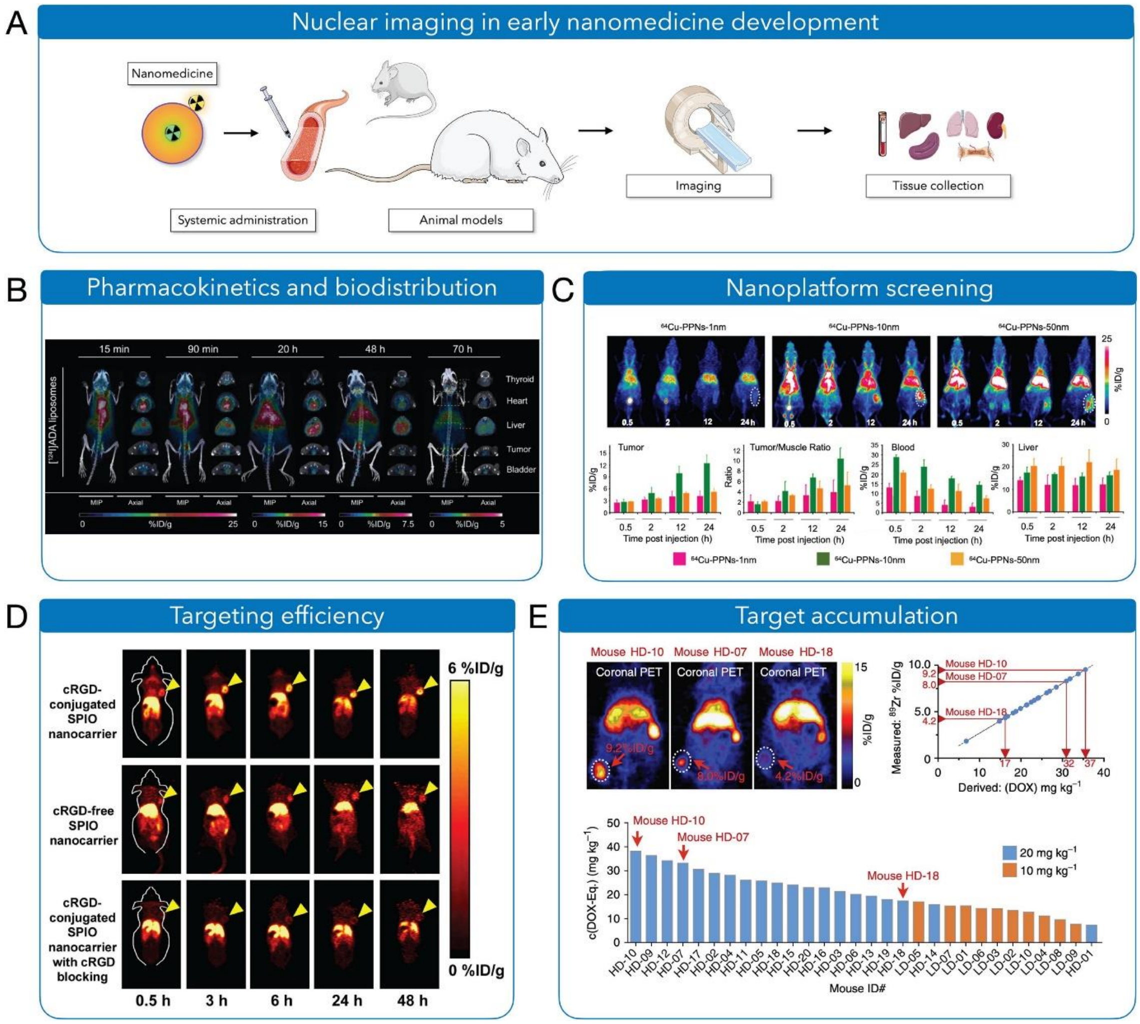

Figure 1.8. Applications of nuclear imaging in nanomedicine: (**A)** Nuclear imaging in early nanomedicine development for validation of various formulations in small animal disease models with non-invasive tracking followed by further validation using ex vivo tissue collection. **(B)** The pharmacokinetics and biodistribution of ^{124}I-labeled liposomes in the murine model were monitored over 3 days by PET imaging.[116] **(C)** For screening of formulations: Three pegylated porphyrin nanocomplexes radiolabelled with ^{64}Cu and their biodistribution was monitored longitudinally over 24 h using PET revealing the best formulation and size for tumour targeting to be chosen for further evaluation and development.[117] **(D)** Evaluation of targeting efficiency: The effect of incorporation of targeting ligands on the doxorubicin-loaded iron oxide nanoparticles was studied by PET imaging of ^{64}Cu labelled particles.[118] **(E)** Dose quantification of target accumulation: The dose of therapeutic delivered to the tumours can be estimated using companion PET/SPECT imaging. ^{89}Zr-labelled liposomes were used as companion imaging for Doxil to obtain the intratumoural doxorubicin delivered dose from the quantified ^{89}Zr PET signal.[119] Image adapted and reproduced from Medina et al.[120]

1.2.2.2 PET imaging

Positron emission tomography (PET) works on the principle of coincidence detection of two 511 KeV gamma rays. The radionuclides used for PET imaging decay by emitting positrons (β^+), a positively charged particle with a mass of an electron. This positron on release during decay interacts with surrounding electrons to undergo annihilation releasing two gamma rays in diametrically opposite directions which are detected by the principle of coincidence detection in PET detectors which are arranged in the form of a ring of detectors for the detection of gamma rays. This coincidence detection allows the prediction of the site of the positron-electron pair annihilation event and therefore, the approximate location of the radionuclide *in vivo* in the body.[87] The energy of the positron emitted by the radionuclide decides the distance travelled by the emitted positron before annihilation and is responsible for the determination of spatial resolution using each PET radionuclide. With increasing advancements in PET imaging, the resolutions have increased progressively over the years and the capability of total-body PET imaging has also been achieved.[121–123]

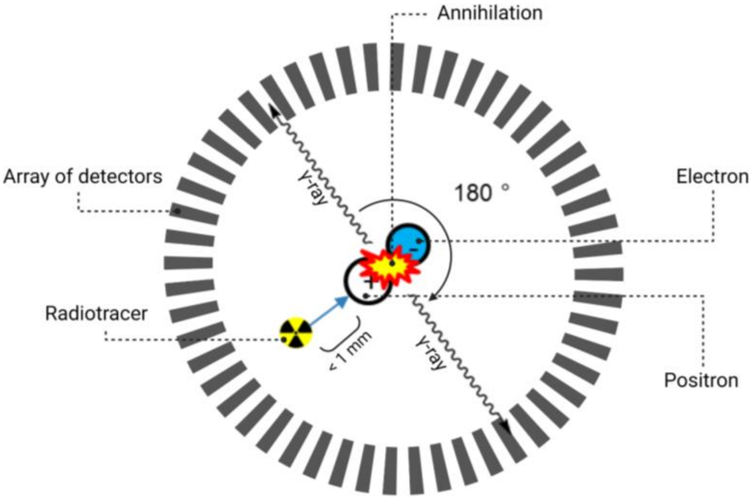

Figure 1.9. Schematics of the working of a PET scanner: The emitted positron from the PET radiotracer annihilates in the presence of an electron to produce two diametrically opposite γ-ray photons. Created with BioRender.com.

1.2.2.3 SPECT imaging

Single photon emission computed tomography (SPECT) imaging works via the detection of different energy gamma-ray photons emitted by SPECT radionuclides during their radioactive decay. The radionuclides for SPECT imaging emit specific gamma rays with specific energy levels. These emitted gamma rays are detected using a gamma camera that rotates around the patient to capture the emissions in 3D. The origin of these gamma rays is determined by only collecting gamma rays with a low incidence angle at the detector. This is performed by using narrow collimators, only allowing parallel rays, and excluding any rays with higher incidence angles providing increased spatial resolution and localization of the site of gamma-ray origin. However, the process of collimation which is responsible for the increase in spatial resolution also leads to decreased sensitivity compared to PET. This decreased sensitivity is due to exclusion of a significant number of gamma rays.[87,124]

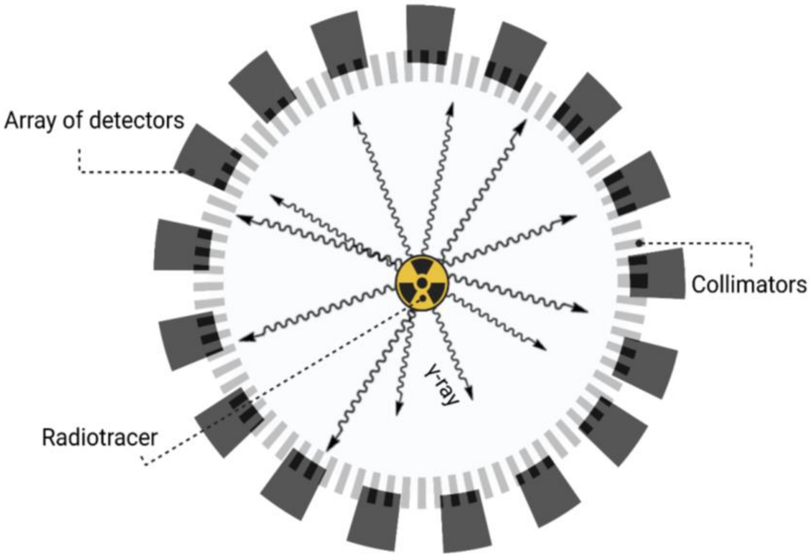

Figure 1.10. Schematics of the working a SPECT scanner: The emitted gamma photons from the SPECT radiotracer is collected by a collimator which is detected by the array of detectors. Created with BioRender.com.

1.2.2.4 PET vs SPECT

SPECT and PET have both been extremely useful in the field of diagnostics as well as theranostics. They both have their advantages and disadvantage compared to each other depending on the properties described above. The sensitivity of the PET is higher than that of SPECT due to the absence of collimation in PET. The spatial resolution of clinical PET (3-6 mm, depending on radionuclide) is also higher compared to clinical SPECT (5-12 mm) scanners.[125] The lower spatial resolution of SPECT is a result of the balance that needs to be struck between spatial resolution and sensitivity in presence of collimators. The spatial resolution and sensitivity for SPECT can be increased by increasing the radionuclide dose and collimator aperture, respectively.[87,126]

On the other hand, SPECT imaging in a clinical and preclinical setting has a few advantages. The clinical SPECT scanners are less costly and thus, easily available in the clinical setting. However, recently, PET scanners due to their higher resolution and sensitivity are increasingly being used in a clinical setting. Moreover, SPECT imaging can be used to perform multiple radionuclide (radiotracer) imaging in the same patient due to the detection of different characteristic energy emissions from different SPECT radionuclides. This technique of imaging multiple SPECT radionuclides concurrently is called multiplexed imaging.[127] The multiplexed imaging cannot be performed using PET imaging as all the gamma-ray photons collected by PET detectors for different radionuclides have the same 511 keV energy. However, recent advancement in clinical PET imaging has allowed the development of full-body PET imaging capabilities allowing for full-body measurements with lower radiation doses which will have great implications for the development of nuclear imaging.[123]

1.2.2.5 Nuclear imaging for non-invasive tracking of nanomedicines

As stated above, the nuclear imaging modalities have characteristics ideally suited for imaging the biodistribution, drug delivery and pharmacokinetics of nanomedicines *in vivo* clinically and preclinically. The key advantages of using nuclear imaging for drug delivery vehicles are the lack tissue depth penetration limit and high sensitivity allowing imaging with low radiation doses to patients and minimal effect on properties of nanomedicines. Moreover, the availability of full-body imaging functionality allows the assessment of full-body biodistribution and incidental findings.[128]

1.2.2.6 Multimodality imaging

The clinical studies on drug delivery rely on imaging modalities to obtain a profile of nanomedicine biodistribution, pharmacokinetics, and therapy outcome.[83] Nuclear imaging as described above seems to be particularly suited for these due to its non-invasive nature and ability to combine with other modalities. One such multimodal imaging setup is hybrid PET/MRI imaging systems which allow the tracking and quantification of radionuclides by PET whereas MRI obtains highly detailed soft-tissue images to provide maximum information.[129–131] The integration of nuclear imaging with other imaging techniques has been successfully done to obtain comprehensive information.[121,132–134] MRI, optical and ultrasound imaging combined with PET and SPECT have allowed a combination of molecular information from PET/Optical with anatomical and functional information from other modalities with enhanced resolution and higher soft tissue detail.[135] The use of multimodality imaging complements nuclear imaging data in improved assessment of nanomedicines, *in vivo* stability, cellular level interactions and tissue-specific uptake. (*e.g.*, mechanism of cellular uptake of liposomes using optical imaging, drug efficacy in atherosclerotic plaques using MRI).[136] These hybrid techniques also facilitate improvement of our quantitative ability of nuclear imaging through data processing (*e.g.,* attenuation and partial volume effect correction using CT or MRI).[137,138]

1.2.2.7 Radionuclide nanotheranostics

In addition to SPECT and PET radionuclides which emit gamma rays and positrons respectively, certain radionuclides also emit other particles which can be used as therapeutics. These radionuclides, when attached or loaded on the nanoparticles, can be used as radionuclide nanotheranostics. These radionuclides are either alpha emitters, Beta emitters or Auger electron emitters which have high mass and high amount of energy and therefore the ability to deposit large amounts of energy in surrounding tissues, causing damage in the process. However, these radionuclides - if delivered without targeting - can cause damage to tumour tissue as well as healthy tissue. By incorporation of these therapeutic radionuclides into drug delivery systems such as nanomedicines, they can be delivered via passive or active targeting to specific tumour tissues.[139,140] The therapeutic efficacy of these radionuclides is dependent on the linear energy transfer (LET) which is dependent on the decay type, energy, and mass of the particle emitted.[141] These radionuclides, due to this energy transfer, are expected to destroy the tumour cells by different mechanisms including DNA damage, cell membrane damage and generation of reactive oxygen species (ROS).[142] The three different therapeutic radionuclide emissions are briefly described below alongside their LET values.

1.2.2.2.1 Alpha-particle radiation.

An alpha particle was the first nuclear radiation to be discovered. They are composite particles consisting of two neutrons and two protons that are tightly bound together. They are emitted from the heavy mass nucleus of unstable radionuclides during radioactive decay, called alpha decay. An alpha particle is identical to a doubly ionised helium atom and is considered to have a high linear energy transfer (LET in water) (80 keV/mm) and can deposit energy over a range of 50-100 µm.[141,143] Some common alpha-emitting radionuclides used for labelling nanomedicines can be found in Table 1.4.

1.2.2.2.2 Beta-particle radiation

Beta particles (β^-) carry a negative charge and have a mass which is equal to an electron. They have a very small mass compared to alpha particles and are released at relativistic speeds and therefore, have very high energy. Their light mass and high energy mean they exhibit a quick loss of energy through interaction with matter. Beta particles are less ionising than alpha particles and cause less damage. They also have a low LET in water (0.1–1.0 keV/mm) and deposit energy over a particle range of 12 mm. These properties result in energy transfer over hundreds of cell diameters.[141,143] Some of the most common Beta particle-emitting radionuclides used for the labelling of nanomedicines are listed in Table 1.4.

1.2.2.2.3 Auger electron radiation

Auger electrons are very low-energy electrons that are emitted by gamma-ray emitting radionuclides that decay through electron capture or internal conversion (e.g., indium-111, gallium-67). The Auger effect, found by Lisa Meitner and Pierre Auger, is the phenomenon in which a vacancy in a K-shell orbital is filled by the transfer of an electron from an L-shell orbital. The energy difference of this transition is emitted as either an X-ray or as an ejected electron which is referred to as an Auger electron. This energy is deposited over a short linear range (nm or µm), with a high LET in water (1–26 keV/mm) and has the potential for causing lethal damage to tumour cells.[143,144] The Auger electron-emitting radionuclides are preferable for killing tumour cells in micrometastases or small tumours. The common Auger electron emitters used for labelling nanomedicines are in Table 1.4.

Table 1.4. Therapeutics radionuclides for applications radionuclide therapy

Type of emission	Radionuclide	Half-life	Max energy	Decay	Production
β^- -emission	Y-90	64.0 h	2280 keV	β^-	Generator
	Lu-177	6.7 d	500 keV	γ, β^-	Cyclotron
	I-131	8.0 d	610 keV	γ, β^-	Fission
	Re-188	16.9 h	2120 keV	γ, β^-	Generator
	Re-186	91 h	1080 keV	γ, β^-	Cyclotron
α-emission	Ac-225	10 d	8000 keV	B^-, α	Cyclotron
	Ra-223	11.4 d	7000 keV	B^-, α	Cyclotron
Auger emission	Ga-67	78.3 h	300 keV	Auger e, γ	Cyclotron
	I-123	13.3 h	159 keV	Auger e, γ	Cyclotron
	I-125	60.5 d	27 keV	Auger e, γ	Neutron activation

1.2.2.2.4 Nanoradiotherapeutics

These therapeutic radionuclides are ideal candidates for loading onto nanomedicine platforms via similar approaches used for imaging purposes. This would allow the therapeutic radionuclides to work in a targeted manner post-accumulation of these nanomedicines in tumour tissue due to the EPR effect. Moreover, some of these radionuclides are either conveniently emitting gamma photons/positrons to be used for SPECT/PET imaging or have an imaging pair radionuclide such as ^{124}I/^{131}I, ^{64}Cu/^{67}Cu, ^{68}Ga/^{67}Ga, ^{110g}In/^{111}In, ^{44g}Sc/^{47}Sc, ^{83}Sr/^{89}Sr, ^{152}Tb/^{161}Tb, ^{152}Tb/^{149}Tb and ^{86}Y/^{90}Y.[145] These imaging counterparts of therapeutic radionuclides will provide information about pharmacokinetics, efficacy and biodistribution. Therefore, the studies using these diagnostic/therapeutic pair have the crucial ability to provide dosimetry information and predict the dose required for treatments.

Some examples of liposomes being used for the delivery of radionuclide theranostics are highlighted here. ^{188}Re-labelled liposomes due to the high energy beta (2.1 MeV) and gamma photon emitting properties of Re-188 have been used for theranostic purposes allowing therapy, biodistribution and dose determination.[146–148] Liposomes labelled with the diagnostic/therapeutic pair of ^{64}Cu/^{177}Lu have also been used in a preclinical mouse model to determine biodistribution, therapeutic effect, dosimetric information and absorbed dose.[149] Similar studies have been performed with other types of nanoparticles including porphyrin-PEG nanoparticles (^{64}Cu/^{177}Lu, PET imaging)[150], HPMA micelles (^{177}Lu, ^{90}Y, SPECT imaging)[151,152], nanospheres (^{131}I, SPECT imaging)[153], polyamine dendrimers (^{131}I, SPECT)[154] and more recently with gold nanoparticles (^{103}Pd, ^{117}Lu)[155,156] for image-guided radiotherapy in various murine cancer models.

1.3 Radiolabelling liposomes: How?

In the previous section, we discussed the benefits of imaging nanomedicines, specifically nuclear imaging of liposomes to unlock their complete theranostic potential and assist with efficient drug-delivery and precision nanomedicine. For nuclear imaging of liposomes *in vivo*, the radionuclide needs to be attached to a liposome with minimal modification to its chemical and physical properties. There are two major methods for radiolabelling liposomes: (i) the radionuclide attached/embedded in the lipid bilayer of liposomes and (ii) the radionuclide is captured inside the intraliposomal aqueous core. Depending on the radionuclide used for radiolabelling, the two nuclear imaging techniques PET or SPECT are used. SPECT isotopes Tc-99m and In-111 have been used for liposomal radiolabelling historically due to their prevalence in SPECT imaging, but recently PET imaging has been favoured over SPECT due to its higher sensitivity and quantitative nature.[125]

1.3.1 List of PET/SPECT radionuclides

Now that we have discussed nuclear imaging techniques and the selection of different diagnostic (simultaneously therapeutic in some cases) radionuclides available, it is important to determine the factors affecting the selection of radionuclides for specific imaging needs. The first crucial factor affecting the choice of radionuclides is the imaging technique. The choice of the imaging technique depends on the key advantages of each for tracking nanomedicines such as high spatial resolution and multi-isotope imaging for PET and SPECT, respectively, as discussed above. Secondly, the choice of radionuclide is dependent on the radionuclide's half-life which should be in the same range as the biological half-life of the nanomedicine being monitored or tracked. Next, the choice of radionuclide also depends on the radiolabelling methods required for tracking the nanomedicine. This radiolabelling should result in minimal modifications of the physicochemical characteristics and the structure of the parent molecule/nanoparticle being tracked. Minimal modifications are necessary to preserve the biological activity and therapeutic properties of nanomedicine. The radiolabelling of molecules can be performed in two main methods: *(i)* non-metallic radionuclide-based radiolabelling which causes the least modifications to the chemical structures of organic compounds for example ^{18}F, ^{11}C or radioiodine,[157,158] and *(ii)* radiometal based radiolabelling which allows attachment of radiometals to molecules of interest via a chelator.[159]

The choice of chelator is dependent on the complexation chemistry of the radionuclide of interest. A high chelating affinity towards the radiometal and the high stability/inertness of the radiometal-chelator bond is essential for the effective tracking of molecules of interest.[160,161] The stability of the radiometal-chelator complex is essential as the biodistribution of the free radionuclide can lead to the wrong interpretation of the biodistribution and tracking of the molecule of interest. Therefore, it is important to study the biodistribution of the free radionuclide/radiotracer and choose the radionuclide to minimize the interference between the uptake of the molecule of interest and free radionuclide in different target organs. For example, free

^{89}Zr selectively accumulates in the bones and the stability of ^{89}Zr chelator complex while tracking bone targeting nanomedicines should be carefully examined as a control.[162] Now that we are aware of the parameters affecting the choice of radionuclide, we can categorize the different radionuclides and the methods of radiolabelling.

1.3.1.1 PET radionuclides: relevant examples

The earliest PET radionuclides utilised for clinical use included ^{11}C, ^{18}F, ^{13}N and ^{15}O.[163] They all are cyclotron produced and have short half-lives compared to the half-life of liposomal nanomedicines especially ^{11}C,^{13}N, ^{15}O, (2-20 minutes), making them a suboptimal choice for this purpose. ^{18}F ($t_{1/2}$ = 109.7 min) is the main PET imaging radionuclide for tracking small molecules due to their short blood circulation times (a few hours).[164,165] ^{68}Ga, a metallic radionuclide which can be generator produced, has a short half-life ($t_{1/2}$=68 min) in the range of ^{18}F. ^{18}F and ^{68}Ga have been used to radiolabel liposomes to examine their retention *in vivo* and accumulation in tumour lesions with PET imaging.[166,167] However, the blood circulation half-life of PEGylated liposomes is of the order of tens of hours to multiple days. Therefore, the initial tumour uptake of liposomes can be observed with ^{68}Ga and ^{18}F but with limited ability for pharmacokinetics, biodistribution and longitudinal studies at longer time points using PET imaging.[168]

Liposomal nanomedicines and other nanoparticle drug delivery systems tend to have longer biological half-lives that are better matched by long-lived PET radionuclides. The long-lived radionuclides such as ^{64}Cu ($t_{1/2}$ = 12.7 h) and ^{89}Zr ($t_{1/2}$ = 78.4 h) will allow us to image for up to a week (2 weeks for ^{89}Zr) for evaluation of dynamics of the liposomal accumulation in tumours.[169,170] PEG-liposomes labelled with ^{64}Cu were used to evaluate PET imaging of cancer lesions and tumour-associated macrophages.[171–173] Recently PET radionuclide ^{89}Zr ($t_{1/2}$=3.3 day) with a half-life comparable to antibodies has found many applications in immunoPET accelerating the developments in the field of immunotherapy.[169] Liposomes have been labelled with ^{89}Zr to evaluate their pharmacokinetics, biodistribution and dose monitoring over a week with PET for the monitoring.[174] The properties and applications of the above-mentioned radionuclides in the context of liposomal nanomedicines have been discussed in Table 1.5.

Table 1.5 Commonly used PET radionuclides for radiolabelling of liposomal nanomedicines

Radionuclide	Half-life	Photon energy	Decay	Production
C-11	20.4 min	961 keV	β^+	Cyclotron
F-18	109.7 min	634 keV	EC, β^+	Cyclotron
Ga-68	67.6 min	1899 keV	EC, β^+	Generator/ Cyclotron
I-124	4.2 d	2100 keV	EC, β^+	Cyclotron
Cu-64	12.7 h	656 keV	EC, β^+	Cyclotron
Mn-52	5.6 d	1434 keV	β^+	Cyclotron
Zr-89	78.4 h	900 keV	β^+	Cyclotron

1.3.1.2 SPECT radionuclides: relevant examples

Gamma-emitting radionuclides kickstarted the field of nuclear medicine starting with gamma-scintigraphy and later SPECT imaging.[175,176] SPECT imaging of radionuclide labelled liposomes has been applied to human as well as animal models including multiple liposome formulations for cancers, infection, inflammation, and blood pool imaging.[177,178] The SPECT radionuclides can be categorised and chosen for varied applications based on the energy emitted, accompanying therapeutic emissions and the half-life. ^{99m}Tc and ^{111}In with a half-life of 6.6 h and 2.8 days respectively have been utilised widely for tracking liposomes *in vivo* via SPECT imaging.[179,180181,182] More recently, ^{111}In labelled liposomes *in vivo* SPECT imaging contributed to gaining insight into the *in vivo* behaviour of newly developed liposomal formulations including an understanding of the size dependence of liposomes on properties showing higher accumulation in the macrophages for larger liposomes as compared to smaller vesicles.[178,183] Other SPECT radionuclides including ^{67}Ga, ^{186}Re, ^{125}I, and ^{123}I have been used recently for labelling liposomes to study their properties *in vivo*. The iodine isotopes unlike other metallic SPECT isotopes can be used for chelator-free radiolabelling by modification of organic compounds with minimal modification to the molecule of interest. Also, iodine radionuclides have different isotopes with varying half-lives to perform different scale longitudinal studies: ^{123}I ($t_{1/2}$ = 13.3 h), ^{125}I ($t_{1/2}$ = 60.5 d) and providing dosing information about the companion therapeutic radionuclide (^{131}I, $t_{1/2}$ = 8 d)[184]. The properties and applications of the above-mentioned SPECT radionuclides for radiolabelling of liposomal nanomedicines have been discussed in Table 1.6.

Table 1.6. Commonly used SPECT radionuclides for radiolabelling of liposomal nanomedicines

Radionuclide	Half-life	Photon energy	Decay	Production
In-111	2.81 d	245 keV	γ	Cyclotron
Ga-67	78.3 h	300 keV	Auger e, γ	Cyclotron
Tc-99m	6.0 h	140 keV	γ	Generator
I-123	13.3 h	159 keV	Auger e, γ	Cyclotron
Re-186	91 h	1080 keV	γ, β^-	Cyclotron
I-125	59.4 d	35 keV	Auger e, γ	Cyclotron

1.3.2 Strategies for radiolabelling:

Liposome radiolabelling strategies can be broadly categorised into three categories, namely:

1.3.2.1 Surface labelling

Liposomal nanomedicines can be directly or indirectly labelled on the surface. The direct labelling strategy involves the attachment of the radionuclide to the nanomedicine without any intermediate steps. Indirect labelling involves the incorporation of prosthetic groups which acts as a chelator/synthon for the radionuclide which is in turn attached to the nanomedicine giving us much more versatility and options compared to direct labelling.[157]

Direct labelling was one of the first methods used for forming radiolabelled liposomes. In this method, the radionuclide of choice or a radionuclide-containing hydrophobic molecule can be incorporated into the bilayer of the liposomal membrane by incubation with preformed liposomes (Figure 1.11(A)). Although higher labelling efficiency has been obtained with this method, the low stability and release of radionuclides *in vivo* under interaction with serum proteins can result in false images of liposomal biodistribution and pharmacokinetics *in vivo.*[174,185,186]

Alternatively, surface labelling can be achieved by incorporating an exposed chelator on the surface of the liposomes (Figure 1.11(B)). This is achieved by inserting a phospholipid or a PEGylated derivatised phospholipid with a chelator into the lipid bilayer during the formulation of liposomes or in preformed liposomes. This was performed initially with two SPECT isotopes ^{67}Ga and ^{99m}Tc with a suitable chelator for both radiometals, DTPA (diethylenetriaminepentaacetic acid) conjugated to stearylamine, phospholipid forming the bilayer of the liposomes.[187] Subsequently, there have been studies where different membrane components such as distearoylphosphatidylethanolamine (DSPE), PEGylated DSPE and cholesterol have been derivatised with different chelators such as DOTA, HYNIC, NODAGA, BAT, DTPA, DFO to radiolabel the liposomes with ^{68}Ga/^{177}Lu, ^{99m}Tc, ^{64} Cu, ^{64}Cu, ^{89}Zr respectively with excellent yields and stabilities.[188–195]

However, the attachment of these chelators on the surface of the liposomes must not modify the surface properties and biological activity of the liposomal drug delivery vehicles. The attachment of larger chelators, modifications of phospholipids, and length of the PEG chain on chelator-attached phospholipids increase the risk of modification of the liposome pharmacokinetics leading to an increased clearance from the blood in most cases. Therefore, it is important to completely characterise these liposomes post chelator attachment to monitor any potential change in the physicochemical properties of the liposomes.

Another method of indirect surface labelling includes modification of the liposome constituting phospholipids/PEGylated phospholipids with non-metallic radionuclides: iodine and fluorine (Figure 1.11(C)). This method of labelling allows radiolabelling of liposomes without bulky modifications in the form of chelators which can be beneficial, thereby minimizing the effect on their biodistribution. The iodine isotope ^{125}I has been used for the tracking of antibody-conjugated liposomes.[196] Similar phospholipid modification has also been used for the short-lived radionuclide ^{18}F.[197,198] The biorthogonal chemistry-mediated reaction has also been used for liposome modification to attach either non-metallic radionuclides or chelated radiometals to phospholipids for studies involving short-lived isotopes allowing quicker labelling. These labelling methods have been used to track fast-circulating liposomal formulations, blood pool imaging and pretargeting methods which will be later discussed in section 1.4.1.

To summarize the surface labelling methods, the indirect methods have distinct advantages over the direct method and are used techniques presently. These advantages include the ability to label liposomes with high-specific activity, and high stability. Further research into avoiding the use of bulky chelators can be beneficial and limit their impact on liposomal properties.

1.3.2.2 Core labelling

Encapsulation of a radionuclide carrying organic species in polymers and liposomes or doping of metallic nanomaterials with radio-metals improves the stable attachment of radionuclides to nanomedicine. This strategy minimises the potential early release of radionuclide from the nanomedicine until it is degraded,[199,200] and minimizes interaction with plasma proteins. The core labelling strategy has selective application to nanomedicines like liposomes, and particularly, the oxine labelling method of liposomes has been highly efficient and clinically viable.[201]

The core labelling methods or encapsulation methods can be categorised into three methods: i) Ionophore binding; ii) Remote loading and iii) Unassisted loading (Figure 1.11). These three methods are discussed in brief below:

1.3.2.2.1 Ionophore binding method

This method is the major workhorse of core labelling methodology, allowing high loading efficiency and stable radiolabelling with minimal surface modification. This is achieved using lipophilic complexes/chelators known as ionophores, these ionophores chelate the radiometal ions and transport them across the lipid bilayer to the core. The ionophore-radiometal complex which is metastable is responsible for carrying the radiometal inside the liposome. After crossing the liposomal membrane, the radiometal can be transchelated to a pre-entrapped hydrophilic chelator and in some cases, hydrophilic drugs.

The first such ionophore used for this method is A23187 which was embedded into the liposomal bilayer facilitating the transfer of ^{111}In to the liposomal core followed by transchelation of ^{111}In by encapsulated nitrilotriacetic acid (NTA).[202,203] In further studies, ionophore A23187 could also be used to transport the therapeutic radionuclide ^{90}Y in DTPA-containing liposomes.[204] Several small ionophores including tropolone[205], acetylacetone[206], and oxine[207–213] have been used since then for ionophore-assisted core labelling of liposomes with ^{111}In and ^{67}Ga with different enclosed chelators. With increased interest and availability of long-lived isotopes, oxine and its derivatives have been used for radiolabelling of DOTA-loaded liposomes with ^{64}Cu[214–216] and ^{52}Mn[217] and DFO-loaded liposomes with ^{89}Zr.[218]

Furthermore, the drugs loaded in the liposomes have been used as a substitute for liposome entrapped chelator to chelate and stabilize the radiometal inside the liposomal core thereby minimizing the modifications to the liposomal formulations. This has been performed using oxine as the ionophore for ^{89}Zr, ^{64}Cu and ^{52}Mn for labelling of PEGylated liposome alendronate (PLA) and Doxil respectively with high loading efficiencies and *in vivo* stability.[109,201,219,220]

1.3.2.2.2 Remote loading

The core labelling of liposomes can also be performed using direct loading of stable radiometal-chelator complexes in preformed liposomes. The main advantage of remote loading is the ability to radiolabel preformulated liposomes without modification on the surface of the loaded drugs. The encapsulated radiometal complex is released from the liposomes on decomposition at the target tissue and cleared from the body. This method has been widely used for ^{99m}Tc labelling of different formulations of liposomes using different chelators including HMPAO[221,222], DISIDA[223], and BMEDA.[224–226] This method has also been explored for labelling of Doxil with theranostic pairs of ^{186}Re/^{188}Re using a BMEDA chelator.[227,228] Recently, core labelling via remote loading of liposomes has also been explored for organic radionuclide ^{125}I, ^{124}I and ^{18}F. In this method, the radioiodinated (amino diatrizoic acid (ADA) ^{125}I-ADA and ^{124}I-ADA)[229] or radiofluorinated compounds (^{18}F-carboplatin) are loaded into liposomes using a pH gradient method.[230]

1.3.2.2.3 Unassisted loading

The final and the simplest method of core labelling of liposomes is unassisted loading of the radionuclide by creating a concentration gradient of radiometal. The liposomes containing DOTA have a copper-depleted core due to the chelation of free copper by DOTA causing a steep transmembrane copper gradient. The incubation of DOTA liposomes with ^{64}Cu with mild heating to 55^{0}C allows spontaneous diffusion of ^{64}Cu into the liposomal core with high loading efficiency and high stability. [231] The advantages of this method include ease of labelling, removal of the need for ionophores and short labelling times. However, the need for the formulation of chelator-loaded liposomes will have limited applications to commercially available liposomal formulations.

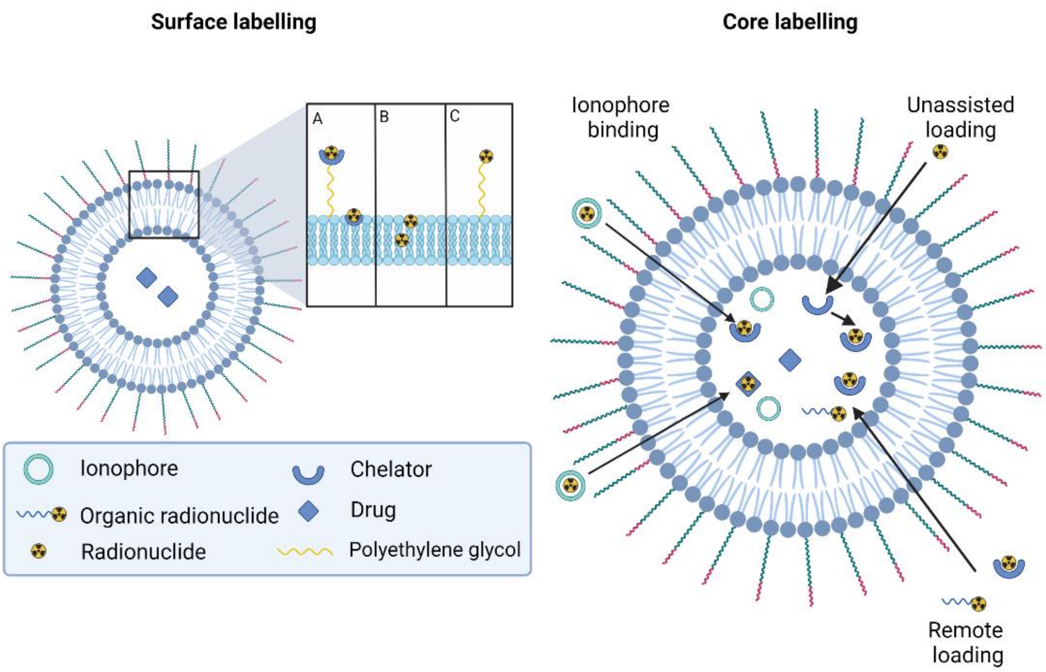

Figure 1.11. Schematic illustration of the different methods for radiolabelling liposomes: Surface radiolabelling: the radionuclide (A), with a chelator (B) or an organic radionuclide compound (C), can be linked to the liposomal surface. Core radiolabelling: the radionuclide is encapsulated within the aqueous core. Ionophores can be used to transport radionuclides across the bilayer where they can be bound by chelators or drugs inside the liposomes, or radioactive compounds/complexes can passively cross the bilayer and become trapped. Created with BioRender.com.

1.3.3 Limitations of current liposome radiolabelling methods

The various radiolabelling approaches discussed above allow labelling of liposomes pre- and post-formulation, and core and surface labelling with a vast library of radioisotopes. However, the accumulation of nanomedicines in tumours has slow pharmacokinetics which is a key trait for these passive targeting vectors that may be problematic in the context of nuclear medicine. This means that nanomedicines can take multiple days, especially for PEGylated formulations, to accumulate in their target tissue at optimal concentrations *in vivo*. Thus, as described in the above section about radiolabelling liposomes, to harness the full radionuclide theranostic potential of the liposomal nanomedicines, we need to match the blood half-lives of these particles to the radionuclides with multiday half-lives such as ^{111}In, ^{89}Zr, ^{177}Lu, ^{186}Re, ^{131}I among others.

The use of such radionuclides, however, is a double-edged sword. The prolonged circulation of nanomedicines labelled with long-lived therapeutic and diagnostic radionuclides creates significant clinical considerations: low therapeutic doses for radionanotherapy to the target tissue, high radiation doses to healthy tissue during circulation and logistical consideration for patients and caretakers in the clinical setting due to shielding considerations. The radionuclides suitable for imaging the slow pharmacokinetics of antibodies/nanomedicines are long-lived making the non-target organs/patients susceptible to high effective radiation doses (0.3-0.7 mSv/MBq), leading to an absolute dose of 40-50 mSv to patients per scan (equivalent to allowed annual radiation dose limit for adults in the UK). This issue is often called the radionuclide dilemma.[219,232–234]

Similar obstacles due to this radionuclide dilemma were faced in the field of radioimmunotherapy due to the long blood half-lives up to days and weeks of antibodies. Significant efforts have been made to overcome these obstacles, most notably using the *in vivo* pretargeting strategy.[235,236] The idea was conceived and first executed in the 1980s based on a simple principle: decoupling the slow circulating targeting vector and the radionuclide moiety.[237] The radiolabelling is performed at the tumour itself after the introduction of both the components *in vivo* facilitating the use of short-lived radionuclides (e.g., ^{18}F, ^{68}Ga, ^{99m}Tc). Taken together, these traits should translate to improved tumour-to-background activity concentration ratios and dramatically lowered radiation dose rates in healthy tissues.

Drawing inspiration from the success of pretargeting in the field of immunotherapy, this strategy could be used to resolve this radionuclide dilemma which encompasses the imaging of nanomedicine. The use of short-lived radionuclides for pretargeting should drastically decrease this observation time from days to hours. In the next section, we will discuss the concept of pretargeting in more detail, the different types of pretargeting explored to date, and its applications to nanomedicine.

1.4 The concept of pretargeting

To circumvent the slow pharmacokinetic-related issues found when imaging using antibodies, the concept of pretargeting was introduced and has been widely explored in the field of antibody imaging and therapy.[238]

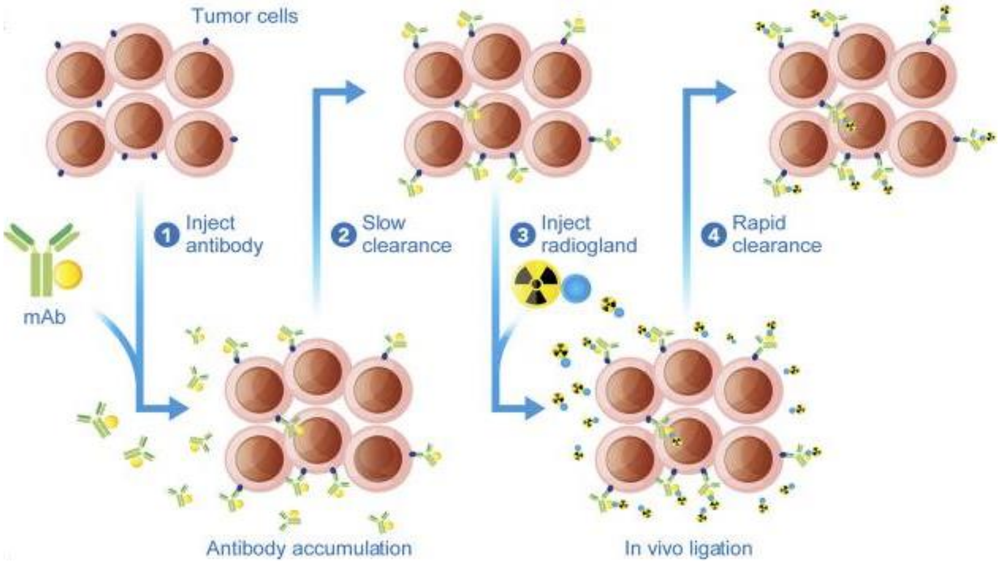

Figure 1.12. General scheme of Pretargeting imaging concept used for imaging of antibodies. Image reproduced from reference. [239]

1.4.1 Introduction to pretargeting

The pretargeting approach involves the sequential administration of two components: (i) a macromolecular (usually antibody or nanomedicine based) targeting vector with a long pharmacokinetic half-life, and (ii) a small molecule radiolabelled conjugate. The two components of a pretargeting system are modified with complementary groups to bind each other at the site of interest with fast kinetics and exhibit *in vivo* stability. In pretargeting, the radiolabelled species is administered after a known lag period to allow sufficient time for macromolecule (antibody/nanomedicine) accumulation at the tumour whilst residual macromolecule is cleared from the circulation. This approach is beneficial for overcoming slow pharmacokinetics systems, such as antibodies and nanomedicines with blood half-lives in the order of days, allowing the use of short-lived radioisotopes and decreasing non-target specific absorbed doses in patients.

This process can be broken down into four steps as observed in all major approaches utilised for pretargeting. Firstly, injection of a modified targeting vector in the bloodstream. Secondly, slow accumulation of the vector in the target site and removal of the free vector from the blood. Thirdly, injection of the complementary small molecule radioligand after the known lag time, finally followed by binding of radioligand to antibody/nanomedicine and removal of excess free radioligand before imaging.

1.4.2 Types of pretargeting

The pretargeting approaches can be broadly categorised based on the interactions involved between the complementary reactive species:

1.4.2.1 Non-covalent interaction approach

These approaches are also known as conventional pretargeting approaches in the pre-biorthogonal chemistry era. The driving force for these interactions is the high affinity supported by highly specific hydrogen-bonding interactions in biological systems (*e.g.,* avidin/streptavidin-biotin).

1.4.2.1.1 Bispecific antibody-hapten binding

The primary pretargeting approach was based on the utilization of bispecific antibodies (bsAb), capable of simultaneous binding to target antigens as well as radiolabelled haptens.[240,241] The application of this approach to nanomedicine is limited only to antibody-based nanomedicines. The only example of an antibody-based nanomedicine study is by Rauscher[242] in which tumour accumulation was increased using the pretargeting strategy.

The system utilised a primary administration of bsAb labelled liposome followed by secondary imaging agent introduction as radiolabelled liposome functionalised with haptens which led to an increase in higher uptake than conventionally labelled liposomes. The inherent possible limitation associated with this antibody model includes the complexities and excessive costs involved in the synthesis of bispecific antibodies. Also, these bispecific antibodies can elicit an immunogenic response. In conclusion, for passively targeted nanomedicine, this approach is unsuitable due to excessive cost, complexity in synthesis and application to only antibody-based nanomedicines.

1.4.2.1.2 Avidin/Streptavidin-Biotin binding

Hnatowich in 1987 utilised the multiple binding sites and high-affinity pair (10^{15} M) of avidin and biotin for pretargeting.[243] In his first approach, streptavidin was conjugated to an antibody targeting vector and following a lag time of 2-3 days post antibody injection, radiolabelled biotin is injected binding rapidly to tumour-localised streptavidin. The large size of the streptavidin-antibody assembly leads to the slow removal of the antibody from the blood. This led to the utilization of the cleaning agent glycosylated avidin in the second approach to remove excess streptavidin-antibody conjugate from the blood before the introduction of the radiolabelled biotin in a second approach. Whilst this system has clear advantages, some limitations to this approach have a considerable effect on its applications. The most noticeable is the immunogenicity of the system due to the introduction of foreign proteins. Moreover, the usage of the cleaning agent adds another variable to circulating components in the pretargeting system.[244,245] Due to the drawbacks mentioned above, there has been a marked decrease in the number of ongoing clinical trials using this pretargeting system.

1.4.2.1.3 Complementary oligonucleotide binding

The high-affinity requirement and need for avoiding immunogenicity led to the development of a new binding system based on complementary oligonucleotides. Morpholino oligomers (MORFs) which are water-soluble, synthetic DNA analogues with highly specific complementarity have shown stability to nuclease hydrolysis. High hybridization affinities and fast renal clearance of MORFs have led to several clinical and preclinical studies.[246] The associated complexities and cost has delayed its acceptance in a clinical setting and optimization is required to incorporate short-lived radionuclides for clinical translation and other systems such as nanomedicines.

1.4.2.2 Covalent interaction approach

It has been a decade since the first report of click ligation (Staudinger ligation) by Bertozzi *et al.* was published with its applications *in vivo.*[247] Since then, this covalent interaction approach of click ligations has found increased applications within biological systems and was awarded the Nobel Prize for Chemistry in 2022. The first *in vivo* application was on labelling cell-surface glycans in mice *via* azide and phosphine derivatives followed by deployment of strain-promoted alkyne-azide cycloaddition (SPAAC) on azidoglycans in zebrafish, elegans, and mice.[248–250] The slow reaction kinetics and limitations of the SPAAC reaction are overcome by the inverse-electron-demand Diels-Alder (IEDDA) reaction between strained cyclooctenes and electron-deficient tetrazines (Tz).[251] It has an added advantage in the field of pretargeting due to its ultrafast reaction kinetics with first-order rate constants in the range of 10^4-10^5 $M^{-1}s^{-1}$. Rossin *et al.* have been a forerunner in the field of pretargeting with IEDDA-based ligation, successfully pretargeting the immunoconjugate CC49-TCO with In-111 for SPECT imaging of colorectal cancer xenografts.[252] Post this report, several groups around the world have continuously developed better systems via synthesis of highly reactive, more stable TCO-tags[251] and Tz-probes radiolabelled with copper-64,[253] fluorine-18,[254] gallium-68,[255] carbon-11.[256]

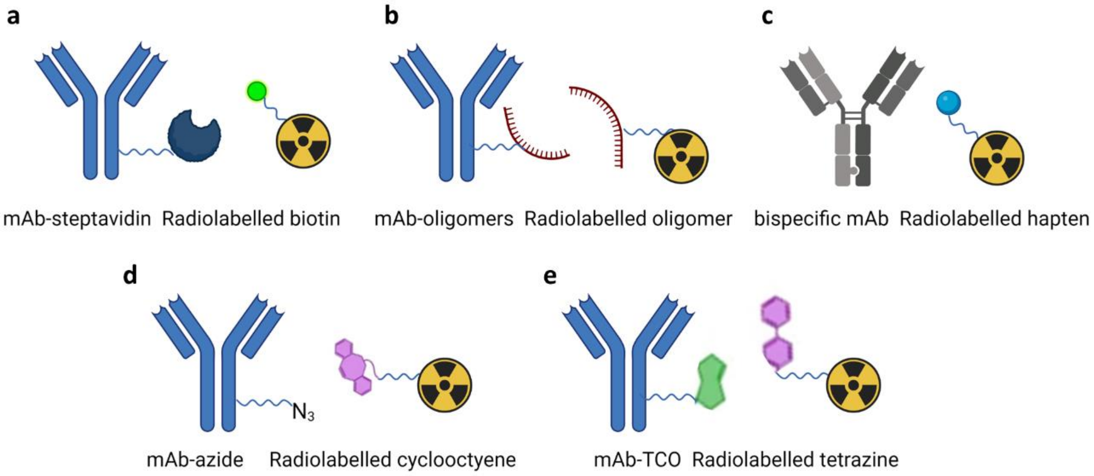

Figure 1.13. Types of pretargeting: The library of different approaches of pretargeting available for imaging of antibodies: (a) Streptavidin-biotin; (b) Complimentary oligonucleotide binding; (c) Bispecific antibody-hapten; (d) Strain promoted alkyne-azide cycloaddition (SPAAC): alkyne-azide; (e) Inverse electron demand Diels-Alder reaction (IEDDA). Created with BioRender.com.

1.4.3 Role of pretargeted imaging in nanomedicine

Nanomolecules as passively targeted drug carriers have improved the field of cancer research and therapeutics in general. The passively targeted nanomedicine is affected by variation of EPR effect with individuals and tumour properties, making it difficult to determine the patient response to the treatment. The use of these nanomedicines on non-responding patients may lead to being ineffective and a toxic build-up of drugs inside the body. The pretargeting approach has the potential to improve imaging of long-circulating nanomedicine by increasing the contrast, decreasing the radiation exposure, and allowing longitudinal imaging beyond the half-life of the radionuclide. Pretargeted imaging study examples have been reported widely in the field of antibody-based therapy due to their slow pharmacokinetics, similarly to nanomedicines.[257,258] These examples include different approaches to pretargeting with some approaches even being accepted for clinical evaluation. On the other hand, the pretargeted imaging studies with passive targeting nanomedicines have been extremely limited in number which is surprising due to two reasons. Firstly, compared to antibodies, pretargeted imaging is potentially more efficient with nanomedicines due to their high loading ability, which is essential for the likelihood of pretargeting. Nanomedicines have at least ten-fold higher reactive tags than antibodies depending on the type of nanoparticles.[259] Secondly, the antibody on high loading has issues like immunogenicity and detection by the reticuloendothelial system due to aggregation. Therefore, the potential clinical impact of nanomedicines can be exploited using pretargeted imaging.

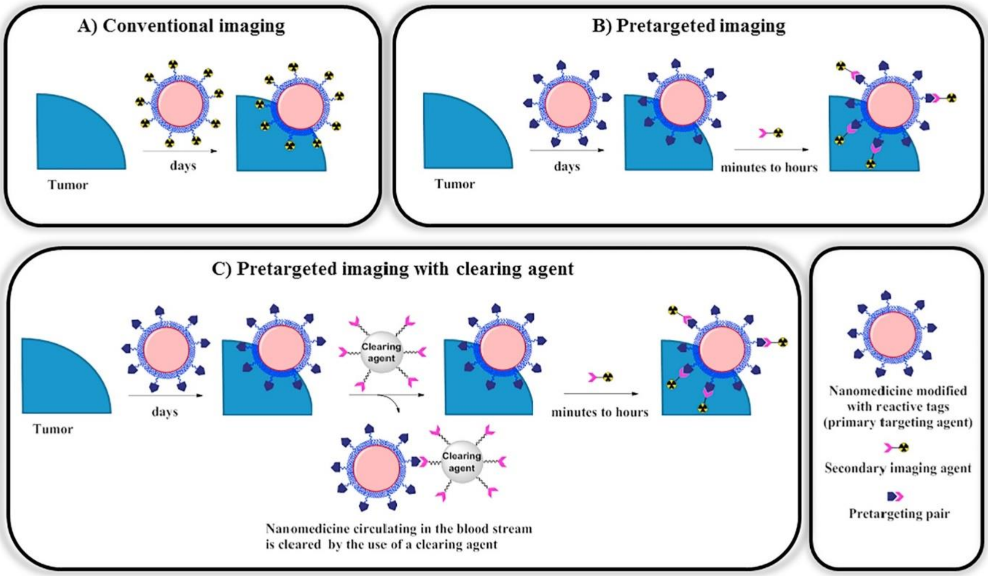

Figure 1.14. Different nuclear imaging methods for nanomedicines: (A) Conventional Imaging (B) Pretargeted Imaging (C) Pretargeted Imaging with clearing agent. Image reproduced. [260]

1.4.4 Limitations of pretargeted imaging in nanomedicine

Despite the above-mentioned potential advantages, pretargeting strategies may present some drawbacks. First, the main methodologies listed above have not been compared head-to-head using a single vector system such as an antibody or nanomedicine. This has led to no quantitative comparisons on the benefits of a particular pretargeting approach which can be used as a one size fits all. Moreover, the different approaches are at different stages of their development to be compared or expanded for use in different systems of antibodies and nanomedicines.

One key concern is the internalization of the primary targeting agent *i.e.*, antibody or nanomedicine. The internalization renders the presence of reactive tags on the surface of the targeting agents unsuitable for binding with the secondary imaging agent and requiring further exploration into these complex systems and incorporating further variables in a complicated system. As seen in Figure 1.14(C), the use of a clearing agent also leads to a further complication of the pretargeting system leading to an extra biomolecule that can accumulate in the body and might not necessarily lead to clearing of the secondary imaging agent from the tumour.[261] Furthermore, the limitation of secondary imaging agent of the pretargeting system to extracellular targets and inability to cross cell membranes.

Specifically, for pretargeting, the nanomedicine is expected to be a more suitable candidate over antibodies due to their ability to carry more reactive tags. However, many nanomaterial-based medicines internalise specifically in the macrophages depending on the properties of tumour vasculature and nanomedicines, which limits their availability for radionuclide binding. The secondary targeting vector carrying the radionuclide should be designed to be highly specific, stable and exhibit fast clearance. If the radionuclide/radionuclide carrying vector does not exhibit any of these properties, it can lead to low contrast and high background activity. Thus, each component in a pretargeting system should be carefully chosen to overcome these limitations.

Table 1.7. Advantages and disadvantages of pretargeted imaging in nanomedicine over conventional imaging methods

Pretargeted Imaging of nanomedicine vs Conventional Imaging

Pros	Cons
1. Ability to stratify patients depending on therapeutic response and imaging results	1. Antibody based pretargeting methods might not necessarily work for nanomedicines
2. Overcome EPR heterogeneity	2. Internalisation of nanomedicines making reactive tags inaccessible
3. Decreased radiation exposure to patients	3. Lower specific uptake at the target
4. Longitudinal imaging	4. The secondary targeting vector should have highly specific properties to reach reactive tags on nanomedicine surface
5. Benefits over antibody pretargeting:	
• Higher number of reactive tags	
• Low immunogenic response	

1.5 Hypothesis and aims of the thesis

Previous work in our lab has developed various labelling methods for liposome, cell and nanoparticles that allows *in vivo* tracking non-invasively using optical, PET, and SPECT preclinical imaging. Through this work, we aim to utilise this knowledge of imaging and liposomal tracking to bridge the present two major gaps in the clinical application of liposomal nanomedicines, specifically PEGylated liposomes. The first major gap that we have endeavoured to address is the EPR heterogeneity through pretargeted imaging of liposomal nanomedicines which will not only provide us an improved method of tracking liposomal nanomedicines but will also find applications in nanomedicine assisted radionuclide therapy. The second gap that we aim to address is the inability to utilise liposomal nanomedicines for treatment of brain ailments due to their large sizes compared to small molecule drugs. To overcome this issue, we attempted to deliver PEGylated liposomes to the brain using a novel RaSP sequence of focused ultrasound efficiently and safely.

Thus, the overall aim of this project was to develop new methods for pretargeted PET imaging of PEGylated liposomes and the delivery of the PEGylated liposomes to the brain. To achieve this, the project was broken down into several step wise parts involving development of radiolabelled phospholipid bioconjugates based on the highly efficient Ga chelator THP, utilising these phospholipid bioconjugates to build two different pretargeting systems (Chapter 2 and Chapter 3), and their *ex vivo* and *in vivo* validation. Also, the delivery of the fluorescent PEGylated liposomes to the brain using focused ultrasound, their delivery assessment using optical imaging and *ex vivo* pretargeted imaging (Chapter 4). These chapters are outlined below along with their graphical abstracts:

Chapter 2: An *in vivo* radiolabelling approach for pretargeted imaging of long circulating PEGylated liposomes nanomedicines based on metal chelation is developed. THP, an efficient Ga chelator, was used to synthesise a THP-phospholipid conjugate which was characterised extensively before being embedded into the bilayer of PEGylated liposomes to give THP-PL liposomes. The THP-PL liposomes are characterised before being pretargeted using ^{68}Ga *in vitro* and *in vivo* in a healthy mouse model.

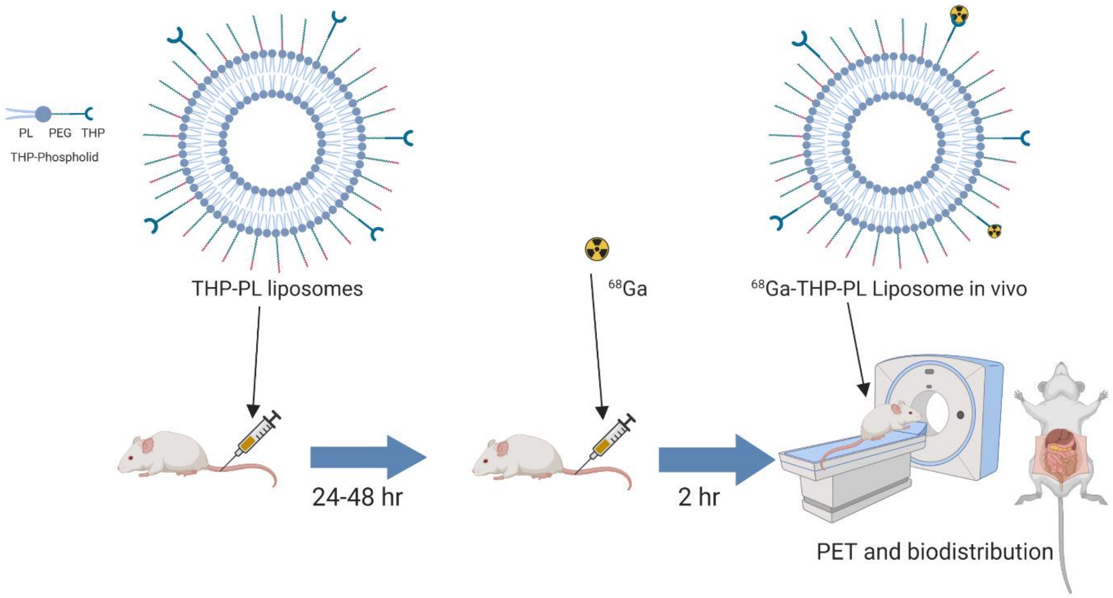

Figure 1.15. Graphical abstract of Chapter 2: Metal chelation based pretargeted PET imaging of PEGylated liposomes using the high chelating affinity of tris(hydroxypyridinone) towards Ga. Created with BioRender.com.

Chapter 3: The biorthogonal chemistry based pretargeting methods have been widely validated for pretargeting for antibodies. Using this IEDDA biorthogonal chemistry, we hypothesised a pretargeted method for *in vivo* radiolabelling of PEGylated liposomes to compare with the metal chelator based pretargeting system developed in Chapter 2. The first step was the synthesis and characterisation of two components of this pretargeting system: a THP-tetrazine and a TCO-phospholipid. The TCO-phospholipid was incorporated in the bilayer of PEGylated liposomes to give TCO-PL liposomes followed by validation of the pretargeting TCO-PL liposomes *in vivo* and *in vivo* with ^{68}Ga-THP-tetrazine. The *in vivo* validation was performed in both in healthy mice and in a fibrosarcoma mouse model.

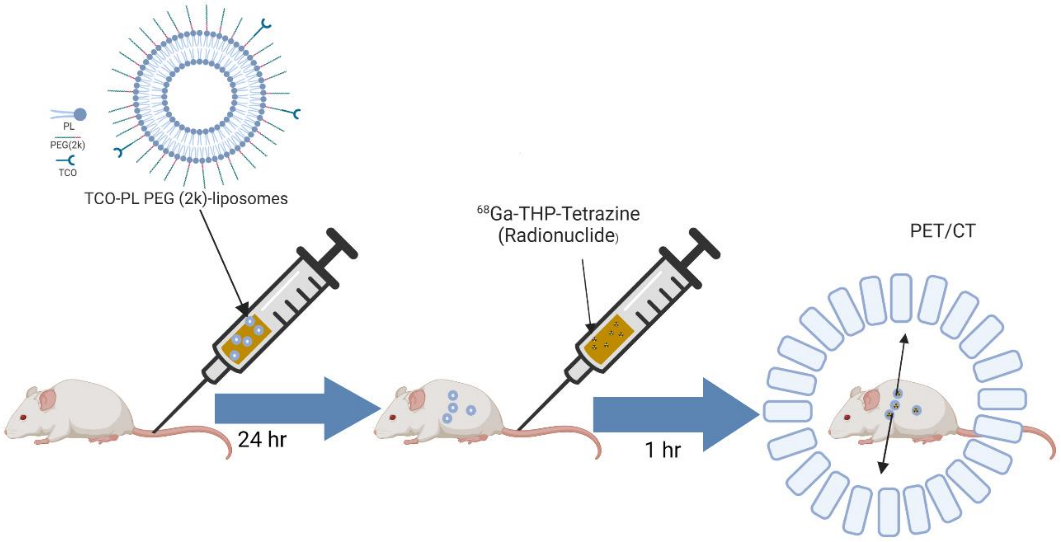

Figure 1.16. Graphical abstract of Chapter 3: Biorthogonal IEDDA reaction based pretargeted PET imaging of PEGylated liposomes exploiting the fast and efficient reaction kinetics between tetrazine and transcyclooctene. Created with BioRender.com.

Chapter 4: The desirable properties of low systemic toxicity and high drug carrying capability make liposomes an excellent candidate for drug delivery to the brain. The field of brain therapeutics suffers from lack of non-specific drug delivery and low therapeutic doses and the liposomal nanomedicines could be the answer to this problem. However, when targeting brain or solid tumours, liposomes suffer from inability to reach their targets due to biological barriers and their large size. In chapter 4, we have investigated the feasibility of using focused ultrasound in combination with microbubble treatment as a method to deliver liposomal nanomedicines (~100 nm) to the brain. Fluorescent DiD-PEGylated liposomes were synthesised and injected intravenously alongside microbubbles. The left hippocampus of mice was then sonicated with either a rapid short pulse (RaSP) sequence or a long pulse sequence, with each pulse having pressure either 0.35 or 0.53 MPa. The delivery and distribution of the fluorescently labelled liposomes were assessed by fluorescence imaging of the brain sections. The safety profile of the sonicated brains was assessed by histological staining. The ex vivo imaging was also performed using pretargeting method developed in Chapter 2.

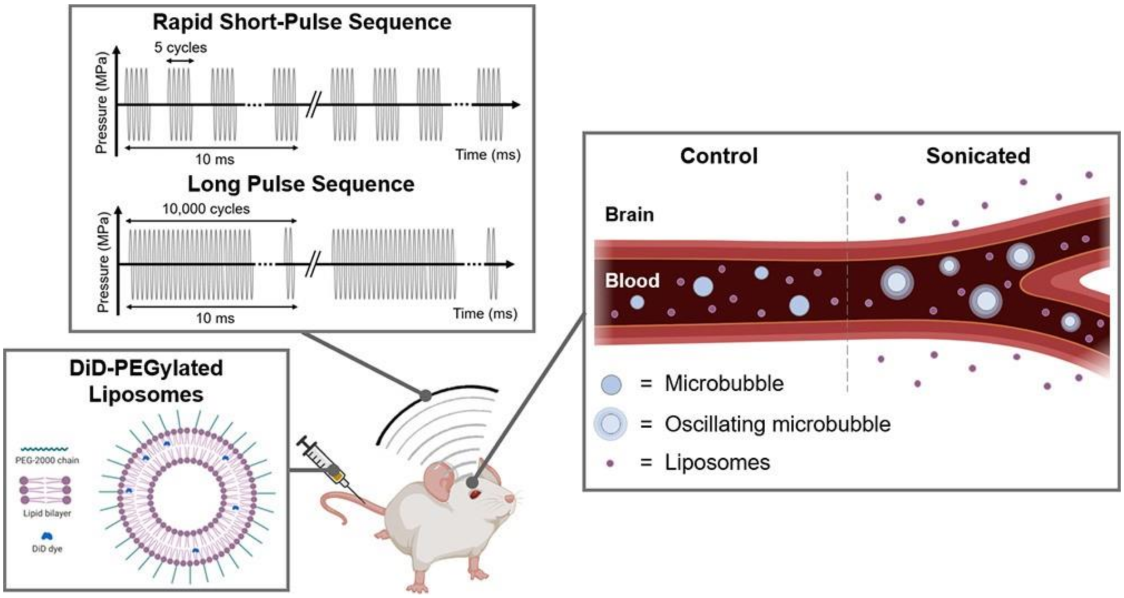

Figure 1.17. Graphical abstract of Chapter 4: Focussed ultrasound and microbubble assisted delivery of fluorescent PEGylated liposomes to the brain followed by quantification and safety assessment. Created with BioRender.com.

2 METAL CHELATION BASED PRETARGETING OF LIPOSOMAL NANOMEDICINES

2.1 Introduction: Trishydroxypyridinone and Ga: A promising pair for metal chelation-based pretargeted imaging

The tris(hydroxypyridinone) (THP) chelator and its bifunctional analogues (Figure 2.1) possess a high binding affinity for the gallium ion in the +3 charged state[262,263] and are known to complex ^{68}Ga rapidly at low chelator concentrations and physiological pH.[262] The formed radiolabelled complex is highly stable for several hours in the presence of serum, which is an essential requirement for successful radiotracer development. The fast chelation and high stability properties of THP have been utilised to perform one step, fast ^{68}Ga radiolabelling of small molecules, proteins, and nanoparticles,[264–269] including *in vivo* chelation of pre-injected ^{68}Ga by THP.[263]

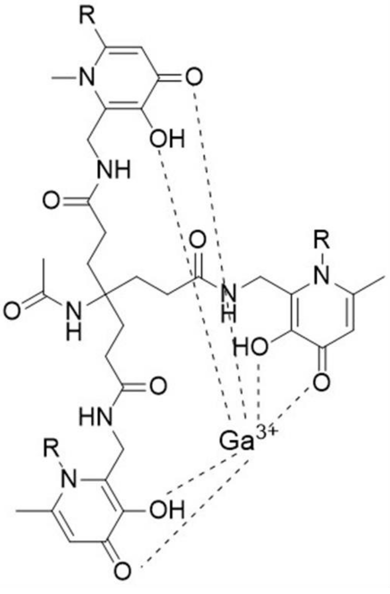

THP^{Me} R = CH_3
THP^{H} R = H

Figure 2.1 Structure of Trishydroxypyridinone (THP): A tripodal framework of 3,4-hydroxypyridinones was formed to give this hexadentate chelator. THP can be derivatised for bioconjugation from the root of three arms, away from the binding groups minimising the impact of the chelation ability. Two different variants of THP are available for use as chelators: THP^{Me} and THP^{H}.

We hypothesised that the high-affinity between Ga and THP could be exploited to form an efficient pretargeting pair for *in vivo* imaging of liposomal nanomedicines. This has been partially explored recently for pretargeting of antibodies. However, before we state the hypothesis and describe the experimental results and discussion, it is important to briefly discuss the different gallium isotopes, their relevance in nuclear imaging, as well as an expanded introduction to the efficient bifunctional chelation properties of THP in brief.

2.1.1 Ga isotopes: PET and SPECT pair

Gallium element occurs in nature as two non-radioactive stable isotopes: ^{69}Ga and ^{71}Ga. The main radioactive isotopes of interest for imaging are the positron-emitting ^{68}Ga and the gamma/Auger emitting ^{67}Ga, which are obtained synthetically. The key properties of these two isotopes relevant to use in nuclear imaging are summarised in Tables 1.5 and 1.6 in Chapter 1.

^{67}Ga is a cyclotron-produced isotope, which can be obtained by either proton irradiation (^{68}Zn(p, 2n)^{67}Ga), deuteron irradiation (^{66}Zn(d, n)^{67}Ga) or α-particle irradiation (^{64}Zn(α, p)^{67}Ga) of different isotopes of Zn.[270] ^{67}Ga decays to stable ^{67}Zn by electron capture (EC) accompanied by a gamma ray (91-393 keV) and auger electron emission (7-9 keV) with a half-life of 78.26 hours.[271] The gamma photon emission and high energy Auger electron emission make it a useful radionuclide in SPECT imaging and radionuclide therapy, respectively.[272,273] Its long half-life is compatible with imaging studies over several days. The long half-life and ability to bind to serum protein transferrin allows the use of ^{67}Ga for the detection of lymphoma,[274,275] inflammation[276] and infection[277]. However, ^{67}Ga SPECT images suffer from low contrast and resolution due to the presence of different photopeak energies, down scatter of high energy photons, and SPECT limitations.[278]

^{68}Ga is most commonly produced from germanium-68/gallium-68 generators, allowing a relatively inexpensive, steady and cyclotron-independent supply. ^{68}Ga decays to stable ^{68}Zn by positron emission with a half-life of 68 min[233,279] which is responsible for PET imaging. The short half-life of ^{68}Ga makes it useful for radiolabelling small molecules and receptor-targeting peptides using a bifunctional chelator (BFC).

The ^{68}Ga bench-top generators have a long shelf life due to the parent isotope ^{68}Ge which has a half-life of 271 days. This parent isotope immobilised on a lead shielded glass column decays *via* electron capture over time to provide the daughter radionuclide ^{68}Ga. The selective elution of ^{68}Ga by exploiting the difference in radiochemical properties of two radioisotopes provides the radioisotope of interest.[157,233,271]

Different generations of generators with different solid/mobile combinations have been used to isolate the ^{68}Ga from the ^{68}Ge loaded in the generator. However, we will only briefly discuss the pharmaceutical grade Eckert & Ziegler generator that has been used in this thesis. In this generator, germanium-68 is adsorbed on a TiO_2 bed enclosed in a borosilicate glass column. Ultrapure 0.1 M hydrochloric acid is used as an eluent to yield Ga^{3+} as a chloride salt. The daily elution of the generator minimises the level of contaminants and due to the continuous production of gallium-68 allows for multiple elutions to be performed in a day, with the maximum achievable activity already being observed 4-hour post-elution. Contaminants include natural elements (aluminium, iron, titanium, lead, etc.), as well as ^{68}Zn and ^{68}Ge, which is a major concern due to competition in chelator binding and thereby a potential decrease the radiolabelling efficiency and specific activity of the final radiotracer of interest.[280] Different procedures have been developed to increase the specific activity and purity of the ^{68}Ga from the generator eluate. These methods, based on anion/cation exchange chromatography, are simple and effective in removing impurities but increase the time required for radiolabelling which is a key factor for a short-lived isotope ^{68}Ga.[280,281]

For the purpose of this thesis and this chapter, which is based on gallium chelation pretargeting, it is important to understand the chemical properties of this metal. Ga with an atomic number of 31 belongs to the 13th group and 4th period of the periodic table. The complexation chemistry of gallium is dependent on the behaviour of Ga(III) oxidation state ions in aqueous solutions which is amphoteric and exists as its aqua ion $[Ga(H_2O)_6]^{3+}$ in acidic conditions. At pH values above 4, hydrolysis occurs forming hydroxide species with low solubility in water. These species redissolve in water at higher pH as gallate $[Ga(OH)_4]^-$ [282] and at pH > 7.4 accounts for 98 % of gallium species in aqueous solutions.[283,284] The high propensity of gallium towards hydrolysis from slightly acidic pH to basic pH range in aqueous solutions leads to low availability of Ga(III) species for chelation with ligands to form complexes. These insoluble hydroxide species, also called colloids, are responsible for low radiolabelling yields. To overcome this issue, fast complexation kinetics, an optimal pH range and presence of stabilising ligands are required to assist the complex formation.[285]

In terms of size, the Ga^{3+} ion exhibits a similar ionic radius as Fe^{3+} (62 pm and 64.5 pm respectively) while forming hexacoordinated complexes with hard ligands in the aqueous medium.[286] Ga^{3+} also shares some biological characteristics with Fe^{3+}. Similar to Fe^{3+}, Ga^{3+} is rapidly chelated by transferrin (a blood serum protein) and with even higher affinity by lactoferrin (neutrophil-released protein at the sites of inflammation).[287] Due to the high affinity of these proteins towards Ga^{3+}, tracking of transferrin and lactoferrin is performed using ^{68}Ga or ^{67}Ga. ^{67}Ga–citrate is used for tracking increased transferrin for imaging infection and inflammation. $^{67/68}Ga$ labelled transferrin and lactoferrin have been used to image uptake mechanisms in tumours and lymphocytes at the site of inflammation.[276,288,289] Similar to iron, gallium also has the potential of binding to siderophores which are small iron-chelating molecules secreted by bacteria and fungi at the site of infection. The siderophores form gallium complexes that are isostructural with the iron complexes and therefore $^{67}Ga/^{68}Ga$ siderophores are used for imaging of infection.[290–295]

The similarity of iron to gallium has been utilised to develop a library of bifunctional chelators for Ga which have been used for labelling various antibodies and small molecules through bioconjugates. Among these chelators, THP has been a forerunner for Ga chelation due to its desirable properties which are discussed in the next section.

2.1.2 Tris(hydroxypyrdinone): an ideal chelator for Ga, but also Fe

Different bifunctional chelators have been developed for Ga^{3+} coordination.[296–299] The key characteristics of a perfect chelator for radiometal include *(i)* fast complexation kinetics, *(ii)* single isomer or species formation upon chelation, *(iii)* mild labelling conditions and *(iv)* high *in vivo* stability. Fast complexation kinetics and mild labelling conditions are essential for the labelling of biomolecules with ^{68}Ga. The chelator leading to a single isomer species upon complexation allows for fast complexation without purification and easier production of radiotracer in the clinical setting. High *in vivo* stability and inertness of the radiometal chelator complex prevents transchelation of ^{68}Ga to serum proteins and dissociation of the chelator *in vivo,* which may complicate image analyses of tracer accumulation.

THP is a tripodal, acyclic, hexadentate O6 donor. It binds gallium through three bidentate 1,6-dimethyl-3-hydroxypyridin-4-ones via the ketone and deprotonated hydroxyl groups.[296,300] The similarities between gallium(III) and iron(III) and the affinity of siderophores towards iron(III) have led the structure of siderophores to be a starting template for the design of THP.[301,302] THP has derived its structure from the siderophore mimic deferiprone, clinically used for iron sequestration and treatment of iron overload,[303] with an intention to further increase its affinity towards Ga^{3+} ions.

THP is a highly efficient chelator for ^{68}Ga with multiple desirable properties making it a suitable candidate for labelling biomolecules as a bifunctional chelator. THP has a high thermodynamic affinity for ^{68}Ga leading to fast complexation at physiological pH and with ligand concentrations as low as 0.5 µM[262,263,296,304]. Moreover, despite being an acyclic chelator, the kinetic stability of the ^{68}Ga-THP complex is high even at pH values higher than 10 which can be explained due to branched structure. The $^{68/67}$Ga-THP complex has also demonstrated high stability in serum and is non-susceptible to transchelation for up to 4 hours and 8 days, respectively[262].

The ability of THP to bind ^{68}Ga in human serum/plasma is a testament to the high chelating efficiency between THP and gallium, and the stability in the presence of apotransferrin[262]. These outstanding radiolabelling properties also allow THP to bind ^{68}Ga^{3+} *in vivo*, when administered i.v. to mice previously injected with ^{68}Ga despite the dilution of the THP concentration in the blood and the presence of competing proteins transferrin and apotransferrin[305]. Thus, ^{68}Ga^{3+} and THP can be developed as a potential chemical pretargeting pair.

2.1.3 Aims and hypothesis

To evaluate the potential of this high-affinity between THP and ^{68}Ga, we hypothesised an *in vivo* radiolabelling strategy for PEGylated liposomes. In our hypothesis, a pretargeting strategy based on metal chelation could be feasible using a radiometal and a bifunctional chelator (here, THP-NCS) as an *in vivo* pretargeting pair. In this approach, the bifunctional chelator THP-NCS was attached to the surface of PEGylated liposomes and then radiolabelled *in vivo* in a murine model as schematically represented in Figure 2.3. This strategy would have benefits over traditional covalent and non-covalent pretargeting methods including minimal handling of the radioactivity, minimal radiosynthesis work, longitudinal tracking over time, minimal radiation exposure to staff in a clinical setting, and enabling this technique to be used clinically even with lack of advanced expertise and radiochemistry facilities. This is not the first attempt to explore the pretargeting ability of this metal chelation pair. The ability of THP and Ga as a pretargeting pair has been recently explored for pretargeted imaging of antibodies with limited success. In this study, THP-antibody bioconjugates were injected followed at a later time point by ^{68}Ga and the ensuing results are shown in Figure 2.2.

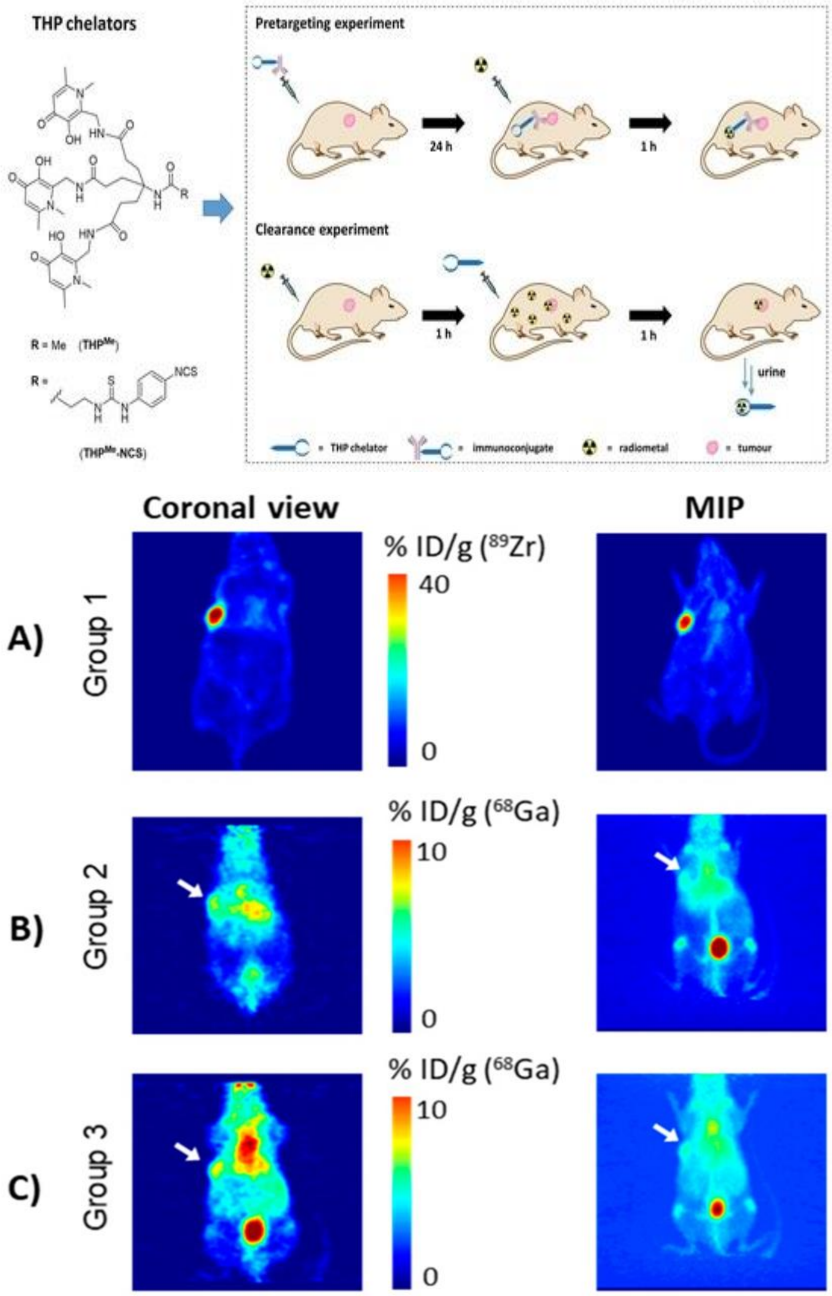

Figure 2.2. Metal chelation pretargeting of antibodies: (Top) Schematic representation of the experiment workflow of the reported metal chelation pretargeting of antibodies**.** (Bottom) The Representative PET images of nude mice bearing SW1222 xenografts. (A) Mouse treated with directly labelled 89Zr-DFO-NCS-huA33 (Positive control group, 25 hours p.i.); (B) Mouse pre-treated with THP^{Me}-NCS-huA33 (Test group) followed at 24 h by ^{68}Ga acetate (imaged at 2 h p.i.); (C) Mouse injected with ^{68}Ga acetate only (2 h 30 min p.i., Negative control). White arrows indicate location of the tumour. Image reproduced from Imberti et al. [305]

To test our hypothesis of metal pretargeting of PEGylated liposomes, we synthesised a THP-phospholipid conjugate which was inserted into preformed PEGylated liposomes to give THP-liposomes. The presence of the chelator on the liposomal surface acts as a binding site for Ga-68 which was validated *in vitro* in serum and the serum stability of these radiolabelled liposomes was also determined. These *in vitro* results were followed by validation of *in vivo* pretargeting of THP-liposomes. To further validate this approach, the same metal pretargeting chelation was also explored with a bone targeting small molecule THP-pamidronate (THP-Pam).[265]

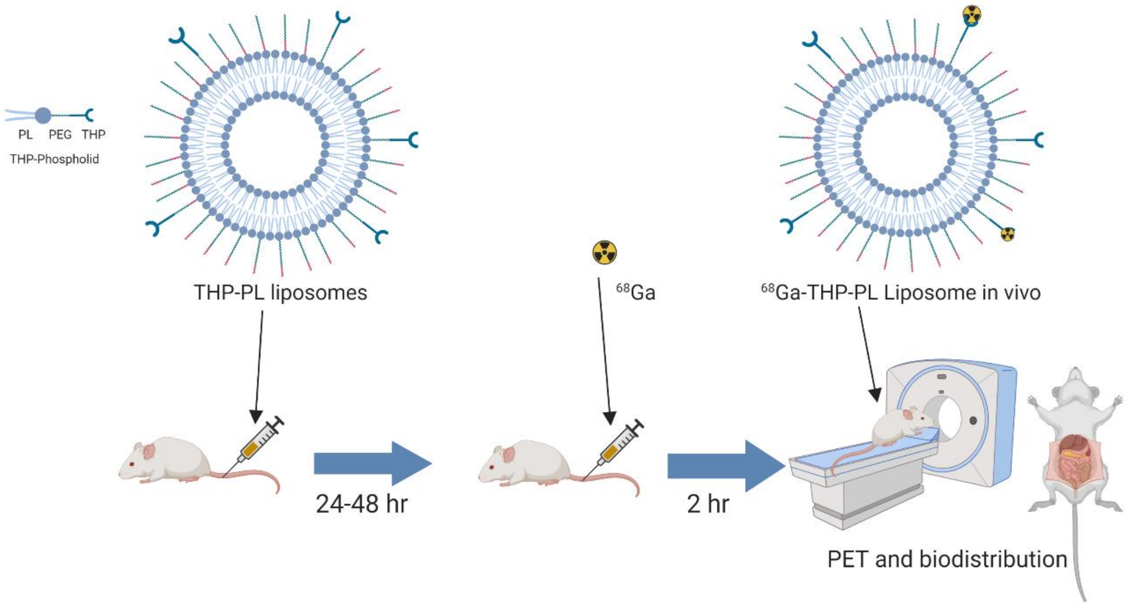

Figure 2.3. Graphical abstract of the metal chelation based pretargeting of PEGylated liposomes in a murine model. Created with BioRender.com.

2.2 Results and discussion

2.2.1 Synthesis and characterisation of THP-Phospholipid

To provide gallium-binding properties to PEGylated liposomes, a chelator-PEG-phospholipid conjugate based on tris(hydroxypyridinone) (THP) was synthesised by amine-thiocyanate conjugation (Figure 2.4).

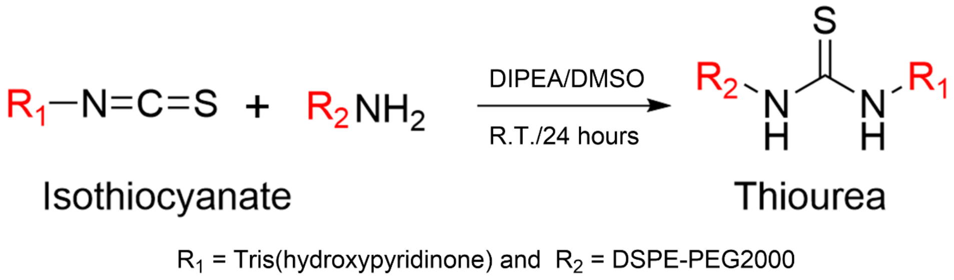

Figure 2.4. Scheme of the reaction between an isothiocyanate and amine: The reactants forming a stable thiourea bond in mild basic conditions where R^1 is Trishydroxypyridinone, and R^2 is DSPE-PEG2000 (phospholipid) in this chapter.

THP was selected over other gallium chelators for its proven high affinity and fast complexation kinetics, even in the presence of competing metal ions as mentioned above in the introduction. The isothiocyanate derivatives which are moderately reactive but quite stable in water and most solvents were chosen to form THP phospholipid conjugates as the thiourea bond formed upon reaction with amines is known to be highly stable *in vivo* for up to 24-48 hours but comparatively less stable than amide bonds.[306–308] An amide bond formation using THP-NHS esters would have been an alternative bioconjugation strategy in case of stability issues with thiourea bond, but the commercial availability of THP-isothiocyanate allowed for an easier one-step synthetic approach. The NH_2-PEG2000-DSPE phospholipid was chosen to form the THP-phospholipid conjugate as PEG2000-DSPE is the basic phospholipid component of stealth liposomes and it has been used routinely to form folate-targeted liposomes via embedding of the folate-phospholipid conjugate in the bilayer of the liposomes.[309] The length of the PEG chain is determined to make THP chelators available on the surface of PEGylated liposomes as seen in figure 2.5. The length of the PEG chain determines whether the targeting molecule or the chelator at the end of the phospholipid chain is accessible for interaction with surrounding and in our case, the radiometal ^{68}Ga. The amine derivative of the PEG2000-DSPE has been widely used for conjugation with various targeting and imaging motifs and here, provides an easy method for conjugation with THP-NCS.

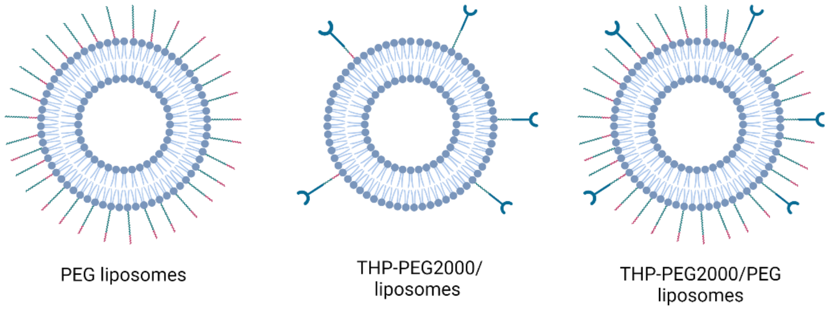

Figure 2.5 Impact of PEG2000 on chelator availability: Accessibility of the THP chelators on the surface depending on the different formulation of liposomes/PEGylated liposomes and THP-phospholipid with a PEG chain. The addition of a PEG2000 chain to THP-phospholipid allows them to be accessible to Ga for chelation. Created with BioRender.com.

As a solvent, anhydrous DMSO proved to be an ideal choice to overcome the low solubility of DSPE-PEG2000 amine in water and the tendency of THP-NCS to undergo degradation or hydrolysis in water or ethanol (ideal solvent for DSPE-PEG2000 amine). Thereby, DMSO minimised solubility and degradation concerns allowing for the reaction to proceed slowly without the need for high pH and temperature conditions. The reaction was performed at room temperature with DIPEA as a base to achieve a pH of 9-10 to facilitate the reaction via deprotonation of the amine of DSPE-PEG2000. The use of mild conditions and DMSO thereby minimised the formation of side products.

To remove the unreacted THP-NCS and excess reaction components (*i.e.,* DIPEA, DMSO), solvent extraction using chloroform/water was used as the first method. The reaction mixture was diluted with water and brought down to pH 7 to extract the lipophilic THP-PL in the chloroform layer whereas DMSO, DIPEA and THP-NCS were collected in the water layer. However, the NMR of the obtained purified product showed the presence of impurities.

Dialysis purification was chosen as an alternative method considering the large MW weight of PEGylated phospholipid and the large difference between the MW of the desired product THP-PL, and the impurities THP-Bz-SCN, DIPEA, and DMSO. Due to the susceptibility of the dialysis membrane toward DMSO, the reaction mixture was diluted to 5% DMSO to prevent damage or solvation of the dialysis membrane during purification. Lyophilisation of the retentate yielded THP-PL as a white light powder with a yield of 84 ± 6 %.

To confirm the success of the conjugation reaction and purity of the synthesised THP-PL, the ^{1}H NMR spectrum in $CDCl_3$ of THP-PL was compared to that of the starting material PL (NH_2-PEG2000-DSPE) (Figure 2.6). The presence of the characteristic broad peaks of THP (δ 7.3, 6.9 -NH; 6.4 -ArH; 3.74 -CH_2) in the spectra of THP-PL and not PL supported the successful synthesis of THP-PL in the reaction. In addition, the formation of the thiourea bond is evidenced by the disappearance of the –NH_2 peak at δ 1.69 ppm, and the appearance of thiourea protons at *ca.* δ 9 ppm as broad peaks. Integration of peaks could not be performed due to the broadness of most peaks and the high-intensity ethylene peak of PEG at δ 3.6 ppm in both spectra, which marred the resolution of both spectra.

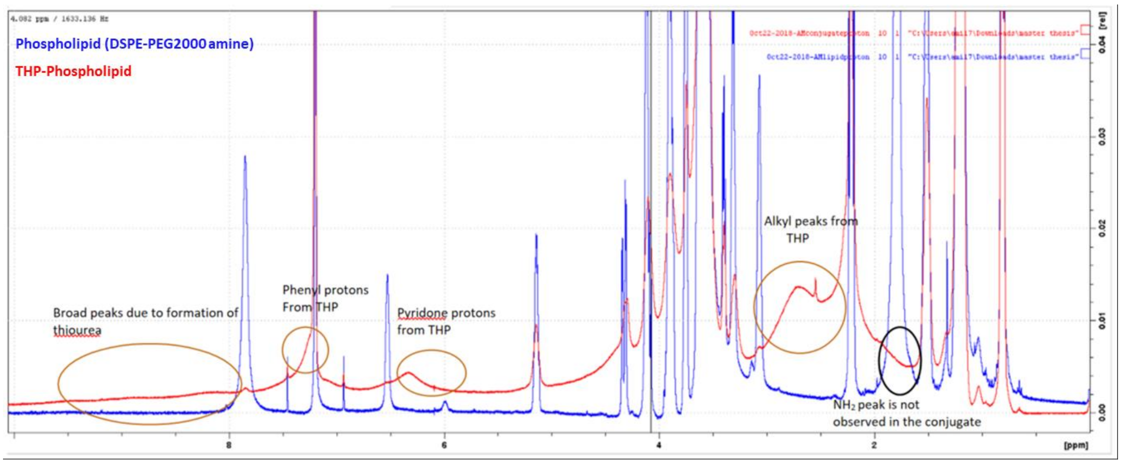

Figure 2.6. Comparative ^{1}H-NMR of THP-PL and DSPE-PEG2000 amine using 400 MHz NMR in $CDCl_3$ (1024 scans): THP-PL is characterised by the presence of broad THP peaks (highlighted using red circles) and absence of NH_2 peak unlike the NMR of DSPE-PEG2000-amine (highlighted using black circle).

Further confirmation of the success of the conjugation reaction was provided by electrospray ionisation mass spectrometry (ESI-MS). The spectrum of THP-PL (THP-PL exact MW=3733) showed the expected electrospray envelope nature of PEG polymers and the z = 2 species in the range 1700-2000 m/z (peak found at 1866; calculated for THP-PL = 1866), the z = 3 species in the range 1200-1350 m/z (peak found at 1245; calculated for THP-PL = 1244), and the z = 4 species in the range 850-1000 m/z (peak found at 938; calculated for THP-PL = 933) (Figure 2.7). These peaks were not observed in the ESI-MS of PL performed under identical conditions.

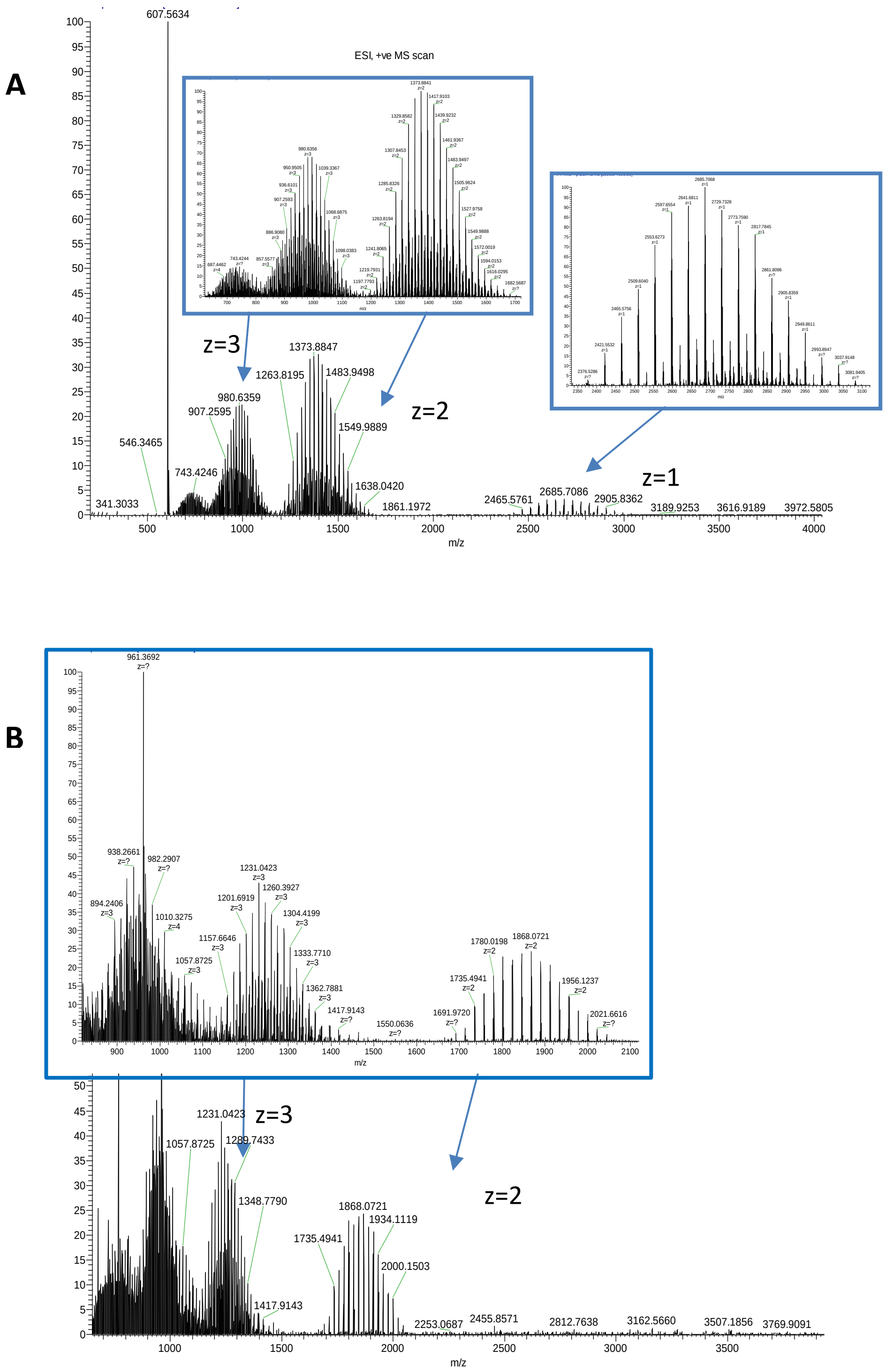

Figure 2.7. Mass spectra recorded with MALDI-TOF High Resolution Mass spectrometry: The envelope like nature is a characteristic of the mass spectra of PEGylated molecules due to the polydispersity in MW of PEG chains attached to the phospholipid: (A) DSPE-PEG2000-amine: z=1 species 2500-3000 (Exact mass: 2790); z=2 species 1250-1650 (Exact mass: 1395); z=3 species 800-1100 (Exact mass: 930), (B) THP-PL: z=2 species 1700-2100 (Exact mass: 1866); z=3 species 1140-1360 (Exact mass: 1244); Z=4 species 840-1060 (Exact mass: 933). Base peak in both the spectra is at 607.5 due to formation of stable phospholipid fragment on ionisation.

2.2.2 Synthesis and characterisation of THP-PL-PEG(2k)-liposomes

Surface modifications of PEGylated liposomes can be performed during the formation of liposomes or in preformed liposomes. Here, we desired insertion of the THP-PL in the bilayer of the preformed PEGylated liposomes, which were chosen for having the same physicochemical properties as stealth liposomes extensively used in the clinic such as Doxil/Caelyx (size 89.4 ± 0.6 nm, concentration: 60.0 ± 0.9 mM, PDI: 0.03 ± 0.01). THP-PL was inserted into the lipid bilayer of PEGylated liposomes using a standard protocol, previously shown to allow insertion of folate targeting phospholipids without significant modification of the original properties of PEGylated liposomes.[310] The insertion process occurs at an elevated temperature which is just below the phase transition temperature of HSPC (58°C).[310] As mentioned in the introduction chapter, at this temperature there is an increased fluidity in the bilayer of the membrane allowing for the incorporation of the external phospholipids (here, THP-PL) in the bilayer. The optimisation of insertion is dependent on the relative concentration of phospholipid being inserted, incubation time, and incubation temperature. The incubation temperature and time were chosen as 50°C and 30 minutes respectively as these conditions have been routinely used in our lab for core radiolabelling of preformed liposomes. [109,220,311] The concentration of THP-PL in the incubation mixture was optimised to be less than 5 mol % to minimise any impact on the surface of the liposomes and hence its properties. When the concentration was higher than 5 mol %, it led to an increase in the liposomal size possibly due to aggregation, as observed in dynamic light scattering (DLS) measurements. After the insertion reaction, which involved co-incubation of THP-PL and PEG(2k)-liposomes at 50°C for 30 min (Figure 2.8), the THP chelator was expected to be accessible on the liposome surface, hence retaining its chelation affinity towards gallium. To facilitate this, THP-PL was to contain a PEG chain of the same molecular weight as the PEG chains present in PEG(2k)-liposomes (*i.e.,* 2000 Da).

To assess the success of the insertion reaction, the product (THP-PL-liposomes) was purified by size exclusion (PD10 minitrap G-25 size exclusion column) and analysed via DLS (Figure 2.9), nanoparticle tracking analysis (NTA, Figure 2.9), cryo-electron microscopy (cryo-TEM, Figure 2.10) and radiolabelling studies (Figure 2.13). The insertion was considered successful if the properties of THP-PL-liposomes were the same as PEG(2k)-liposomes and the THP-PL-liposomes could bind ^{68}Ga. The DLS studies were performed to monitor the impact of surface modification on hydrodynamic size and zeta potential of the PEGylated liposomes (2.2.2.1). The nanoparticle tracking analysis was also performed to monitor the impact on the size, polydispersity and concentration of the PEGylated liposomes post-modification (2.2.2.2). The cryo-electron microscopy was performed on the PEGylated liposomes before and after insertion to assess the impact on the size, size distribution and most importantly, the shape of the liposomes (2.2.2.3). The radiolabelling of the liposomes was performed to verify that the THP chelator was present, and accessible on the liposomal surface. The radiolabelling results are discussed in section (2.2.3.2).

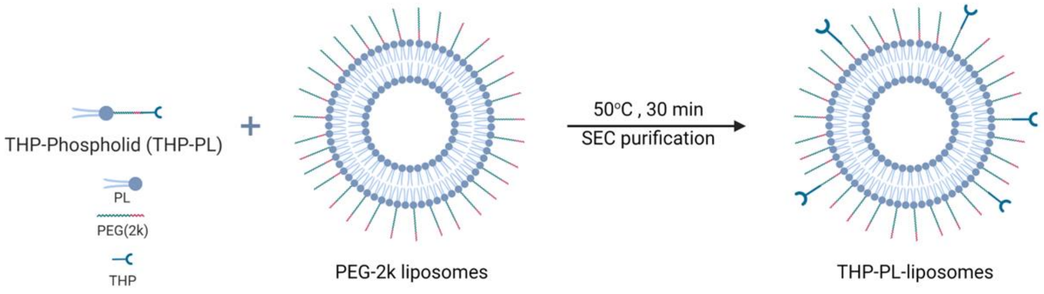

Figure 2.8. Synthesis of THP-PL-liposomes: Insertion of THP-PL into PEGylated liposomes by co-incubation of THP-PL and PEG-2k liposomes. Created with BioRender.com.

2.2.2.1 Dynamic light scattering (DLS)

DLS is a powerful tool to measure the hydrodynamic size, zeta potential, and polydispersity of nanomolecules and particles. In our case, dynamic light scattering allows us to explore the effect of attachment of THP on the physicochemical properties of the PEGylated liposomes post modification in our experiments (zeta potential and hydrodynamic size). The average size (z-average) of the PEG(2k)-liposomes without modification was 97 ± 3 nm and after modification, it was 95 ± 2 nm. In addition to size, the surface charge of the liposomes was also measured because the surface charge plays a key role in their *in vivo* behaviour as mentioned in the introduction. The zeta potential measurement of the non-modified PEGylated liposomes gave us a surface charge of -5.2 ± 1.3 mV and post modification the surface charge was -5.7 ± 0.9 mV. Finally, the polydispersity index (PDI) was also measured. PDI is a measurement of the number of species of a particular size providing information if the particles are monodispersed or not. Clinically used liposomes are highly monodispersed to minimise the variability in the injected samples. Therefore, we aimed to minimise the increase in polydispersity after modification. The PDI of the THP-PL-liposomes was 0.10 ± 0.03 and for the unmodified PEGylated liposomes was 0.05 ± 0.02. Taken all together, these results confirmed that the insertion reaction had no major impact on the surface charge (zeta potential), polydispersity and hydrodynamic size.

2.2.2.2 Nanoparticle tracking analysis

The high-resolution nanoparticle concentration and size distribution were determined by using Nanoparticle Tracking Analysis (NTA). NTA utilizes dynamic light scattering and Brownian motion of multiple free-flowing sample frames to obtain important information about the size distribution and concentration of the sample. The size measurement was an important high-resolution reaffirmation of the DLS results. The determination of liposome concentration is important as it plays a vital role in the *in vivo* clearance of liposomes. The liposome concentration for the unmodified PEGylated liposome was $9.01 \times 10^{14} \pm 7.15 \times 10^{13}$ particles/mL and for the THP-PL-liposome was $4.20 \times 10^{12} \pm 1.05 \times 10^{11}$ particles/mL. The size distribution of both liposome samples was 80-200 nm with peak maxima at 80 nm and 106 nm for unmodified liposomes and

THP-PL-liposomes respectively. In both samples, the liposomal size is concentrated towards the ~100 nm region with a small shoulder representing the particles with a slightly larger size greater than 100 nm. From these results, we can conclude there is a non-significant increase in the average liposome size which was confirmed with DLS measurements.

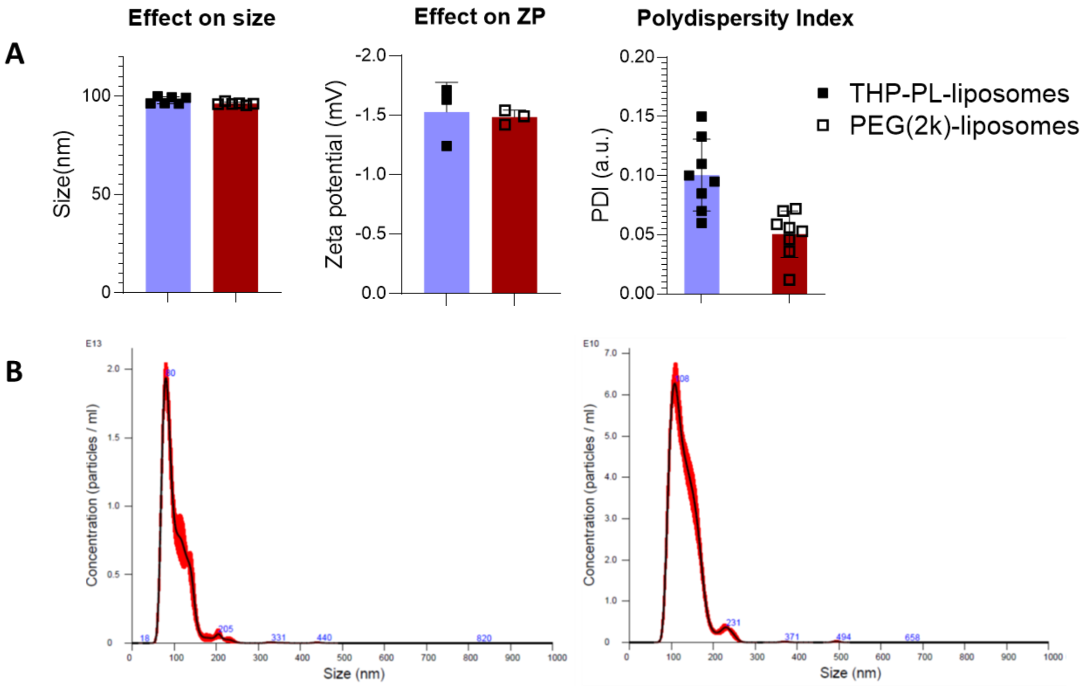

PEG(2k)-liposomes THP-PL-liposomes

Figure 2.9. Characterisation of THP-PL-liposomes using dynamic light scattering and Nanoparticle Tracking Analysis**:** **(A)** The hydrodynamic size of THP-PL-liposomes and PEG(2k)-liposomes was recorded showing no effect on size (Z-average) due to insertion of THP-PL into the liposomes; the surface charge was measured as zeta potential (ZP) of the liposome samples showing minimal change in the magnitude of surface charge with no change in the polarity post-insertion of THP-PL in the liposomal bilayer; the polydispersity index (PDI) was determined showing small increase in the polydispersity of THP-PL-liposomes compared to unmodified PEG(2k)-liposomes. **(B)** Nanoparticle Tracking Analysis (NTA) results: PEG(2k)-liposomes (concentration: 9.01 x 10^{14} ± 7.15 x 10^{13} particles/mL, mode:80 nm, mean: 102.4 nm); THP-PL-liposomes (concentration: 4.20 x 10^{12} ± 1.05 x 10^{11} particles/mL, mode: 106.2 nm, mean: 131.6 nm)

2.2.2.3 Cryo-electron microscopy

Cryo-electron microscopy allows the study of biological samples at very low concentrations at their bioactive physiological state. The fixation of the sample involves rapid freezing and fixation in a vitreous ice film which preserves their hydrated state. Here, THP-PL liposomes and unmodified PEGylated liposomes were frozen in vitreous ice to examine if the insertion of THP-PL had caused any modifications to their shape, bilayer structure and size distribution. As seen in figure 2.10, the THP-PL liposomes (A) retain their bilayer, spherical structure as observed in the unmodified PEGylated liposomes (B). 50 representative microscopic images were taken for each sample to confirm the above observations. Analysis of these microscopic images using ImageJ allowed us to create a size distribution which is shown as a histogram in figure 2.10. Thereby, cryoEM along with the data from DLS and NTA confirmed that non-significant change in the liposomal size, PDI and zeta size and no change in shape and structure of the liposomes was observed post-modification.

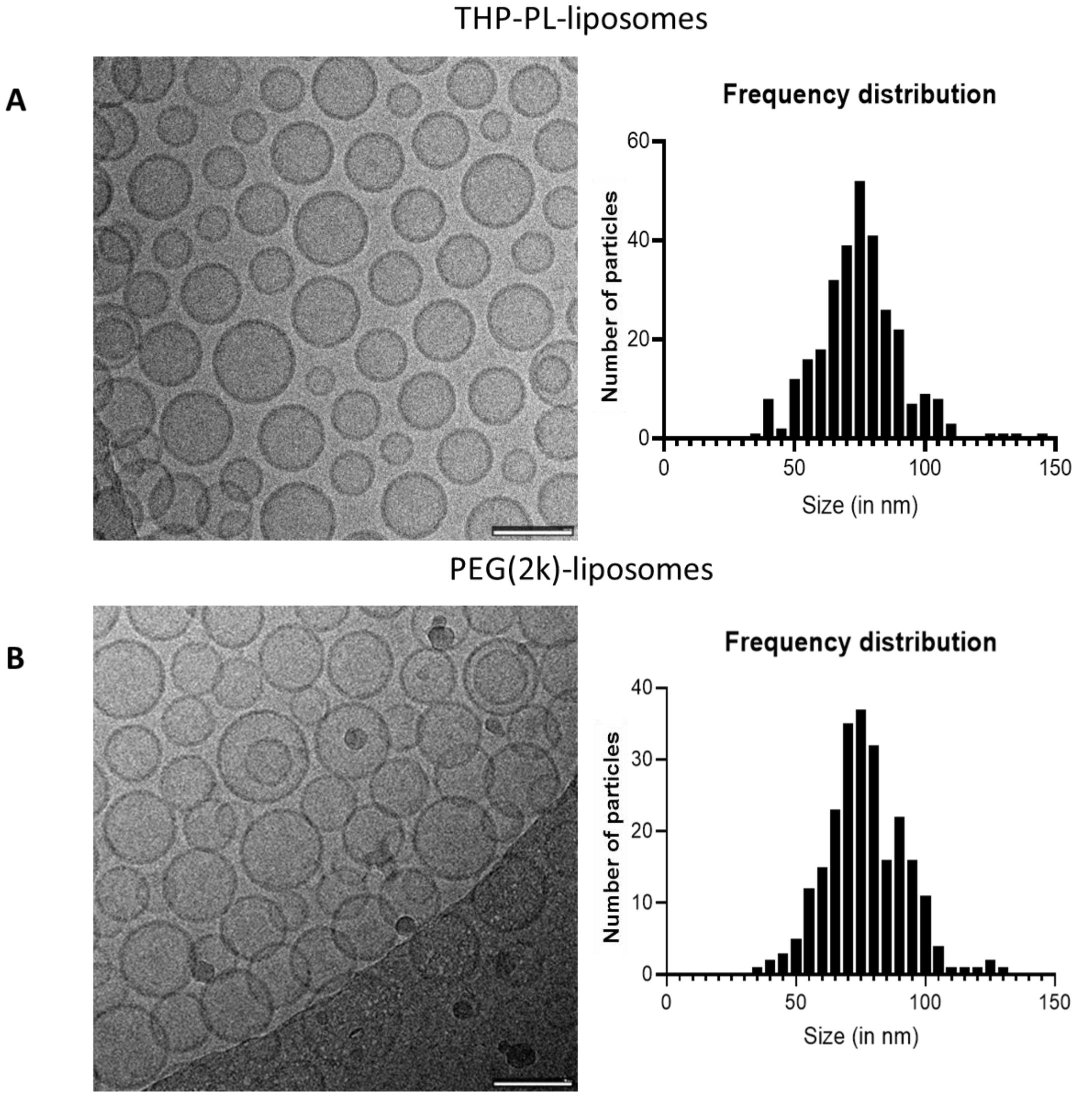

Figure 2.10. Cryo-electron microscopy of liposomes pre- and surface post-modification with THP-PL: (A) showing THP-PL-liposomes have retained their spherical nature and the size distribution is not altered by insertion of THP-PL into the bilayer of liposomes and bilayer nature is also retained; (B) showing PEG(2k)-liposomes spherical morphology and bilayer structure. Size quantification of liposomes from analysis of cryoEM images showing frequency distribution of diameter of liposomes: (A) Unmodified PEG(2k)-liposomes; (B) THP-PL liposomes. The scale shown in the cryoEM image is 100 nm.

2.2.3 Radiochemistry

2.2.3.1 Radiolabelling of THP-PL

Having obtained spectroscopic confirmation of the success of the conjugation reaction to form THP-PL, its binding affinity towards gallium was tested by radiolabelling with ^{68}Ga. The radiolabelling reaction was performed by eluting $^{68}GaCl_3$ from the generator with 0.1M HCl, followed by neutralisation and purification of an aliquot with concentrated sodium carbonate to pH 6, and mixing with an aqueous solution of THP-PL at room temperature for 30 min (final buffer concentration 600 mM carbonate). These reaction conditions were chosen as they have been shown to exceed the minimum concentration and reaction times required for an efficient ^{68}Ga reaction with THP (sub-micromolar ligand concentrations and 5 min are sufficient for >95% RLY with other THP-containing molecules)[262]. The radiolabelling yield of THP-PL was compared to that of PL, THP, and buffered free ^{68}Ga as controls. The analysis of ^{68}Ga radiolabelling of synthesised THP-PL and controls by radioTLC showed high radiolabelling yields (Figure 2.11). Two solvent systems were used as mobile phases to confirm this result. Using citrate buffer as a mobile system facilitated separation between PL and THP-PL species whereas using a 75:36:6 chloroform/methanol/water mixture facilitated separation between THP and THP-PL. However, the high molecular weight of THP-PL restricted the complete migration of the conjugate on the TLC plate and thereby prevented the quantification of radiochemical yield. Quantification of radiolabelling was achieved using size exclusion chromatography, allowing complete separation of THP-PL and unreacted ^{68}Ga giving a non-optimised radiolabelling yield of 76.5 ± 4 % (Figure 2.11).

One key consideration for the radiolabelling of THP-PL here is the pH, specific activity and the purity of Ga utilised for radiolabelling. The slightly acidic pH is chosen to minimize the formation of the insoluble hydroxide or colloids as discussed in the introduction of this chapter. The colloid formation competes with the radiolabelling of the chelator and provides an impure final reaction mixture requiring a need for purification of the radiolabelling mixture post labelling. However, even at the pH of 6, small amounts of colloids are formed which can be seen in Figure 2.12 at the origin of the citrate radioTLC.

To further minimise the presence of colloids, post buffering of generator eluate to pH 6, buffered Ga was purified using a centrifugal spin filter which removed any colloids formed. This was verified using radioTLC as seen in figure 2.12. This purified and buffered ^{68}Ga was also used for pretargeting experiments *in vivo* as the presence of colloids will decrease our ability to determine the biodistribution of free Ga. The colloids, due to their aggregated large size, are known to accumulate in the liver which is an organ of interest in liposome delivery thereby potentially hindering our study. Henceforth, all procedures involving ^{68}Ga/^{67}Ga labelling, *in vitro* validation or *in vivo* administration were purified as above unless mentioned explicitly.

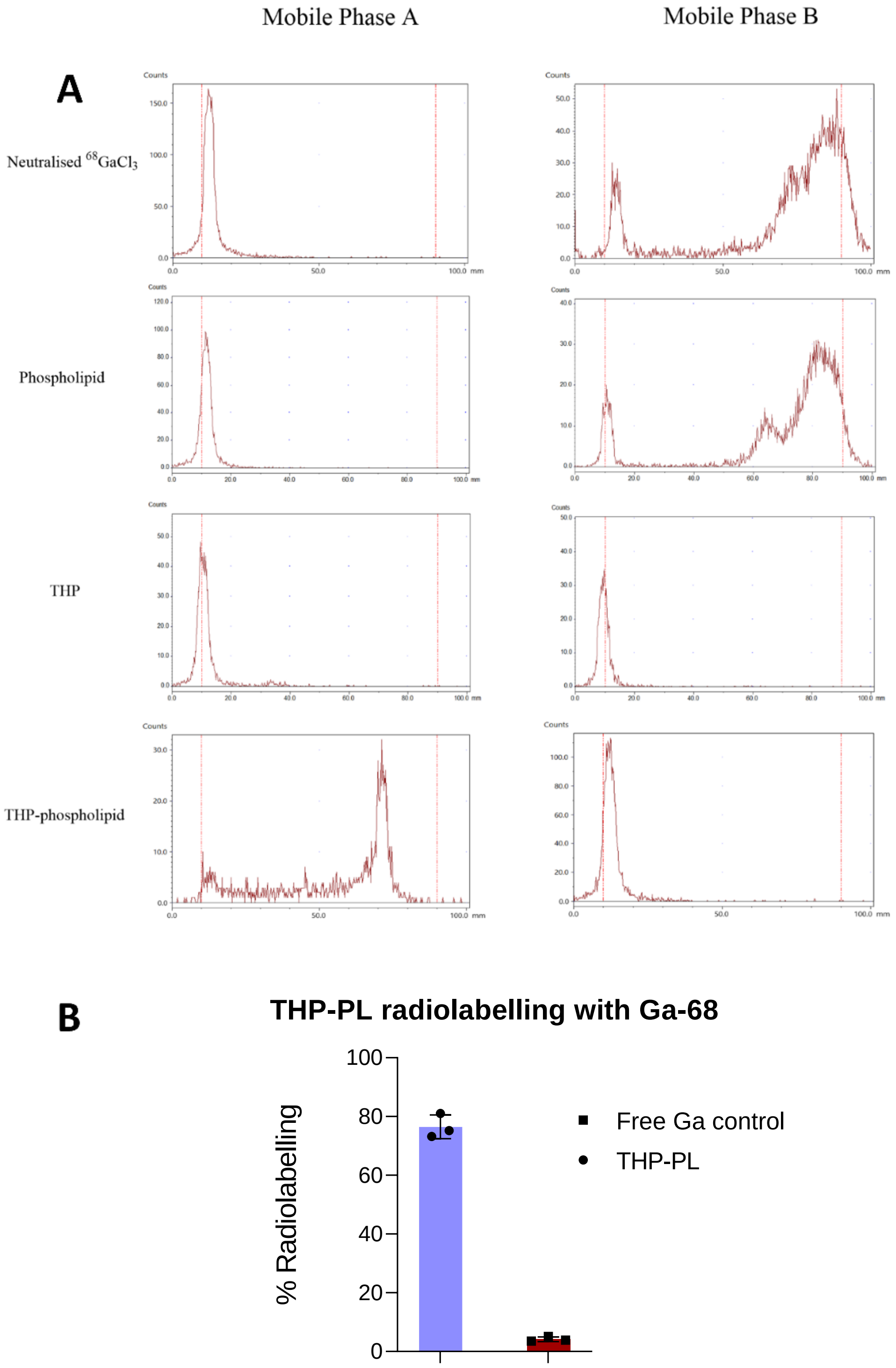

Figure 2.11. Radiolabelling of THP-PL: (A) RadioTLC trace for the radiolabelling of the THP-PL conjugate with ^{68}Ga compared to controls: (left) TLC Mobile phase A system (Chloroform:Methanol:Water in the ratio 75:36:6) and (right) TLC mobile phase B system (Citrate buffer); (B) Quantification of radiolabelling yield of THP-PL was performed using size exclusion chromatography

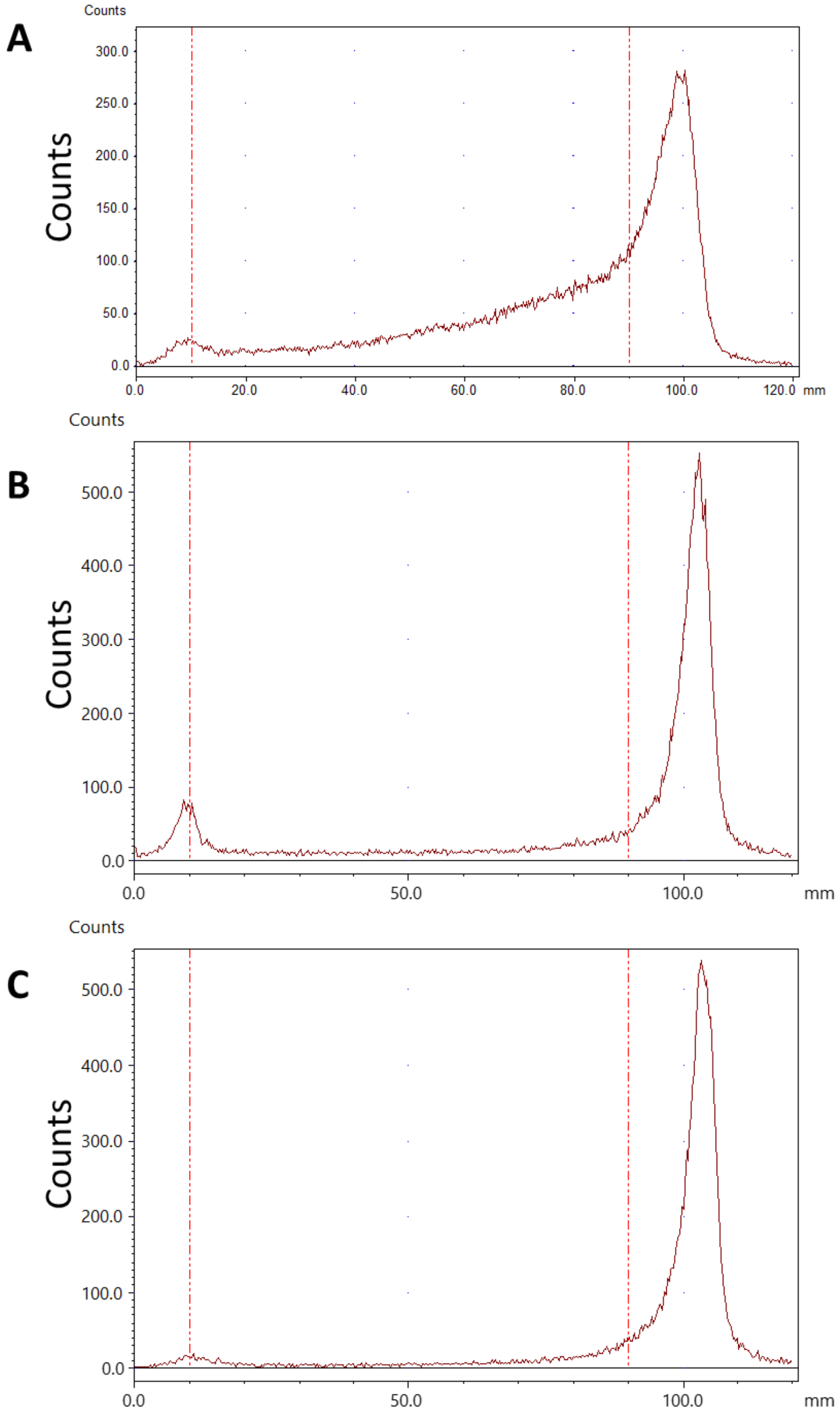

Figure 2.12. Purification of ^{68}Ga: The colloids generated after neutralisation of gallium generator eluate are removed and the different gallium samples pre and post purification are characterised using ITLC (A) Generator eluate; (B) Neutralised ^{68}Ga pre-purification and (C)Neutralised ^{68}Ga post-purification

2.2.3.2 Radiolabelling of THP-PL-liposomes

After confirming that THP-PL can be radiolabelled with gallium at low concentration under mild conditions, the radiolabelling of THP-PL-liposomes was evaluated. To confirm the presence of THP on the liposomal surface, the synthesised THP-PL-liposomes were reacted with ^{68}Ga for 30 min and passed through a size exclusion column to collect the labelled fraction. Unmodified PEG(2k)-liposomes and THP-phospholipid were also reacted with ^{68}Ga and passed through the size exclusion column as controls. After purification, the THP-PL-liposomes showed RLY of 94.6 ± 1.9 % (Figure 2.13), whereas unmodified PEG(2k)-liposomes only showed a RLY of 3.4 ± 1.1 %, demonstrating the success of the insertion reaction. This radiolabelling confirmed that THP-PL has been successfully incorporated into PEG(2k)-liposomes, with no major impact on the original liposomal properties that were verified using other characterisation techniques.

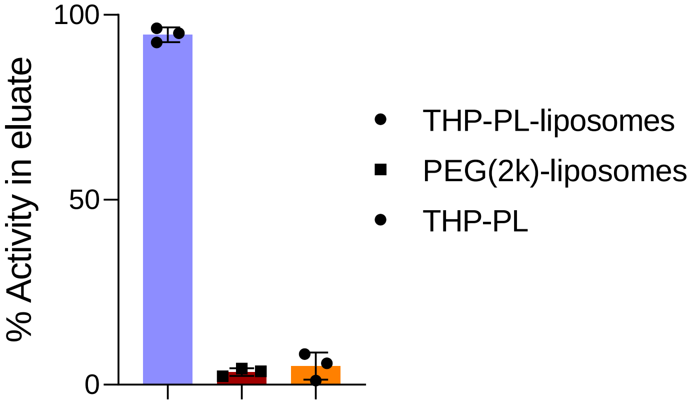

Figure 2.13. Radiolabelling of THP-PL-liposomes: Elution from the size exclusion column confirmed the incorporation of THP chelators on the surface of liposomes. THP-PL and unmodified PEG(2k)-liposomes were labelled as controls showing less than 5% radioactivity eluted in liposome fraction of a size-exclusion chromatography system while the THP-PL-liposomes showed % radiolabelling of 94.6 ± 1.9 %

The *in vivo* half-life of these PEGylated liposomes that we aim to pretarget in this chapter should be 24-48 hours, based on previous studies. To image these liposomes and monitor their pharmacokinetics and biodistribution over time, the liposomes should be radiolabelled with long-lived isotopes as described in section 1.3 of chapter 1. In the context of this chapter, we have also labelled THP-PL-liposomes with ^{67}Ga ($t_{1/2}$ = 78 hours) to understand the pharmacokinetics and the biodistribution of the THP-PL-liposomes. This also allowed us to determine the blood half-life of the THP-PL-liposomes and monitor the effect of the surface modification of the PEGylated liposomes if any. The ^{67}Ga-THP-PL-liposomes were also used as the positive control group of our pretargeting experiments providing information about the pharmacokinetics and biodistribution of the liposomes at time points of interest. The ^{67}Ga-THP-PL-liposomes were prepared using the same protocol as the ^{68}Ga-THP-PL-liposomes.

The radiolabelling of THP-PL-liposomes with ^{67}Ga presented a few challenges. Unlike ^{68}Ga, ^{67}Ga is cyclotron produced and has limited availability commercially in favourable forms. ^{67}Ga utilised for labelling here is procured as ^{67}Ga-citrate from a clinical radiopharmacy. Citrate is a chelator for ^{67}Ga and the transchelation of ^{67}Ga from citrate to THP leads to insufficient and slow THP labelling yields. Moreover, the ^{67}Ga-citrate obtained contains metal impurities including iron which has an excellent affinity for binding to THP. Therefore, the procured ^{67}Ga-citrate was converted into ^{67}Ga-chloride which is used for the radiolabelling of the liposomes. The THP-PL-liposome radiolabelling yields with ^{67}Ga were 42.3 ± 11.8%, which are expectedly lower compared to ^{68}Ga (94.6 ± 1.9%), presumably due to the presence of metallic impurities in the ^{67}Ga source that we described above. The ^{67}Ga-THP-PL-liposomes thus obtained were purified using a PD10 size-exclusion column and concentrated using a centrifugal filter before being used for *in vitro* and *in vivo* validation.

2.2.4 *In vitro* stability of ^{68}Ga-THP-PL-liposomes and ^{67}Ga-THP-PL-liposomes

Some blood serum proteins like transferrin and lactoferrin among others could lead to transchelation of gallium from the THP-PL-liposomes *in vivo*. It has been previously demonstrated that $^{68}Ga/^{67}Ga$-THP complexes are stable *in vivo*, with no signs of demetallation.[263] This was an important factor in the design of our strategy, as any release of free gallium from the liposomes could undermine our *in vivo* radiolabelling approach. To provide further support prior to the *in vivo* imaging studies, we used size-exclusion chromatography to test the radiochemical stability of $^{68}Ga/^{67}Ga$-THP-PL-liposomes *in vitro* in human serum at 37 ^{o}C. Using this system, both liposomes and serum components can be efficiently separated and quantified via UV and radioactivity measurements, allowing the determination of liposome and serum protein-associated radioactivity at different time intervals. ^{68}Ga-THP-PL-liposomes showed high stability in human serum with 90.9 ± 0.6 % of the radioactivity associated with the liposomes over 3 h (Figure 2.14). This high stability was retained for longer periods, as demonstrated by the >94% radiochemical stability found for ^{67}Ga-THP-PL-liposomes after 48h under the same conditions.

2.2.5 *In vitro* pretargeting validation

One of the main challenges of our proposed *in vivo* radiolabelling strategy is that radiometal binding to the liposome must occur in the presence of a myriad of potential competitors present in tissues. It is well established that free Ga^{3+} binds to the Fe^{3+}-transport protein serum transferrin (Tf), present in high concentrations of 2.2–4 mg/mL in blood.[284,312]

The *in vitro* pretargeting methods were designed to confirm that *in vivo* labelling strategy (pretargeting system) can be executed under two key conditions: (i) high dilution of the ^{68}Ga and THP-PL-liposomes to simulate the blood dilution conditions *in vivo* and (ii) potential ^{68}Ga binding with serum proteins as mentioned above. The first attempt at this was using THP-PL-liposomes (100 µL, 60 mM) loaded into a vial containing a semipermeable membrane placed in a diluted ^{68}Ga containing PBS reservoir (50 mL, 20 MBq) and incubated at 37^{0}C. However, no labelling was observed for the THP-

PL-liposomes. This could be due to the semipermeable membrane not allowing for enough time/surface area for direct interaction. Therefore, we moved on to a direct incubation protocol in which we incubated THP-PL-liposomes in a vial containing commercially available human serum with ^{68}Ga. However, as seen in figure 2.15(A), the reaction rates were very slow and even after 45 minutes only 50 % labelling was observed. This can be explained by the presence of citrate in commercially available human serum which may interfere with the chelation of ^{68}Ga to THP on the account of citrate being a good chelator for gallium.

Therefore, to assess the ability of ^{68}Ga to preferentially bind THP-PL-liposomes in the presence of serum components, we chose human serum obtained from fresh blood samples. Two *in vitro* radiolabelling experiments were performed: (*i*) pre-incubation of THP-PL-liposomes with human serum for 1 h at 37 ^{o}C, followed by addition of ^{68}Ga; and (*ii*) pre-incubation of ^{68}Ga with human serum for 1 h at 37 ^{o}C, followed by addition of THP-PL-liposomes. Size exclusion chromatography was used in both cases to isolate and quantify liposome-bound ^{68}Ga radioactivity from that bound to serum components. In (*i*), an experiment that closely resembles our proposed *in vivo* radiolabelling approach was conducted where serum pre-incubated THP-PL-liposomes were successfully radiolabelled with high efficiency of 94 ± 2 % (n=3) in 15 minutes post addition of ^{68}Ga (Figure 2.15(C)). In (*ii*), THP-PL-liposomes were radiolabelled with high efficiency of 87 ± 2 % (n=3) in 30 minutes post addition of THP-PL-liposomes to serum pre-incubated with ^{68}Ga (Figure 2.15(B)). These results further confirmed the high affinity of the THP chelator towards ^{68}Ga within a biologically-relevant environment and supported the *in vivo* evaluation of this approach.

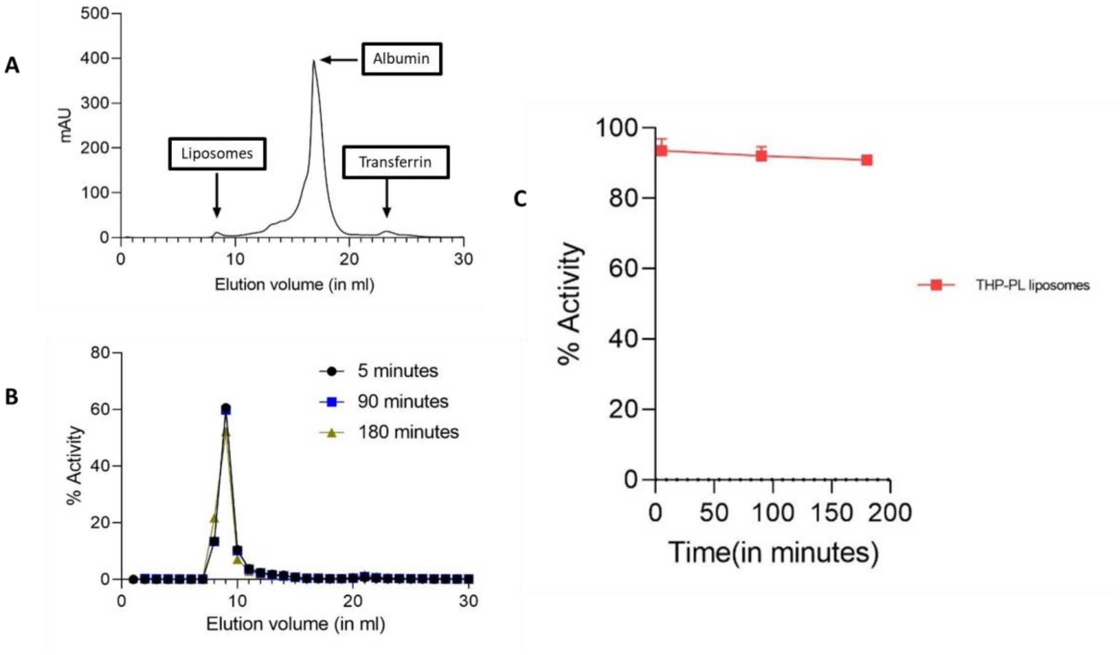

Figure 2.14. Serum stability assessment of ^{68}Ga-THP-PL-liposomes using AKTA system: (A) UV profile shows three UV active species: liposomes, albumin protein from serum and transferrin protein from serum; (B) Radioactivity profile shows all the radioactivity associated with liposomes; (C) Serum stability of THP-PL-liposomes in human serum over 180 minutes: 90.9±0.6% of the ^{68}Ga is attached to the liposomes after 180 minutes showing minimal transchelation to serum proteins

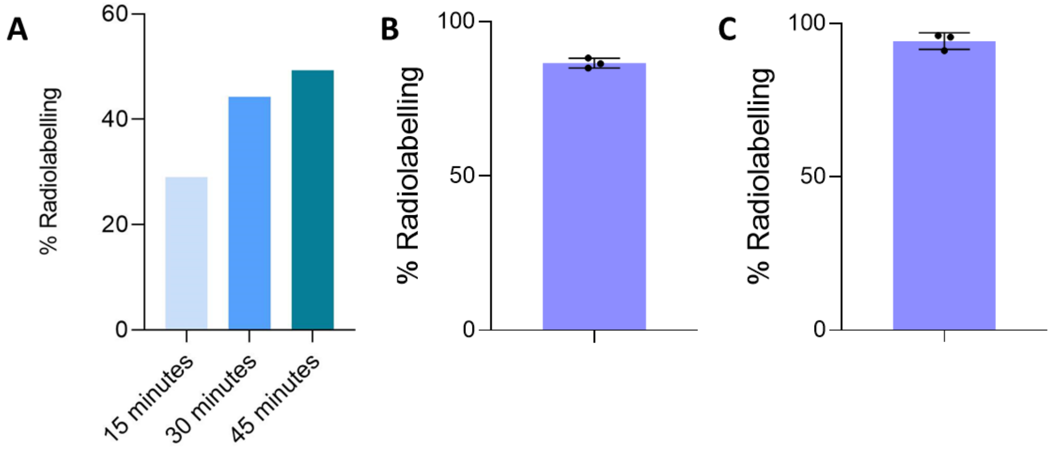

Figure 2.15. *In vitro* pretargeting of THP-PL-liposomes: (A) Pretargeting in commercially obtained human serum (containing citrate) with ^{68}Ga. The radiolabelling yield was determined after 15, 30, and 45 minutes of incubation showing less than 59 % labelling after 45 minutes; (B) Pretargeting of THP-PL-liposomes with ^{68}Ga incubated in citrate free human serum after 30 minutes**;** (C) Pretargeting of THP-PL-liposomes incubated in citrate free human serum with ^{68}Ga after 15 minutes

2.2.6 *In vivo* evaluation of pretargeting of THP-PL-PEG(2k)-liposomes in healthy mice

Following the synthesis and characterization of the components of the system *i.e.,* THP-PL phospholipid and neutralised, colloid-free ^{68}Ga and *in vitro* assessments, the next step was to perform *in vivo* PET imaging and biodistribution experiments. The most important variable in the development of an *in vivo* labelling system was the duration between the introduction of the liposomes and the administration of the radioisotope. The time point was determined from previous liposomal imaging studies[313] and blood kinetic study of prelabelled ^{67}Ga-THP-PL liposomes (Figure 2.17). As evident in SPECT images of labelled liposomes for determining the blood kinetics, the liposome concentration in the blood was reduced to less than a quarter of their value at t = 25 h (8.2 ± 3.7 %ID/g) from the initial time point of administration at t = 0 h (38.9 ± 7.3%). Thus, 24 hours post liposomal injection represented a promising interval between the administration of THP-PL liposomes and the subsequent injection of the radioisotope. The earlier time point of 5 hours post liposome injection for imaging was used to observe *in vivo* radiolabelling when most of the liposomes were circulating in the bloodstream.

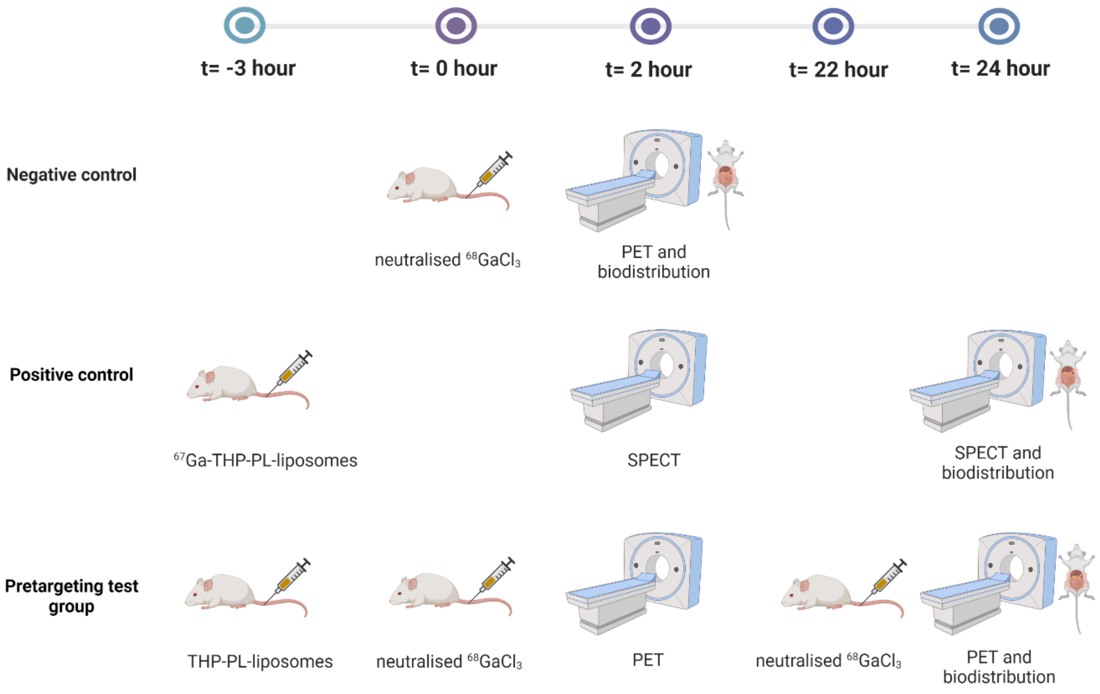

Figure 2.16. Scheme of *in vivo* pretargeting PET experiments: Negative control: Group 1; THP-PL liposome pretargeting group: Group 2; Positive control group: Group 3. Created with BioRender.com.

The positive control group with ^{67}Ga-THP-PL PEG (2k)-liposomes shows the biodistribution of PEG (2k)-liposomes (Figure 2.17). The radioactivity was observed in the liver, spleen and bloodstream including circulatory vasculatures such as the heart, carotid arteries, and aorta at t = 2 h. At t = 24 h p.i., the activity was cleared from the blood and concentrated mainly in the liver and spleen. The one-phase decay fit of the blood kinetics of liposomes as observed in Figure 17 showed initial blood clearance half-life ^{67}Ga-THP-PL-liposomes as $t_{1/2}$ = 7.9 hrs with >11 %ID/g still in circulation 25 hrs p.i. This slow and steady accumulation in the spleen and liver is typical of Doxebo *i.e.,* PEGylated liposomal nanomedicine which inhibits recognition by the reticuloendothelial system (RES) (insert reference). However, the blood clearance of these liposomes was comparatively faster than observed for Doxil®, this could be attributed to minor differences in the structure of these empty PEGylated liposomes used in our study such as absence of the drug, presence of higher DSPE-PEG2000 in the bilayer on account of insertion, and presence of THP chelators on the surface. [314]

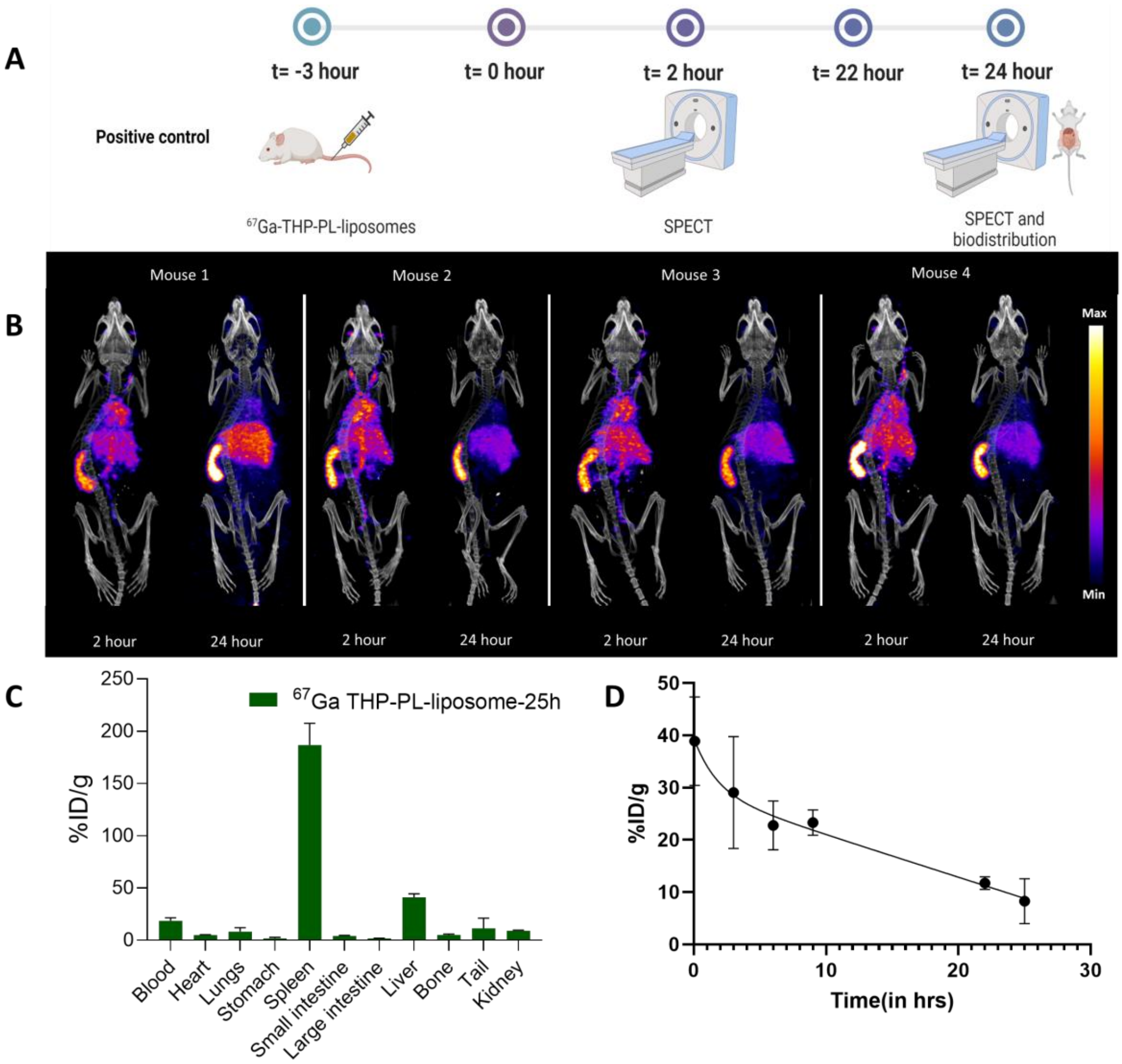

Figure 2.17. Positive control group: (A) Schematics of the positive control group of *in vivo* experiment; (B) *In vivo* SPECT image for positive control group i.e.,^{67}Ga-THP-PL-liposome at t = 2 h and t = 24 h; (C) Biodistribution at t = 25 h (n=4), (D) Blood *kinetic in vivo* study to determine the circulation characteristics of THP-PL-liposomes: ^{67}Ga-THP-PL-liposomes are injected intravenously followed by sampling of blood liposomes concentration at different intervals (n=4).

The negative control group with free ^{68}Ga administered and imaged at t = 2 h with biodistribution performed post imaging and results are as seen in Figure 2.18. Free gallium was cleared from the blood pool via the kidneys leading to high radioactivity in the urinary bladder. Uptake was also observed in bones (especially joints) and gut post t = 2 h. The acetate neutralised ^{68}Ga showed very similar *in vivo* behaviour to ^{68}Ga-citrate on the account of acetate, like citrate, being a weak chelator for ^{68}Ga.[290,291,315] The administered ^{68}Ga transchelates from acetate and binds to transferrin, ferritin and other iron-binding proteins explaining high blood pool values of ~10% ID/g even after 3 h and also being responsible for accumulation observed in the lungs, bones and small intestine.[316] High liver uptake was not observed due to the absence of colloids in administered ^{68}Ga post purification step.

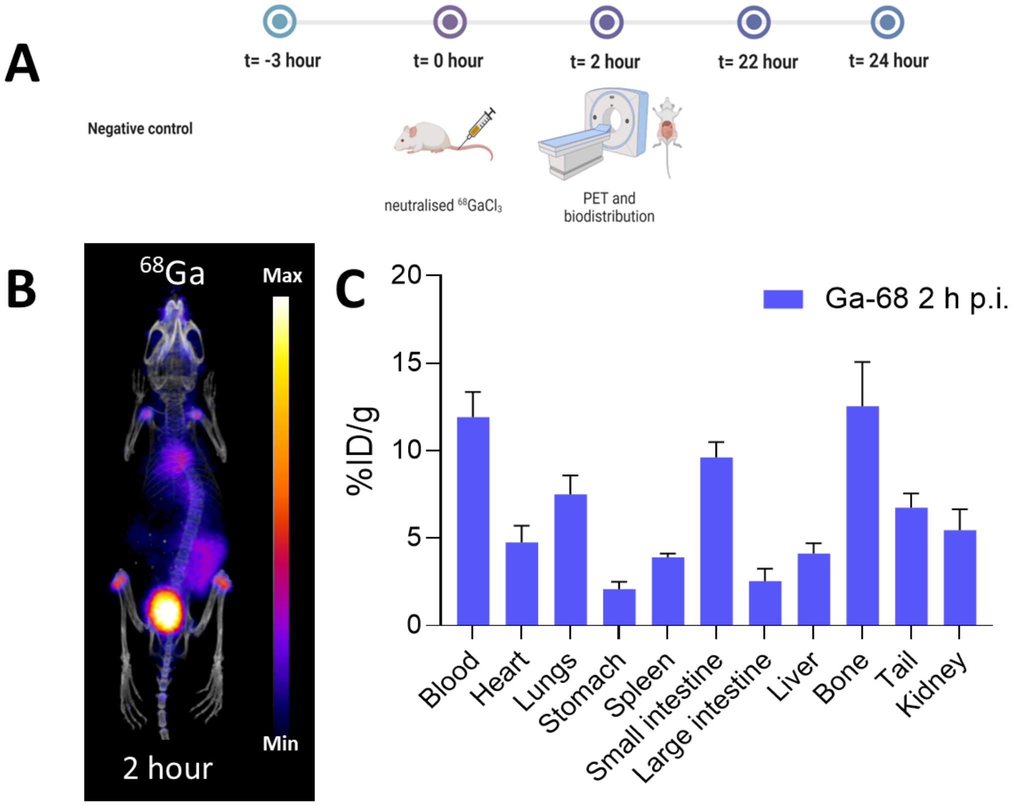

Figure 2.18. Negative control group: (A) Schematics of the negative control group of *in vivo* experiment; (B) *In vivo* PET image for negative control group t = 2 h; (C) Biodistribution at t = 3 h (n=3)

The *in vivo* radiolabelling group was imaged at two-time points; t = 2 h and t = 24 h (Figure 2.19). At t = 2 h, the radioactivity signal was observed in the blood pool (heart, carotid arteries and aorta), However, low uptake was observed in the liver and spleen. This points to labelling of the THP-PL liposomes *in vivo* in the blood pool. At t = 24 h post gallium administration, the radioactivity uptake was observed in the blood pool, bones and urinary bladder showing no *in vivo* labelling, which was also confirmed by the biodistribution data. The comparison of the pretargeting group PET image and its quantification (Figure 2.20, 2.21) at earlier time point with negative control show higher accumulation in the liver, spleen, blood whereas lower accumulation in the bones, and bladder showing effective tracking of liposomes circulating in the blood whereas the free ^{68}Ga has cleared off from the blood and majority of the injected ^{68}Ga has bound to the THP-PL-liposomes. This has been further plotted as heatmaps in figure 2.21 for ease of comparison among uptake values for different organs among different *in vivo* groups. For the later time point of pretargeting, the PET image, biodistribution (Figure 2.19), and image quantification (Figure 2.20) showed similarities with the negative control (Figure 2.18, 2.20). However, higher uptake observed in the blood (14.6±0.4 %ID/g vs 11.9±1.4 %ID/g), heart (7.6±1.5 %ID/g vs 4.7±0.9 %ID/g), and spleen (6.4±0.6 %ID/g vs 3.9±0.2 %ID/g) for pretargeting group compared to negative control can be attributed to *in vivo* labelling of liposomes even at the later time point.

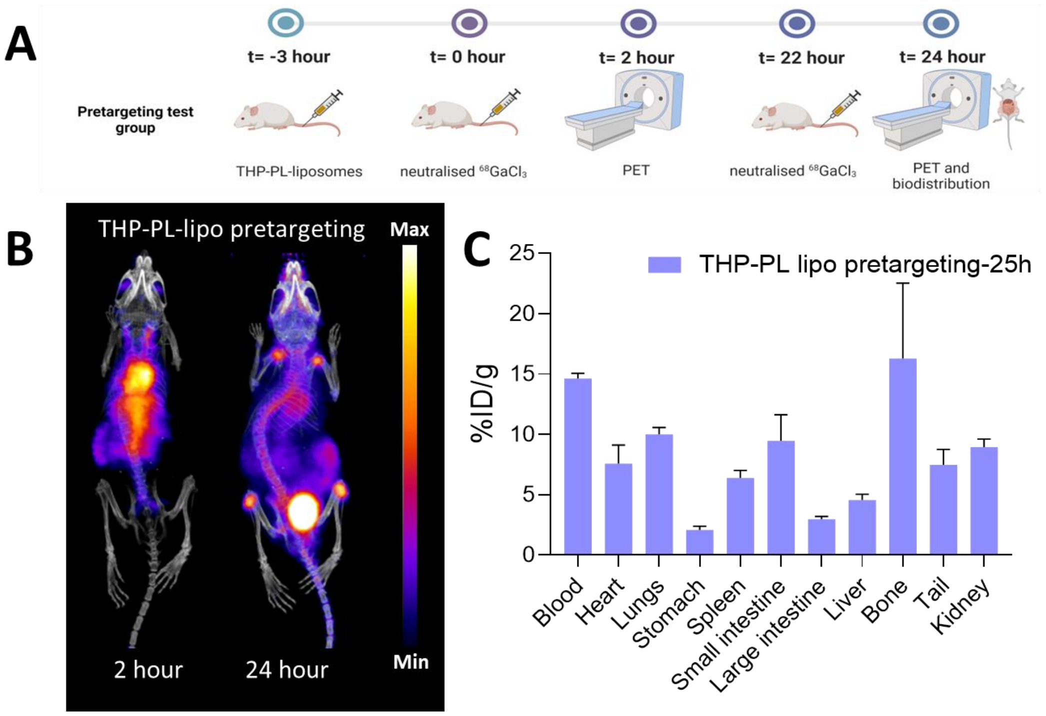

Figure 2.19. Pretargeting group: (A) Schematics of the pretargeting group of *in vivo* experiment; (B) *In vivo* PET pretargeted imaging of THP-PL liposome at t=2 h and t=24 h; (C) Biodistribution at t = 25 h (n=4)

These *in vivo* PET results showed that labelling of THP-PL liposomes with unchelated ^{68}Ga works in the blood pool. At the time point of t= 2 h, the liposomes were mainly in circulation in the blood pool and were labelled by injected ^{68}Ga. At a later time, point (i.e., t = 24 h), however, the images and biodistribution suggest minimal gallium chelation by THP-PL-liposomes and clearance from the blood via the urinary system thereby showing high bladder uptake of 45.7 ± 10.8 %ID/g. In figure 2.21, the comparison of radioactivity uptake for each organ within different groups at different time points was performed and plotted as a heat map. This heat map again confirmed that pretargeting works effectively at earlier time point when the THP-PL-liposomes are circulating in the blood allowing their tracking post *in vivo* radiolabelling showing high concentration of radioactivity in blood, heart and liver compared to both positive and negative control. The heat map for later time point confirmed minimal pretargeting with administered ^{68}Ga in pretargeting group showing a fate similar to negative control.

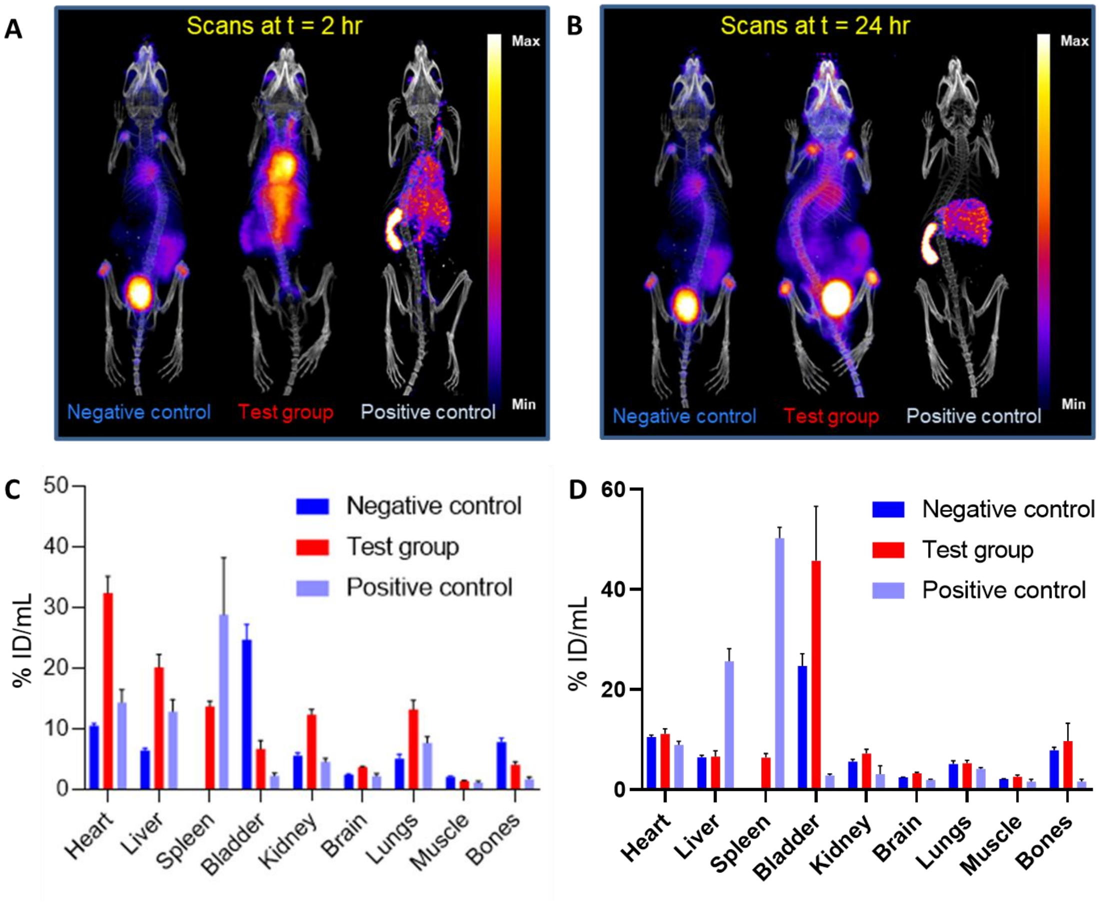

Figure 2.20. Comparison of the images and radioactivity uptake values quantified from images: THP-PL-liposome pretargeting PET/SPECT scans at two different time points of interest (A) at t = 2 h and (B) at t = 24 h; Image quantification performed on the THP-PL-liposome pretargeting PET/SPECT scans by drawing ROIs using vivoquant (n=4) at two different time points of interest (C) at t = 2 h and (D) at t = 24 h.

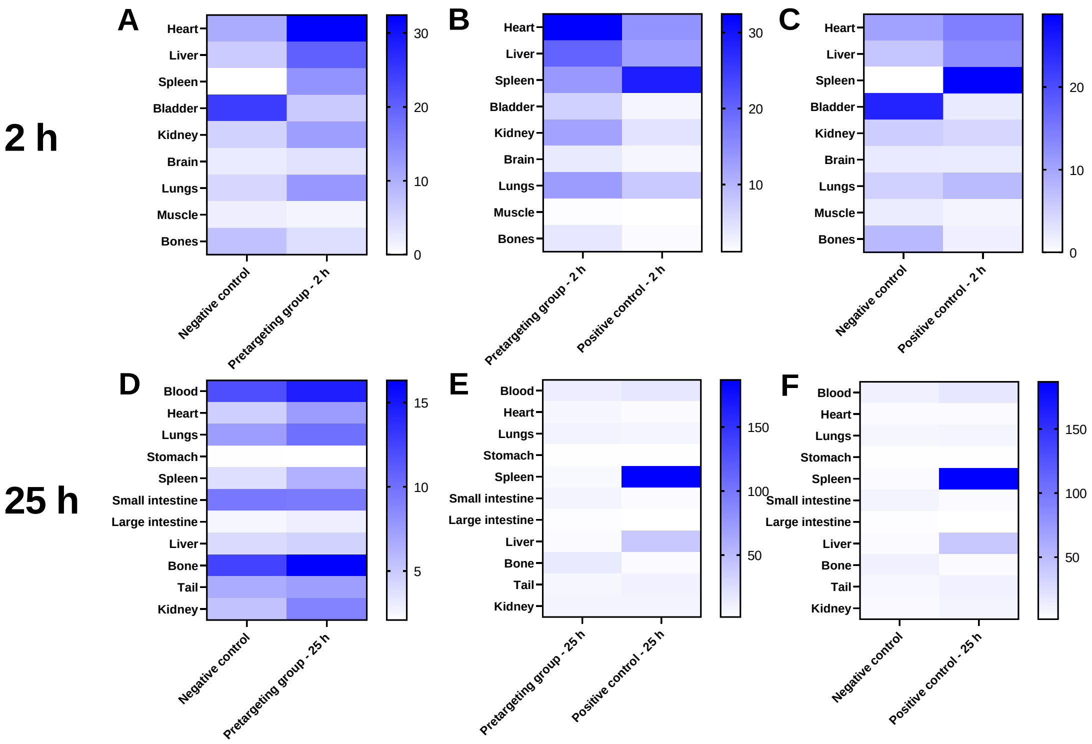

Figure 2.21 Comparison heat map showing radioactivity uptake in different organs among different experimental groups (in % ID/g): (A) Negative control vs Pretargeting – 2 h; (B) Pretargeting – 2 h vs Positive control- 2 h; (C) Negative control vs Positive control- 2 h; (D) Negative control vs Pretargeting group- 25 h; (E) Pretargeting group- 25 h vs Positive control- 25 h; (F) Negative control vs Positive control- 25 h. A, B, and C heat map are created from image analysis data and D, E, and F heat map are created from biodistribution data.

The observation of low *in vivo* labelling at the later time point may be due to two main reasons. Firstly, the saturation of the THP chelator on the liposomal surface by iron, of which there is a large amount in the blood. Secondly, the hydrophilicity of ^{68}Ga (injected as one of the components of the *in vivo* labelling system) can hinder its penetration in tissues and reach organs such as the liver and spleen, which are known to be passive targets for liposomes in healthy subjects as seen in positive control group ^{67}Ga-THP-PL liposomes. Finally, the other possible explanation behind the low pretargeting could be inaccessibility of the THP-PL-liposomes for pretargeting due to engulfing by cells and macrophages.

The *in vivo* labelling between preinjected THP-PL liposomes and free ^{68}Ga was observed successfully at earlier time points when the liposomes are circulating in the blood, leading to imaging of the blood pool as well as uptake of liposomes in the organs at the earlier time point of five hours post administration of liposomes. This could present us with a promising method of blood pool imaging and *in vivo* radiolabelling applications. However, at the later time point of interest *i.e.,* 24-48 hours, when the liposomes are expected to be localised in tissues of interest such as liver, spleen and tumours (in tumoured animals), no or low *in vivo* radiolabelling of liposomes was observed. The way to overcome this hurdle can be the injection of weakly chelated gallium as the second vector of the pretargeted system (instead of free ^{68}Ga) which will allow the ^{68}Ga to reach the target organs such as the liver and spleen. Also, a better understanding of the internalisation of THP-PL liposomes at the target tissue might shed light on the unavailability of THP chelators on the liposomal surface at the target tissue. To further explore the potential of this pretargeting system, we used this system to pretarget a small molecule bone tracer (THP-Pam) which is discussed in the next section.

2.2.7 *In vivo* evaluation of pretargeting of THP-Pam in healthy mice

To further examine the *in vivo* labelling capabilities of a metal chelation-based pretargeting system, we set out to explore it using a THP-based radiotracer with a well-established biodistribution. THP-Pamidronate (THP-Pam) was chosen as it has proven bone targeting capabilities and reported data was available from Dr. George Keeling. An in-depth analysis of this study can be found in a recent peer-reviewed paper.[265] Moreover, a recent study performed by Zeglis and coworkers has attempted to pretarget bisphosphonate-based bone tracer with biorthogonal pretargeting and this study will act as a direct comparison against for metal pretargeting concept.[317]

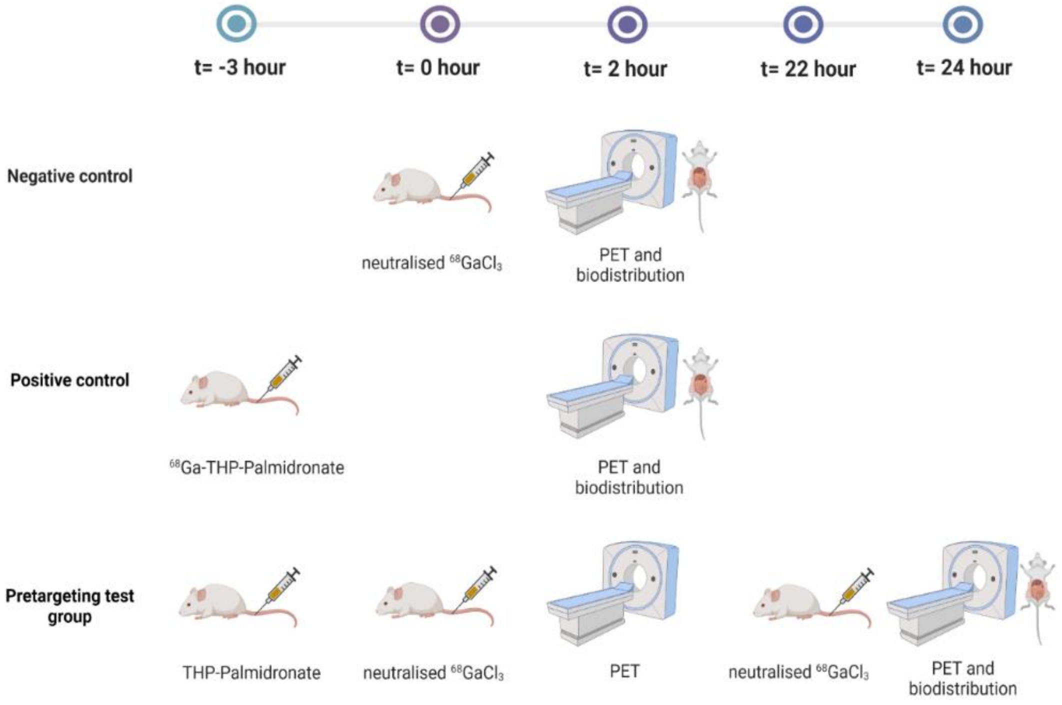

Figure 2.22. Scheme of *in vivo* pretargeting PET experiments: Negative control: Group 1; THP-Pam pretargeting group: Group 2; Positive control group: Group 3. Created with BioRender.com.

As discussed in the previous section, one of the potential explanations for no/negligible observation of pretargeting of liposomes at the second time point of t = 24 h could be attributed to internalisation of the liposomes in the soft tissue such as liver and spleen which is not accessible to ^{68}Ga injected later. Therefore, THP-Pam tracer was selected due to its proven biological target (hydroxyapatite in bones) resulting in high accumulation in the joints, thereby potentially making THP available for *in vivo* ^{68}Ga chelation (Scheme figure 2.22). THP-Pam is not expected to be internalised in the soft tissue of organs such as the liver and spleen and should be available for *in vivo* labelling.

The *in vivo* labelling of THP-Pamidronate was attempted at two-time points t = 2 h and t = 24 h (Figure 2.24). The uptake observed was identical at both time points showing high uptake in the urinary bladder, bones specifically joint, and spinal column. The tibia and femur both showed high uptake values: 10.0 ± 1.3 and 14.0 ± 1.3 %ID/g respectively. Due to the fast clearance of the THP-Pam from the body, low uptake was observed in the liver, large intestine, spleen and kidney and any uptake in these organs might be due to free ^{68}Ga. No uptake was observed in the brain.

The positive control group for bone targeting THP-Pam was pre-injection radiolabelled ^{68}Ga-THP-Pamidronate which was imaged at 1 h p.i. and biodistribution performed at 2 h p.i (Figure 2.23). The bone uptake was greater than 20 % ID/g as expected due to its bone targeting properties and negligible uptake in the rest of the organs due to fast renal clearance.

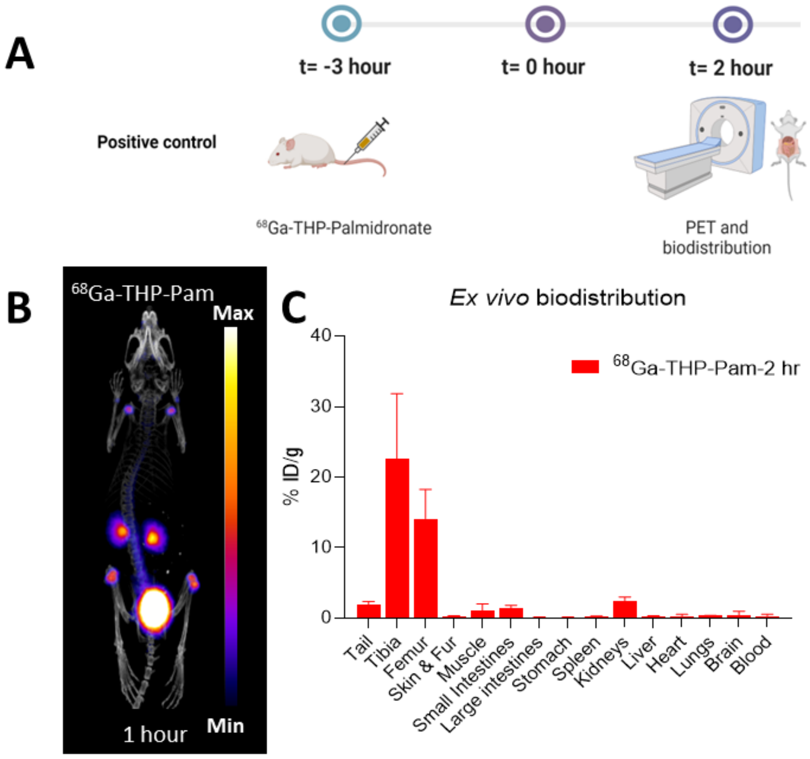

Figure 2.23. Positive control group: (A) Schematic of the positive control *in vivo* experiment of THP-Pam pretargeting; (B) *In vivo* PET imaging of ^{68}Ga-THP-Pam at 1 h p.i.; and (C) Biodistribution performed at 2 h p.i.

The imaging and biodistribution data do show high bone uptake similar to the positive control of ^{68}Ga-THP-Pam. The uptake in the bones is higher than free gallium negative control but less than ^{68}Ga-THP-Pam, thereby showing moderate pretargeting.

Further analysis and comparison of the biodistribution and quantification of PET images recorded for different experimental groups confirmed these observations of moderate pretargeting and the results are in agreement with observations previously made for pretargeting of bisphosphonates.[317] The directly labelled conventionally targeted THP-Pam showed high accumulation in the bones (22.5 ± 9 % ID/g) and fast clearance from the blood. Similar to this, in the pretargeted THP-Pam group, high uptake was observed in the bones (14 ± 2 % ID/g) and very fast clearance of free neutralised ^{68}Ga was observed with majority of clearance observed via urine. This observation confirmed that the injected THP-Pam could still be traced 24 h after administration by *in vivo* labelling. The observed bone uptake trend observed in all analysis methods was Positive control > Pretargeting- 2 h > Pretargeting – 24 h > Negative control as expected. However, the bone uptake observed for free ^{68}Ga makes the analysis aspect of this study challenging.

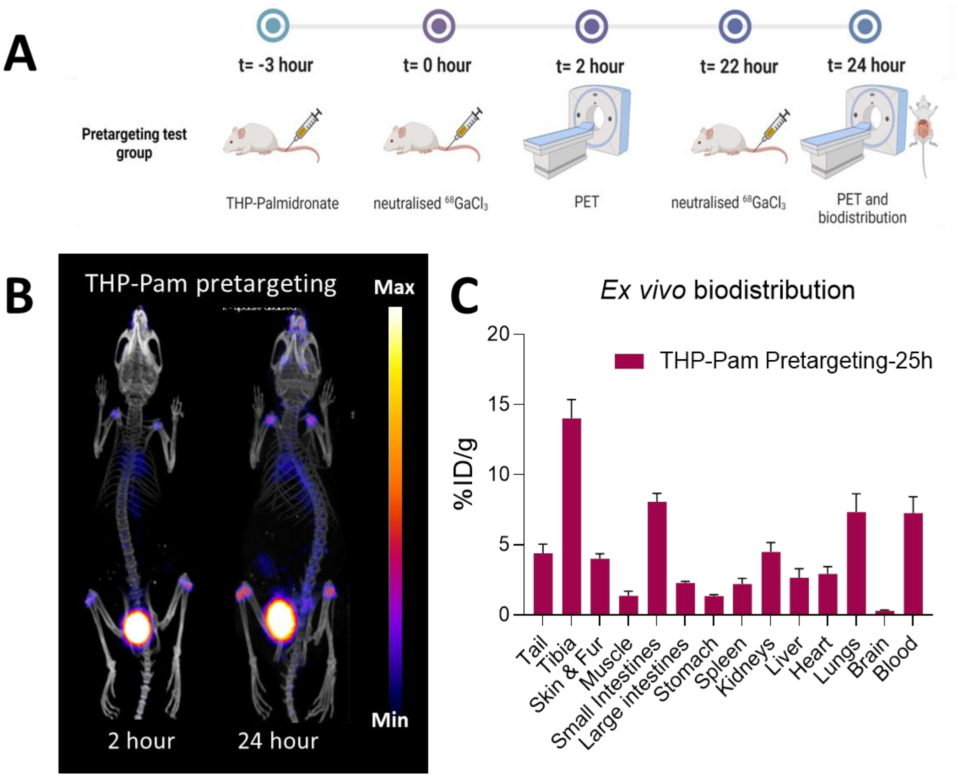

Figure 2.24. Pretargeting group: (A) Schematics of the pretargeting group of *in vivo* experiment; (B) *In vivo* PET pretargeted imaging of THP-Pam at t=2 h and t=24 h; (C) Biodistribution at t = 25 h (n=4).

The THP-Pam pretargeting experiments showed the ability of this pretargeting system to react with THP-Pam post clearance and accumulation in the bone tissue. This proves the affinity of THP towards ^{68}Ga is strong enough to show chelation *in vivo* not just in the blood but also in the bone tissue. The bone uptake in the pretargeted system was 15% ID/g and higher compared to free ^{68}Ga control but less compared to ^{68}Ga-THP-Pam. However, due to the fast blood clearance of the THP-Pam, the pretargeting mechanism is irrelevant but is used in our study as a method to validate this metal chelation pretargeting system in a system other than the long-circulating liposomes.

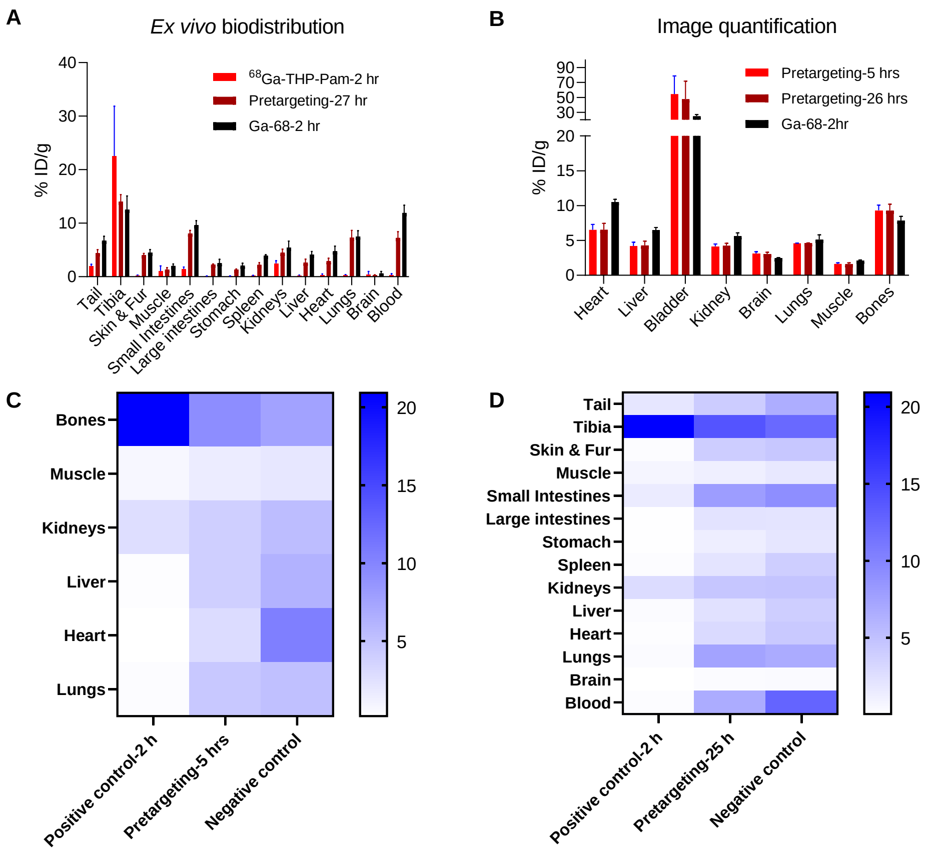

Figure 2.25. Biodistribution and image quantification performed on the THP-Pam pretargeting PET/SPECT scans by drawing ROIs using vivoquant (n=4) at two different time points of interest: (A) Ex vivo biodistribution comparison of Positive control i.e. directly labelled THP-palmidronate (^{68}Ga-THP-Pam) vs Pretargeting at t = 24 h (27 h post THP-Pam injection) vs Negative control (neutralised ^{68}Ga); (B) Image quantification comparison of Pretargeting at two time points and negative control: Pretargeting at t = 2 h vs pretargeting at t = 24 h vs Negative control; (C) Heat map comparison between three experimental groups at t= 24 h time point; and (D) Heat map comparison between three experimental groups at t = 2 h time point.

2.3 Conclusion

This study presents a novel method for radiolabelling and tracking liposomes *in vivo* using ^{67}Ga/^{68}Ga. Exploiting the proven gallium/iron-chelating properties of THP, we have developed a method for *in vivo* and *in vitro* radiolabelling of preformed PEGylated liposomes which can be further used for radiolabelling of different formulations of liposomes with ^{68}Ga/^{67}Ga with minimal impact on properties. The modification does not interfere with the properties of the PEGylated liposomes which are used in this study showing no modification in physical, chemical and *in vivo* properties. Our *in vivo* results indicate that radiolabelling using this system is only effective while the THP-modified liposomes are in the bloodstream, and less effective when the liposomes have accumulated in other tissues. Hence, our aim of achieving pretargeted labelling of PEGylated liposomes *in vivo* using this approach was successfully accomplished only at the earlier time point of 5 hours post liposomes administration, when most liposomes are still circulating in blood, and not at 24 hours post liposomal administration. When using a short-circulating small molecule such as the bone targeting THP-Pamidronate, moderate pretargeting was observed. This demonstrates that pretargting using this system is still feasible in non-blood tissues. Further optimisation of the different components may allow for improved outcomes from this strategy but based on these results it appears that THP-gallium *in vivo* radiolabelling is limited to blood-circulating molecules.

3 BIORTHOGONAL CHEMISTRY BASED PRETARGETING OF LIPOSOMAL NANOMEDICINES

3.1 Introduction: Biorthogonal chemistry for pretargeting of nanomedicines

The concept of biorthogonal chemistry as described in the first chapter has been widely explored for the pretargeting of antibodies with successful outcomes and finding applications in imaging and therapeutics. This concept has also been recently applied for the first time to the nanomedicine field and could find excellent applications specifically for pretargeted imaging of liposomal nanomedicines and further develop their application to the development of theranostic nanomedicines by combined use of radiotherapy nuclides and PET diagnostic radionuclides. In the context of this thesis, due to extensive validation of the inverse electron demand Diels-Alder (IEDDA) reaction for use in pretargeted imaging of antibodies,[235,318–320] this system can be used to supplement the research performed in Chapter 2 of this thesis. The TCO (electron-poor diene)-tetrazine (electron-rich dienophile) system can be used to create a pretargeted imaging system for PEGylated liposomes and acts as a comparison against the metal chelation-based pretargeting system described in Chapter 2. Before we discuss these results, we will briefly introduce this biorthogonal chemistry and its application to nanomedicine pretargeting.

3.1.1 Biorthogonal Chemistry: inverse electron demand Diels Alder reaction and strain-promoted azide-alkyne reaction

Bioorthogonal reactions have been defined as: “chemical reactions that neither interact nor interfere with a biological system.”[321] The importance of the field of biorthogonal chemistry was recognised recently when the Nobel Prize in Chemistry 2022 was awarded jointly to Carolyn R. Bertozzi, Morten Meldal and K. Barry Sharpless for the development of bioorthogonal chemistry. The key requirements for a reaction to be classified as biorthogonal include the following: *(i)* fast kinetics and high specificity, *(ii)* the reaction should occur in physiological and biocompatible conditions, and *(iii)* the components of a biorthogonal reaction should be inert or have limited reactivity towards other biological macromolecules such as those present in blood. The foundation of biorthogonal reactions was based on the Staudinger reduction of azides with triphenylphosphine and water which paved way for the Staudinger ligation and its modification which involves an azide and a phosphine reacting to form an amide bond.[247,322,323] The Staudinger ligations are limited by slow rate constants and low stability in biological conditions.[324] However, this paved the way for the two most used click chemistry based biorthogonal reactions (Figure 3.1): strain-promoted azide-alkyne cycloaddition (SPAAC) and inverse electron demand Diels Alder reaction (IEDDA), which have been utilised widely for cell labelling, *in vivo* pretargeting of antibodies as well as nanoparticles.

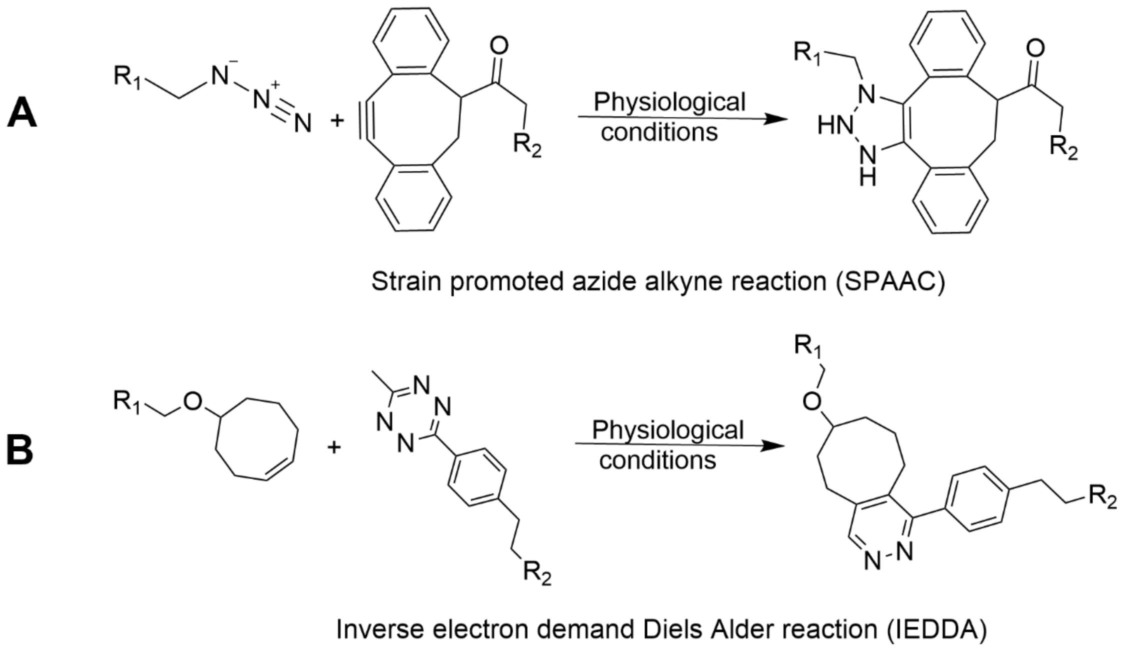

Figure 3.1. The components of an two main biorthogonal reactions used for pretargeting: (A) Azide attached to a targeting molecule R_1 reacts with DBCO (dibenzocyclooctyne) attached to an imaging molecule R_2 in physiological conditions to provide a conjugate (B) Transcyclooctene attached to a targeting molecule R_1 reacts with tetrazine attached to an imaging molecule R_2 in physiological conditions to provide a conjugate.

3.1.2 SPAAC and its application in nanoparticle pretargeting

Sharpless and colleagues defined click chemistry in 2001 as a high yield, stereospecific reaction which is non-sensitive to oxygen and water and generates minimal or no side-products that can be removed by simple purification (non-chromatographic). Moreover, as a biorthogonal reaction, this reaction should occur under physiological conditions.[325] In the following year, Sharpless and Meldal reported first such reaction which is called the Cu-catalysed azide-alkyne [3 + 2] cycloaddition (CuAAC).[326] However, Cu(I) used in CuAAC prohibits the use of this reaction for *in vivo* chemistry as Cu-ions can be poisonous due to chelation with biomolecules.[327] This hurdle was overcome by activation of alkyne by addition of electron withdrawing groups (EWG). Bertozzi and co-workers increased the reactivity of alkynes by introducing the ring strain in the form of cyclooctyne to provide the biorthogonal reaction SPAAC. (Figure 3.1(A))[328] This reaction was then successfully applied to living cells followed by *in vivo* experiments in organisms.[248,250,329]

3.1.3 Preclinical pretargeted imaging of nanoparticles using SPAAC

The SPAAC biorthogonal reaction has been utilised initially in two cases for pretargeting of mesoporous silica nanoparticles and antibodies in the same year (2013).[330,331] The PEG-modified mesoporous silica nanoparticles (NPs, size: 100-150 nm) are reported to have shown EPR mediated passive targeting of tumours. These NPs modified on the surface with a cyclooctene derivative (dibenzo- azacyclooctyne (DIBAC)) were injected in mice *in vivo* followed by administration of ^{18}F-azide derivative as a secondary imaging agent (Figure 3.2(A)). The time interval between administration of DIBAC-NPs and ^{18}F-azide, respectively, was set to 24 h.[330] Two different concentrations of DIBAC-NPs (12 nmol and 30 nmol of DIBAC) were pretargeted *in vivo* with ^{18}F-labeled azide showing increasing tumour accumulation with increasing NP concentration while the biodistribution of ^{18}F-labeled azide showed negligible tumour uptake in non-pretargeted animals (Figure 3.2(B,C)).[332] In contrast, the study by Bosch and coworkers for pretargeting of antibodies showed negligible *in vivo* labelling of antibodies in blood. In short, the antibody rituximab (primary targeting vector) was functionalised with azides and pretargeted with radiolabelled cyclooctynes (secondary imaging agent). The low loading ability of biorthogonal reactive tags on antibody compared to NPs, limited reaction kinetics, and serum proteins interaction of cyclooctynes has been attributed the reason behind these contrasting results.[331,333]

Due to the above considerations, the SPAAC reaction has been further used in only a limited number of preclinical pretargeting studies with varying levels of success. The common key approach of these studies was a high concentration loading of biorthogonal reactive tags on targeting components to improve the reaction kinetics and overcome the issue of blood proteins interaction. Recently, the SPAAC reaction was successfully used for pretargeting of antibodies with the therapeutic radionuclide ^{90}Y. A tumour-targeting antibody CD20 was functionalised with DIBO (dibenzocyclooctyne) and injected into mice followed by administration of ^{90}Y labelled azide-functionalised dendrimer 24 hours after the antibody administration. The incorporation of multiple azides on the dendrimer allowed for a successful pretargeted approach to a nanoradioimmunotherapy.[334] In 2020, SPAAC has also been utilised for pretargeted imaging of azide functionalised biomimetic nanoparticles (RBC camouflaged upconversion nanoparticle) using ^{18}F derivatised DBCO as the secondary imaging agent.[335] However, the SPAAC reaction has slower reaction kinetics compared to IEDDA which poses challenges for their use in pretargeted imaging.

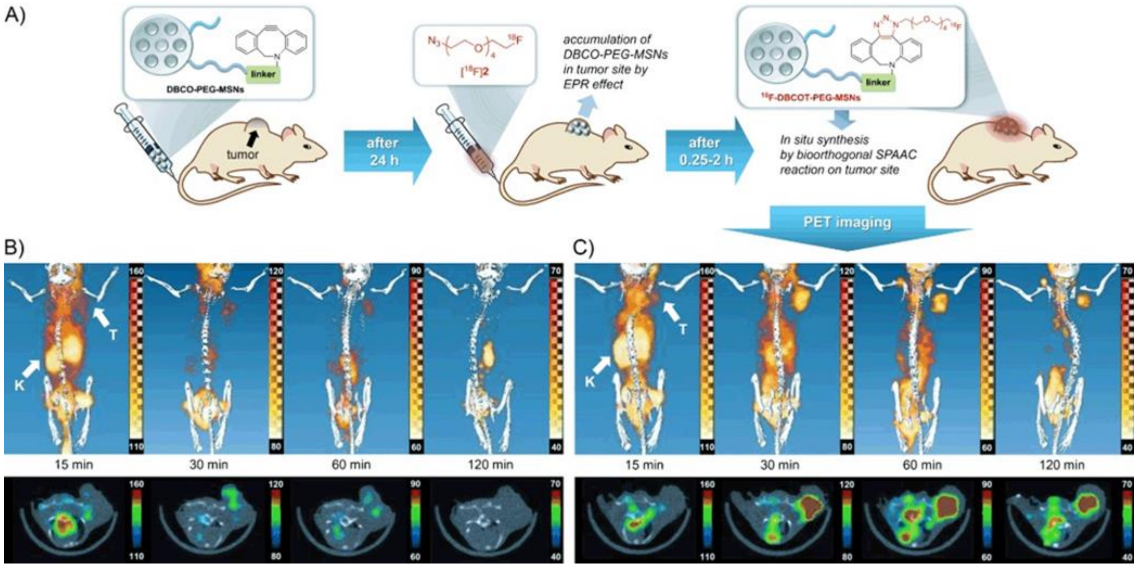

Figure 3.2 Pretargeting PET imaging study by Biorthogonal covalent ^{18}F-labelling: (A) The procedure of the biorthogonal SPAAC reaction for the DBCO-PEG-MSN-pretargeting PET-imaging study; (B) Negative control: PET-CT images of non-pretargeted ^{18}F-labeled azide in a U87 MG tumour-bearing mouse; (C) Pretargeting group: Mouse given DBCO-PEG-MSNs 24 h earlier in a U87 MG tumour-bearing mouse recorded at 15, 30, 60, and 120 min after injection of before ^{18}F-labeled azide. T=tumour, K=kidneys.[332]

3.1.4 IEDDA and its application in pretargeted nuclear imaging

The first evidence of the fast kinetics and biorthogonality of IEDDA reaction was reported by Blackman and colleagues in 2008.[336] The system was validated *in vitro* in serum by fluorescent labelling of A549 cancer cells using TCO/tetrazine pair of transcyclooctene modified antibody (TCO-modified anti-EGFR cetuximab) and fluorescent tetrazine probe.[337] The IEDDA based PET pretargeting was successfully validated *in vivo* in a preclinical setting for pretargeting of antibodies.[338] In this study, mice bearing colon-cancer xenografts were injected intravenously with TCO-modified mAb CC49 followed by administration of ^{111}In-labelled-DOTA-tetrazine (^{111}In-tetrazine) 24 hours later, and by SPECT imaging three hours post injection. A tumour uptake of 4.2 %ID/g in the pretargeting group compared to 0.3 % ID/g in unmodified mAb group was observed. Following this, various studies as mentioned in the introduction chapter have been performed for pretargeted radioimmunotherapy in preclinical setting with major success. Zeglis and colleagues have performed various studies in mice for pretargeting of humanised antibodies A33, trastuzumab and cetuximab with ^{64}Cu, ^{18}F and more recently, ^{177}Lu for radiotherapy with excellent results showing high tumour uptake values comparable to conventional imaging methods with additional benefits of pretargeted imaging such as low radiation dose.[235,318–320,339,340]

The tetrazine ligation shows superior reaction kinetics, where impressive rate constants of up to 10^{6-7} M^{-1} s^{-1} have been reported.[341,342] In addition, the high specificity, the small molecule character, and the orthogonality towards biological moieties make this ligation highly interesting for pretargeting approaches *in vivo*.

The diene/dienophile pair in IEDDA with complementary electronic character with the diene Tz being electron poor, and the dienophile TCO being electron rich have high reactivity towards each other (Figure 3.1(B)). The rate of the ligation reaction is affected by the energy gap between the HOMO of the dienophile and the LUMO of the diene. The rate of the reaction increases with the decrease in this energy gap. The addition of electron withdrawing groups (EWGs) to the tetrazine moiety decreases the energy level leading to faster reaction rates. However, this also leads to a decreased stability *in vivo*.[343–347] The addition of electron donating groups (EDGs) in the dienophile raises its HOMO to improve the reaction rate.[348] Moreover, the ring strain in dienophile ring strain further improves the reaction and thereby the trans-cyclooctenes (TCO) have been the most favourable and widely used dienophile for the IEDDA reaction.[336,342,349]

3.1.5 Preclinical pretargeted imaging of nanoparticles using IEDDA

After several successful preclinical application of IEDDA in pretargeted imaging and therapy, this system has also recently found applications in nanoparticle systems with varying levels of success and, to the best of our knowledge, pretargeted imaging has not yet been applied with liposomes. However, it has been used for active targeting of ^{18}F-liposomes towards sites of antibody accumulation using TCO-tetrazine pair.[197] Other nanoparticles/nanomedicines have been subjects of pretargeted imaging studies with varying levels of success at various investigation points. A ^{11}C-tetrazine has been used to perform pretargeted imaging of TCO-modified mesoporous silica nanoparticles in healthy mice.[350] In this study, the fast lung accumulating TCO-modified mesoporous silica nanoparticles were introduced in mice followed by introduction of ^{11}C-tetrazine 5 minutes post nanoparticle administration allowing visualisation of accumulated TCO-modified silica nanoparticles by pretargeted PET imaging. However, this study does not study pretargeting imaging at desired longer time points but the ^{11}C-tetrazine developed is a the low-molecular-weight and water-soluble tetrazine has highly desirable pharmacokinetic properties such as homogeneous biodistribution, rapid renal excretion and stability.[350] Another study to track TCO-modified mesoporous silica nanoparticle using pretargeted imaging was attempted using ^{18}F-tetrazine. In this study, the *in vivo* biorthogonal reaction was fast, resulting in high radioactivity accumulation in desired organs when the time interval between administration of NPs and radioactive tracer was 15 minutes but when the time difference was 24 hours, no pretargeting was observed.[351] A multimodality pretargeted imaging study showed promise for potential of pretargeting TCO-tetrazine system for tracking of trans-cyclooctene (TCO) modified P-FFGd-TCO (small molecule fluorescent monomer) which can be activated in the presence of alkaline phosphatase and undergo self-assembly into nanoaggregates (FMNPs-TCO) retained on the cell membrane. This nanoaggregate with the presence of an enriched TCO on the surface of nanoaggregate allows imaging of these nanoaggregates by ^{68}Ga-labelled-tetrazine administered 4 hours after the administration of TCO-modified compound. However, it is important to note that pretargeting significantly decreases if the time between administration of TCO and tetrazine compounds is increased to 8 hours[352].

Another ^{11}C-tetrazine ([^{11}C]AE-1) has been developed and evaluated for pretargeting of polyglutamic acid and bisphosphonate system in both mice and pigs. This pretargeted imaging system was unsuccessful for both these targeting agents.[353] Two pretargeted imaging studies have also been performed with long lived radioisotope labelled tetrazines to monitor the long-term interaction of radiolabelled tetrazine with TCO modified nanoparticles. A biorthogonal reactive nanoparticle TCO⊂SNPs were synthesised and administered in U89 glioblastoma bearing mice followed by *in vivo* tracking of these NPs with ^{64}Cu labelled tetrazine as seen in figure 3.3.[354] The other long-lived radioisotope study performed pretargeted imaging of TCO-functionalised PeptoBrushes using ^{111}In-tetrazine with high success (Figure 3.4). The polypeptide-graft-polypeptide polymers based PeptoBrushes were functionalised with trans-cyclooctene (TCO) with a high up to 30% loading efficiency leading to increased reaction rates in the bioorthogonal ligation. An ^{111}In labelled tetrazine was chosen from a library of tetrazine systems and evaluated for pretargeted imaging in tumour-bearing mice. Pretargeted showed tumour accumulation at 2 h p.i. of ^{111}In-tetrazine with maximum tumour to muscle ratio being observed at 22 h p.i. This in-depth analysis of the different parameters and excellent tumour to muscle ratio in this study provide momentum for further investigation into field of pretargeted theranostic with other types of nanoparticles.[355]

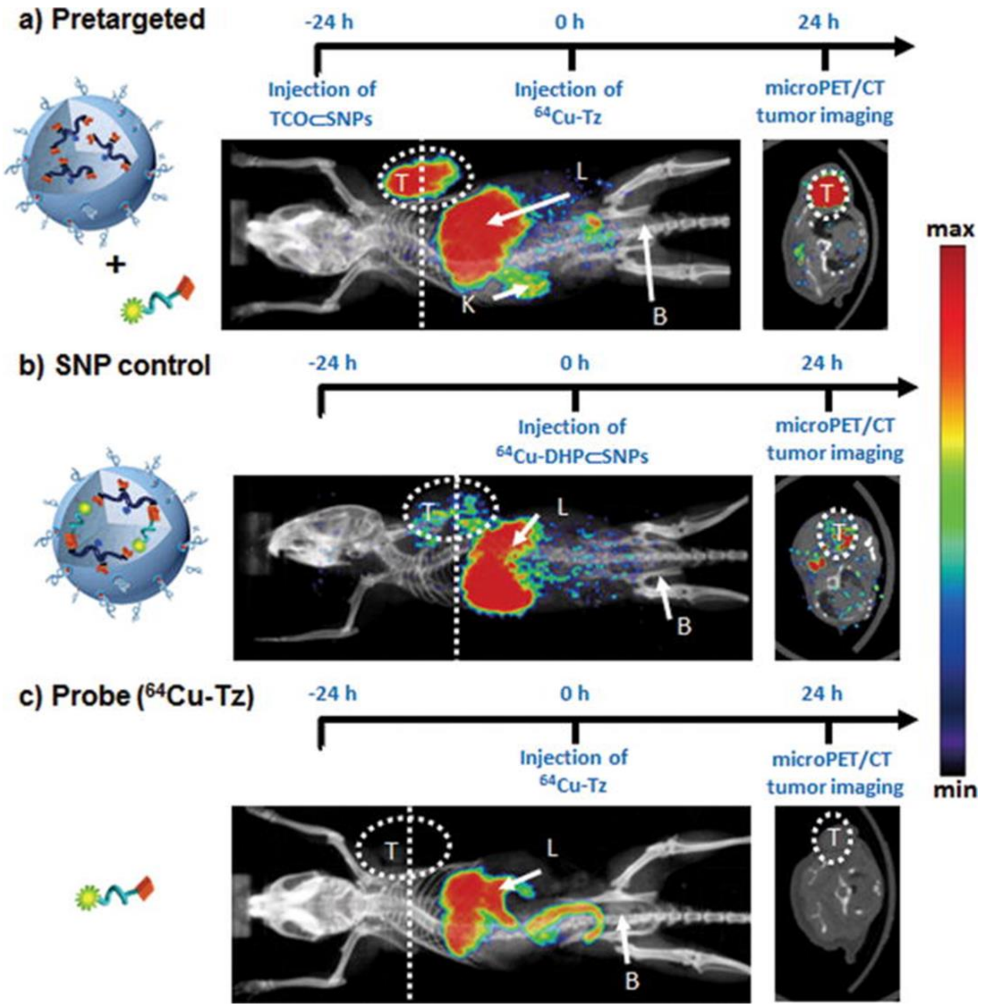

Figure 3.3 Timeline of the injection protocol employed for (a) pretargeted, (b) SNP positive control group (^{64}Cu-DHP⊂SNPs), and (c) negative control group Cu-Tz. Preclinical *in vivo*-PET/CT images of the mice for each group at 24 h p.i. Labels T, L, K, and B refer to the tumour, liver, kidney, and bladder, respectively. Image reproduced.[354]

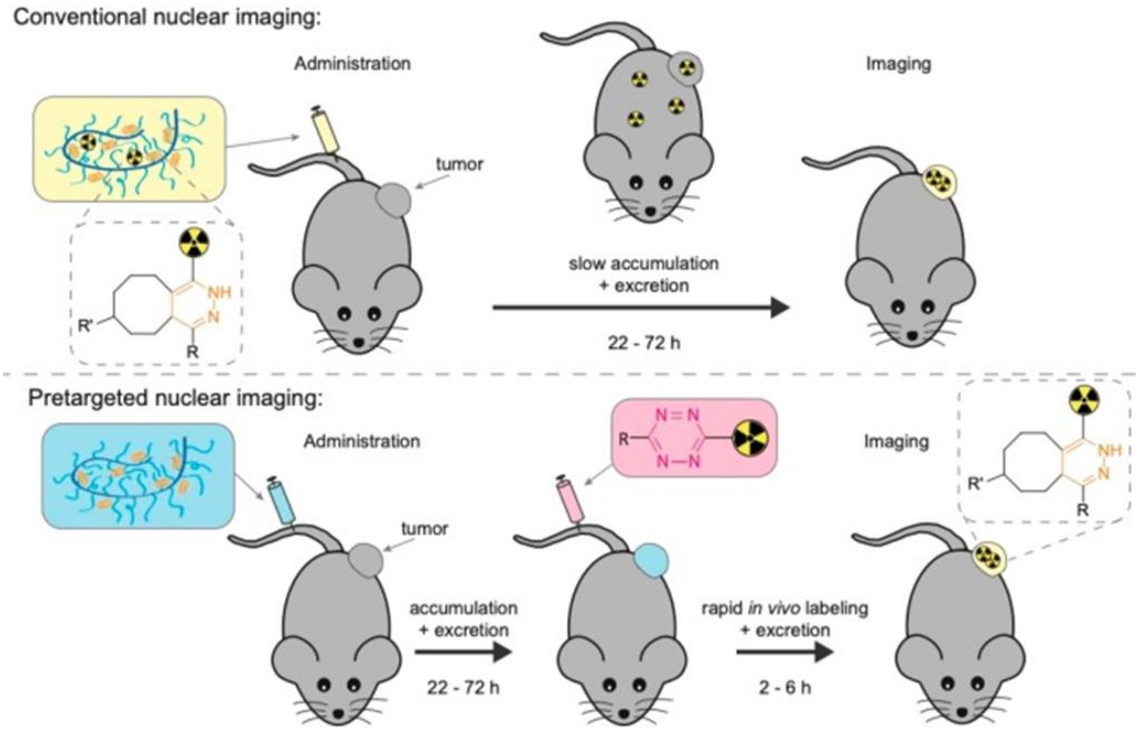

Figure 3.4. Scheme of the pretargeted nuclear imaging experiment for tumour targeting nanomedicine using IEDDA reaction compared to conventional nuclear imaging: The primary targeting agent is Peptobrush modified with trans-cyclooctene (TCO), and the secondary imaging agent is a ^{111}In labelled tetrazine (Tz). Top: Conventional nuclear imaging involving administration of the radiolabelled nanomedicine, administered, and allowed to circulate for days to achieve tumour accumulation up to 72 h. Bottom: Pretargeted nuclear imaging involving the TCO-modified Peptobrush (blue box) is administered and allowed to circulate until tumour accumulation followed by administration of radiolabelled Tz. Imaging is performed with the first few hours of the administration of Tz. Image reproduced.[355]

The key lessons from the pretargeted nanoparticle imaging studies summarised above include the importance of the relative ratios of TCO/tetrazine, the properties of the nanoparticles such as cell internalisation, the time required for reaching the target to find the optimal times for administration of imaging agent, and the impact of the TCO concentration loaded on the targeting molecule. Moreover, these studies inform about the different properties of the different tetrazine based small molecule imaging agents, their normal biodistribution and the pathways through which tetrazine imaging agents are cleared from the body. Now that we have briefly discussed about the pretargeted imaging of nanoparticles and the current need for pretargeted imaging of long circulating nanomedicines like liposomes, we will discuss our hypothesis and aims to build a biorthogonal pretargeting system for imaging of PEGylated liposomes, as a comparison to the metal pretargeting system explored in Chapter 2.

3.1.6 Aims and Motivations

In this chapter, we aim to develop a pretargeted PET imaging system for liposomal nanomedicines which can be used to efficient pretarget long circulating liposomes and can be potentially utilised for pretargeted imaging and theranostics. The highly reactive biorthogonal pair of transcyclooctene and tetrazine has been chosen due to its fast reaction kinetics and high specificity as a biorthogonal reaction, that has been already proven for antibodies as well as non-liposome nanoparticle systems. To this end, a novel small molecule bifunctional metal chelator THP-tetrazine conjugate was developed and characterised. THP-tetrazine was radiolabelled with $^{68/67}$Ga and the stability of the radiolabelled conjugate was determined *in vitro.* Alongside the synthesis of the imaging agent ($^{68/67}$Ga-THP-tetrazine), a transcyclooctene-phospholipid conjugate (TCO-PL) was also synthesised and characterised. This TCO-PL was utilised to incorporate the TCO functionality on the liposomal surface providing biorthogonal reactive TCO-PL liposomes with TCO-PL embedded in the lipid bilayer. The developed components were characterised and validated *in vitro* for pretargeting in blood serum. Finally, this biorthogonal system components were examined *in vivo* in a healthy and fibrosarcoma murine model for pretargeted imaging of PEGylated liposomes (Figure 3.5).

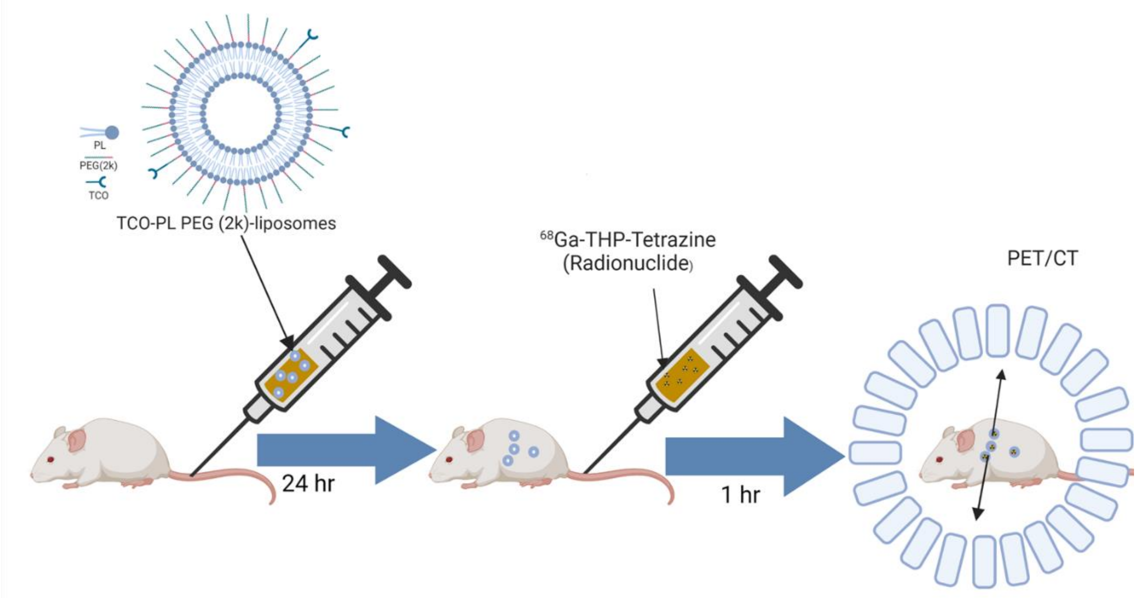

Figure 3.5. Schematic of the biorthogonal pretargeted imaging of PEGylated liposomes experiment: The pretargeted imaging involves administration of TCO modified PEGylated liposomes (TCO-PL-liposomes) in either healthy or tumour mice and allowing them to circulate and accumulate in organs of interest. This is followed by administration of small molecule imaging agent ^{68}Ga-THP-tetrazine followed by imaging of the mice after allowing enough time for interaction of the TCO-PL-liposomes and tetrazine *in vivo*. Created with BioRender.com.

3.2 Results and discussion

3.2.1 Synthesis of TCO-DSPE-PEG(2000) amine (TCO-PL)

3.2.1.1 Synthesis and Purification

The TCO-DSPE-PEG(2000) amine (TCO-PL), required to functionalise the surface of PEGylated liposomes with TCO, was synthesised by reaction between the NHS ester derivative of TCO (trans-cyclooctene-PEG$_4$-NHS) and the amine derivative of the phospholipid:1,2-distearoyl-sn-glycero-3-phosphoethanolamine-N-amino(polyethylene glycol)-2000] ammonium salt powder (DSPE-PEG(2000)-amine). The NHS ester-activated crosslinking reaction with amine was chosen as the reaction proceeds in neutral to slightly alkaline conditions (pH 7-9) to provide the desired compounds with stable amide bonds. This reaction releases N-hydroxysuccinimide (NHS) as a by-product which can be easily removed to purify the reaction. The PEG spacer in TCO-NHS allows for increased ease of handling by increasing water solubility, and an increased distance between the amine containing compound (here, phospholipid) to be modified, and the reactive alkene.

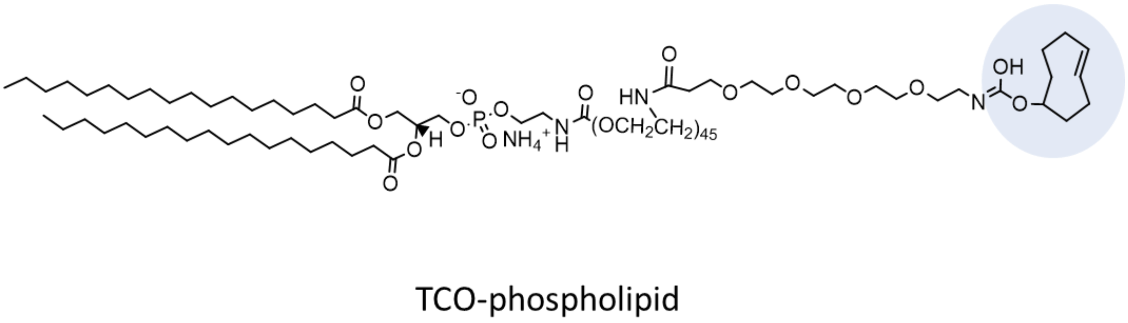

Figure 3.6. Structure of the TCO-phospholipid conjugate (TCO-PL): The synthesised TCO-PL has three major components: TCO (biorthogonal reactive moiety), PEG2000 linker (allows for the TCO to available on the surface of the PEGylated liposomes), the phospholipid chain (gets embedded into the bilayer of the PEGylated liposomes).

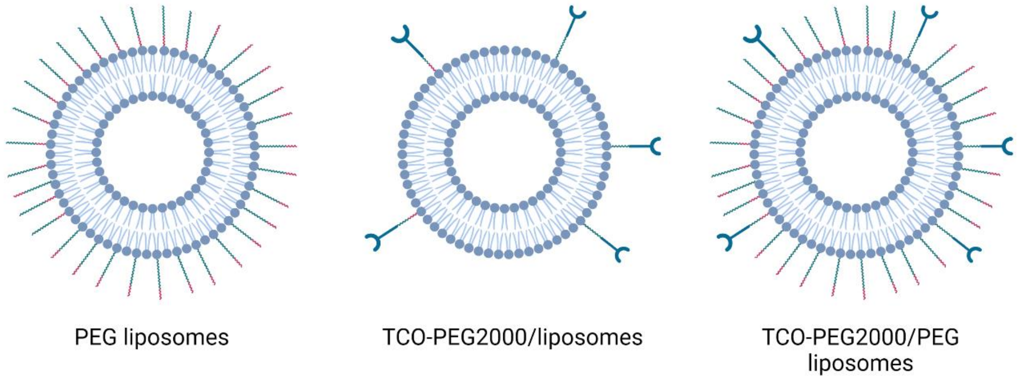
PEG liposomes

TCO-PEG2000/liposomes

TCO-PEG2000/PEG liposomes

Figure 3.7. Different combinations of surface modifications of liposomes: TCO-PEG2000 represents the TCO-PL synthesised in this chapter which has a PEG2000 chain. The images above show how PEGylation of liposomes provide a brush like exterior to the liposomes and presence of PEG2000 in the TCO-PL allows TCO to be available at the surface for interactions with tetrazine imaging agent. Created with BioRender.com.

The 2000 Da length PEG linker in the DSPE-PEG2000 amine used has an important relevance in accessibility of TCO molecule on the surface of long-circulating PEGylated liposomes. The PEG2000 coating on PEGylated liposomes which provides extended systemic circulation *in vivo* but interferes with specific targeting agents on the surface. Therefore, to counteract that interference, we have used DSPE-PEG2000 amine to create a phospholipid-TCO (TCO-PL) allowing the retention of TCO reactivity in the surface. The comparison between effect of non-PEG phospholipid conjugate and PEG phospholipid can be seen in figure 3.7.

Hydrolysis of the NHS ester in this crosslinking reaction competes with the reaction with the primary amine. The pH of the reaction mixture increases the rate of hydrolysis while the low concentration of reactants contributes to increase in the hydrolysis as well. The reaction was performed at pH<9 in high concentration of both reactants and dry DMSO to avoid the hydrolysis of the NHS ester at basic pH. The reaction was performed at room temperature over night to completion. The purification of the final product was performed using dialysis due to the large MW of the compound of interest and to increase the recovery of synthesised TCO-PL after purification. The reaction mixture was diluted to 5% DMSO/water before performing dialysis as the membrane of the dialysis cassette is reactive to high DMSO or organic solvent concentrations. The compound obtained after purification and freeze drying was a white solid in a high yield (93 ± 3%) which is expected because of the ease of the NHS ester activated amine crosslinking reaction and presence of excess TCO-NHS ester which limits the effect of hydrolysis on the yield of the reaction.

3.2.2.2 Characterization

The large MW of TCO-PL (3305 g/mol) and the presence of the PEG chain on the molecule made the characterization particularly challenging. The high-resolution mass spectrometry facility at the National Mass spectrometry facility, Swansea was used to obtain the data as seen in figure 3.9. The presence of the TCO-PL in the product was confirmed by comparison of the mass spectra of the TCO-PL and DSPE-PEG2000 amine. A clear shift was observed for the m/z = 1 species towards the higher molecular weight from DSPE-PEG-amine (observed MW = 2818, calculated MW = 2790) to TCO-PL (observed MW = 3305, calculated MW = 3305). The mass spectra also showed an electrospray envelope nature due to the presence of PEG chain with a difference of 44 between each peak which is equal to the molecular weight of PEG molecule. The envelope for DSPE-PEG-amine spanned over m/z= 2400-3200 representing z = 1 species whereas the TCO-PL spectra electrospray envelope spanned over m/z = 2900-3700 representing z = 1 species.

The NMR spectra further characterised and assessed the purity of TCO-PL. The ^{1}H NMR spectrum in $CDCl_3$ of TCO-PL (Figure 3.8) was compared to that of the starting material DSPE-PEG2000-amine. The presence of the characteristic broad peaks of TCO (δ 2.5 -CH; 5.5 =CH in cyclooctene) in the spectra of TCO-PL and not DSPE-PEG2000 amine supported the successful synthesis of TCO-PL in the reaction. Integration of peaks could not be performed quantitatively due to the high intensity ethylene peak of PEG at δ 3.64 ppm in both spectra, which marred the resolution of both spectra. The labelled signal peaks and integration performed account for the protons of TCO-PL are seen in figure 3.8. The characterization of the synthesised TCO-PL using NMR and mass spectrometry confirmed the purity and expected structure showing that the TCO-PL was synthesised in high yield and purity.

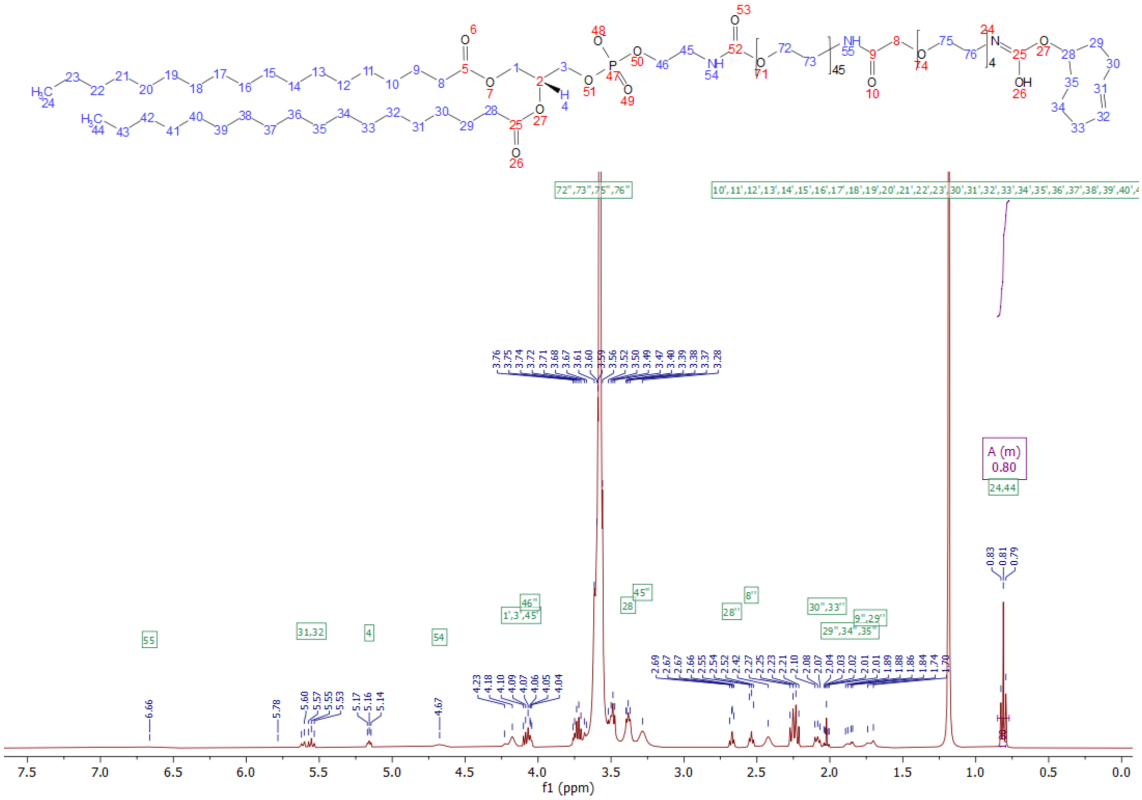

Figure 3.8. NMR spectra of TCO-PL: The synthesised TCO-PL is characterised by the presence of characteristic peaks of TCO incorporated in the phospholipid: δ 2.5 -CH; 5.5 =CH in cyclooctene. The integration of the peak's accounts for 283 out of 293 protons. The integration is not quantitative due to the relative high intensity of protons from ethylene peak of the PEG2000 chain which decrease the resolution of other peaks.

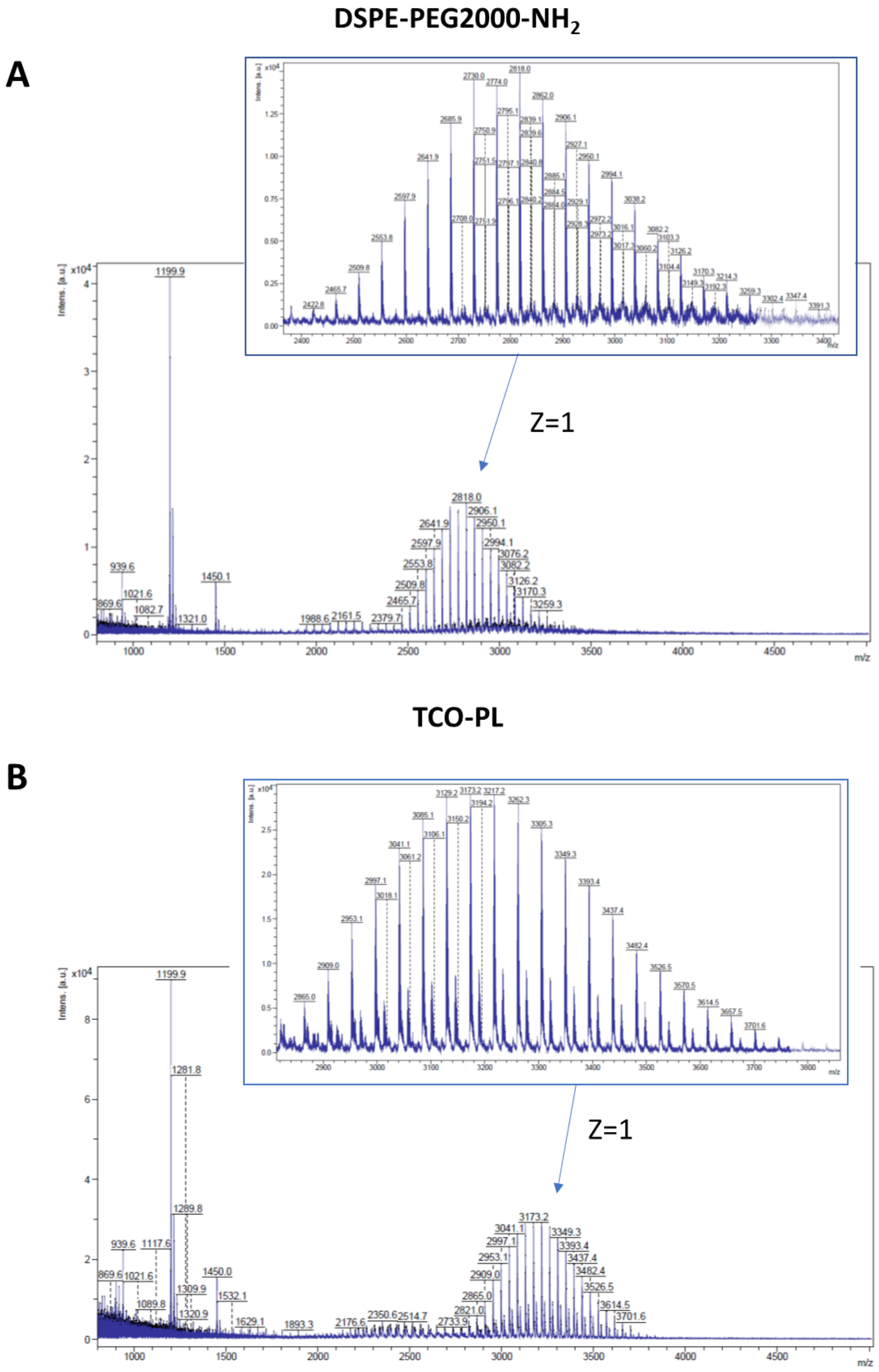

Figure 3.9. The mass spectrum of the TCO-PL (A) and DSPE-PEG2000 amine (B): The envelope nature observed in both spectra is due to the polydispersity of the PEG2000 chain which is characterised by a difference of 44 between each peak within the envelope. The TCO-PL is characterised by the higher m/z=2700-3700 compared to the lower m/z for DSPE-PEG2000 amine m/z=2400-3200.

3.2.2 Synthesis of 6-methyl tetrazine-THP

3.2.2.1 Synthesis and Purification

The secondary imaging agent of the pretargeting system was THP-tetrazine. This was synthesised by reaction of THP-Bz-SCN with 6-Methyl tetrazine amine to give 6-Methyl Tetrazine-THP (THP-tetrazine) (Figure 3.10). The reaction proceeded by amine-thiocyanate conjugation. Trishydroxypyridinone (THP) was chosen as the ideal choice from a library of gallium chelators due to its high affinity towards ^{68}Ga and fast complexation kinetics. The 6-Methyl tetrazine amine was chosen to form the THP-tetrazine conjugate due to favourable stability features of 6-methyl tetrazine over its hydrogen substituted derivative of tetrazine-amine.[356] The stability of methyl tetrazine amine further improves its handling and storage in aqueous solutions. However, the addition of an EWG such as a methyl group leads to a minor decrease in the reactivity of tetrazine towards TCO, as has been shown recently.[347] The amine derivative of the methyl tetrazine has been widely used for conjugation with various imaging motifs and provides a straightforward method for conjugation with THP isothiocyanate.

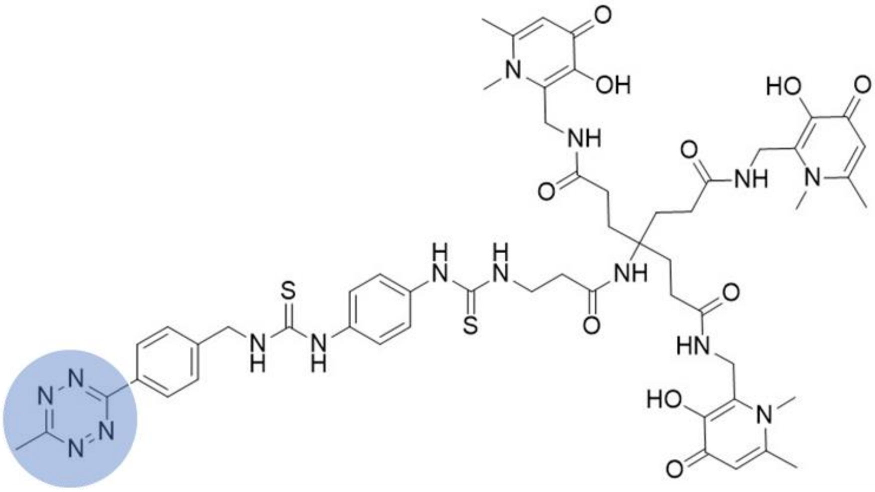

Figure 3.10. Structure of the THP-tetrazine: the synthesised THP-tetrazine has two important components: Trishydroxypyridinone which is an excellent chelator for Ga as well as Fe, and Tetrazine (in the highlighted circle) which has high reactivity towards transcyclooctene (TCO).

Anhydrous DMSO proved to be an ideal choice as solvent to overcome the low solubility of methyl tetrazine-amine in water and the tendency of THP-NCS to undergo degradation or hydrolysis in water. Thereby, DMSO minimised solubility and degradation concerns allowing for the reaction to proceed slowly without need of high pH and temperature conditions. The reaction was performed at room temperature with DIPEA to achieve a pH of 9-10 and initiate the reaction via deprotonation of amine of DSPE-PEG2000. The use of mild conditions and DMSO thereby minimised the formation of side products which is evident in the LCMS trace of the reaction mixture showing minimal side products. The LCMS trace of the reaction mixture as seen in figure 3.11(B) shows desired THP-tetrazine (m/z [M + 2H]2+ = 581.52), unreacted methyl-tetrazine amine (m/z [M+Na]$^+$= 225.92), and small amount of THP-NCS hydrolysed to a primary amine (m/z [M +2H]2+ = 460) as expected.

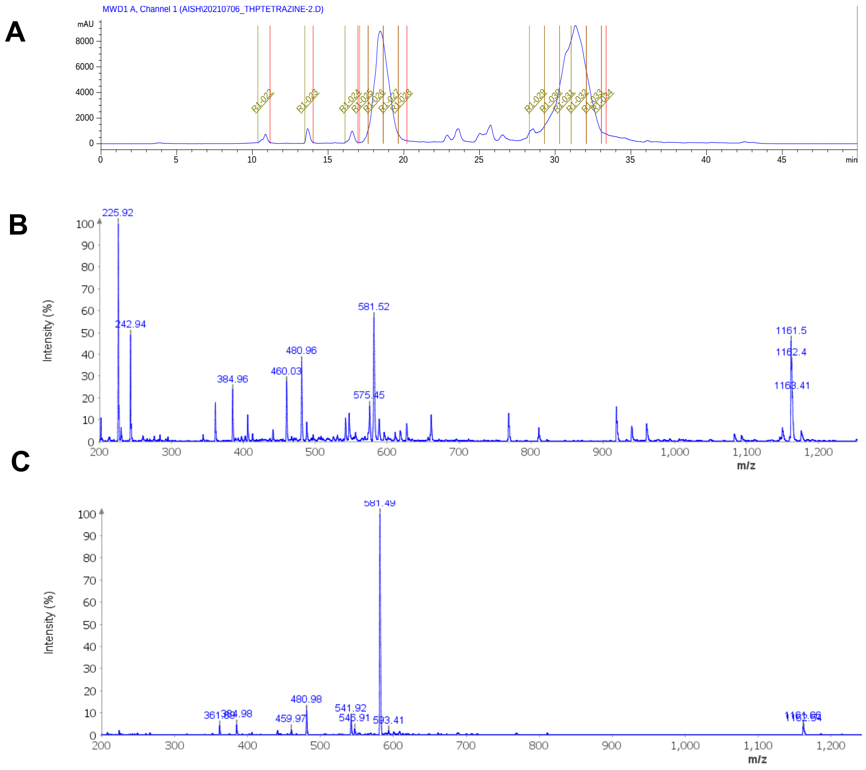

Figure 3.11. Purification of THP-tetrazine: (A) HPLC chromatogram of the semi-prep HPLC method used for isolation of THP-tetrazine from the reaction mixture. Fraction collected between t_r =29 min-33 min contained the THP-tetrazine; (B) Mass spectra of the THP-tetrazine crude reaction mixture showing the THP-tetrazine as the major product alongside unreacted Methyl-tetrazine amine and hydrolysed THP; and (C) Mass spectra of the THP-tetrazine fraction collected after semi-prep HPLC showing the pure isolated THP-tetrazine.

To remove unreacted THP-Bz-SCN and excess reaction components (*i.e.,* DIPEA, DMSO), semi-prep HPLC (method 2) on a reverse phase column was utilised to provide the pure THP-tetrazine. The reaction was monitored by LCMS showing that the THP-tetrazine is collected in the fraction where the mobile phase is approximately between 40-50% acetonitrile/water. Using the information obtained from LCMS, we estimated that for HPLC purification, acetonitrile concentration higher than 25 % will be required to elute the THP-tetrazine product. Therefore, a slow gradient as shown in HPLC method 2 was applied with a semi-automated system. The THP-tetrazine was collected at $t_r = 29$ minutes whereas unreacted tetrazine was collected at $t_r = 17$ minutes as shown in figure 3.11(A). The purity of collected THP-tetrazine was verified using LCMS of the collected fractions showing THP-tetrazine (m/z $[M + 2H]^{2+}$ = 581.52) and (m/z $[M+H]^{+}$ = 1162.5) (figure 3.11(C)).

The isolated pure product was obtained in average yield (57 ± 5 %) as a bright pink hygroscopic solid and stored for later use at -20^{o}C. Further characterisation and confirmation of the purity of the synthesised THP-tetrazine was obtained from ^{1}NMR spectrum in a mixture of CD_3CN/D_2O. The characteristic peaks of the THP-tetrazine observed were δ 8.43-8.41 (d, (*J* = 8.3 Hz), 2H Ar-H from tetrazine), 7.57 (d, (*J* = 8.2 Hz), 2H)7.25-7.36 (4H from N-H), 6.96 (m, 6H from Ar-H from tetrazine), 4.89(s, 3H from Ar-H from THP), 4.54 (s, 2H), 3.79-3.82 (m, 9H from CH_3-N, 8H from CH_2-N), 3.01 (s, 2H) 2.48 (s, 3H), 2-42-2.44 (m, 2H), 2.11-2.15 (m, 4H), 1.95 (m, 9H), 1.85 (s, 2H), 1.25 (m, 4H).(Figure 3.12) 1H NMR (400 MHz, CD_3CN).

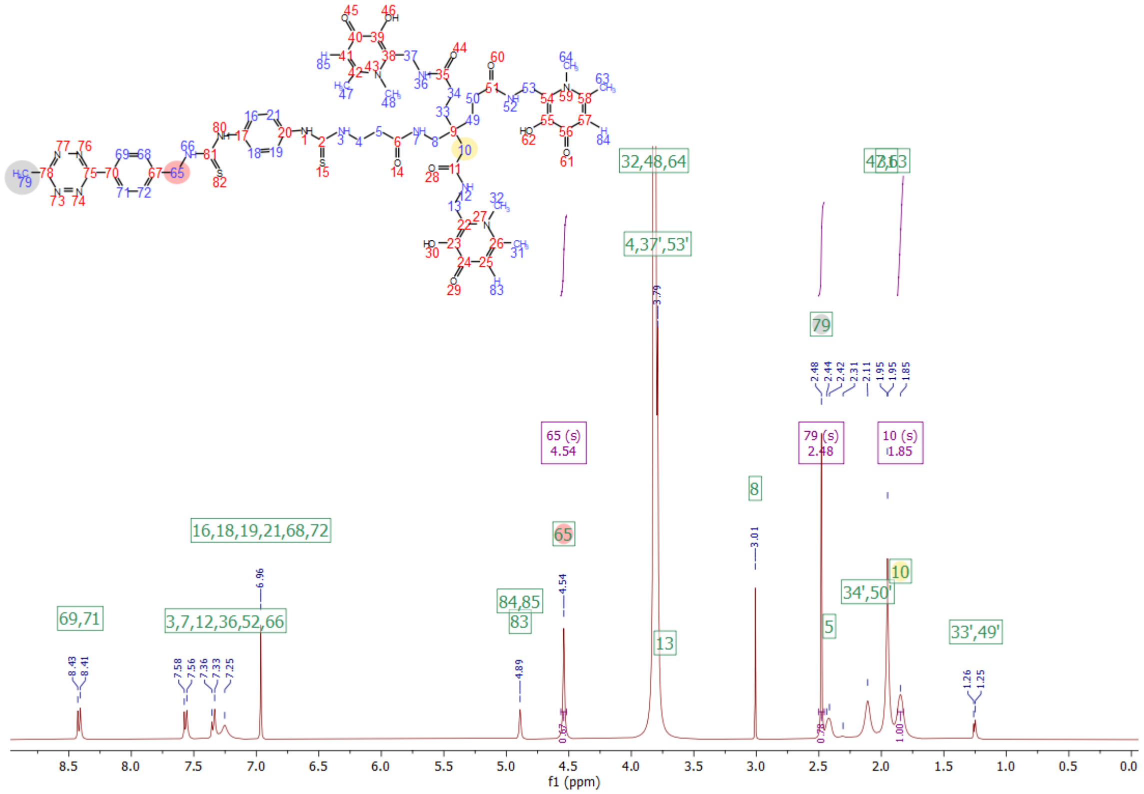

Figure 3.12. NMR spectra of the THP-tetrazine: The synthesised THP-tetrazine was characterised by the presence of the above peaks. The spectrum was recorded in CD_3CN/D_2O due to low solubility in $CDCl_3$. ^{1}H NMR (400 MHz) δ 8.43-8.41 (d, (*J* = 8.3 Hz), 2H Ar-H from tetrazine), 7.57 (d, (*J* = 8.2 Hz), 2H)7.25-7.36 (4H from N-H), 6.96 (m, 6H from Ar-H from tetrazine), 4.89(s, 3H from Ar-H from THP), 4.54 (s, 2H), 3.79-3.82 (m, 9H from CH_3-N, 8H from CH_2-N), 3.01 (s, 2H) 2.48 (s, 3H), 2-42-2.44 (m, 2H), 2.11-2.15 (m, 4H), 1.95 (m, 9H), 1.85 (s, 2H), 1.25 (m, 4H). Non-deuterated solvent H_2O and CD_3CN impurity peaks are also observed in the spectrum.

3.2.2.2 Radiolabelling

The binding affinity of THP-tetrazine towards ^{68}Ga was determined using radiolabelling experiments where the THP-tetrazine was reacted with either ^{68}Ga/^{67}Ga, and the radiolabelled compounds were characterised for purity and stability. The stocks of THP-tetrazine for radiolabelling were made in 10% DMSO/water due to the low solubility of THP-tetrazine in water.

The radiolabelling reaction was found to be fast under mild conditions, similar to other THP compounds.[264,265,268,357] In a typical reaction, incubation of different amounts of THP-tetrazine (5 µg, 10 µg, or 50 µg, 1 mg/mL) in 10% DMSO/water were added to 200 µL of sodium carbonate neutralised ^{68}Ga for 15 minutes followed by radio-TLC and radio-HPLC, indicating formation of a single radiolabelled species. The radio-HPLC of the reaction using 5 µg of THP-tetrazine showed a single peak at t_r=8 minutes, consistent with ^{68}Ga-THP-tetrazine, with no peak observed for free ^{68}Ga. This was also confirmed by the ITLC as seen in figure 3.13 where radioTLC performed in glass microfibre chromatography paper impregnated with silicic acid in 0.5 M citrate buffer. Unbound ^{68}Ga moved with the solvent front (R_f=1), giving a clear distinction from ^{68}Ga-THP-tetrazine that appears on the baseline (R_f=0). The absence of the unbound ^{68}Ga in the reaction mixture confirmed by radioHPLC and radioTLC gave confirmation of the formation of a single radiolabelled species with quantitative labelling.

^{68}Ga-THP-tetrazine was often found irreversibly bound to the glass vial and formed a colloid-like impurity which could not be detected by previous characterisation methods of radioHPLC and radioTLC in citrate buffer. However, these colloids were detected in subsequent experiments of radiolabelling of TCO-liposomes, and *in vitro* pretargeting. Therefore, we explored two purification methods to remove this colloidal impurity. The first method of purification involved centrifugal size exclusion filters, but the separation could not be achieved as ^{68}Ga-THP-tetrazine was also retained in the size exclusion filters alongside the colloidal impurities. This could be possibly due to the lipophilic nature of ^{68}Ga-THP-tetrazine. The second method involved a SEP-PAK separation, which is often employed for purification of lipophilic compounds. Using this method, the pure ^{68}Ga-THP-tetrazine was eluted in methanol from a SEP-PAK plus light C18 cartridge and dried under nitrogen followed by resuspension in 5% DMSO/water and subsequently used for further *in vitro* and *in vivo* validation. The characterisation of the isolated compound with radioTLC in ammonium acetate: methanol (1M, 80% v/v) showed presence of greater than 95% pure ^{68}Ga-THP-tetrazine (R_f = 0.8 – 1) and absence of colloidal impurities (R_f = 0) (Figure 3.13).

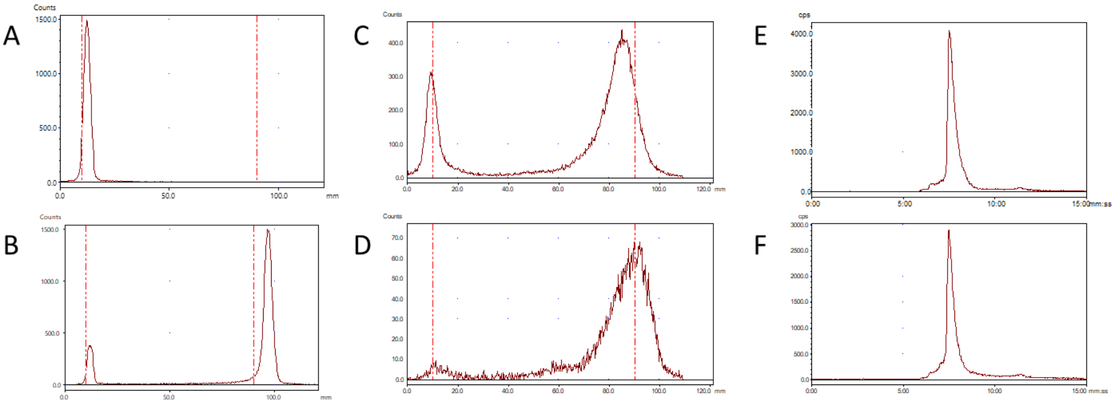

Figure 3.13. Radiolabelling of THP-tetrazine: (A-D) radioTLC chromatogram: **(A)** ^{68}GaCl3 (R_f=0) in citrate buffer; **(B)** ^{68}Ga-THP-tetrazine(R_f=1) in citrate buffer; **(C)** ^{68}Ga-THP-tetrazine in 80% v/v ammonium acetate/methanol; **(D)** SEP-PAK purified ^{68}Ga-THP-tetrazine in 80% v/v ammonium acetate/methanol(R_f=0.8-1 for ^{68}Ga-THP-tetrazine and R_f=0 for lipophilic impurity); **(E-F)** radioHPLC chromatogram: **(E)** ^{68}Ga-THP-tetrazine characterised using analytical radioHPLC method 3; **(F)** SEP-PAK purified ^{68}Ga-THP-tetrazine characterised by analytical radioHPLC method 3.

Measurement of logP = -0.47 ± 0.01 and logD$_{7.4}$ = -0.44 ± 0.03 showed that ^{68}Ga-THP-tetrazine was slightly lipophilic as expected for tetrazine compounds, and more lipophilic compared to existing gallium-68 labelled conjugates of THP.[357] Comparison with the logP and logD$_{7.4}$ of other tetrazine imaging agents, suggest that ^{68}Ga-THP-tetrazine is as lipophilic as other tetrazine based imaging molecules, which generally leads to slow pharmacokinetic clearance from the body and a preference for hepatobiliary excretion showing uptake in the liver, gall bladder and intestines.[347,358,359]

THP-tetrazine was also radiolabelled with ^{67}Ga to provide ^{67}Ga-THP-tetrazine. ^{67}Ga for radiolabelling was obtained as ^{67}Ga-citrate from Guy's radiopharmacy. The labelling of THP-tetrazine from ^{67}Ga citrate poses a few challenges which need to be overcome. The citrate bound ^{67}Ga has low binding affinity towards others chelator on the account of citrate being a chelator for Ga. Therefore, ^{67}Ga-citrate was converted to

^{67}GaCl$_3$ *via* anion-exchange chromatography. Another challenge was the presence of metallic impurities such as Fe, Mn, Cu in the ^{67}Ga-citrate sample. The presence of even trace amounts of Fe can lead to decreased radiolabelling efficiency of THP-tetrazine due to saturation of THP binding sites as THP is an excellent chelator for both Fe and Ga. To overcome this, the ^{67}Ga labelling of THP-tetrazine is performed with converted ^{67}Ga-chloride at very dilute conditions to minimise the metallic impurities. This provided us with radiolabelling yields ranging from 20%-30%. The radiolabelled ^{67}Ga-THP-tetrazine was characterised and purified as mentioned above and further used for the synthesis of ^{67}Ga labelled TCO-liposomes.

3.2.3 Synthesis of TCO-liposomes

3.2.3.1 Synthesis and purification

PEGylated liposomes can be modified either during the formation of the liposomes or in preformed liposomes to provide surface anchored targeting groups. Here, we desired insertion of the TCO-PL in the bilayer of the PEGylated liposomes to provide biorthogonal reactive TCO-liposomes. The insertion process is performed at elevated temperature but below the phase transition temperature as the higher temperature increases the fluidity of the lipid bilayer for the incorporation of the external phospholipids in the bilayer. This procedure was exploited in the first instance for formation of folate targeting liposomes and is also used in Chapter 2 for insertion of THP-PL in the bilayer of PEGylated liposomes. The optimisation of insertion is dependent on the relative concentration of phospholipid being inserted, incubation time, and incubation temperature. The conditions optimised for insertion of THP-PL in the bilayer of PEGylated liposomes in Chapter 2 and routinely used for core-radiolabelling of preformed liposomes were used here. Thus, the final insertion conditions chosen were incubation temperature: 50°C, incubation time: 30 minutes, and TCO-PL relative concentration: 5 mol %. The PEGylated liposomes used were chosen for having the same physicochemical properties as stealth liposomes extensively used in the clinic such as Doxil/Caelyx (size: 89.4 ± 0.6 nm, concentration: 60.0 ± 0.9 mM, PDI: 0.03 ± 0.01). After the insertion reaction, the biorthogonal reactive TCO was expected to be accessible on the liposome surface, hence retaining its high reactivity towards tetrazine. This was facilitated by incorporating a PEG chain in the TCO-PL of the same molecular weight as the PEG chains present in the PEG(2k)-liposomes (*i.e.,* 2000 Da). The product (TCO-PL-liposomes) was purified by size exclusion (PD10 minitrap G-25 size exclusion column) and analysed via dynamic light scattering (DLS) (Figure 3.14(A)), Nanoparticle tracking analysis (NTA, Figure 3.14(B)), and cryo-transmission electron microscopy (Cryo-TEM; Figure 3.15). The insertion was considered successful if the physicochemical properties of TCO-PL-liposomes were same as PEG(2k)-liposomes and the TCO-PL-liposomes had gained biorthogonal reactivity towards tetrazine to undergo cycloaddition at high reaction rates. The DLS studies were performed to monitor the impact of surface modification on the hydrodynamic size and zeta potential of the PEGylated liposomes. The NTA was also performed to monitor the impact on the size, polydispersity and the concentration of the PEGylated liposomes post-modification. The cryo-electron microscopy was performed on the liposomes before and after insertion to assess the impact on the size, size distribution and most importantly, morphology of the liposomes. The radiolabelling of the liposomes was performed to verify that the TCO was embedded and accessible on the liposomal surface and the results are discussed in section 3.2.4.

3.2.3.2 Dynamic light scattering (DLS)

As mentioned previously in Chapter 2, in the context of characterisation of nanoparticles, DLS is a powerful tool to measure the hydrodynamic size, zeta potential, and polydispersity of particles in a sample. Similar to the work described in Chapter 2, the characterisation via DLS allowed us to measure the impact of insertion of TCO-PL on the PEGylated liposomes. We measured both the PEG(2k)-liposomes and TCO-PL-liposomes and there was no major impact observed on the surface charge (zeta potential), polydispersity and hydrodynamic size. The average size of the PEG(2k)-liposomes without modification was 88.8 ± 0.5 nm and after modification it was 89 ± 2 nm. In addition to size, the surface charge of the nanomedicines is also measured, as the surface charge plays a key role in how the liposomes reached the target and the mechanism of uptake as discussed in the introduction chapter. The zeta potential measurement of the non-modified PEGylated liposomes gave us a surface charge of -0.7 ± 0.3 and post modification the surface charge was observed to be -1.7 ± 0.2 which is a negligible change in terms of the sign of the surface charge and its magnitude and should not cause any impact on the *in vivo* behaviour of the liposomes. Finally, the polydispersity index was also measured, which is a measurement of the number of species of a particular size and provides information if the particles are monodispersed or not. Clinically used liposomal samples are highly monodispersed to minimise the variability in the injected samples. In context of the PDI, for lipid based nanocarriers such as liposomes, a PDI ≤ 0.3 is considered to be a homogenous and monodispersed sample.[360,361] Therefore, we aimed to minimise the increase in the polydispersity after modification. The PDI of the TCO-PL-liposomes was 0.06 ± 0.02 and for the unmodified PEGylated liposomes was 0.07 ± 0.01 showing high monodispersity.

3.2.3.3 Nanoparticle tracking analysis

The high-resolution nanoparticle concentration and size distribution was determined using Nanoparticle Tracking Analysis (NTA). The liposome concentration is a key factor affecting clearance of liposomes as the concentration of liposomes affects their *in vivo* pharmacokinetics and clearance from the body by the RES. The liposome concentration for the unmodified PEGylated liposome was $2.88 \times 10^{16} \pm 2.17 \times 10^{15}$ particles/mL and for the TCO-PL-liposome was $3.74 \times 10^{15} \pm 2.36 \times 10^{14}$ particles/mL. The size distribution of both liposome samples was 60-150 nm with the peak maxima at 99.4 nm and 98.2 nm for unmodified liposomes and THP-PL-liposomes, respectively. In both samples, the liposomal size is concentrated towards the 100 nm region with a small shoulder representing the particles with slightly larger size greater than 100 nm. From these results, we can conclude there is no observed increase in the average liposome size which was observed with DLS measurements, and this modification should not affect the liposomal properties.

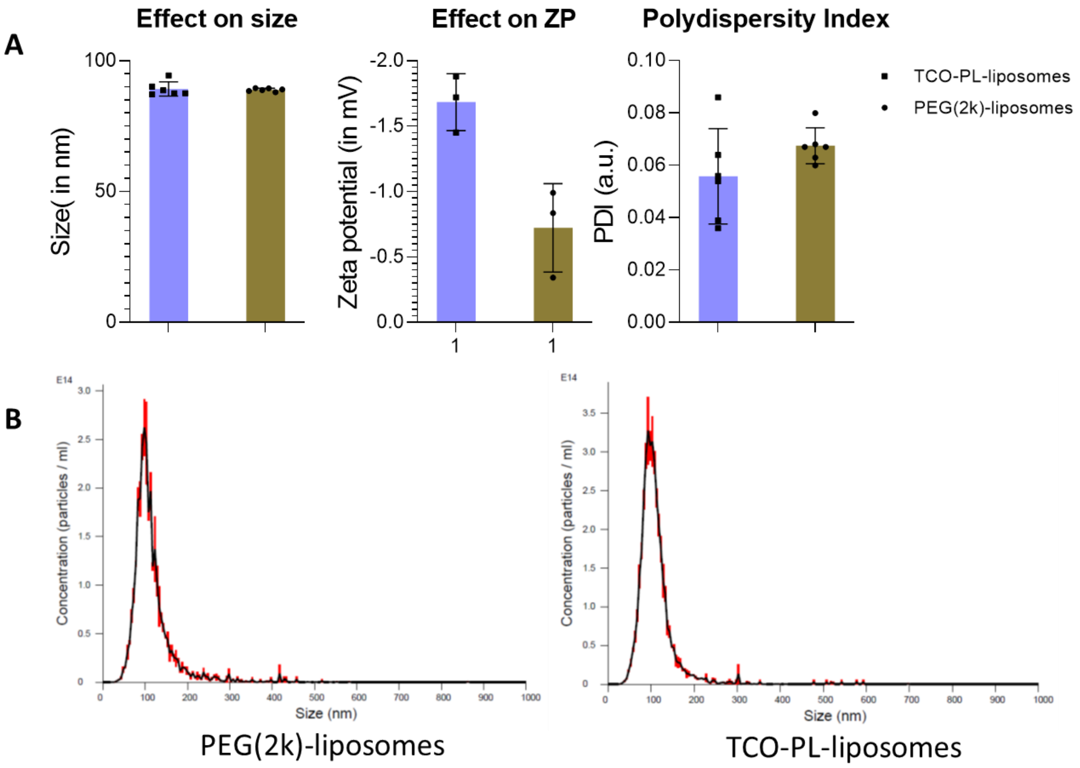

Figure 3.14. Characterisation of liposomes using Nanoparticle Tracking Analysis (NTA) to determine concentration and size distribution: (A) PEG(2k)-liposomes (concentration: $2.88 \times 10^{16} \pm 2.17 \times 10^{15}$ particles/mL, mode:97.8 nm, mean: 116.2 nm); (B) TCO-PL-liposomes (concentration: $3.74 \times 10^{15} \pm 2.36 \times 10^{14}$ particles/mL, mode: 93.1 nm, mean: 110.6 nm)

3.2.3.4 Cryo-electron microscopy

Cryo-electron microscopy was utilised to visualise the potential impact of TCO modification on the PEGylated liposomes. Here, the TCO-PL liposomes and unmodified PEGylated liposomes were frozen in vitreous ice and examined if the insertion of TCO-PL has caused any modifications to the shape, bilayer structure and size distribution of the liposomes. As seen in figure 15, the TCO-PL liposomes (A) retain their bilayer and spherical structure as observed in the unmodified PEGylated liposomes (B). 50 representative microscopic images taken for each sample confirm the above observations. Analysis of these microscopic images using ImageJ allowed us to create a size distribution which is shown as a histogram in Figure 3.15. Thereby, cryoEM along with the data from DLS and NTA confirmed the negligible change in the liposomal size, PDI and zeta potential as well as no change in the shape and structure of the liposomes post-modification.

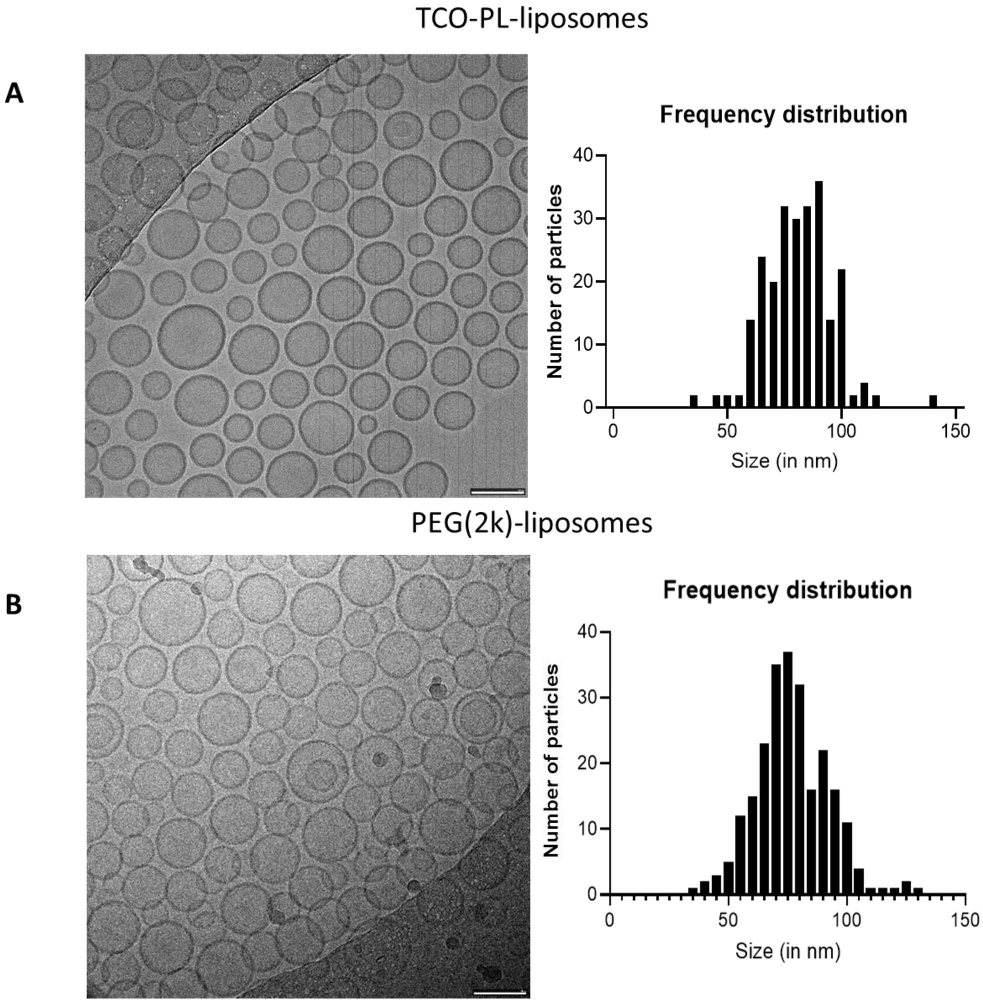

Figure 3.15. Cryo-electron microscopy of liposomes pre- and surface post-modification with TCO-PL: (A) showing TCO-PL-liposomes have retained their spherical nature and the size distribution is not altered by insertion of TCO-PL into the bilayer of liposomes and bilayer nature is also retained; (B) showing PEG(2k)-liposomes spherical morphology and bilayer structure. Size

quantification of liposomes from analysis of cryoEM images showing frequency distribution of diameter of liposomes: (A) Unmodified PEG(2k)-liposomes; (B) TCO-PL-liposomes

3.2.4 *In vitro* evaluation of TCO-PL liposomes

Now that both the components of the pretargeting system have been successfully synthesised and characterised, it is essential to evaluate the stability of the radiolabelled components and the feasibility of biorthogonal reaction in serum before conducting *in vivo* pretargeting experiments.

3.2.4.1 Serum stability

Blood serum proteins such as transferrin and lactoferrin could lead to transchelation of gallium from the THP-tetrazine *in vivo*. Using the serum stability experiments described below, we aimed to examine the stability of both ^{68}Ga-THP-tetrazine, and of ^{67}Ga-TCO-PL-liposomes post-radiolabelling. Choosing THP as a Ga chelator was an important factor in our design strategy to avoid the demetallation in blood serum. The stability of ^{68}Ga-THP-tetrazine was evaluated at 37˚C in commercially obtained human serum for up to 3 hours using HPLC SEC which separated THP-tetrazine and serum components. The serum protein bound ^{68}Ga eluted at t_r = 9 min whereas ^{68}Ga-THP-tetrazine eluted at t_r = 20 min when the serum incubated samples were analysed using serum stability HPLC method 4. The analysis of serum incubated samples showed minimal transchelation of ^{68}Ga to blood serum proteins and high stability of >95 % after 3 hours of incubation as shown in figure 3.16.

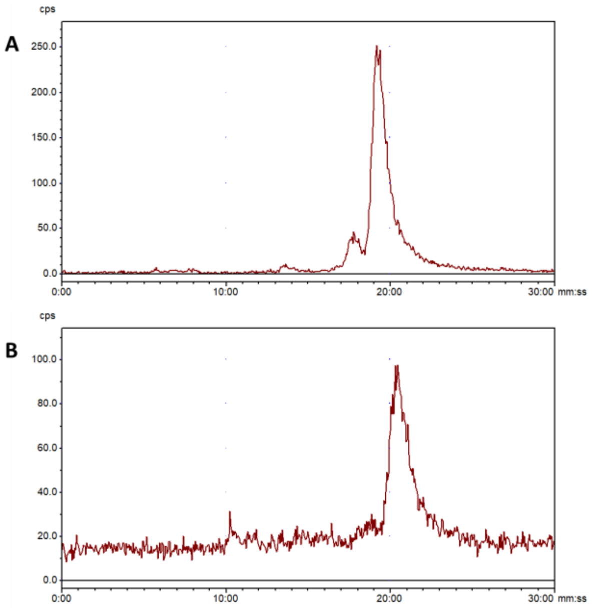

Figure 3.16. Serum stability assessment of ^{68}Ga-THP-tetrazine using HPLC SEC method 4: (A) RadioHPLC chromatogram of serum incubated ^{68}Ga-THP-tetrazine at t = 15 minutes; (B) RadioHPLC chromatogram of serum incubated ^{68}Ga-THP-tetrazine at t = 3 hours; RadioHPLC chromatogram species: serum bound ^{68}Ga (t_r= 9 min), ^{68}Ga-THP-tetrazine (t_r = 20 min).

To provide further support prior to the *in vivo* imaging studies, we used size-exclusion chromatography to test the radiochemical stability of ^{67}Ga-TCO-PL-liposomes *in vitro* in human serum at 37°C. Using this system, both liposomes and serum components can be efficiently separated and quantified via UV and radioactivity measurements, allowing determination of liposome and serum protein associated radioactivity at different time intervals. This high stability was retained for longer periods of time, as demonstrated by the >90% radiochemical stability found for ^{67}Ga-TCO-PL-liposomes after 48h under the same conditions.

3.2.4.2 *In vitro* pretargeting

The biorthogonal reaction for radiolabelling of TCO-PL-liposomes was evaluated under laboratory conditions for the formation of $^{67/68}$Ga-TCO-PL liposomes by incubation of radiolabelled $^{67/68}$Ga-THP-tetrazine with TCO-liposomes for 15 minutes providing ^{67}Ga-TCO-PL-liposomes and ^{68}Ga-TCO-PL-liposomes with a yield of 65 ± 9% and 74 ± 6%

respectively. However, the reaction was not performed under *in vitro* conditions that can simulate conditions of high dilution and interference from blood components. Therefore, it was essential to perform *in vitro* pretargeting assessment in high dilution conditions and in the presence of serum.

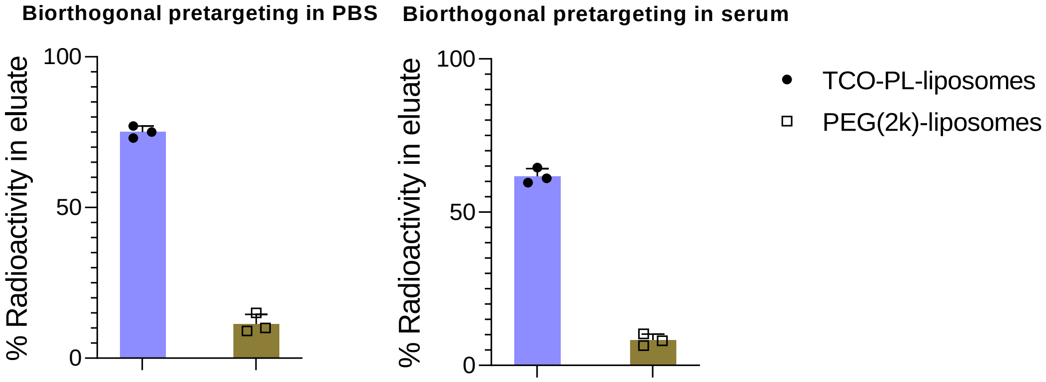

Figure 3.17. Radiolabelling of TCO-PL-liposomes: *In vitro* biorthogonal pretargeting was performed to validate the TCO/tetrazine pretargeting system. Two different *in vitro* biorthogonal pretargeting experiments were performed where TCO-PL-liposomes were incubated in either PBS or serum followed by addition of ^{68}Ga-THP-tetrazine and incubation at 37^{o}C for 30 minutes. The incubated samples were then purified via size exclusion chromatography and radioactivity attached to the TCO-PL-liposomes was determined. Unmodified PEG(2k)-liposomes were labelled as controls. The experiments showed showing % radiolabelling of 75 ± 2 % (n=3) and 61.7 ± 3.1 % (n=3) for PBS and serum incubated samples respectively.

The *in vitro* pretargeting was performed in both PBS and serum. The radiolabelled ^{68}Ga-THP-tetrazine and TCO-liposomes were incubated in four-fold dilution conditions in either human serum or PBS. This involved pre-incubation of TCO-PL-liposomes with human serum or PBS for 1 h at 37^{o}C, followed by addition of ^{68}Ga-THP-tetrazine for 30 minutes at 37^{o}C under continuous agitation. Size exclusion chromatography was used in both cases to isolate and quantify liposome-bound ^{68}Ga radioactivity from that bound to serum components. These experiments closely resemble our proposed *in vivo* biorthogonal pretargeting approach and the results showed successful radiolabelling with a high efficiency of 75 ± 2 % (n=3) in PBS dilution conditions. In serum conditions, TCO-PL-liposomes were radiolabelled with a high efficiency of 61.7 ± 3.1 % (n=3) in the presence of human serum components (Figure 3.17). These results further confirmed the high reactivity of the liposome embedded TCO towards tetrazine within a biologically relevant environment and supported the *in vivo* evaluation of this approach.

3.2.5 *In vivo* evaluation of pretargeting of TCO-PL liposomes in healthy mice

Following the synthesis and characterisation of the components of the system *i.e.,* TCO-PL phospholipid and ^{68}Ga-THP-tetrazine and *in vitro* pretargeting assessments, the next step was to perform an *in vivo* PET imaging and biodistribution experiment. The most important variable in the development of an *in vivo* biorthogonal pretargeting system was the duration between the introduction of the TCO-PL liposomes and the administration of the radioisotope bound tetrazine (^{68}Ga-THP-tetrazine). The time point was determined from previous liposomal imaging studies[313] and blood kinetic study of prelabelled ^{67}Ga-THP-PL liposomes in Chapter 2. The biorthogonal pretargeted *in vivo* imaging study was designed to have either a 3 h or 24 h wait time between administration of TCO-PL liposomes and ^{68}Ga-THP-tetrazine. Following administration of ^{68}Ga-THP-tetrazine, the mice were scanned after an initial wait time of 1 hour to allow for the *in vivo* interaction between tetrazine and TCO groups. The scanned mice were culled and biodistribution was performed post scanning. For the *in vivo* preclinical pretargeting evaluation, the healthy animals were divided into three groups (n= 4-5): positive control group (^{67}Ga-TCO-PL liposomes), test pretargeting group, and negative control group (^{68}Ga-THP-tetrazine) as shown in figure 3.18.

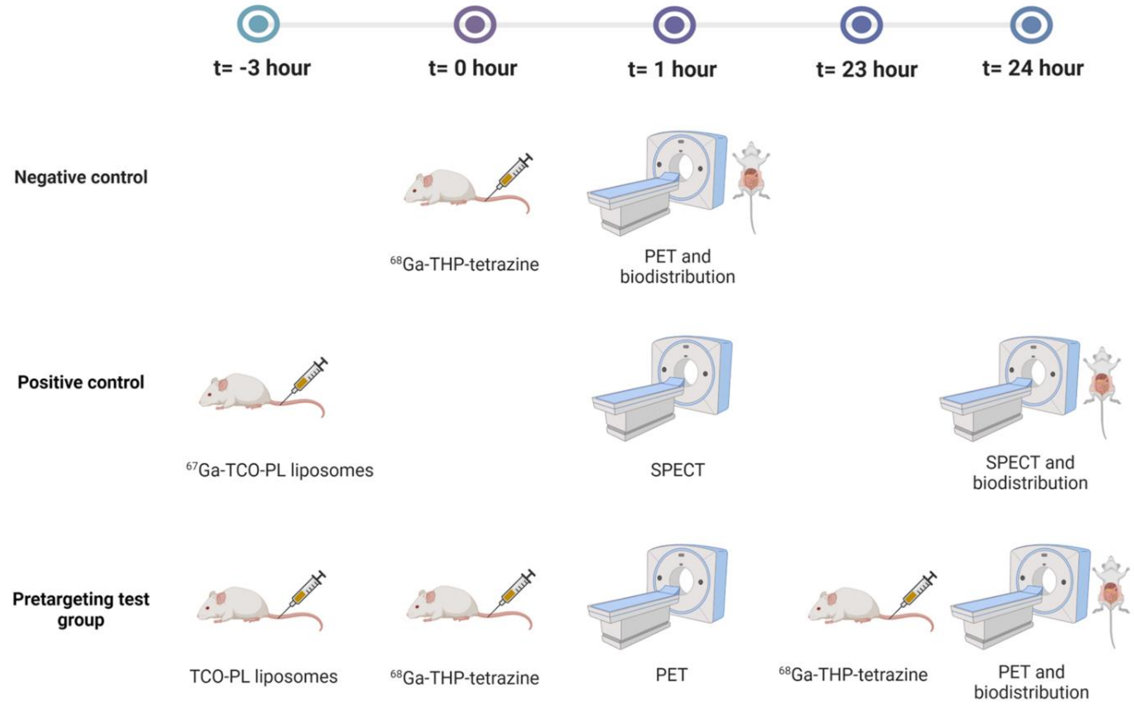

Figure 3.18. Scheme of *in vivo* pretargeting PET experiments: Negative control: administration of ^{68}Ga-THP-tetrazine; pretargeting test group: administration of TCO-PL-liposomes followed ^{68}Ga-THP-tetrazine; Positive control group: administration of ^{67}Ga-TCO-PL-liposomes. Created with BioRender.com.

The biorthogonal pretargeting experiment plan as seen in figure 3.18 was designed to act as a direct comparison against the metal chelation pretargeting experiments in Chapter 2. The two time points chosen for pretargeting of TCO-PL-liposomes were same as the metal pretargeting experiments *i.e.,* 3 h p.i. and 27 h p.i. of TCO-PL-liposomes to visualise the liposomes circulating in the blood and the target organs (liver, spleen) respectively. The 1 h wait post administration of imaging agent ^{68}Ga-THP-tetrazine was chosen to allow enough time for biorthogonal reaction between the imaging agent and the liposomes and minimise background signal due to any ^{68}Ga-THP-tetrazine circulating in the blood.

The negative control group involved administration of ^{68}Ga-THP-tetrazine and imaging at t = 1 h with biodistribution performed post imaging. Because of being a small molecule, ^{68}Ga-THP-tetrazine is expected to clear from the blood quickly. However, due to its lipophilic nature, it is also expected to clear through both hepatobiliary and renal excretion pathways. The images in figure 3.19 show high uptake in urinary bladder, gall bladder, and intestines which is consistent with mixed hepatobiliary/renal clearance. No retention was observed in the blood due to fast clearance. The high uptake in the urinary bladder and gall bladder is expected due to clearance of the imaging agent via renal and hepatobiliary excretion pathway, respectively. From the biodistribution and image quantification data in figure 3.19 (B,C), high uptake was also seen in the lungs, liver and spleen (5-10% ID/g). This can be explained by the lipophilic nature of THP-tetrazine, and colloidal impurity present in the ^{68}Ga-THP-tetrazine. The uptake observed in the liver and spleen poses a challenge for our pretargeting study in healthy animals as these organs are also sites of accumulation of PEGylated liposomes and will make the analysis of pretargeting test group challenging.[353,359]

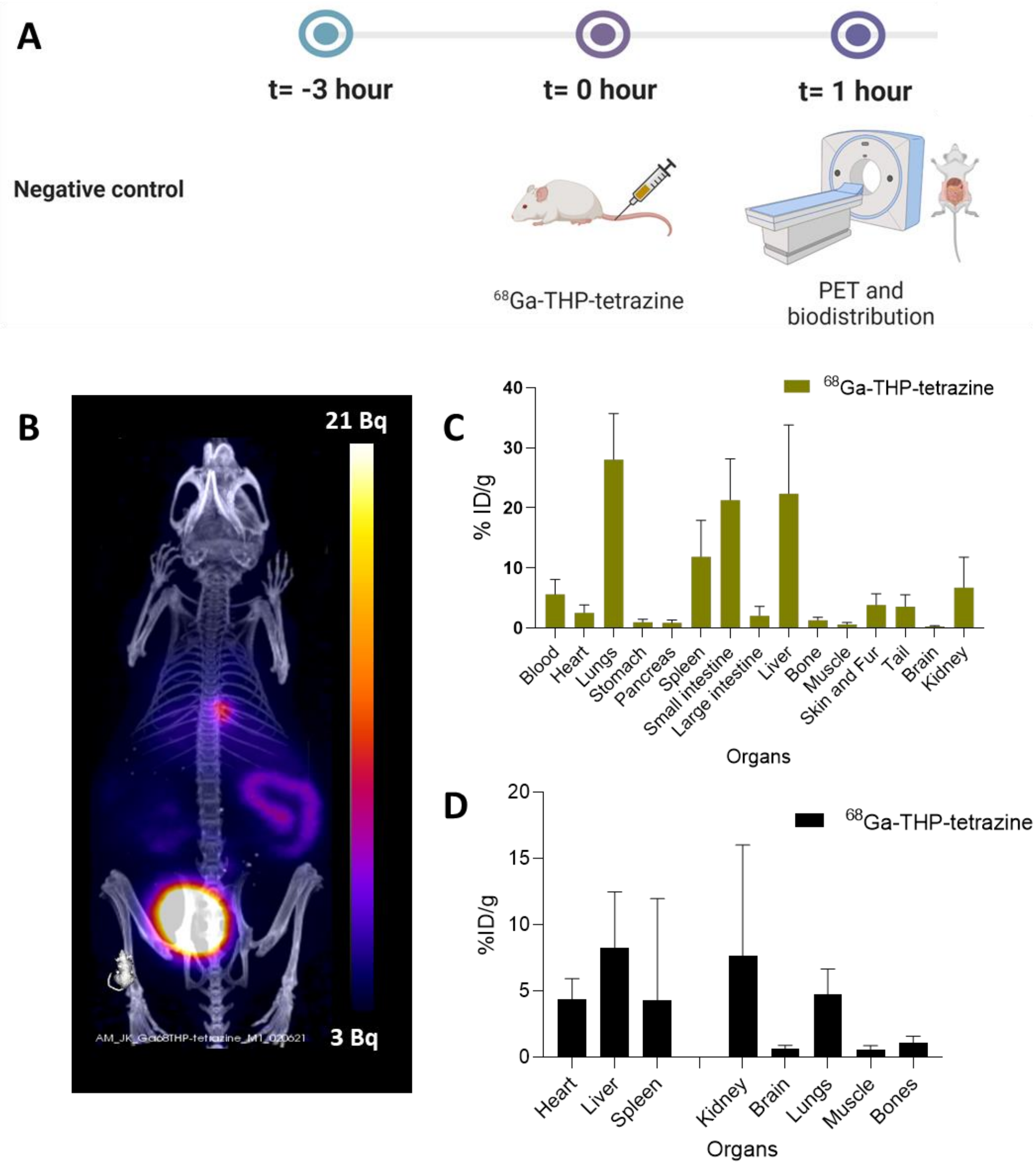

Figure 3.19. Negative control *in vivo* group (n=4): (A) Schematic of the negative control group (B) PET image of healthy animal administered with ^{68}Ga-THP-tetrazine at 1 h p.i.; (C) Biodistribution at 2 h p.i. after the PET scan; (D) Image quantification performed on the PET images acquired at 1 h p.i.

The positive control group involved administration of ^{67}Ga-TCO-PL-liposomes followed by imaging at two time points at t = 1 h and t = 24 h followed by biodistribution at t = 25 h. Figure 3.20(A) shows PEGylated liposomes circulating in the blood pool especially carotid arteries, heart, and perfused organs like liver and spleen at 4 h p.i. At the next imaging point at 27 h post injection of the liposomes, an increased uptake was observed in the liver and spleen and decreased circulation of liposomes in the blood due to clearance by liver/spleen macrophages. This slow and steady accumulation in the spleen and liver is typical of Doxebo *i.e.*, PEGylated liposomal nanomedicine which inhibits recognition by the reticuloendothelial system (RES). The biodistribution and image quantification data confirmed the observations from the SPECT images showing liposomal uptake in blood pool, liver, and spleen with decreasing blood concentration of liposomes with increasing time.

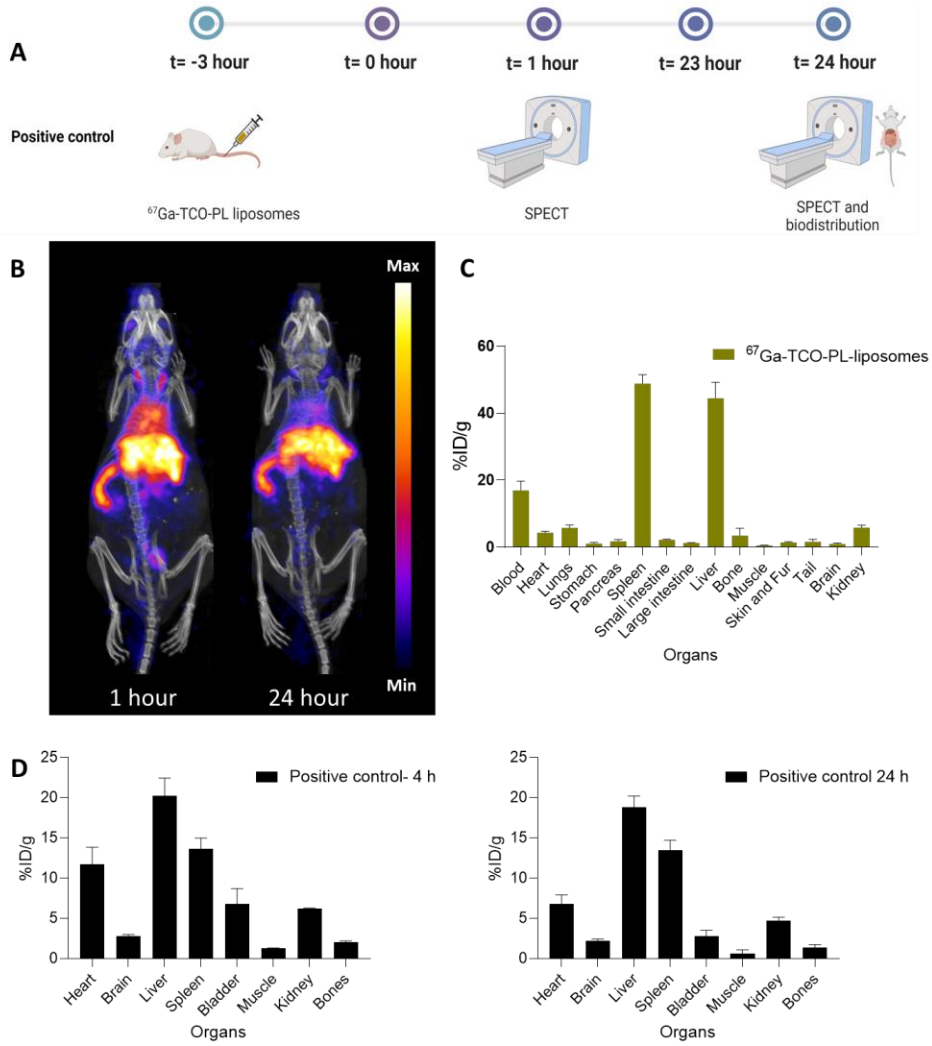

Figure 3.20. Positive control *in vivo* group (n=4): (A) Schematic of the positive control group; (B) SPECT image of healthy animal administered with ^{67}Ga-TCO-PL-liposomes at t = 1 h and t = 24 h; (C) Biodistribution at 28 h p.i. (t = 25 h) after the SPECT scan; (D) Image quantification performed on the SPECT images acquired at both time points

The pretargeting test group was designed to image the TCO-PL-liposomes at two time points: t = 1 h and t = 24 h post injection (Figure 3.21). At t = 1 h, the PET image showed the radioactivity uptake in urinary bladder, gall bladder, intestine, liver and spleen. The high urinary bladder, gall bladder and intestine accumulation observed is representative of the observed biodistribution of ^{68}Ga-THP-tetrazine (negative control) showing the clearance of the unreacted ^{68}Ga-THP-tetrazine. The positive control showed high activity from the blood pool at 4 h p.i. at 12 ± 2 % ID/g , as expected for long-circulating liposomes. However, in this was absent in pretargeting group results showing blood uptake value at earlier time point was 3.9 ± 0.7 % ID/g, suggesting that blood-circulating liposomes were not labelled. The uptake observed in the liver and spleen is higher compared to the negative control showing validation of biorthogonal pretargeting and ability to image the TCO-PL-liposomes in the liver and spleen. The image quantification further supported this observation showing higher accumulation in liver and spleen compared to image quantification from the negative control images but lower than the positive control. At t = 24 h, the PET images showed major accumulation in the urinary bladder, liver and spleen with minor uptake also in lungs and intestines. The uptake observed in lungs, bladder and intestines is expected due to the unreacted ^{68}Ga-THP-tetrazine. However, the high uptake in the liver and spleen shows biorthogonal pretargeted radiolabelling of the TCO-PL-liposomes at 24 h. These observations were also confirmed by the biodistribution and image quantification data. However, the liver and spleen uptake values observed for positive control (spleen: 48.8 ± 2.6 % ID/g and liver: 44.4 ± 4.7 % ID/g) were higher than uptake values in the pretargeting test group (spleen: 32.8 ± 16.3 % ID/g and liver: 31.3±21.5 % ID/g). Also, the observed uptake values for liver, spleen and lungs are highly variable which can be possibly explained by the lipophilic nature and colloidal impurities present in the ^{68}Ga-THP-tetrazine.

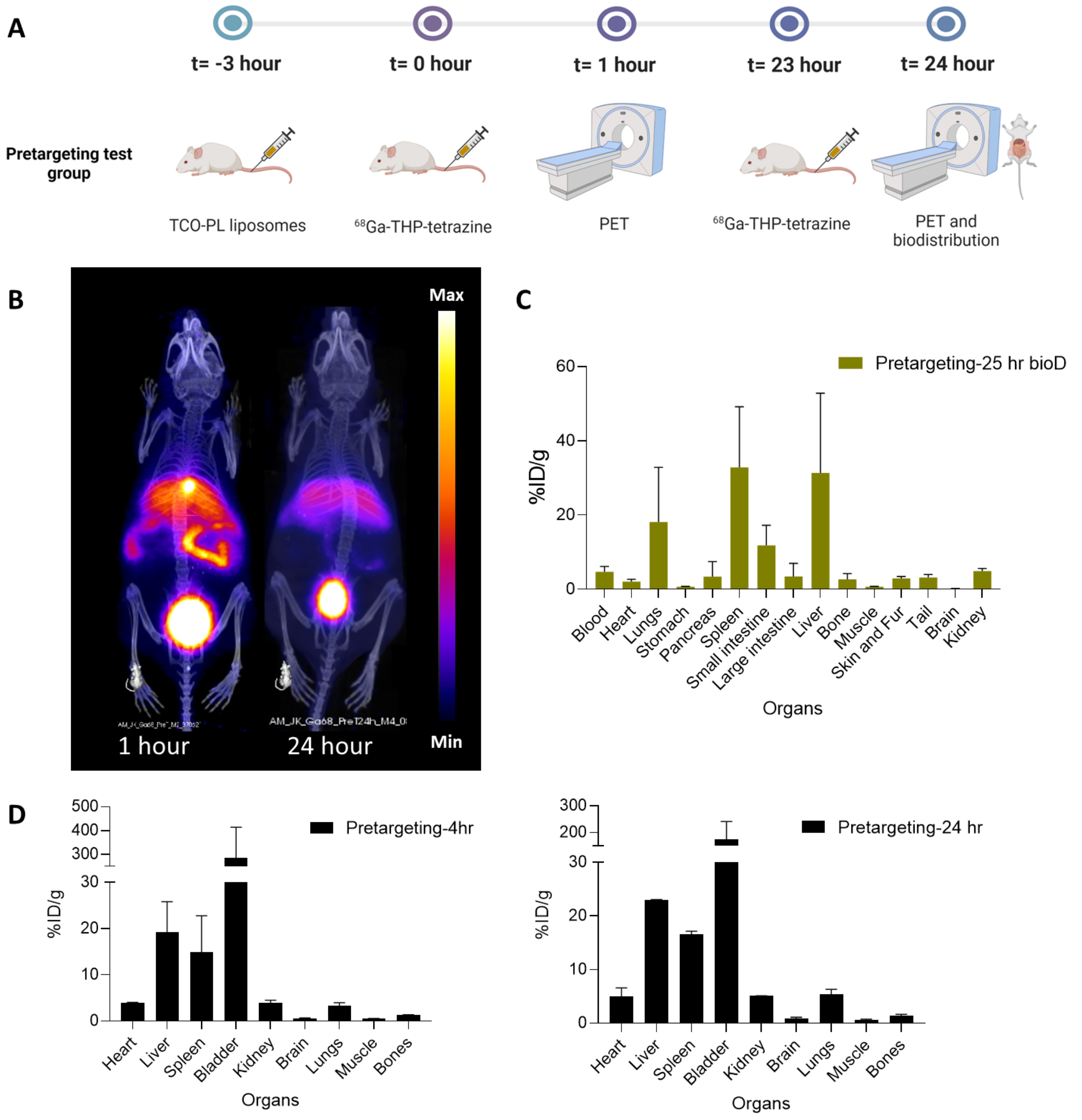

Figure 3.21. Pretargeting test *in vivo* group(n=4): (A) Schematic of pretargeting test group (B) PET image of animal administered with TCO-PL-liposomes followed by administration of ^{68}Ga-THP-tetrazine at t = 0 h and PET scan at t = 1 h, and at t = 23h and PET scan at t = 24 h; (C) Biodistribution at t = 25 h after the PET scan; (D) Image quantification performed on the PET images acquired at both time points

3.2.6 *In vivo* evaluation of pretargeting of TCO-PL liposomes in a syngeneic mouse cancer model

Further *in vivo* validation of pretargeted imaging was performed in tumour mice. The pretargeting experiments performed in healthy animals showed partial success as the non-specific uptake of ^{68}Ga-THP-tetrazine in the liver and spleen complicates the analysis of pretargeting test group. The validation of pretargeting in a tumour model provides an option to better evaluate the success of pretargeting reaction at the site of tumour uptake of PEGylated liposomes in addition to other organs such as liver and spleen. The tumour is expected to have minimal uptake and retention of the small molecule radiotracer ^{68}Ga-THP-tetrazine and therefore any uptake observed in the tumours in the test group should be observed due to pretargeting of liposomes. The immunocompetent mice bearing subcutaneous fibrosarcoma tumours were chosen due to their characteristic well-perfused tumours exhibiting high levels EPR effect, as well as a complete immune system. The tumour growth was variable depending on the different inoculation batch of WEHI-164 cells with less variability within the batch and sensitive to small changes in concentration and inoculation technique. The animals were kept under constant observation post inoculation and animals reached the desired tumour size between 7-13 days post-inoculation. The desired tumour size was between 70 mm^3 and 100 mm^3 to allow for well perfused and vascularised tumours. The tumour growth trends can be seen in figure 3.22(A). However, in general, the tumour growth was aggressive with mice developing crust over the tumours in 10% of total inoculated mice. The animals were chosen for imaging studies as soon as the total volume of the tumours was above 70 mm^3. The pretargeting experimental study groups were as seen in figure 22(B).

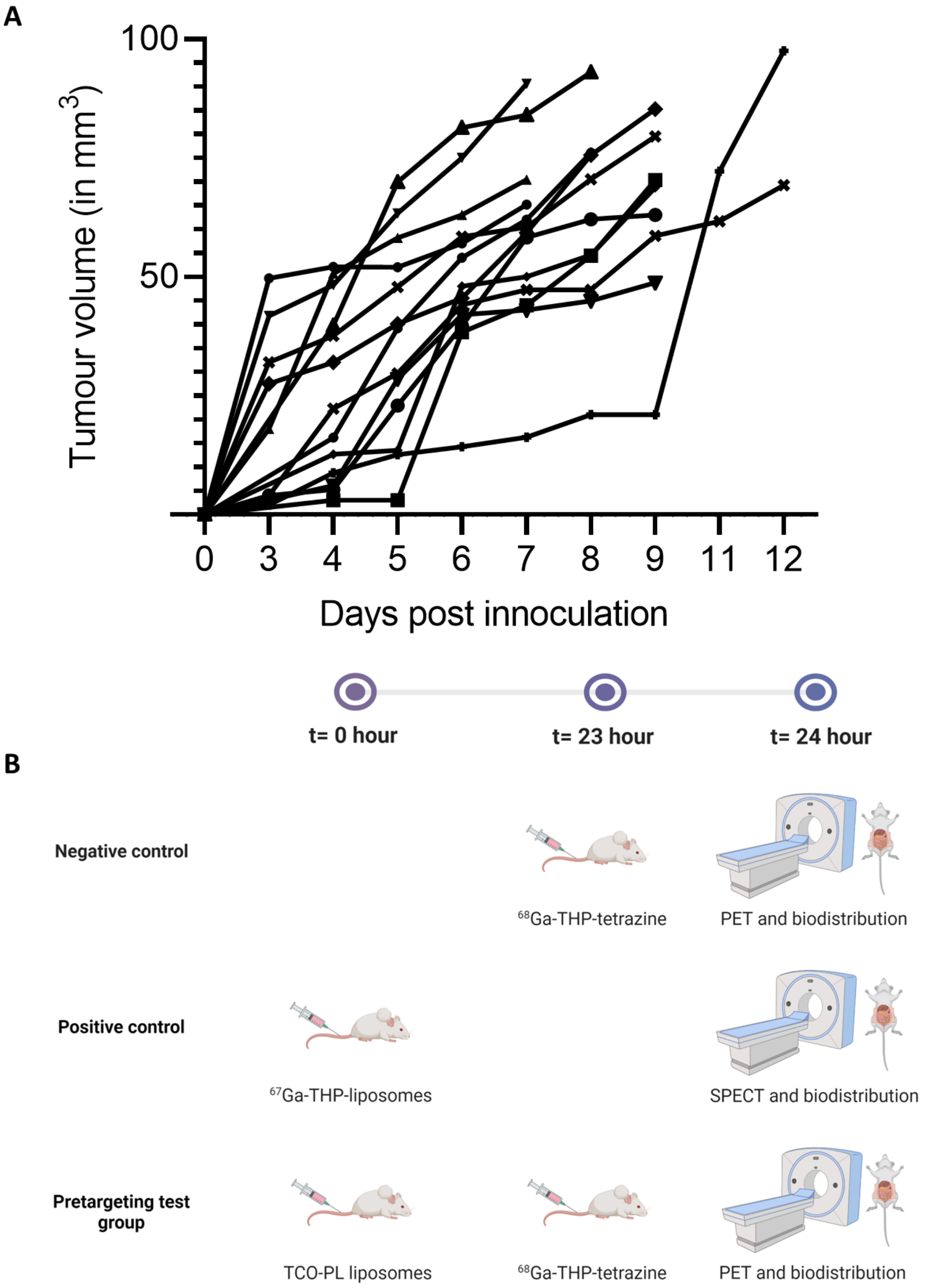

Figure 3.22. Biorthogonal *in vivo* pretargeting experiments in fibrosarcoma tumour model: (A) shows tumour growth curve for the different animals against the number of days post inoculation with WEHI-164 cells. The tumour growth is plotted as tumour volume and calculated using the formula V= 0.5*l*b*h; (B) Scheme of *in vivo* pretargeting PET experiments: Negative control: administration of ^{68}Ga-THP-tetrazine; pretargeting test group: administration of TCO-PL-liposomes followed ^{68}Ga-THP-tetrazine; Positive control group: administration of ^{67}Ga-TCO-PL-liposomes. Created with BioRender.com.

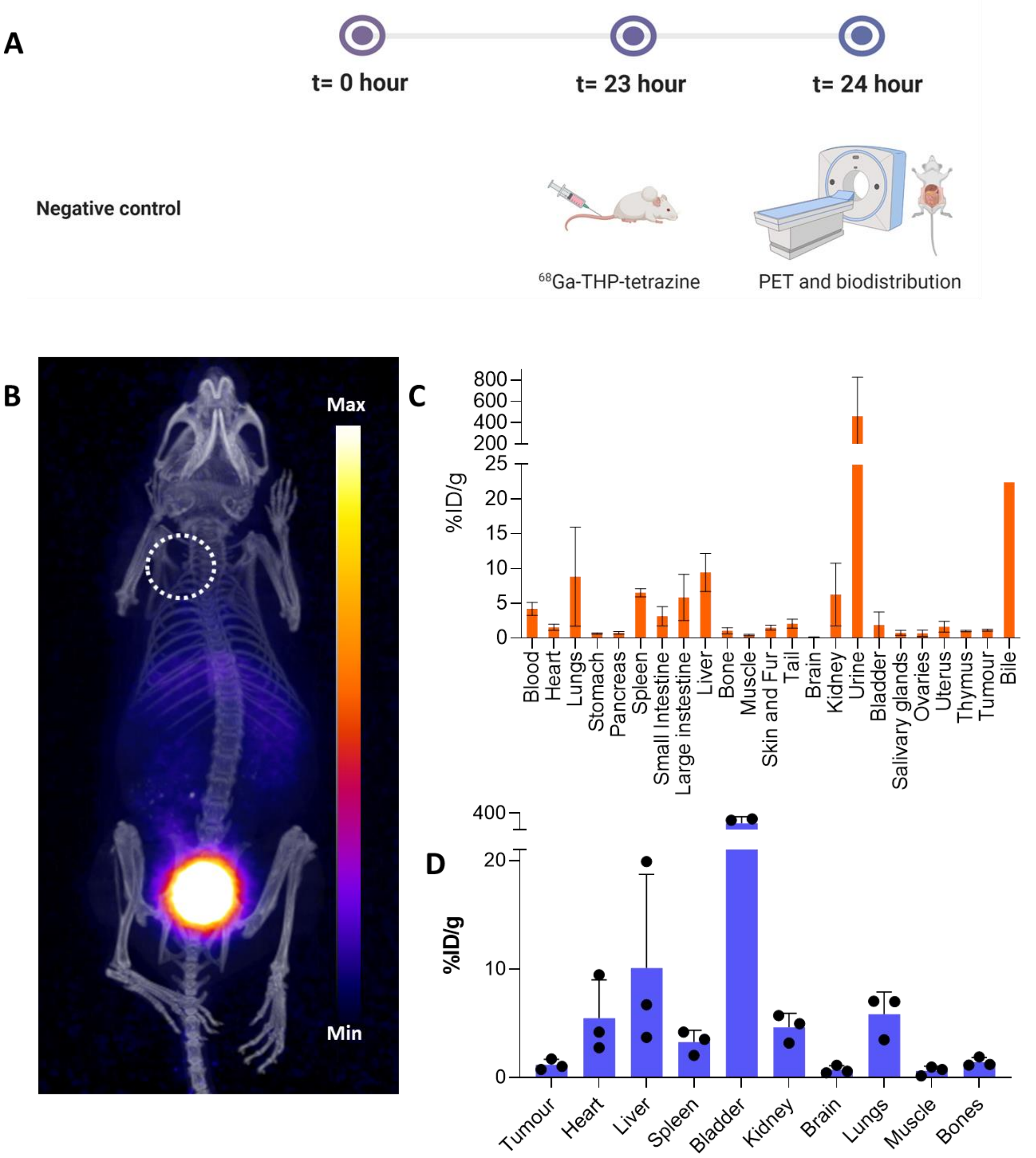

Figure 3.23. Negative control *in vivo* group for tumoured animals (n=4): (A) Schematic of the negative control group; (B) PET image of mice administered with ^{68}Ga-THP-tetrazine at 1 h p.i. (dotted circle shows the tumour region); (C) Biodistribution at 2 h p.i. after the PET scan; (D) Image quantification performed on the PET images acquired at 1 h p.i.

The negative control group involved administration of ^{68}Ga-THP-tetrazine and imaging at t = 1 h with biodistribution performed post imaging. The PET image (Figure 3.23(A)) showed high uptake in the urinary bladder and the gall bladder as expected due to renal and hepatobiliary clearance. There was no observed tumour uptake in the PET image and the biodistribution analysis showed the tumour uptake was minimal at 1.1 ± 0.1 % ID/g. (Figure 3.23)

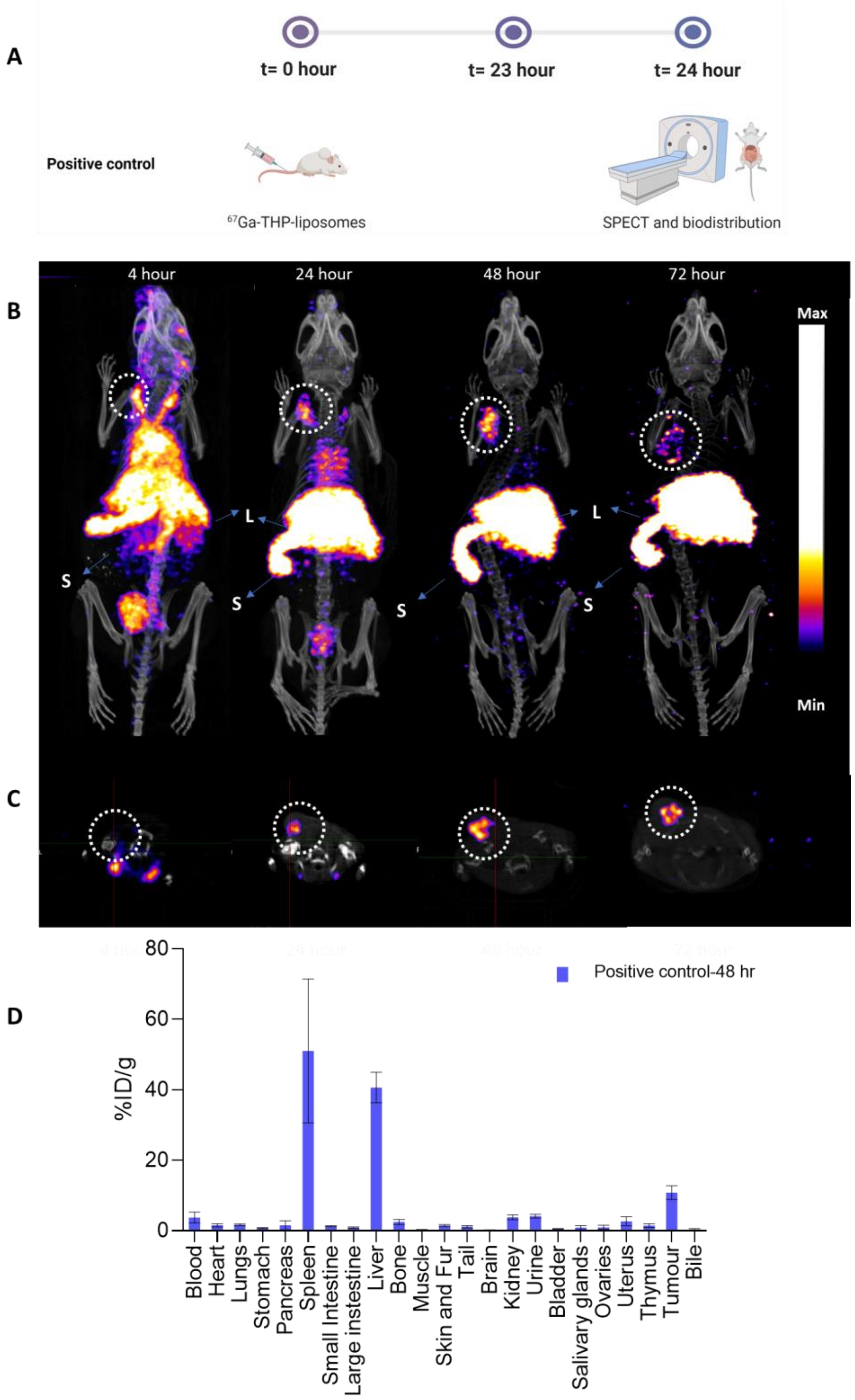

Figure 3.24. Positive control *in vivo* group for tumoured animals(n=4): (A) Schematic of the positive control group; (B) SPECT image of animal administered with ^{67}Ga-TCO-PL-liposomes at 4 h p.i.(t = 1 h), 27 h p.i.(t = 24 h), 51 h p.i.(t = 48 h), 75 h p.i.(t = 72 h)(S-spleen, L-liver, dotted circle-tumour); (C) Transverse section of SPECT images showing tumour cross-section at different time points, tumour highlight within dotted circular lines (D) Biodistribution at 52 h p.i. (t = 49 h) after the SPECT scan.

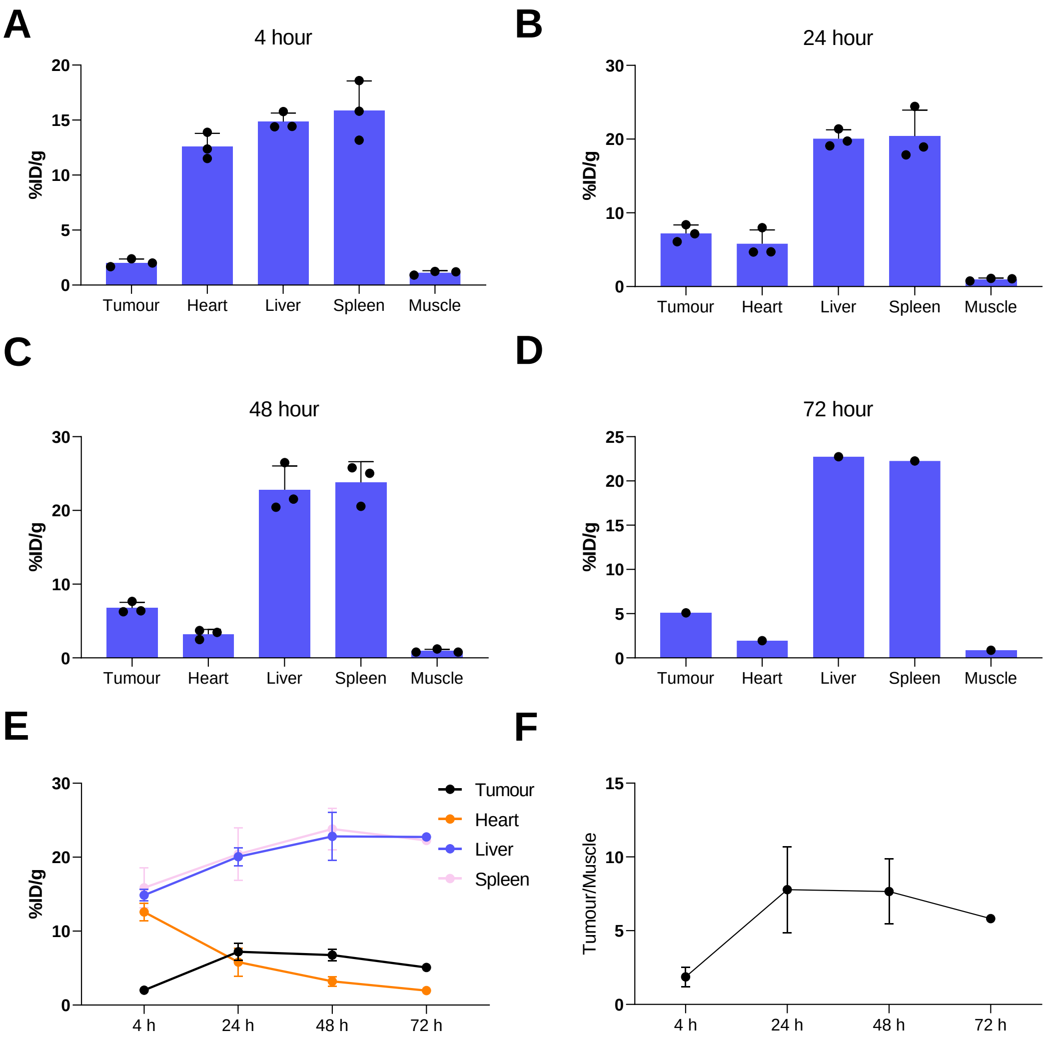

Figure 3.25 Image analysis of the positive control group SPECT images recorded at different time points: Tissue accumulation of radiolabelled liposomes ^{67}Ga-TCO-PL-liposomes in tumour, heart, liver, spleen and muscle at different time points (A) 4h, (B) 24 h, (C) 48 h, (D) 72 h; (E) Variation of observed uptake of liposomes in different organs with time; (F) Variation of T/M contrast over different time points of scanning.

The positive control involved administration of ^{67}Ga-TCO-PL-liposomes followed by imaging at t = 4 h (n=4), t = 24 h (n=4), t = 48 h (n=4) and t = 72 h (n=1), and biodistribution post imaging at t = 48 h (n=3) and t = 72 h (n=1). The multiple time points were chosen for imaging to determine the pharmacokinetics of ^{67}Ga-TCO-PL-liposomes and accumulation of the liposomes at the tumour site over time. In figure 3.24(A, B), the SPECT images at different time points showing increasing accumulation of ^{67}Ga-TCO-PL-liposomes in the liver, spleen and tumour over time until t = 48 h followed by decrease in tumour retention post 48 hours. The uptake was also observed in the urinary bladder at t = 4 h time point due to clearance of small proportion of injected dose of liposomes and no uptake was observed in the tumour at this earlier time point due to long circulating nature of PEGylated liposomes. Image quantification of the SPECT images was performed using Vivoquant confirmed the observations from the SPECT images (figure 3.25).

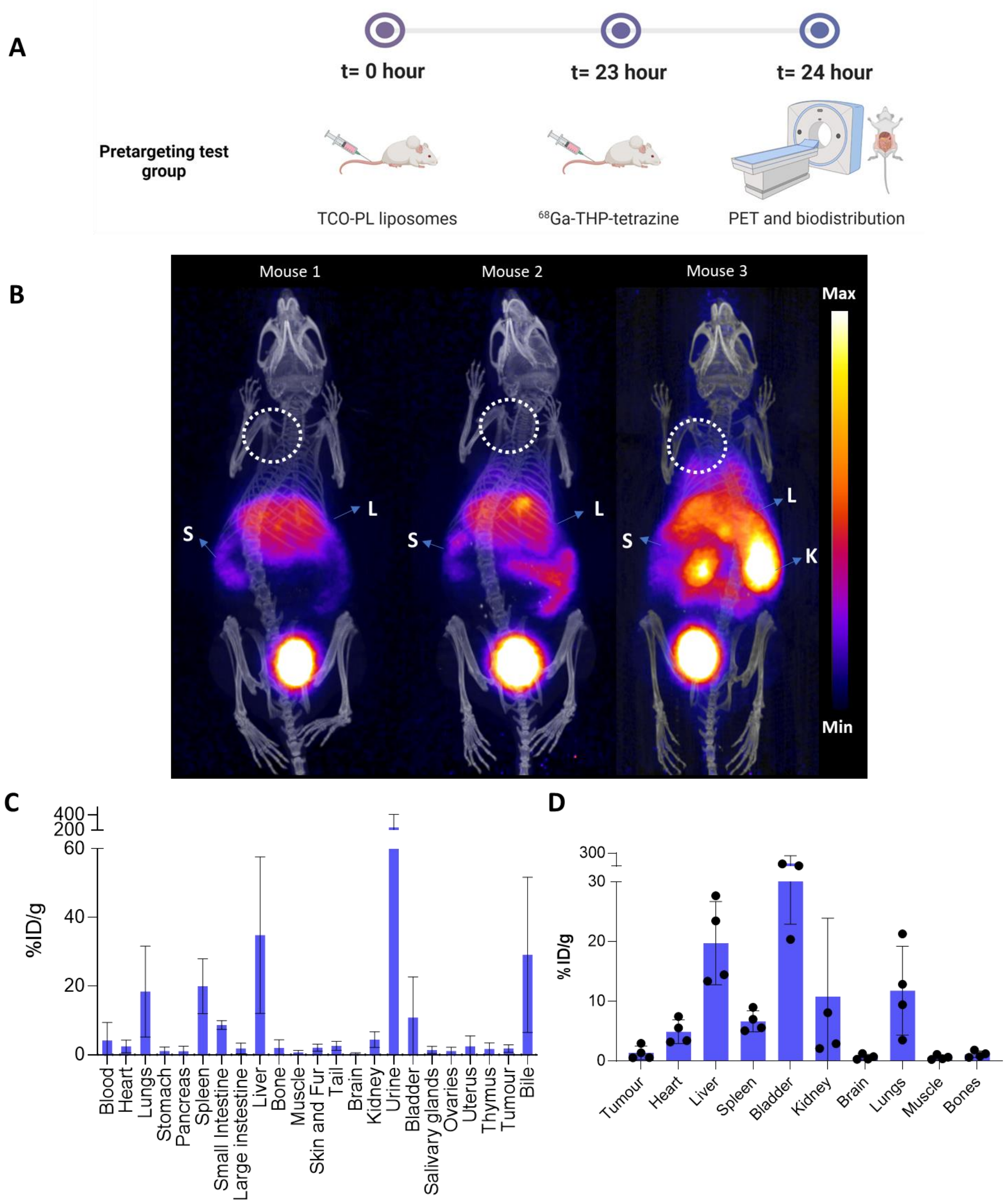

Figure 3.26. Pretargeting test *in vivo* group for tumoured animals(n=4): (A) Schematic of the pretargeting test group; (B) PET image of animal administered with TCO-PL-liposomes followed by administration of ^{68}Ga-THP-tetrazine at t = 23h and PET scan at t = 24 h; (C) Biodistribution at t = 25 h after the PET scan; (D) Image quantification performed on the PET images acquired.

The pretargeting test group was designed to track TCO-PL-liposomes in tumour, liver and spleen with a short-lived isotope which is desirable for tracking of long circulating nanomedicines and antibodies while minimising the radiation dose and non-specific binding. The pretargeting was only performed at one time point t = 24 h (n=5) to minimize the saturation of TCO sites on the liposomes. The PET images in figure 3.26(A) showed high uptake in the liver and spleen as expected due to successful pretargeting in these organs as observed earlier in healthy animals. The uptake in the liver and spleen was higher compared to the negative control group ($p>0.05$, figure 3.27 (A)) and comparable to the positive control group. The uptake was also observed in gall bladder, intestine and kidney which is representative of the observed biodistribution of ^{68}Ga-THP-tetrazine. However, there was no visible accumulation in tumours as seen in the PET image, and the biodistribution post imaging showed tumour uptake of 1.8 ± 1.1 %ID/g which is much lower compared to the positive control group (10.83 ± 2 %ID/g) showing the pretargeting reaction has not materialised at the site of tumours. Compared to the uptake in tumours in the negative control, the tumour uptake in pretargeting group is higher but the difference between them is non-significant (figure 3.27(B)). This observation of low pretargeting in the tumours can be attributed to multiple factors including the internalisation of the TCO-PL-liposomes making them unavailable for binding, slow kinetics of the biorthogonal reaction due to low TCO/tetrazine relative concentration, low tumour perfusion of ^{68}Ga-THP-tetrazine or the isomerisation of the transcycloctene *in vivo* leading to the loss of reactivity towards tetrazine.

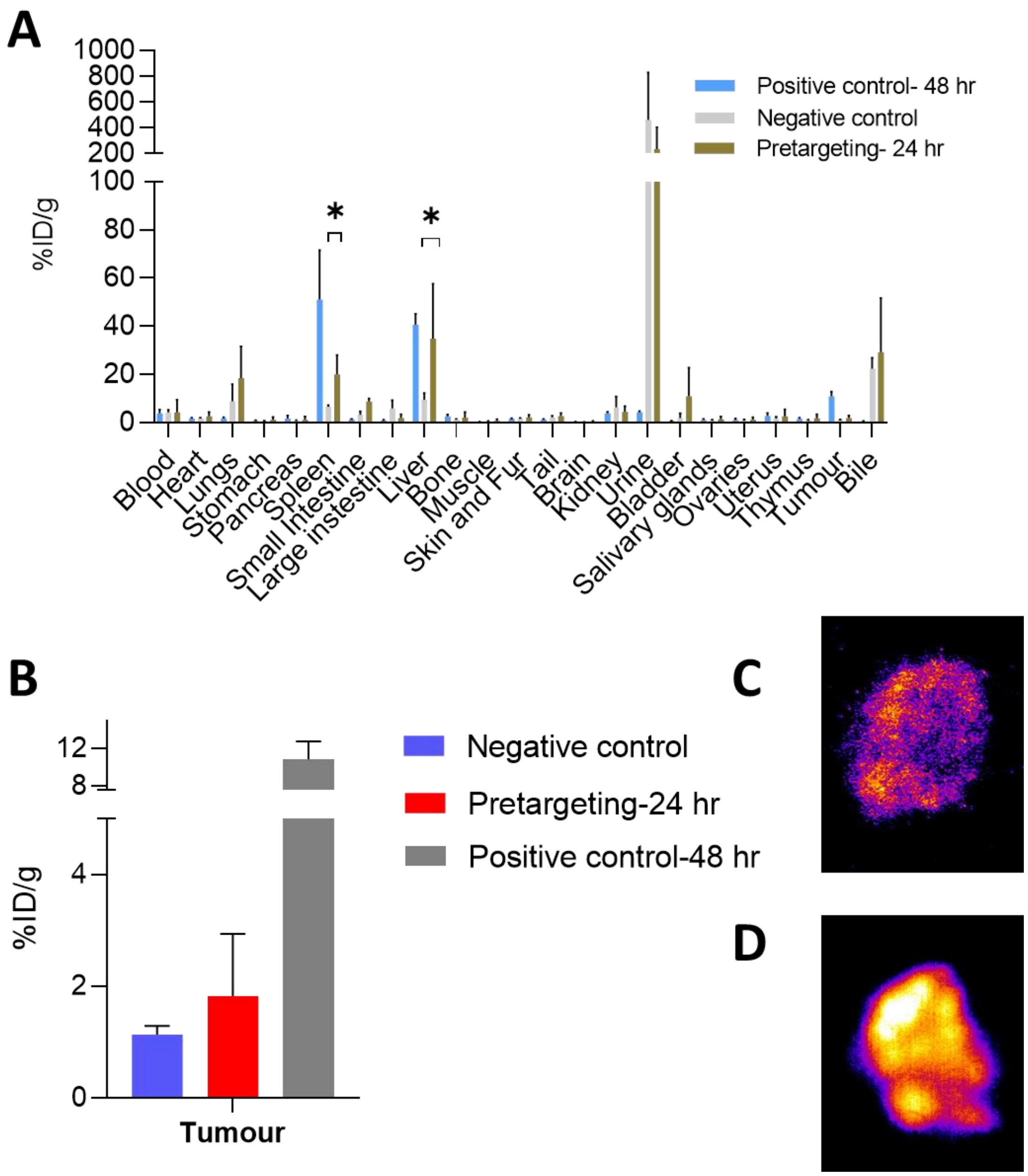

Figure 3.27. Comparative analysis among different groups of the pretargeting tumour study: (A) Comparison of the biodistribution of the different experimental groups. The uptake observed in the liver and spleen for the pretargeting test groups is higher compared to negative control group ($p<0.05$); (B) Comparison of the tumour uptake values observed for negative control and the pretargeting test group. Differences observed in tumour uptake values for the groups was non-significant; (C) Autoradiography of tumour obtained from pretargeting test group showing accumulation of radioactivity was observed on the margins and not spread all over the tumour; (D) Autoradiography of tumour obtained from the positive control group showing the accumulation of radioactivity all over the tissue.

The tumours collected during biodistribution of the pretargeting, and positive control group were fixed in OCT embedding fluid and autoradiography was performed on tumour slices as seen in figure 3.27(C, D). The autoradiography of the tumour slices from pretargeting group (figure 3.27(C)) showed radioactivity accumulation on the margins of the tumour thereby hinting that the TCO-PL-liposomes available on the surface of the tumour are only sites available for binding. The autoradiography of tumour slices from the positive control group showed well perfused radioactivity throughout the tumour showing the ^{67}Ga-TCO-PL-liposomes are well distributed throughout the tumour. This suggests that tumours should be also accessible to THP-Tz, allowing the click reaction to take place, but this reaction could be limited due to internalisation of liposomes within cells or macrophages. This requires further exploration of the fate of the liposomes as soon as they are localised at the site of tumour.

The development of a successful pretargeted system relies heavily on the radiotracer elimination properties. The radiotracer elimination through renal clearance pathway is favoured over the hepatobiliary excretion to minimise background radioactivity due to long residence time of radiotracer in the gut. The high uptake levels in the intestines, gall bladder, and liver complicate the delineation of nearby organs. The addition of a PEG linker could be a strategy to modify the pharmacokinetic profile of the radiotracer based on tetrazine.[362] The various studies utilised for pretargeting of antibodies as well as nanoconstructs shows impact of different tetrazines used on multiple factors contributing to their pharmacokinetics in the body and elimination pathway.[347,351,352,354,355,359] Our THP-tetrazine does show clearance through renal and hepatobiliary excretion but allows for delineation of spleen, liver and tumours but could be further improved by decreasing the lipophilicity by, for example, using a PEG linker. The decreased lipophilicity might also alleviate the issue found with THP-tetrazine attaching to the vials and forming a lipophilic impurity on radiolabelling, thereby allowing us to avoid an extra purification step as well as allow high amounts of tetrazine being administered *in vivo*. The relative higher concentration of tetrazine compared to TCO will allow for higher reaction rates *in vivo* and improving our pretargeting rates.

Other important aspect to note here is the effect of the chemical structure modification of tetrazine based tracers on their reactivity towards TCO. The study by Steen *et al.* showed that the presence of different EWG and EDG has a major impact on the reactivity of tetrazine towards TCO.[347] We chose the methyl tetrazine variant due to it being stable in aqueous buffer, but this might have caused a decrease in the reactivity towards TCO which could be a possible reason for the low pretargeting observed at the tumour. In future experiments, one could aim to examine a library of different tetrazine-THP compounds and their impact on the pretargeting observed.

The concentration of TCO loaded on the targeting agent is also an important factor contributing to the success of pretargeting experiments. There is an observed correlation between the increased pretargeting and TCO concentrating loading on targeting agents. This post formulation insertion method is expected to provide high drug, radioisotope and phospholipid loading to the liposomes. However, it was not possible to determine the concentration of TCO experimentally, but the theoretical calculations showed approx. 1000 TCO molecules/liposome. Further optimisation of the loading procedure to provide high TCO loading and development of methods to experimentally determine the number of TCO molecules present on the liposomes surface is required.

3.3 Conclusion

In conclusion, here, we have developed a new $^{68/67}$Ga-labelled tetrazine (THP-tetrazine) for radiopharmaceutical biorthogonal chemistry. In addition, we have also developed a TCO-phospholipid (TCO-PL) conjugate for reaction with THP-Tz which was successfully incorporated into the bilayer of the PEGylated liposomes to provide TCO-PL-liposomes. These two components: $^{68/67}$Ga-THP-tetrazine and TCO-PL-liposomes, provided a method for conventional and pretargeting imaging of PEGylated liposomes *in vivo* and *in vitro* with minimal impact on liposomal properties. The pretargeted nuclear imaging was performed in both healthy and fibrosarcoma tumour animals. The pretargeting of PEGylated liposomes was observed in healthy animals in the liver and spleen. The pretargeting in tumour animals was observed in the liver and spleen, but limited pretargeting was observed in the tumours which was our target of interest. In the future, further exploration into the optimisation of this TCO/tetrazine pretargeting system may provide higher levels of pretargeting of liposomes accumulated in the tumours.

4 RASP FOCUSED ULTRASOUND MEDIATED DELIVERY OF LIPOSOMAL NANOMEDICINES TO THE BRAIN

Note: This work was performed in collaboration with Dr Sophie Morse. Sophie and I have equally contributed to this work. Parts of this work have been published in a peer-reviewed research article in the Journal of Controlled Release (jointly first authored by Sophie and me) and PhD thesis submitted by Sophie to Imperial College London.

4.1 Introduction: Nanomedicines delivery to the brain

4.1.1 Drug delivery to the brain

The development of therapeutics for targeting areas of the brain suffers from failures due to the blood-brain barrier (BBB).[363] This has led to several CNS pathological conditions remaining untreatable while neurological disorders account for immense healthcare and life cost. The therapeutic molecules unable to cross the BBB include small molecule drugs as well as big macromolecules like nanomedicines. According to estimates and a recent literature survey, 98% of small molecules developed and all the larger therapeutic molecules are prevented from crossing the blood-brain barrier thereby making them suboptimal for treatment of ailments of the central nervous system.[363] The major issues associated with brain drug delivery alongside the inability to cross the BBB include non-spatial targeting, non-target specific toxicity, and low to no delivery.[364] Moreover, most drugs that make it through the BBB also suffer from metabolic degradation.[365]

Encapsulating small molecule therapeutics using liposome-based approaches (Table 1, Chapter 1) hold great potential for applications in brain drug delivery. The ability to carry hydrophilic and hydrophobic drugs at high concentrations, surface modifications to add targeting vectors, targeted drug release at the site of action and high blood circulation half-life (PEGylated liposomes) make them exciting candidates for drug delivery to the brain. The optimization of the ideal liposomes for drug delivery to the brain and across the BBB has important implications for the treatment of diseases of the CNS. Different attempts have been made to develop liposomal formulations for enhancing drug delivery across the BBB.[366] The current formulation and surface modification strategies for using liposomes as brain vectors are cationization of liposomes, active targeting of liposomes, stimuli-responsive liposomes, and multifunctional liposomes.[367–375]

As mentioned in Chapter 1, positively charged liposomes have been developed and utilised as carriers for the delivery of genetic material and therapeutics.[376,377] The positively charged cationic liposomes enhance nanoparticle uptake in the brain via adsorptive mediated endocytosis due to electrostatic interactions between the positive charged liposomal surface and negatively charged cell membrane.[45,374] But the cationic liposomes have associated drawbacks as mentioned in Chapter 1: non-specific uptake in peripheral tissues, serum protein binding and cytotoxicity. The other formulation strategies mentioned above have shown subtherapeutic dose delivery in preclinical models only and achieving therapeutically relevant concentrations of these drugs in the brain remains challenging.[364,366,378] Thus, there is a still need to develop strategies to deliver liposomal nanomedicines in sufficient concentrations across the blood-brain barrier. These strategies might include surface modifications, novel delivery routes and blood-brain barrier disruption. However, for developing these strategies, it is important to understand the blood-brain barrier and possible mechanisms of entry into the brain which are discussed in the next section.

4.1.2 Transport across the blood-brain barrier (BBB)

4.1.2.1 Blood-brain barrier (BBB)

The BBB is a specialised diffusion barrier of the brain to maintain brain homeostasis and protect it from foreign particles in the bloodstream. The BBB differs from a normal capillary, starting from the level of endothelial cells and the surrounding layers. This feature helps facilitate numerous functions like ion regulation[379], neurotransmitter regulation[380] and prevents entry of neurotoxins and macromolecules[380,381] into the CNS. The BBB is formed of an endothelial cell layer with tight junctions, layered with a basal membrane, pericytes and astrocytes to yield tightly packed capillaries as seen in figure 4.1. This tightly packed barrier poses a big issue to drug transport to the brain due to highly selective diffusion properties. The handful ways in which a molecule can cross the

BBB is as shown in figure 1.[382] The main transport mechanisms include passive diffusion (lipid-soluble non-polar molecules), ABC transporters (non-polar molecules and conjugates), endocytosis *via* carriers (histone, avidin, lipoproteins, transferrin, etc.), solute carriers (glucose and amino acids) and paracellular migration through tight junctions (mononuclear cells like leukocytes).

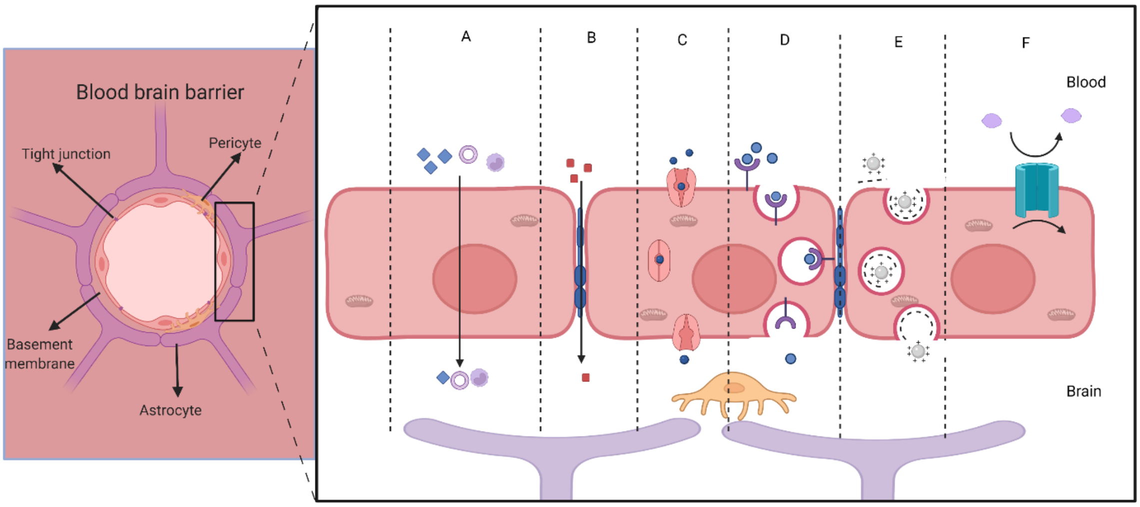

Figure 4.1. Blood-brain barrier: Different components of the BBB vasculature including pericytes, astrocytes, basement membrane, tight junctions (left); Different mechanisms of transport of molecules across the blood-brain barrier: (A) Transcellular lipophilic pathway (lipid-soluble agents); (B) Paracellular aqueous pathway (water-soluble agents); (C) Transport proteins (Glucose, amino acids, nucleosides); (D) Receptor-mediated transcytosis (Insulin, transferrin); (E) Adsorptive transcytosis (Albumin, plasma proteins); (F) Efflux pumps (PgP mediated)(right). Created with BioRender.com.

The BBB serves an important role in limiting the entry of macromolecules, neurotoxins and infectious agents, but this property also limits entry to therapeutic molecules to reach their targets inside the brain. There have been various invasive or non-invasive techniques developed to deliver drugs to the brain with varying levels of success.[382] Techniques include permanent or temporary modification of the BBB to allow the entry of particles into the brain. The delivery can be also increased by utilizing targeting molecules or drug carriers which allow the passage of therapeutic molecules to the brain using different mechanisms utilised for the passage of macromolecules to the brain. Various techniques to circumvent the issue of the blood-brain barrier have been developed including BBB disruption, and modification of therapeutic surface to target transfer mechanisms.[383] However, for larger therapeutic molecules like nanomedicines, the best pathway seems to be BBB disruption and surface modification. In the next section, we will explore the possible ways to disrupt the blood-brain barrier and their potential pros and cons in safe drug delivery to the brain.

4.1.2.2 Disruption of the blood-brain barrier

The three main BBB disruption strategies which have been developed in the last few decades are as follows:

4.1.2.2.1 Osmotic disruption:

The hyperosmotic pressure applied to endothelial cells can cause cells to shrink due to water being drawn out of cells into the lumen of the blood vessel.[384] The vasodilation thus caused leads stretching of the endothelial cell membrane. Conversely, a calcium-dependent mechanism leads to the contraction of the endothelial cell membrane. The above mechanism facilitates the opening of tight junctions allowing paracellular transport to the CNS.[385] The osmotic agents applied to the vasculature include mainly mannitol[386], arabinose[387] and urea.[388] The osmotic disruption has been used for the delivery of particles ranging from nanoparticles, antibodies, stem cells and recombinant proteins. Despite the successful disruption of the blood-brain barrier, this strategy suffers from critical limitations. These include cerebral edema[389], nonspecific disruption throughout causing neurotoxicity, seizures, and neurological defects.[390]

4.1.2.2.2 Chemical disruption:

A calcium-mediated mechanism opens up the tight junctions via activation of bradykinin B2 receptors on the application of bradykinin-analogue RMP-7, Cereport.[391,392] However, the strategy was abandoned post phase II and phase III due to poor effectiveness in the delivery of drugs, specifically carboplatin.

A lipophilic small molecule, Borneol on oral administration in mice is known to transiently open the BBB 20 min after application followed by recovery of the permeability of the BBB after 60 min. This opening is expected to be due to increased expression of ICAM (Intracellular adhesion molecule). This has been used for the treatment of brain diseases in animal models involving co-delivery of drug and borneol in some instances.[393–395] However, similar to cereport, it is highly unlikely that co-administration of a permeability enhancer and drug molecule is enough to achieve the drug delivery to brain in humans because of the transient and non-uniform nature of the opening.

4.1.2.2.3 Physical disruption:

Convection-enhanced delivery (CED), a localised drug delivery strategy that allows the opening of blood-brain barrier (BBB) and enhances drug distribution by generating a pressure gradient at the tip of an infusion catheter which creates a delivery system of therapeutics through the interstitial spaces of the brain.[396–398] Thus, CED represents a localised, invasive method for the treatment of the central nervous system. CED has been utilised for the delivery of various therapeutics, including chemotherapeutic agents, small molecule imaging agents, viral particles, proteins, and nanomedicines.[399–

[402] CED has also found applications in solid-tissue tumours to deliver drugs to the core.[403] However, CED has its limitations which include physical limitations and invasiveness.[404] The physical limitations are backflow, air bubbles, limited flow within brain tissue, heterogeneous distribution, oedema, and flow rate. Another key challenge is the ratio of infusion volume to distribution volume.[405]

A non-invasive and targeted approach to delivering therapeutic drugs to the brain involves using focused ultrasound and microbubbles.[406] With this technique, microbubbles consisting of a lipid or protein shell and a heavy gas core (diameter 1–10 µm) are injected into the bloodstream along with the therapeutic agents of interest. Pulses of ultrasound are then applied to the targeted brain region, driving the microbubbles to oscillate, which ultimately allows the delivery of drugs across the BBB and into the brain.[407,408] We will discuss the focussed ultrasound in the next section in detail.

4.1.3 Focussed ultrasound

Focussed ultrasound pulses in combination with bloodstream-injected microbubbles have shown to be capable of BBB disruption. This technique has been shown to increase the distribution of drugs in the brain by 50% in mice. The technique of focused ultrasound opens the blood-brain barrier by stimulating the microbubbles. The intravenously administered microbubbles (lipid shell with a gas core; size 1-10 um) are subjected to expansion and contraction due to pressure oscillations thereby delivering energy to vessels and opening them for entry of molecules. The long pulse ultrasound has been used to disrupt BBB most commonly until now in both animals and humans with great delivery of molecules across the BBB.[409,410] Through this transient opening of the BBB, small-molecule chemotherapeutic drugs[411], antibodies[407,408], gene delivery[412], and cells[413] have been delivered. The optimization of ultrasound parameters like the pressure (acoustic power density), repetition rate, durations, and number of sonications, and microbubble type, size and concentration, play an important role in achieving non-invasive and localised disruption of BBB and delivery of drugs.[414–419] However, recent research has shown limitations of the method which include non-uniform distribution of drugs in targeted areas[420,421], triggering neuronal damage, micro haemorrhage and red blood cell extravasation.[407,422] Moreover, like other disruptive techniques, the duration of BBB opening is an important parameter and long pulses of the ultrasound lead to the opening of barriers for up to 48 hours. This long duration can lead to the entry of macromolecules like albumin into the brain thereby generating a neurotoxic response. Recently developed RaSP (Rapid short pulse sequence) provides an answer to these limitations of the long pulse sequence. The next section discusses the RaSP ultrasound sequence, and its advantages over conventional FUS pulse sequences.

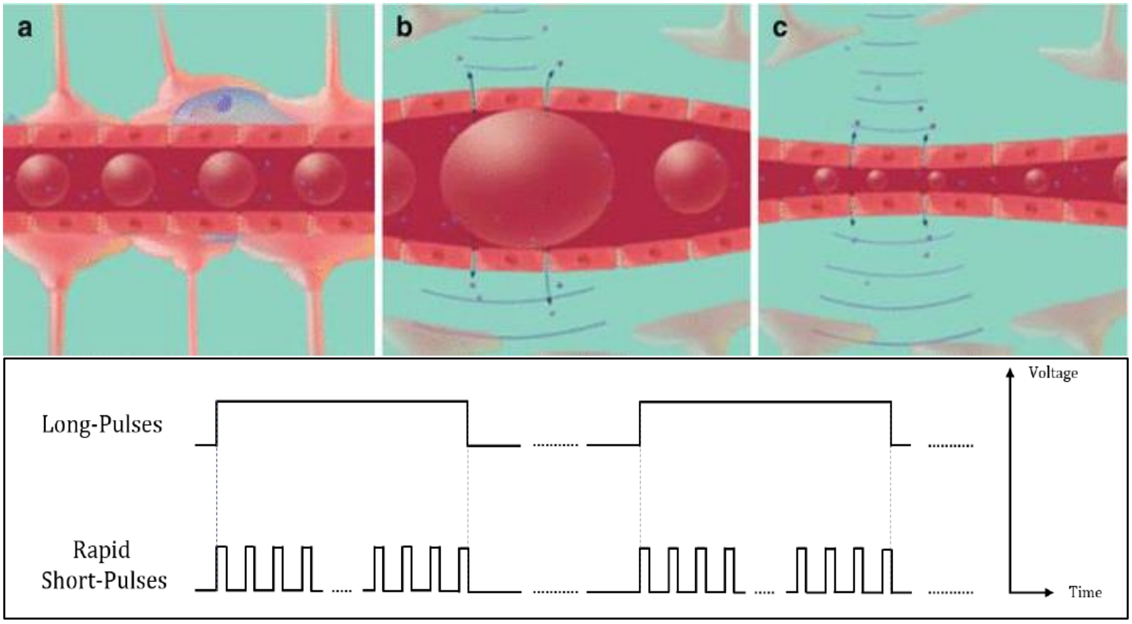

Figure 4.2. Focussed ultrasound and microbubbles: Top: Schematic of mechanism of blood brain barrier opening using focussed ultrasound and microbubbles: (a) Microbubbles (big sphere) and drug molecule (small sphere) injected into the bloodstream; (b & c) Blood brain barrier opening and releasing drugs due to contraction and expansion of microbubbles.[494] Bottom: Rapid short pulse overlayed and compared from conventional long pulse sequence.[424]

4.1.3.1 Rapid short pulse (RaSP) sequence for FUS-mediated BBB opening

RaSP sequence is different from the widely used long sequence as seen in Figure 4.2 in terms of the use of short microsecond pulses emitted at high pulse repetition frequencies instead of long pulses to increase the lifetime of microbubbles and their mobility within the vasculature. The rapid short-pulse (RaSP) sequence has been recently tested *in vitro* and *in vivo* and has been shown to overcome limitations from long pulses[423,424]. The increased pressure threshold due to reduced pulse length increases the lifetime of microbubbles[425]. The mobility is enhanced by reducing forces on each microbubble in the direction of pulse propagation and forces due to bubble-bubble interactions[426]. These modifications decrease the aggregation of microbubbles and enhance spatio-temporal distribution of cavitation in blood vessels thereby providing a uniform distribution of drugs and less damage to blood vessels[424]. The mechanism of opening the blood-brain barrier is not completely understood and is beyond the scope of this report.[427] Recently, RaSP has been used to safely and successfully deliver dextran (3 kDa) and Au nanoparticles (20-25 nm)[428]. In this chapter, we will test the ability of RaSP sequences to increase the vascular permeation of liposomes successfully and safely in the brain *in vivo* and compare it to conventionally used long-pulse sequences (Figure 5.2). The long pulse sequences have been previously explored to deliver liposomes to the brain but at the cost of tissue damage and red blood cell extravasation. In the next section, we will look at how focussed ultrasound can play a role in the delivery of liposomal nanomedicines to the brain in detail and review recent work done on this topic.

4.1.4 Liposome delivery with focussed ultrasound

The focussed ultrasound technique has been shown to deliver liposomes into the brain in several *in vivo* studies [411,429–442]. Different types of liposomes have been delivered, including ones loaded with doxorubicin [411,430,431,435,436,440], paclitaxel [432], genes [434,437,438], and those labelled with imaging agents like quantum dots [436], rhodamine [433,439], and gadolinium-based contrast agents together with rhodamine.[441] The size of the liposomes delivered with focused ultrasound and microbubbles ranges between 55 and 200 nm. Many of these reports have demonstrated delivery in healthy mice and rats [431,433,438–441], however, most of the liposomes loaded with drugs have been delivered in brain tumour models [411,429,430,432,434,436] and have shown improved outcomes. [430,443–445] Although it is worth noting that brain tumour models are known to have compromised BBB integrity allowing for delivery of drugs to the brain.[446]

Once delivered into the brain, fluorescently labelled liposomes have shown heterogenous spot-like patterns of delivery, similar to those of other large compounds delivered with focused ultrasound, such as 2,000 kDa (54.4 nm) dextran [447] and magnetic resonance contrast agents (1-65 nm). [448] This pattern was observed in brains where liposomes between 55-200 nm were delivered. [433,439,441,442] Most of this confined delivery was observed around blood vessels. These results are thought to be due to the size of the pores within the extracellular matrix (60 nm diameter) [449], which would be a limiting factor in the diffusion of most liposomes within the brain parenchyma once delivered across the BBB. However, it is possible that the small drug molecules loaded within the liposomes, once released, can diffuse through the brain parenchyma to reach the desired target.

By increasing the size of the liposomes delivered to the brain with focused ultrasound, lower delivered doses have been detected via both fluorescence and MRI

[441]. This observation is thought to be due to the size threshold of the BBB permeability enhancement *via* focused ultrasound [433,447,450–452]. This threshold would lead to the delivery of a larger number of smaller liposomes into the brain at more sites compared to larger liposomes.

In many of these focused ultrasound-mediated liposome delivery studies, adverse effects have been observed in the form of intratumoural haemorrhage, scars with infiltrating macrophages, activated astrocytes, cysts and damage to the healthy tissue surrounding the tumours. [411,429–431,433,436–440] However, all studies delivering liposomes with this technology have used long ultrasound pulses. The RaSP sequence was shown to improve the efficacy and safety of focused ultrasound-mediated drug delivery when compared to long-pulse sequences. Improvements include a more homogeneous distribution of drugs, a reduced duration of BBB permeability change (<20 min), and no tissue damage.[424] As mentioned above, in a RaSP sequence, short pulses (in the microsecond range) are emitted at a high pulse repetition frequency in what we refer to as a burst. Each burst is then emitted at a slow rate. This sequence structure was intended to promote the spatial distribution of microbubble activity throughout the vasculature and avoid overstressing particular vessel regions. [424,453,454] The delivery of larger molecules such as liposomes, however, has yet to be investigated with RaSP sequences. We here aim to investigate whether these short pulses could improve the distribution of much larger liposomal compounds and improve the safety profile of their delivery.

4.1.5 Aims and objectives

The overall aim of this chapter was to investigate whether ultrasound emitted in a RaSP sequence could deliver clinically approved PEGylated liposomes across the BBB in a similar or improved manner to ultrasound emitted in a long pulse sequence. To achieve this aim, fluorescently labelled PEGylated liposomes (~100 nm diameter) were synthesised and delivered across the BBB using a RaSP or long pulse ultrasound sequence and microbubbles.

The fluorescent liposomes were prepared by incorporation of a fluorescent dye in preformed liposomes followed by their characterisation and stability assessment prior to the *in vivo* experiments.

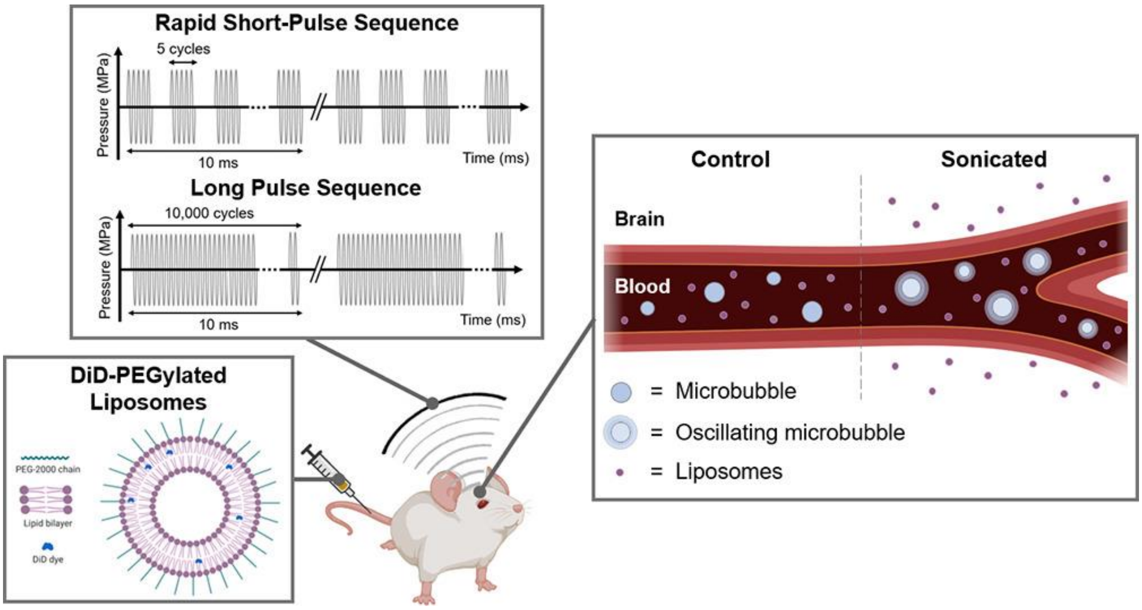

Figure 4.3. Graphical abstract of the chapter: Delivery of fluorescently labelled PEGylated liposomes to the brain using conventional long pulse and novel RaSP FUS sequence. Created with BioRender.com.

To investigate how changing the ultrasound pressure affected liposome delivery, mice were treated with two acoustic pressures, either 0.4 or 0.6 MPa. The delivery and distribution of liposomes was compared qualitatively and quantitatively between brains treated with the two sequence types and both pressures.

We then investigated whether differences could be observed in the distribution of liposomes when waiting for 0 h or 2 h after the ultrasound treatment. These different recovery times were applied to mice treated with both ultrasound sequences and both ultrasound pressures.

To determine whether liposomes were uptaken by neurons, microglia or astrocytes once delivered to the brain, immunohistochemical staining was performed. While uptake within neurons could tell us whether focused ultrasound can deliver liposomes to potential neuronal targets, uptake within microglia and astrocytes could indicate a pathway of excretion of the liposomes from the brain.

Lastly, tissue damage was investigated at a microscopic level in brains treated with both sequence types and both pressures at 0 h. These results were used to determine whether by emitting ultrasound in a RaSP sequence, an improved safety profile could be achieved when delivering liposomes to the brain.

4.2 Results and discussion

4.2.1 Synthesis and characterization of fluorescent DiD-liposomes

The Doxebo liposomes (empty PEGylated liposomes) were labelled with DiD (1,1′-Dioctadecyl-3,3,3′,3′-tetramethylindodicarbocyanine, 4-Chlorobenzenesulfonate Salt), a far-red fluorescent, lipophilic and cationic indocarbocyanine dye used to stain phospholipid bilayers (Figure 4.5, 4.4A)[455]. This labelling process showed negligible changes in the hydrodynamic diameter (pre-DiD: 99.9 ± 3.6 nm vs. post-DiD: 97.9 ± 2.2 nm) and no effect on surface charge (Figure 4.4B), compared to the original Doxebo liposomes. The hydrodynamic size of the liposomes and their polydispersity remained stable following labelling (Figure 4.4B). Using a fluorescence standard curve, we calculated that the DiD concentration in the final DPL sample was 2.1 ± 0.5 µg/mL.

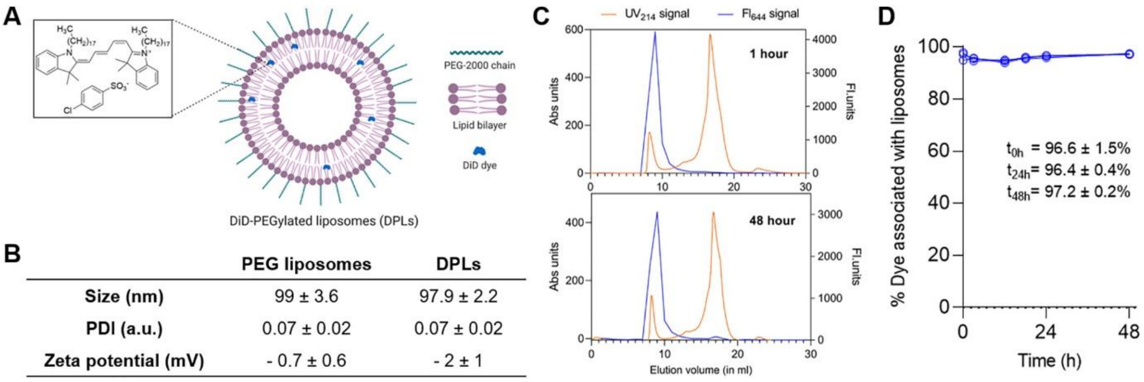

	PEG liposomes	DPLs
Size (nm)	99 ± 3.6	97.9 ± 2.2
PDI (a.u.)	0.07 ± 0.02	0.07 ± 0.02
Zeta potential (mV)	- 0.7 ± 0.6	- 2 ± 1

Figure 4.4. DiD-PEGylated liposomes (DPLs): (A) The carbocyanine dye DiD is incorporated in the phospholipid bilayer of the PEGylated liposome due to its hydrophobic nature. (B) The hydrodynamic size distribution polydispersity index (PDI, measure of size distribution), and zeta potential of the PEGylated liposomes show negligible changes (n = 4) before and after incorporation of the dye. (C) Size-exclusion chromatograms show the stability of the DPLs (fluorescent liposomes) post-incubation in human serum and 37 °C for up to 48 h and confirm high retention of the dye within the liposomes. Fractions 8–10 contained the liposomes and fractions 12–25 contained the serum proteins. The high fluorescence signal in fractions 8–10 at both time points confirmed the retention of DiD in the liposomes up to 48 h. (D) Serum stability curve shows % dye associated with the liposomes post-incubation in serum at time points 0, 3, 12, 18, 24, and 48 h.

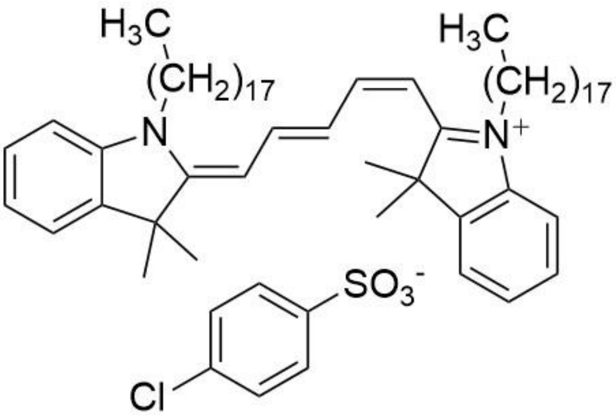

Figure 4.5. DiD: The structure of lipophilic, fluorescent, and cationic dye DiD (1,1′-Dioctadecyl-3,3,3′,3′-tetramethylindodicarbocyanine, 4-Chlorobenzenesulfonate Salt)

4.2.2 *In vitro* validation of fluorescent DiD-liposomes

It has been shown that lipoproteins in blood serum can cause fluorescent dyes to leak from liposomes via lipids passively dissociating from the bilayers of the liposomes[456]. To assess whether DiD was retained in the liposomes in the presence of blood components, we incubated a small amount of DPLs *in vitro* with a large excess of human serum at 37 °C for up to 48 h and used size-exclusion chromatography to detect dye leakage. Using this system, both DPLs and serum components were efficiently separated, identified, and quantified via UV and fluorescence measurements allowing us to determine the liposome and serum protein-associated dye eluted at different timepoints (Figure 4.4C). Co-elution of the liposomes (as measured by UV) and the incorporated dye (from fluoresce detection) over time under these conditions demonstrate high stability of the dye within the liposomes for up to 48 h (Figure 4.4D).

4.2.3 *In vivo* delivery of fluorescent liposomes using focused ultrasound in mice model

To investigate whether liposomal nanomedicines can be delivered to the brain using rapid short-pulse sequences, the left hippocampus of brain of the mice was sonicated with either a focussed ultrasound RaSP or long pulse sequence while injecting microbubbles intravenously. Two different pressures were used for treatment of the brains and extracted either 0 or 2 h post ultrasound treatment.

4.2.3.1 Detected delivery and dose

DPLs were delivered to the brain with either RaSP sequences or long pulse sequences (Figure 4.6). This study is the first attempt of liposomal nanomedicine delivery to the brain using a RaSP sequence. However, with RaSP, liposomal delivery was only observed at 0.6 MPa, with no delivery at 0.4 MPa at both time points of 0 h and 2 h (Figure 4.6 A, C). At the lower pressure (0.4 MPa) in the long pulse treated brains, delivery was observed in 2 out of 3 brains (0 h). Liposomal delivery was observed in all other brains with no delivery observed in the control right hippocampus in any of the brains as expected.

A rise in the fluorescence was detected in the long-pulse treated brains compared to RaSP-treated brains and also for the higher acoustic pressure sonication. (Figure 4.6-4.7). The higher pressure was needed to allow liposomes to be delivered to the RaSP treated brains (Figure 4.7). The normalised optical density (NOD) calculated from these fluorescence regions was found to be 80-fold higher when ultrasound was emitted at higher pressure (0.6 MPa) compared to lower pressure (0.4 MPa) in RaSP sequence treated brains at 0 h. In log pulse treated brains, the NOD was observed to be 23-fold higher at lower pressure (0.4 MPa) and 134-fold higher at higher pressure (0.6 MPa) compared to RaSP treated brains at 0.4 MPa at 0 h.

The recovery time of two hours did not impact the NOD observed other than in long-pulse-treated brains at 0.4 MPa showing a 2-fold increase for the longer recovery time group ($P < 0.05$). A substantial variance in the NOD was also observed among the following experimental groups: RaSP brains at 0.4 MPa (0 h), and all higher pressures and long pulse brains; RaSP brains at 0.4 MPa (2 h), and all higher pressures and long pulse brains at 0.4 MPa (2 h); long pulse brains at 0.4 MPa (0 h) and both sequence types at 0.6 MPa (0 h); and finally between long pulse brains at 0.4 MPa (2 h) and long pulse brains at 0.6 MPa (0 h; $P < 0.05$).

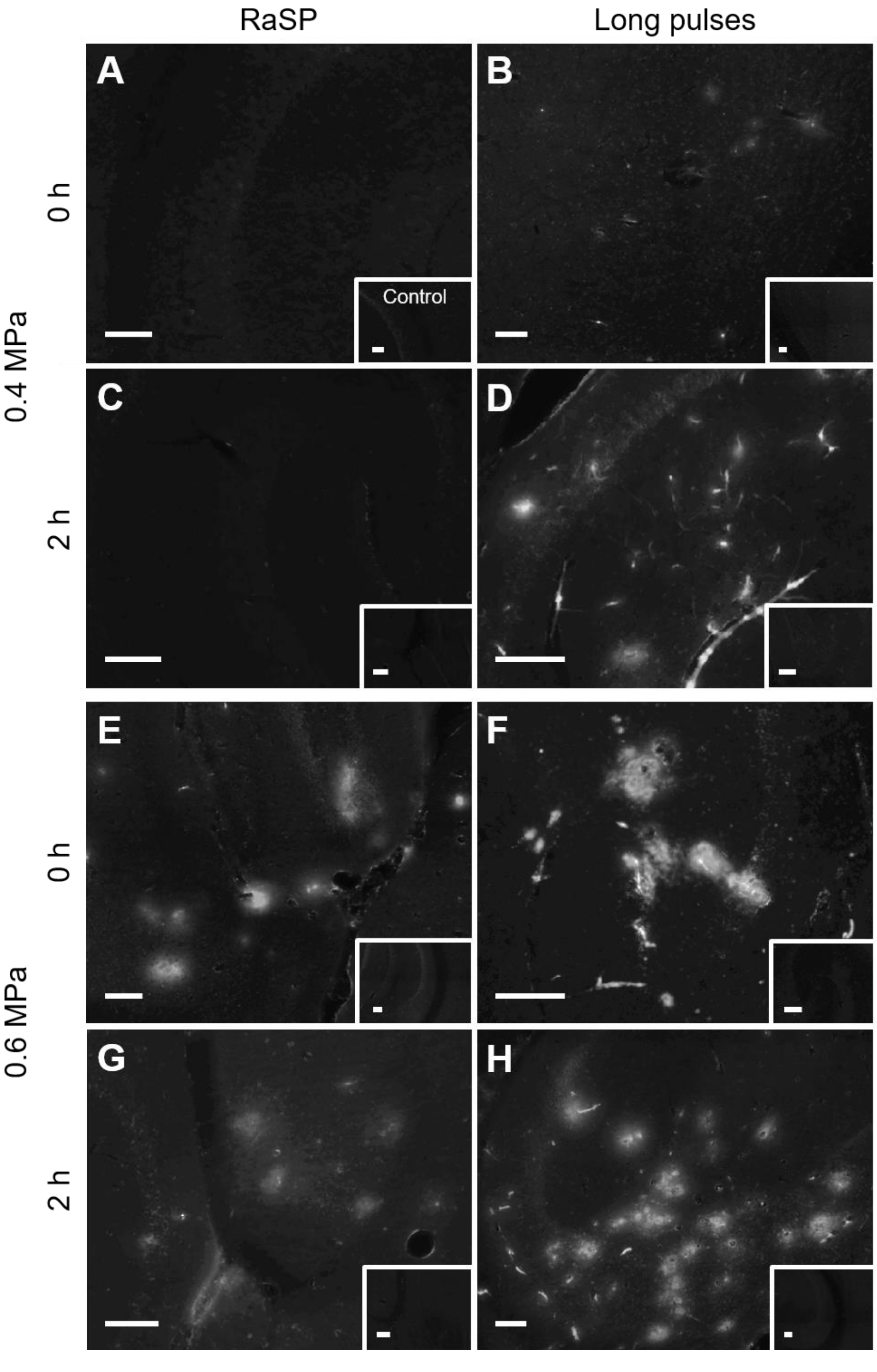

Figure 4.6. Liposomal delivery with rapid short-pulse (RaSP) and long pulse sequences at 0.4 and 0.6 MPa, and at 0 and 2 h after ultrasound treatment: Fluorescence images (10x) show examples of liposomes delivered with (A, C, E, G) RaSP and (B, D, F, H) long pulse sequences at (A-D) 0.4 MPa and (E-H) 0.6 MPa, and at either (A-B, E-F) 0 h or (C-D, G-H) 2 h after the ultrasound treatment. Right hippocampus control regions are shown in white boxes in the bottom right corner of each image. (A, C) No delivery was observed at 0.4 MPa when brains were treated with a RaSP sequence. (E-H) At 0.6 MPa, delivery was observed in all brains. More spots of delivery were observed in long-pulse-treated brains compared to RaSP-treated brains. The scale bars indicate 50 µm.

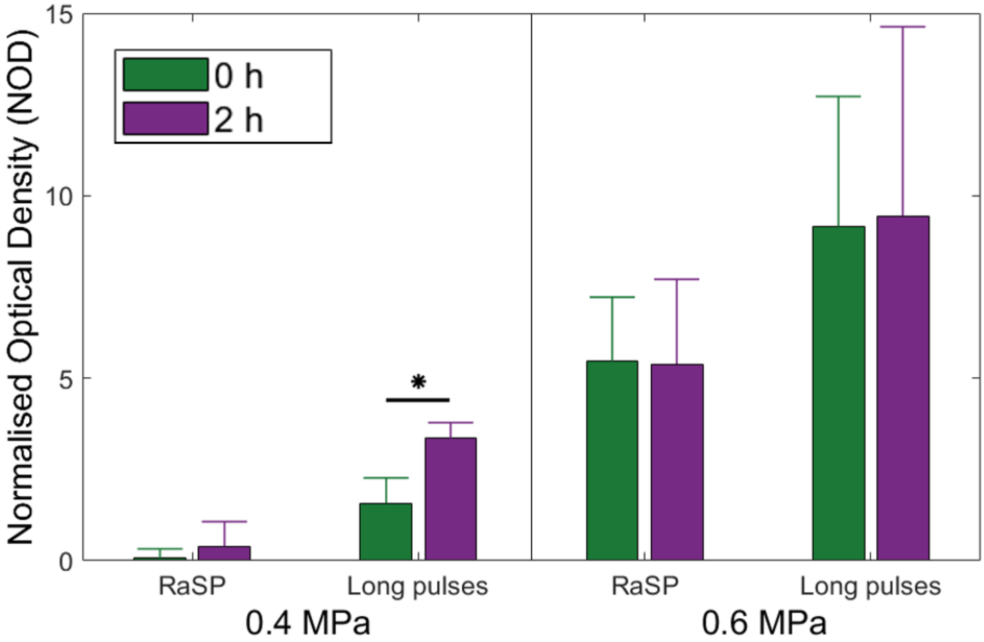

Figure 4.7. Detected dose of liposomes delivered with rapid short-pulse (RaSP) and long pulse sequences at 0.4 and 0.6 MPa, and at 0 h or 2 h after the ultrasound treatment: The threshold for liposomal delivery with RaSP was found to be between 0.4 and 0.6 MPa. The detected dose, quantified with the normalised optical density (NOD), was higher at 0.6 MPa for both RaSP and long pulse sequences ($P < 0.05$). The detected dose was only found to be significantly different between 0 h (green) and 2 h (purple) in long-pulse-treated brains at 0.4 MPa ($P < 0.05$). Significance was also found between RaSP 0.4 MPa (0 h) and all higher pressures and long pulse brains; between RaSP 0.4 MPa (2 h) and all higher pressures and long pulses 0.4 MPa (2 h) brains; between long 0.4 MPa (0 h) and both sequence types at 0.6 MPa (0 h) brains; and between long 0.4 MPa (2 h) and long 0.6 MPa (0 h) brains ($P < 0.05$). For clarity, significance bars were only shown between 0 h and 2 h results and not between different pressures or sequence types.

Thus, we have demonstrated that 100 nm PEGylated fluorescent liposomes can be delivered to the brain using RaSP sequence of focussed ultrasound. According to our literature survey, this study is the first demonstration of PEGylated liposome delivery using short ultrasound pulses, as previous investigations have only used long pulse sequences emitting pressures between 0.33 and 1.6 MPa. [411,429–441]

To investigate whether DPLs could be delivered using RaSP sequence within a similar pressure range used for above long-pulse studies, we tested delivery at two different acoustic pressures 0.4 and 0.6 MPa and found that RaSP required a higher acoustic pressure (0.6 MPa) to achieve delivery and observed dose to the brain was comparably lower than the observed in long-pulse-treated brains (Figure 4.6-7). Thus, using RaSP sequence, the observed threshold for delivery of liposomes was higher compared to that using long pulses.

The increase observed in the pressure threshold can be attributed to the reduced energy provided to the brain while emitting RaSP, leading to a lower chance of more disruptive microbubble activity occurring. This disruptive behaviour would have a higher probability to lead to increased BBB permeability allowing the passage of large sized liposomal agents (~100 nm) into the brain. It was observed that for long-pulse-treated brains, the acoustic pressure increase led to an increased delivery, which could be quantified by both measurements: overall detected fluorescence intensity and the number of delivery spots (Figure 4.6, 4.9-10). These results were as expected based on previous work [433]. It has been previously demonstrated that at 0.4 MPa, smaller dextran molecules cross the BBB when emitting RaSP, whereas the immunoglobulins (~ 15 nm x 9 nm x 4 nm) [457,458] cannot cross the BBB. In line with these results, we did not expect larger 100 nm liposomes to reach the brain at 0.4 MPa, as the larger the compound, the higher the pressure required to deliver it to the brain across the BBB. [447,459]

In previous work in my second supervisor's NSB lab at Imperial, it has been observed that the delivery and distribution of compounds delivered changes with the time they are allowed to circulate and extravasate into the brain post application of ultrasound. Similar time dependent investigations into liposomal delivery at 0 h, 2 h and 4 h after ultrasound exposure have also been performed. [433,434,439] Here, we investigated liposomal delivery at 0 h and 2 h. In RaSP-treated brains, it was found that the detected fluorescence intensity and the number of delivery spots were not significantly different between brains sacrificed zero hours or two hours post ultrasound exposure (Figure 4.7, 4.9-10). However, in long-pulse-treated brains, a significant different was observed at lower pressure (0.4 MPa). These results can be explained by the duration of the increased BBB permeability caused by the different sequences. For long-pulse-treated brains, the increased permeability lasts between 4-48 h depending on the ultrasound parameters used. [419,460–462] Therefore, we expect the BBB permeability increase to last the duration of the two-hour wait in our long-pulse-treated brains. However, for RaSP-treated brains, it has been shown that the BBB permeability increase is observed only for less than 10 minutes which influencing the number of liposomes extravasating into the brain within the duration of two hours.[424] Thus, we hypothesise that observed increased delivery in long-pulse-treated brains but not in RaSP treated brains is due to the BBB being open for longer periods in long-pulse-treated brains. This prolonged opening would allow extravasation of more liposomes into the brain within this chosen time frame of two hours. At the pressure of 0.6 MPa, there was no significant difference between detected delivery at 0 and 2 h in long-pulse-treated brains. This can be explained by the limitation on the diffusion in the brain of the liposomes delivered across the BBB on account of their large size. The network of the extracellular matrix of the brain has pores that are approximately 60 nm in diameter, [463] whereas our PEGylated liposomes are 100 nm. Therefore, we do not expect our liposomes to penetrate and distributed from the vessels post-delivery across the BBB.

4.2.3.2 Delivery distribution

The distribution of the liposomes delivered was found to be heterogeneous in every brain (Figure 4.6). Both RaSP and long-pulse-treated brains equally showed this observation with the concentration of delivery sites around blood vessels. Delivery was more densely concentrated close to the blood vessels in long-pulse-treated brains (Figure 4.6 D, F, H). Lower variation (lower COV values) was quantified for RaSP-treated brains, with significant differences observed between RaSP at 0.6 MPa at 0 h brains and long pulse at 0.4 MPa at 0 h brains, and between RaSP at 0.6 MPa at 0 and 2 h brains, and long pulse at 0.6 MPa at 0 h brains ($P < 0.05$; Figure 4.8). No influence on the COV was observed by the two-hour recovery time with no significant differences observed between 0 h and 2 h brains for respective pressure and pulse sequences (P > 0.05).

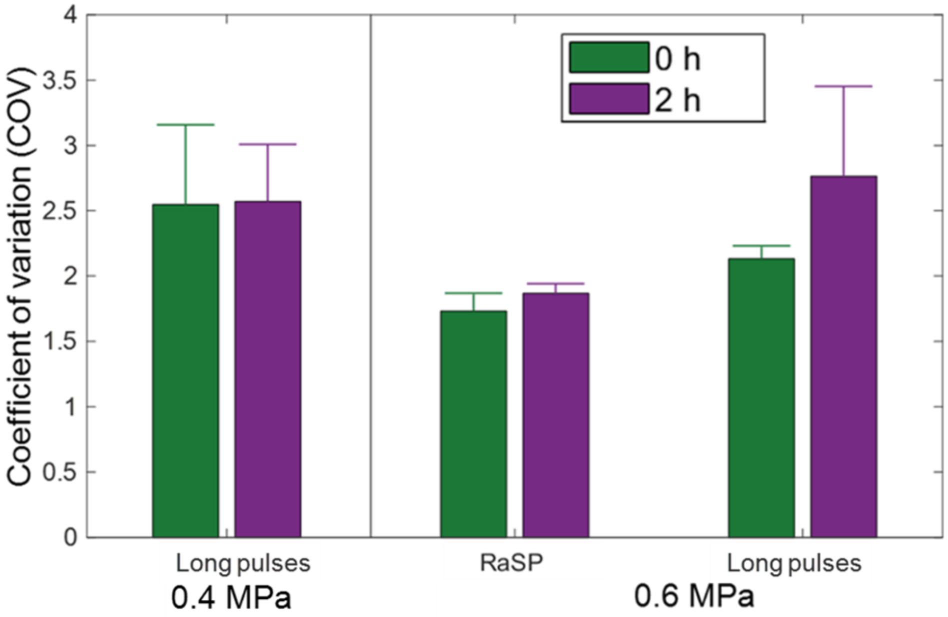

Figure 4.8. Distribution of liposomes delivered with rapid short-pulse (RaSP) and long pulse sequences at 0.4 and 0.6 MPa, and at 0 h or 2 h after the ultrasound treatment: A lower coefficient of variation (COV) was calculated in RaSP-treated brains compared to long-pulse-treated brains, which indicates less variation and therefore a more homogenous distribution. The COV was not found to be significantly different between 0 h (green) and 2 h (purple) recovery times (P > 0.05). However, significant differences in COV were found between long pulse brains at 0.4 MPa (0 h) and RaSP brains at 0.6 MPa (0 h); between RaSP brains at 0.6 MPa (0 h and 2 h), and long pulse brains at 0.6 MPa (0 h). The COV was not quantified for RaSP-treated brains at 0.4 MPa as no liposomal delivery was observed in these brains. For clarity, significance bars were not shown between different pressures or sequence types.

Determination of the differences between the number and size of regions of liposomal delivery between parameter sets was done by quantification of the number of areas above 100 μm^2 and above 500 μm^2. The observed number of delivery regions (areas > 100 μm^2) were found to be higher for long-pulse-treated brains compared to RaSP brains within the same pressure and time parameters (Figure 4.9). Significant differences were observed between long-pulse-treated brains at 0.6 MPa and RaSP brains at the same pressure at 2 h ($P < 0.05$). An increase in the number of delivery sites was also observed with the increasing acoustic pressure. Increasing the pressure for all parameter sets ($P < 0.05$) except at 0.4 MPa 0 h ($P > 0.05$) showed significant differences in the number of delivery sites. The two-hour extravasation time for liposomes to spread within the brain parenchyma led to a high significant difference in long-pulse-treated brains, showing a 21-fold increase at pressure of 0.4 MPa ($P < 0.01$).

Similar trends were observed for the number of sites with an area of delivery above 500 μm^2 (Figure 4.10). The larger sites of delivery were observed more in the long pulse treated brains and at higher pressures with the two-hour recovery time making a significant difference in long-pulse-treated brains ($P < 0.05$). Significant differences were also found among the two-hour recovery brains on using long pulses instead of RaSP ($P < 0.05$) and ultrasound application at 0.6 MPa instead of 0.4 MPa ($P < 0.05$).

A homogeneous distribution is desired to allow therapeutic or diagnostic agents to reach as many targeted sites as possible in the field of brain delivery allowing us to avoid over or under-treatment of regions within the targeted brain parenchyma. Here, a heterogeneous distribution of liposomes in both RaSP and long-pulse-treated brains was observed (Figure 4.6). However, the liposomes being carriers of therapeutics or imaging agents, most commonly small molecules (~ 2 nm diameter),[464] and these molecules are expected to be released from the liposomes into the brain and diffuse through the brain parenchyma.

Our study in agreement with previous studies that have shown heterogeneous delivery patterns of liposomes using long pulse sequences, [433–435,439] which has also been seen for the delivery of other large compounds such as dextran 2,000 kDa (54.4 nm). [447] The spot-like pattern of confined liposome delivery is likely due to the slow diffusion of these large molecules through the 60 nm width of the extracellular matrix pores. [465] This pore size is the limiting factor in the diffusion of liposomes within the brain, making it inefficient. [466]

In RaSP-treated brains, an observed decrease in heterogeneity was seen compared to long-pulse-treated brains. This can be explained by the qualitative observation showing more uniform delivery around blood vessels in RaSP-treated brains, while with long pulses, delivery sites had a brighter centre with a more cloud-like periphery. A measurable steeper decrease intensity around the blood vessels was seen compared to RaSP-treated brains. These qualitative observations indicate that the RaSP sequence is more likely to provide a gentler stimulation to the BBB and cause an increase in BBB permeability with less disruptive events, which are not only responsible for higher accumulation around vessels and more sites of delivery, but also tissue damage.

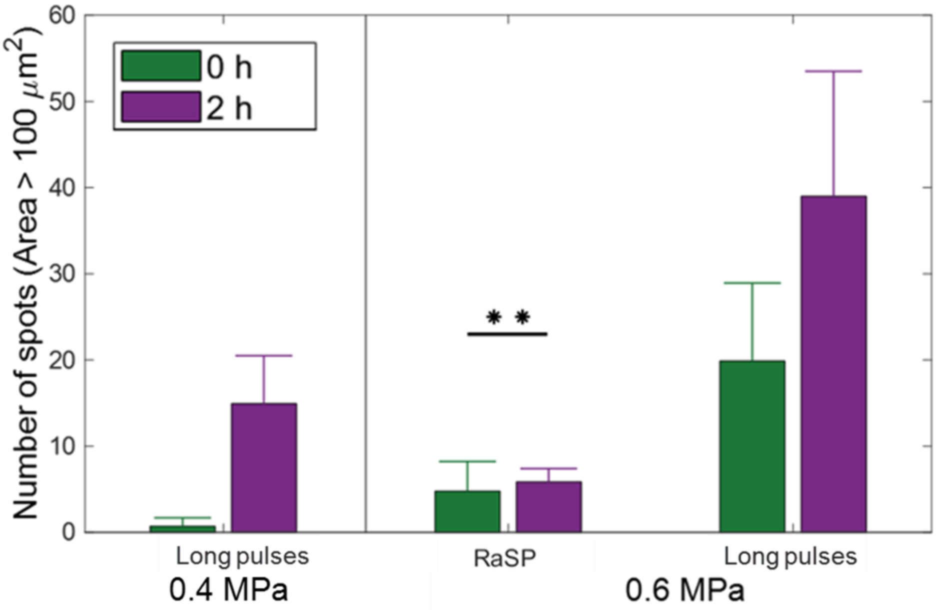

Figure 4.9. Number of areas with liposome delivery above 100 µm^2: The number of areas above 100 µm^2 with liposome delivery was found to be higher in long pulse compared to RaSP-treated brains with the same acoustic pressures. Increasing the acoustic pressure, increased the number of delivery regions. In addition, waiting for 2 h instead of 0 h, led to an increase in the number of delivery spots only in long-pulse-treated brains. Significant differences were found between RaSP 0.6 MPa brains and long 0.6 MPa 2 h brains ($P < 0.05$). The areas of delivery were not quantified for RaSP-treated brains at 0.4 MPa as no liposomal delivery was observed in these brains. For clarity, significance bars were not shown between different pressures or sequence types.

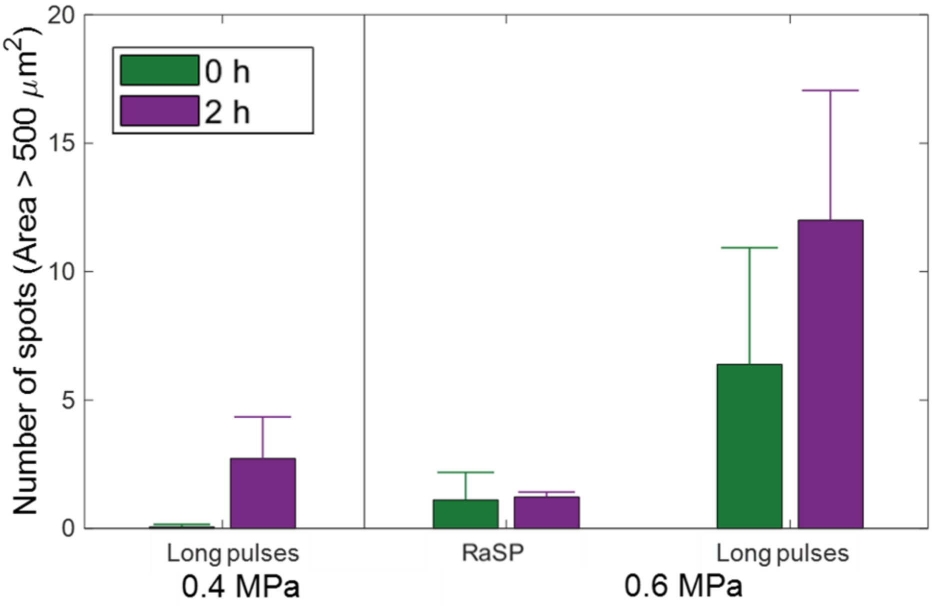

Figure 4.10. Number of areas with liposome delivery above 500 µm^2: The number of areas above 500 µm^2 with liposome delivery was found to be higher in long pulse compared to RaSP-treated brains. Increasing the acoustic pressure, also increased the number of delivery regions. In addition, waiting for 2 h instead of 0 h, led to an increase in the number of delivery spots only in long-pulse-treated brains ($P < 0.05$ at 0.4 MPa). Significant differences were found between long 0.4 MPa brains and all 2 h wait 0.6 MPa brains; between RaSP 0.6 MPa brains and long pulse 0.6 MPa brains at 2 h ($P < 0.05$). The areas of delivery were not quantified for RaSP-treated brains at 0.4 MPa as no liposomal delivery was observed in these brains. For clarity, significance bars were not shown between different pressures or sequence types.

4.2.3.3 Subcellular localisation

The fluorescence images acquired showed liposomes were not only localised within the parenchyma but also within cells within the brain. This subcellular distribution of the liposomes within these cells was investigated by performing the confocal microscopy of the neuronal cells. Fluorescent DPLs were found scattered within the cytoplasm but not in the nucleus (Figure 4.11). The spread of the fluorescent liposomes within the cytoplasm was not uniform and was observed as small dots of fluorescence scattered throughout the cytoplasm. The cells showing liposomal uptake were found to have a neuron-like morphology.

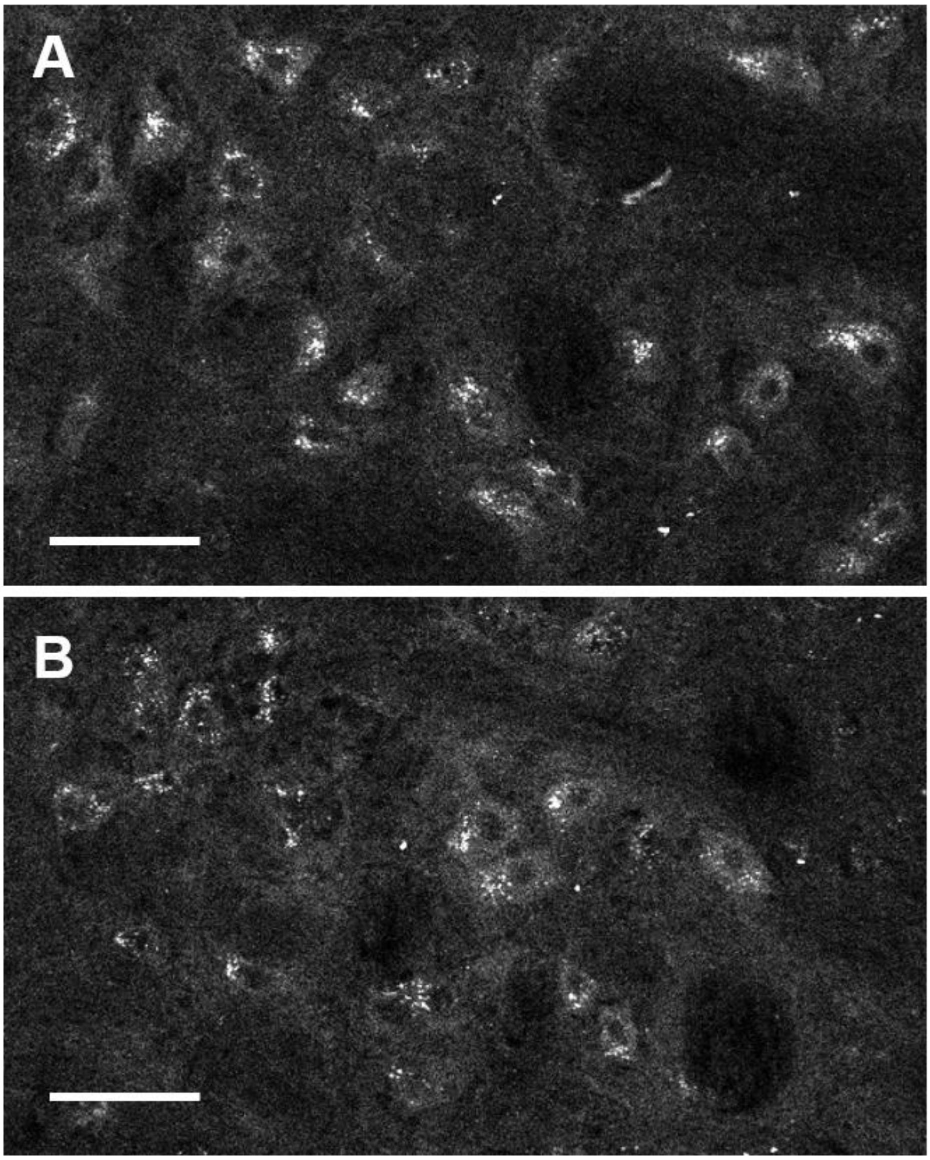

Figure 4.11. Subcellular localisation of liposomes: A and B panel confocal images of different slices of brain with evidence of liposome delivery (20x) show details of the subcellular localisation of the liposomes within ultrasound-targeted regions. These specific examples are from long-pulse-treated brains at 0.6 MPa and two hours after the ultrasound treatment. Fluorescence was observed within cells, specifically within the cytoplasm and not in the nucleus (darker circular centre within cells). Morphologically these cells with uptake appear to be neuron-like cells. The scale bars indicate 50 µm.

4.2.3.4 Cellular uptake

The identification of the cells showing uptake of our liposomes was performed by staining brain slices for neurons, microglia, and astrocytes. Staining was only performed on brain samples showing cellular uptake. Therefore, all brains treated with RaSP at 0.4 MPa, one-third of brains treated with RaSP at 0.6 MPa (0 h) and two-thirds of brains treated with long pulses at 0.4 MPa (0 h) not showing cellular uptake were not stained.

Liposomal uptake within the neurons was observed in all brains showing cellular uptake (Figure 4.12-13). Although due to low sample size, no statistical analysis could be performed but higher neuronal uptake was observed for long-pulse-treated brains compared to RaSP-treated brains. Similar observations were made in brains treated with the higher pressure (0.6 MPa) compared to the lower pressure (0.4 MPa; Figure 4.13) with higher pressure showing higher uptake.

Liposomal uptake in microglia was only observed at 0.6 MPa in brains with brain extraction two hours after the ultrasound treatment (Figure 4.14-15). The observed uptake was higher in long-pulse-treated brains compared to RaSP-treated brains (Figure 4.15). The microglia showing uptake the liposomes appeared branched without a rounded shape, indicating microglia exhibiting characteristics of a resting state. No liposomal uptake was observed within astrocytes for any RaSP or long-pulse-treated brains (Figure 4.16).

Liposomes can be surface modified to selectively target specific cells within the brain or to bind specifically to receptors expressed on the surface of cells. Thus, the study of delivery at the cellular level is important to determine whether the delivery with our focused ultrasound system can reach the areas within the brain where these cells are localised. The investigation of neuronal uptake of liposomes has relevant clinical implications as neurons are a desirable target for delivery of theranostic and neuroprotective drugs. The investigation of liposome uptake by microglia and astrocytes, which would indicate a pathway of excretion from the brain using perivascular pathway.

Liposomal uptake was detected within neurons in both RaSP and long-pulse-treated brains (Figure 4.12-13). Previous investigations have shown neuronal uptake of liposomes without ultrasound both *in vitro*[467–470] and *in vivo*.[469–471] For i*n vitro* studies, fluorescently labelled liposomes have been detected in hippocampal,[468] cerebellar,[469] mammalian[467] and peripheral neurons,[470] while *in vivo* examinations have shown fluorescence has been detected in neurons of the hypothalamus and the cerebellum.[469,471] Here, our observations have showed the liposome uptake within neurons of the hippocampus, confirming that focused ultrasound can deliver liposomes to neurons within the targeted region of the brain parenchyma.

The location of liposome distribution within the cells provides us insight into their method of uptake by the cells. In this study, the liposomes were found scattered within the cytoplasm of neurons and not within the nucleus. Such type of specific localisation has been reported in the case of both cationic and anionic liposomes[468–470] suggesting that liposomes uptake is mediated through lipid-rich compartments in the cytoplasm (i.e., endosomes or lysosomes). Further information on such observations can be obtained by staining for these compartments, helping us identify the pathway of liposome uptake, which can be via either clathrin-dependent or endocytosis pathway depending on the type of liposome delivered.[467–470] Future staining experiments will determine whether the slightly anionic PEGylated liposomes used in this study were compartmentalised. If the liposomal uptake were to be confirmed in lysosomes, this would indicate a possible pathway of excretion from the neurons.

In addition to neurons, liposome uptake in microglia was investigated, which are the phagocytic system of the brain. Previous studies have shown liposome uptake within microglia, with varying results depending on the composition of the liposomes. Liposomes with phosphatidylserine phospholipids for example have been shown to have neuroprotective roles, inhibiting microglial activation.[472,473] Although liposomes have also been synthesised to target microglia,[474] non-targeted liposomes have also been observed within these cells.[474] Here, microglial uptake of liposomes was expected as a method of excretion from the brain. Our results showed liposome uptake within microglia only in long-pulse-treated brains and only two hours after ultrasound treatment. This could be due to the higher delivery of liposomes at more sites compared to RaSP-treated brains. It is also possible that the microglia in long-pulse-treated brains were activated due to more disruptive microbubble activity within the vasculature compared to the RaSP sonication. The higher disruptive activity, and higher delivery could also explain why microglial uptake was observed at the higher 0.6 MPa pressure and not at 0.4 MPa.

It has been previously observed that delivery of dextran via focused ultrasound led to an immediate response from microglia, which phagocytosed the dextran and displayed a more activated morphology.[424] The slower microglial response observed following liposome delivery could be due to PEGylation of the liposomes which delays the detection of the liposomes by the RES system and thereby slowing extravasation of the PEGylated liposomes into the regions of the brain parenchyma where microglia are located. As the uptake by macrophages is also dependent on the type of compound being delivered and the dextran and dextran coated nanoparticles are expected to show an accelerated uptake by macrophages and thereby explaining high uptake of dextran in microglia.[475] Future work will focus on exploring microglia uptake at different time points, to discover timeline of microglial phagocytosis and activation and how it varies over time as this might have important implications for drug delivery to the brain.

Lastly, liposomal uptake was investigated within astrocytes which form another set of glial cells. No visible liposomal uptake was observed in astrocytes in either RaSP-treated brains or long-pulse-treated brains. Previous investigations have only studied uptake of astrocyte targeted liposomes only *in vitro*.[476–478] For *in vivo* conditions, the targeted liposomes have failed to reach astrocytes within the brain. Here, the lack of uptake within astrocytes could be explained by the slower reaction of astrocytes to foreign particles compared to microglia.[479,480] Future work will involve examination of whether astrocytes show uptake of liposomes at later time points.

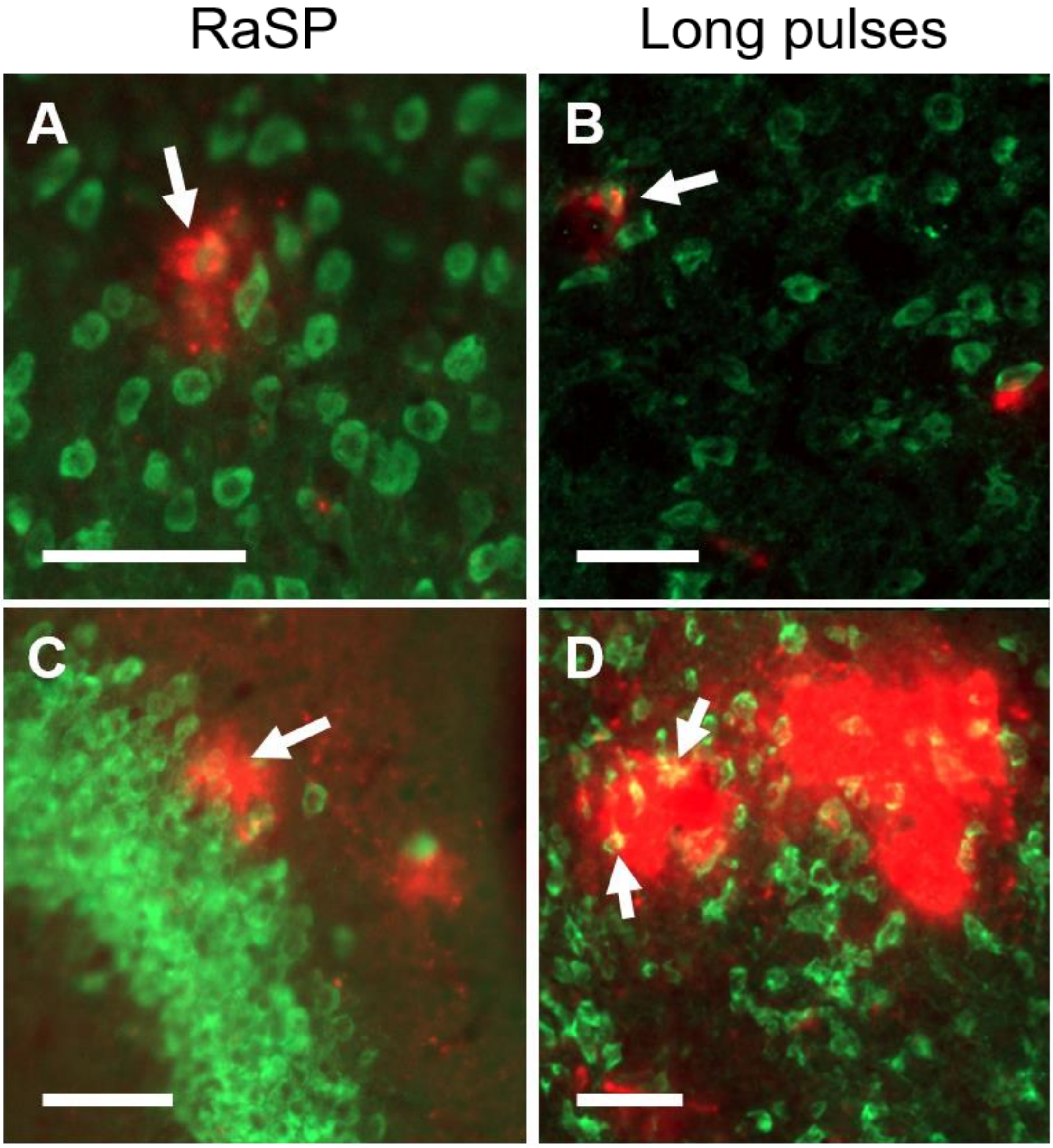

Figure 4.12. Uptake of liposomes within neurons in RaSP and long pulse-treated brains: Fluorescence images (10x) show liposome uptake within neurons in (A, C) RaSP-treated brains

and (B, D) long-pulse-treated brains. Uptake was higher in long-pulse-treated brains than in RaSP ones. White arrows highlight examples of liposome uptake within neurons. The scale bars indicate 50 µm.

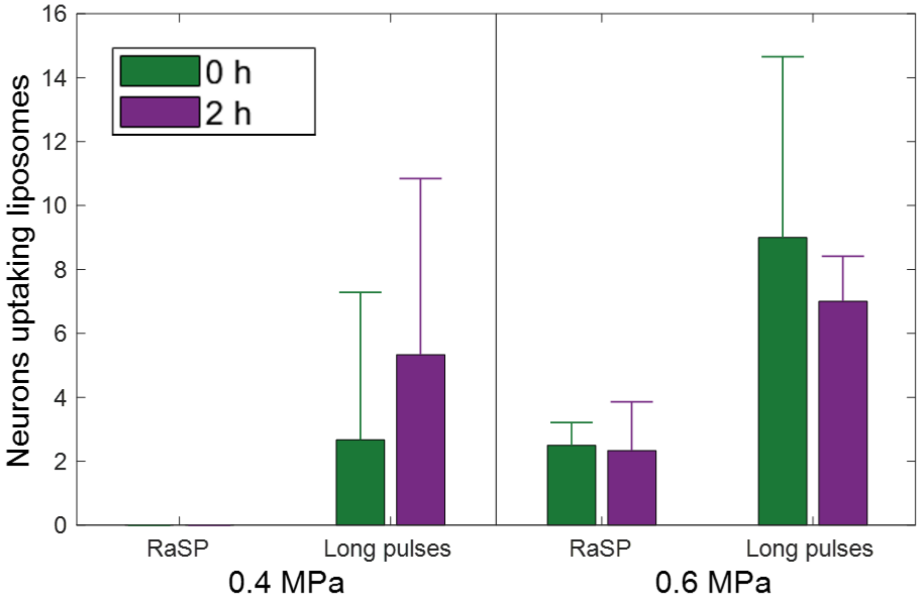

Figure 4.13. Number of neurons with liposome uptake in brains treated with RaSP or long pulses at 0.4 or 0.6 MPa, and at 0 h or 2 h after the ultrasound treatment: Neuronal uptake was observed in all brains where delivery was observed. However, more so in long-pulse-treated brains at 0.6 MPa than at the lower pressure or in RaSP-treated brains. This plot displays the average number of neurons with uptake across the evaluated brain slices. No statistical analysis was performed as the sample size was too small.

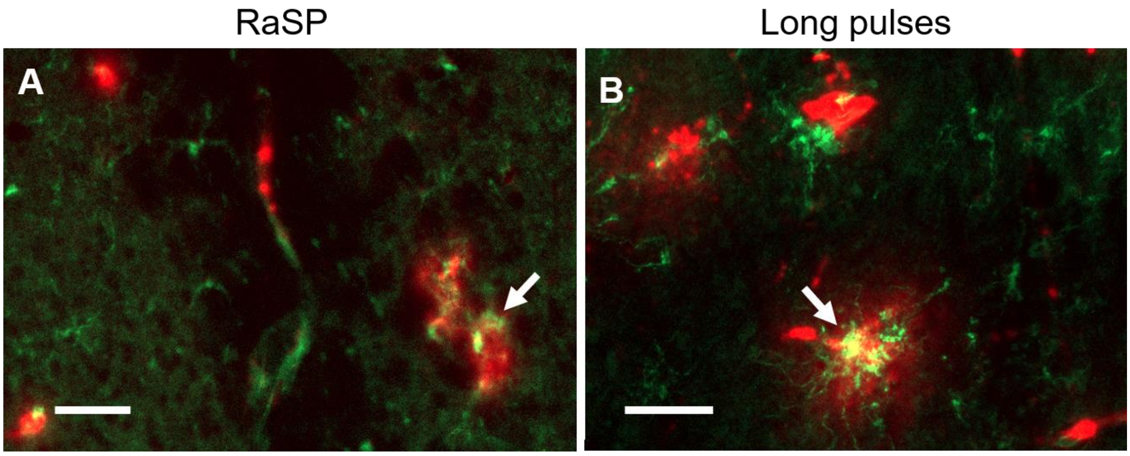

Figure 4.14. Uptake of liposomes within microglia in RaSP and long pulse-treated brains: Fluorescence images (10x) show liposome uptake within microglia in a (A) RaSP-treated brain slice and a (B) long-pulse-treated brain slice. White arrows highlight examples of liposome uptake within microglia. The scale bars indicate 50 µm.

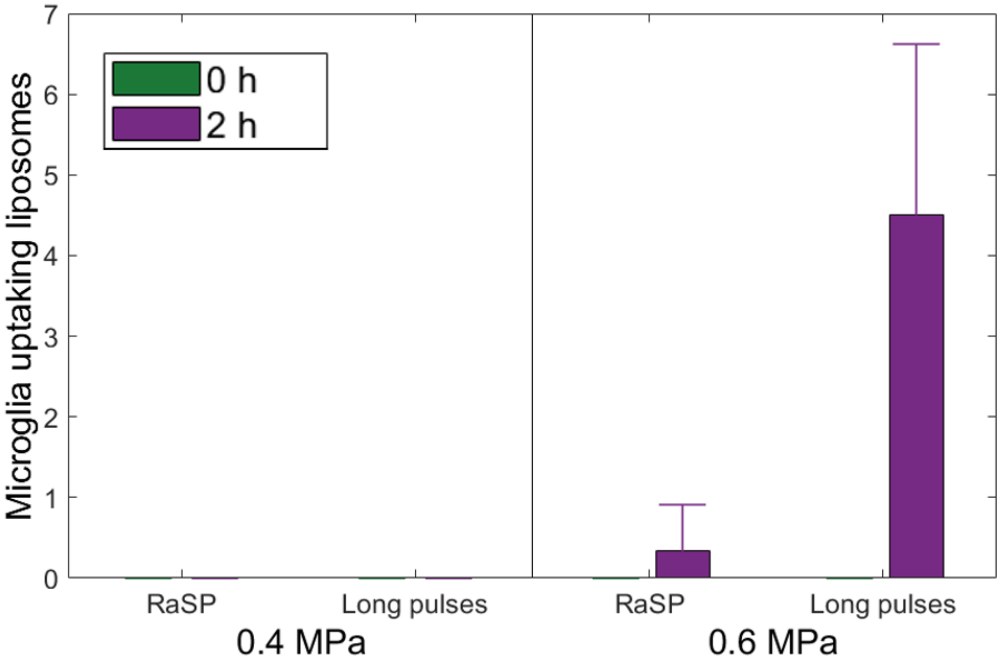

Figure 4.15. Number of microglia with liposome uptake in brains treated with RaSP or long pulses at 0.4 or 0.6 MPa, and at 0 h or 2 h after the ultrasound treatment: Microglial uptake was only observed in 0.6 MPa brains 2 h after ultrasound treatment. Higher uptake was observed in long-pulse-treated brains compared to RaSP ones. This plot displays the average number of microglia with uptake across the evaluated brain slices. No statistical analysis was performed as the sample size was too small.

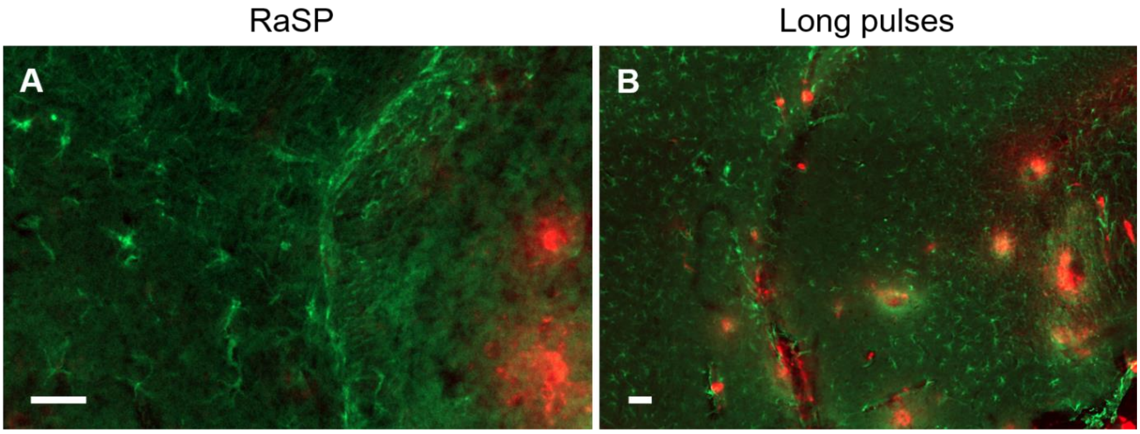

Figure 4.16. Uptake of liposomes within astrocytes in RaSP and long pulse-treated brains: Fluorescence images (10x) show no liposome uptake within astrocytes in (A-B) RaSP-treated brains and (C-D) long pulse-treated brains. The scale bars indicate 50 µm.

4.2.3.5 Safety profile

To evaluate if RaSP-treated and long-pulse-treated brains caused any histological damage at 0.6 MPa, H&E staining was performed. All control regions of right hippocampi showed no damage as expected (Figure 4.17-18 D-F). The targeted left hippocampi in RaSP-treated brains confirmed no evidence of damage except for single site of red blood cell extravasation in a single brain slice (Figure 4.17 C). No other sites of red blood cell extravasation, microvacuolations or dark neurons were detected in the RaSP-treated brains. For long-pulse-treated brains, more than five sites of extravasated RBCs were found in 93% of analysed sections, microvacuolations in 93% of sections and dark neurons in 21% (Figure 4.18-19). No significant differences were found between RaSP and long-pulse-treated brains due to the large variations in numbers between brain slices ($P > 0.05$; Figure 4.19.)

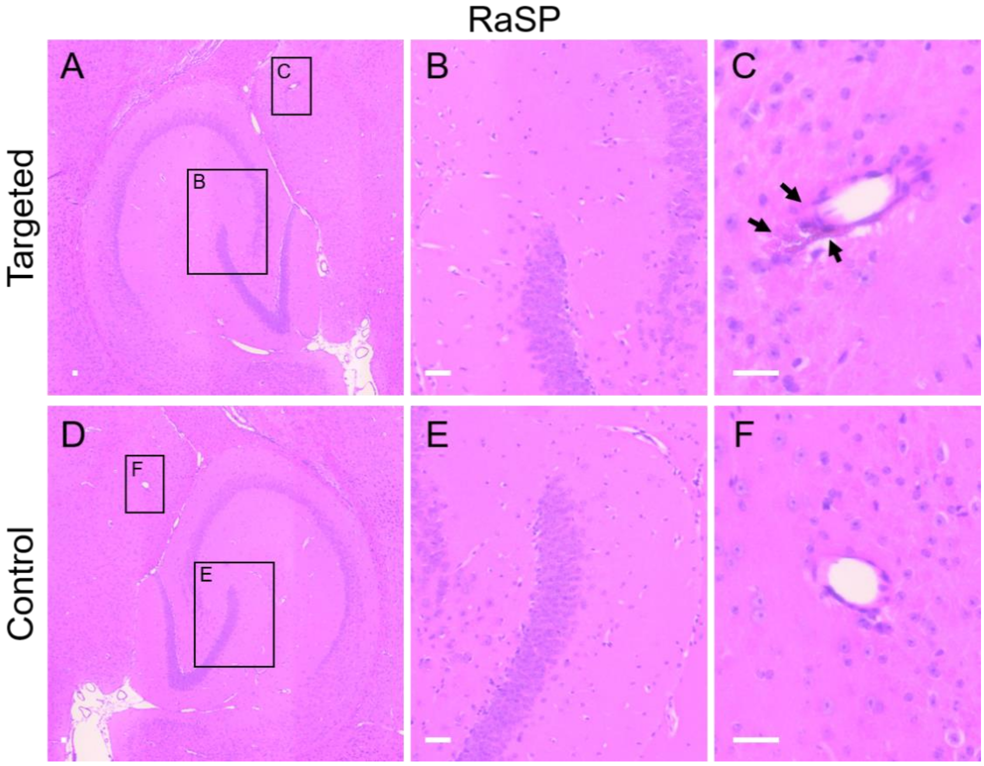

Figure 4.17. H&E staining on RaSP-treated brains at 0.6 MPa to assess tissue damage: microscopic examination of H&E stained (A-C) left (targeted) and (D-F) right (control) hippocampi of RaSP-treated brains show (C) a single site of red blood cell extravasation (arrows), but no histological damage in all other regions and brain slices. The black boxes show the enlarged regions in the middle and right columns respectively. The scale bars indicate 50 µm.

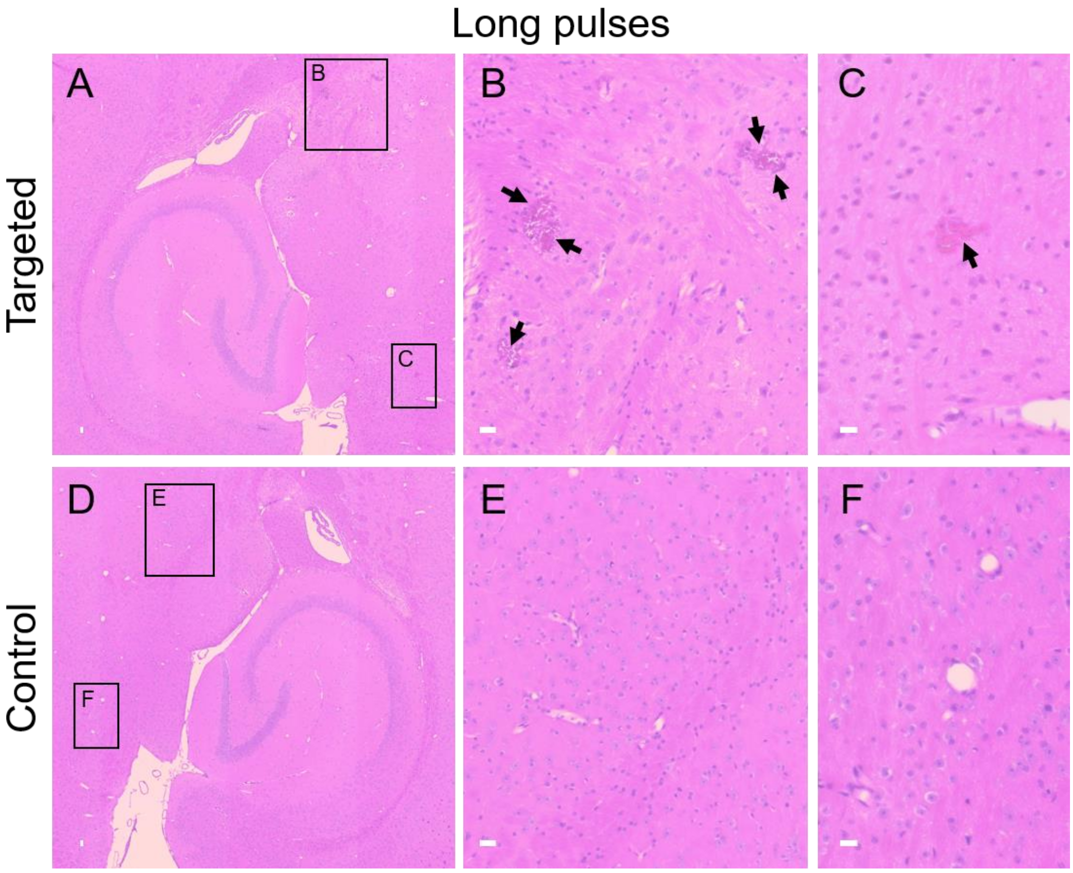

Figure 4.18. H&E staining on long-pulse-treated brains at 0.6 MPa to assess tissue damage: microscopic examination of H&E stained (A-C) left (targeted) and (D-F) right (control) hippocampi of long-pulse-treated brains show (B-C) histological damage at multiple sites within the ultrasound targeted hippocampus (arrows): red blood cell extravasation, microvacuolations and dark neurons. The black boxes show the enlarged regions in the middle and right columns respectively. The scale bars indicate 50 µm.

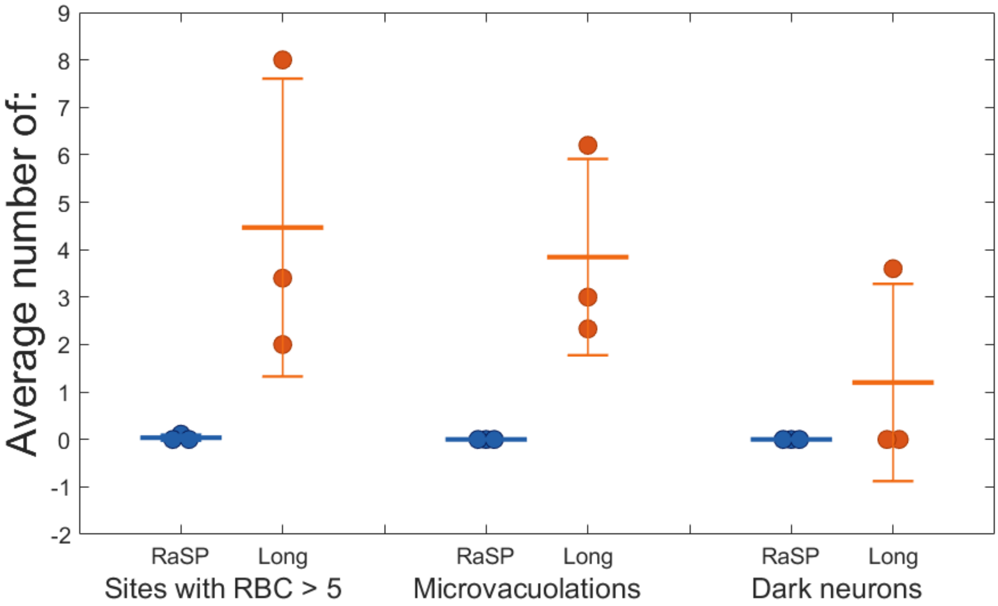

Figure 4.19. Number of sites with red blood cell extravasations, microvacuolations and dark neurons in RaSP and long pulse brains at 0.6 MPa: The average number of sites with more than five extravasated red blood cells (RBCs), microvacuolations and dark neurons is shown for (blue) RaSP and (orange) long-pulse-treated brains. This quantification was performed on nine H&E-stained slices per brain. In all RaSP brains, only one site with more than five extravasated RBCs and no sites with microvacuolations or dark neurons were observed. In long pulse brains, however, damaged sites were found in all brains. No significant differences were found between RaSP and long pulse brains ($P > 0.05$).

The achievement of the efficiency of liposome delivery to the brain should not cause issues with the safety of the brain. In the previous work at the NSB lab, it has been shown that no tissue damage was detected for RaSP sequence at 0.4 MPa. However, here, we sought to investigate the safety profile at higher pressure of 0.6 MPa, at which liposome delivery was achieved, in comparison with that of the lower pressure and brains treated with long pulses. No damage was observed via H & E staining in RaSP-treated brains at 0.4 or 0.6 MPa, except for a single site of red blood cell extravasation at the higher pressure (Figures 4.17 and 4.19). However, in long-pulse-treated brains, the damage was manifested in all brains in the form of RBC extravasations, microvacuolations and dark neurons (Figure 4.18-19). The long pulse results reflect are in agreement with other studies that have shown similar H&E results. [433,438,439] With RaSP we expected the higher pressure to lead to a higher chance of tissue damage occurring, however, the safety profile was found to be improved compared to long pulses.

For the ultrasound emitted at higher pressure of 0.6 MPa, larger sites of tissue damage were observed in long-pulse-treated brains as seen previously.[480,481] This damage is thought to be due to inertial cavitation,[482] however, it may not have long term effects.[419,483] This type of treatment may be suitable for certain applications such as for sonicating tumour cores.

The tissue damage was examined on brains extracted immediately after the ultrasound exposure without any recovery time, as this is hypothesised to be the time point of worst damage. Although it is expected that repair processes occur during the period of two hours, it is possible that the number of red blood cells extravasating increases over an initial period and would require further investigation.

4.2.4 *In vivo* delivery of THP-PL liposomes using focused ultrasound in mice model

Now that we have confirmed that PEGylated liposomes can be successfully delivered to the brain using the RaSP sequence of focussed ultrasound. However, optical imaging of the drug delivery of liposomes to the brain only works ex vivo as seen above. Optical imaging requires the isolation of brain samples to detect the delivered dose and localization of the dose. The optical imaging allows us to observe the liposomal delivery at the cellular level but the nuclear imaging of delivery of liposomes using focussed ultrasound would allow us to non-invasively monitor the delivery in real-time and at longitudinal time points.

To this end, PET imaging of ^{68}Ga-labelled PEGylated liposomes can be performed post their delivery to the brain using focussed ultrasound and microbubbles. However, in the absence of the focussed ultrasound setup in a radiation-controlled area, we were unable to perform this experiment. To circumvent this issue and exploit the advantage of the *in vivo* labelling potential of THP-PL liposomes introduced in Chapter 2, we delivered the THP-PL liposomes to the brain using either RaSP sequence of focussed ultrasound at 0.6 MPa (best conditions for delivery using RaSP while maintaining safety derived from previous experiments) or long pulses and then stained the brain slices ex vivo with neutralised $^{68}GaCl_3$ followed by autoradiography to obtain a proof of concept for the PET imaging experiment. These results are discussed in the next sections.

4.2.5.1 Synthesis of THP-PL liposomes

The THP-PL liposomes were synthesised and characterised as mentioned in Chapter 2 (section 2.2.2). In short, THP-PL was inserted into the lipid bilayer of PEGylated liposomes using a standard protocol, previously shown to allow the insertion of phospholipids without significant modification of the original properties of PEGylated liposomes. The product (THP-PL-liposomes) was analysed via radiolabelling, cryoelectron microscopy, nanoparticle tracking analysis and dynamic light scattering (DLS) studies. The size and zeta potential confirmed no change in liposomal properties and the radiolabelling confirmed the presence of THP on the liposomal surface. In summary, all this data indicated that THP-PL has been successfully incorporated into PEG(2k)-liposomes, with no major impact on the original liposomal properties.

4.2.5.2 Delivery quantification by *ex vivo* pretargeting

THP-PL liposomes were delivered to the brain using either RaSP or long pulses of focussed ultrasound. The opening of the blood-brain barrier during delivery was confirmed by the detected ultrasound signal due to the oscillation of microbubbles. The ex vivo slices were stained with buffered $^{68}GaCl_3$ followed by washing with water, PBS, and weak chelator DTPA or citrate to remove any non-specific bound ^{68}Ga.

Surprisingly, non-specific uptake was observed in the brain as seen in figure 20 which shows an autoradiography image of stained brain slice. ^{68}Ga stained whole brain slices and any specific hotspots were not observed. The resolution at which optical imaging resolved the uptake of liposomes at the cellular level is not possible with the autoradiography setup which might be a possible explanation for non-specific uptake observed in the brain. We hypothesised and expected larger hotspots in areas of high concentration of THP-PL-liposomes either in RaSP or long pulse treated brains but there were no differences observed at this mm-µm resolution. The other possible explanation of the non-specific uptake could be due to the presence of proteins in the brain such as transferrin in high concentrations leading to indiscriminate binding of high concentrations of ^{68}Ga to the brain even in the areas of low THP-PL liposome accumulation.

To further avoid the non-specific binding and obtain some positive results, various steps were performed which included increasing and lowering of brain tissue incubation times in buffered ^{68}Ga solution to provide optimal times for chelation with THP on the liposomal surface. However, no marked improvements were observed, and the radioactivity uptake was found all over the slice due to non-specific binding. ^{68}Ga incubated brain tissues were additionally incubated with chelator DTPA or to remove non-specific ^{68}Ga but did not result in any improvements.

To overcome the resolution limitation, optical imaging was performed on Fe incubated brain tissues to find areas of high Fe binding to the THP-PL-liposomes. We hypothesised that areas of high accumulation of THP-PL-liposome accumulation would show preferential accumulation of iron as THP is an excellent chelator for iron as well as gallium and thereby showing red hotspots which can be imaged using microscopy. However, no significant specific uptake of iron was observed under the microscope. Hence, the ex vivo staining did not provide us with a proof of concept of one of the first attempts of nuclear imaging of focussed ultrasound-mediated liposome delivery to the brain.

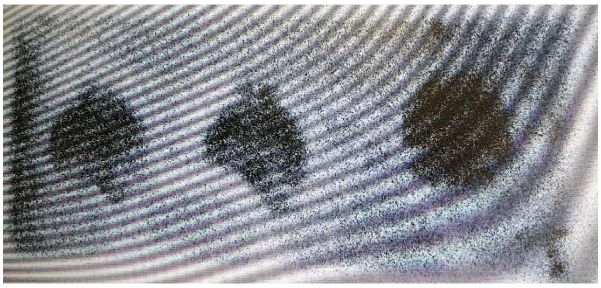

Figure 4.20. Autoradiography of the brain-stained tissue slices.

4.3 Conclusion

Rapid short ultrasound pulses are here shown to allow the delivery of 100 nm liposomes into the brain. Although the efficacy of liposome delivery with this specific RaSP sequence was lower than in long pulse-treated brains, an improved safety profile was observed. The detected dose and number of delivery spots were lower than with long pulses and a higher acoustic pressure was required to enable liposomes across the BBB with RaSP. On the other hand, only a single site of red blood cell extravasation was observed in RaSP brains at the higher pressure tested, while in long pulse brains signs of tissue damage were detected in all brains. The reduced delivery and safer profile of the RaSP results are probably due to the RaSP sequence inputting less energy and stimulating the vasculature more gently.

Neuronal uptake of the liposomes was observed with RaSP, although to a lower degree compared to long pulse-treated brains. Microglial uptake was only observed in brains treated with the higher pressure and after a two-hour recovery period, while no astrocyte uptake was observed in any of the brains. This indicates that drugs that target neurons can reach the desired brain regions by being delivered with this technology. Lower glial cell involvement was observed in RaSP compared to long pulse-treated brains. Within neurons, liposomes were observed in spotty-like patterns within the cytoplasm but not within the nucleus, which could, with further investigation, indicate the pathway of cellular uptake and excretion.

Although ultrasound emitted in a RaSP sequence has been shown here to deliver liposomes across the BBB, a lower delivery efficacy was achieved compared to long-pulse-treated brains. However, when emitting RaSP, the safety profile of liposome delivery was improved. We have yet to investigate whether therapeutically relevant concentrations of drugs carried by liposomes can be reached when emitting RaSP sequences. Such investigation will influence whether RaSP sequences can be used to efficiently deliver liposomes into the brain, which we plan on testing with doxorubicin-loaded liposomes in future work.

Despite the positive results reported above, the RaSP sequence has yet to be optimised for liposomal delivery. Currently, the main limitation of the RaSP parameters used in this study is the lower efficacy of delivery. It is widely believed that the magnitude and number of sites with increased BBB permeability are related to the degree of microbubble-vessel interactions in the ultrasound field [484–486]. In future work, experiments emitting an increased number of pulses within the period of highest microbubble presence (first few minutes), might lead to an increase in the number of liposome delivery sites. This could be done by increasing the pulse repetition frequency, burst repetition frequency and the number of pulses per burst. These changes could improve the efficacy of delivery while continuing to monitor its safety, to see if efficient damage-free delivery can be achieved with RaSP at this higher pressure (0.6 MPa). Ultimately, depending on whether an improved RaSP sequence can demonstrate delivery of therapeutically relevant drug concentrations in the brain, the choice of ultrasound sequence will depend on the targeted disease and tissue region to be treated, with trade-offs in efficacy and safety depending on this choice.

Here, we have shown liposome delivery in a healthy mouse brain. However, liposomes are generally used to deliver drugs to diseased tissue, the treatment of tumours being the most common application. A tumour environment has different permeability, interstitial pressure, and vasculature heterogeneity from the normal brain [487,488]. In future work, doxorubicin-loaded liposomes could be delivered in a glioma mouse model to establish how these factors change the delivery patterns observed in this study. In terms of vascular permeability, the normal brain has an intact BBB while many tumours have a leakier BBB. Therefore, we expect the BBB permeability of the healthy mice used in these experiments to be the worst-case scenario.

We used the fluorescent DiD dye to assess the location of liposome delivery in the brain with the assumption that the dye stays embedded in the liposomal membrane throughout the experiment. The DiD fluorophore was chosen as it dissociated to a very limited extent compared to other commonly used fluorescently labelled lipids [456]. In addition, confirming the literature, we found that the DiD fluorophore was not fluorescent when in water but was strongly fluorescent within the liposome bilayer [489,490]. Therefore, we assumed that the fluorescence signal detected was most probably from the DiD within the liposome bilayer rather than free within the brain. However, we cannot exclude the possibility that some of the fluorescence that is being detected is due to the fluorophore dissociating from the liposomal membrane and entering a different lipid membrane such as a cell membrane where it would be fluorescent. By staining cell membranes in future work, we could explore whether they colocalise with the dye, which would indicate a dye exchange between liposomes and cellular lipid membranes.

Future work will also involve looking into the effect of ultrasound and microbubbles on liposome drug release. Fluorophores and drugs embedded within the liposome bilayer or loaded within the liposome core could be released within the bloodstream due to the ultrasound or microbubble activity. *In vitro* work has previously shown that drugs can be released when emitting ultrasound with microbubbles at 0.17 and 1.5 MPa (at 1 MHz), with more release at the lowest pressure [491]. In high intensity focused ultrasound applications, on the other hand, temperature increases are used to release drugs from thermally sensitive liposomes [102,492,493]. However, most of these studies either injected liposomes that were more sensitive to ultrasound or attached the liposomes to the microbubbles themselves to encourage release during their oscillation.

If drugs were to be released within the vasculature of the ultrasound targeted region, more targeted delivery of drugs would still occur compared to systemic administration of the drug alone. However, toxicity values would need to be assessed.

In our case, if free DiD dye was being released into the bloodstream, it would not be fluorescent. Therefore, the likelihood of us interpreting the fluorescent signal as being from free dye extravasating into the brain is unlikely. In the future, we plan to perform biodistribution studies to investigate how ultrasound affects accumulation in the brain in comparison with other organs such as the heart, liver, spleen, lungs, and kidneys. This could also give us a better idea of whether the dye or drugs loaded within the liposomes are being released within the bloodstream and then being excreted via other organs. Staining for blood vessels could confirm whether any liposome uptake is occurring within endothelial cells. Lastly, by staining for lysosomes, we could confirm whether liposomes are uptaken within these structures in the cytoplasm of neurons and further experiments could be performed to investigate the mechanism of liposome uptake within cells and delivery across the BBB.

Finally, the desired nuclear imaging (specifically PET imaging) of the liposomal delivery using focussed ultrasound will allow us to answer some of the key questions above non-invasively and in real time. However, due to logistical limitations, the radioisotope work could not be performed in the focussed ultrasound laboratory. To circumvent this issue, we performed the *ex vivo* validation using THP-PL-liposomes but with inconclusive results. In the future, the PET imaging of brain delivery of radiolabelled liposomes will allow us to obtain real-time information on brain delivery and the effectiveness of RaSP focussed ultrasound. It will also us effectively and quickly measure the impact of different ultrasound parameters to better develop this tool for clinical translation.

5 METHODS

This chapter summarises the materials and methods for each research chapter within the thesis. Each subsection summarises the methods for each chapter.

5.1 Chapter 2

5.1.1 Materials

5.1.1.1 Equipment and Instrumentation

All NMR spectra were acquired on an NMR Bruker Avance III HD NanoBay 400 MHz NMR spectrometer (Ascend magnet) based at King's College NMR facility. The NMR data was analysed using Bruker Topspin 3.5. High-resolution mass spectrometry was performed on Autoflex, Bruker Daltonics at Mass spectrometry facility at Waterloo campus, King's College London or National Mass Spectrometry facility at Swansea on Bruker ultrafleXtreme MALDI-TOF/TOF. Size exclusion chromatography (SEC) was performed on a Superose 10/30 column (GE Healthcare Life Sciences) run at 0.5 mL/min in PBS. UV detection was performed at 214 and 280 nm on a GE Purifier ÄKTA™ HPLC. Radioactivity for all samples was measured in a gamma counter (LKB Wallac 1282 Compugamma S) or dose calibrator (Capintec. Inc.). The analytical software used for radioTLC measurement and analysis was Laura (Lablogic). The centrifuge used was a Hettich MIKRO 20. Lyophilisation was performed using an Edwards Freeze Dryer Modulyo. Hydrodynamic size and zeta potential were measured on Zetasizer NanoZS from Malvern Panalytical using specialised plastic cuvettes. The electron microscopy facility at Imperial College London and part of the London Centre for Nanotechnology was used to image the liposome samples under CryoEM.

5.1.1.2 Reagents

All inorganic and organic chemicals were of the highest purity grade available and used as received. 1,2-distearoyl-sn-glycero-3-phosphoethanolamine-N-[amino(polyethylene glycol)-2000] ammonium salt powder (DSPE-PEG(2000) Amine) was obtained from Avanti Polar Lipids, Inc. (Alabaster, AL) via Merck. Isothiocyanate derivative of tris(Hydroxypyridinone) was obtained from CheMatech (Dijon, France) as a white solid. Plain HSPC/Choline/mPEG2000-DSPE-liposomes were either obtained from FormuMax Scientific Inc., USA or collaborator Barenholz lab (Israel) as a translucent whitish liquid in a clear glass vial. Primuline dye, dimethyl sulphoxide, chloroform, and diisopropylethylamine were obtained from Sigma (St. Louis, MO). Deionised water of resistivity > 18 MΩ (MilliQ) was used for all aqueous preparations. Deionised water treated with Chelex-50 resin was used for all metal-free chelation reactions. Gallium-68 was eluted as $^{68}GaCl_3$ from an Eckert & Ziegler $^{68}Ge/^{68}Ga$ generator in ultra-pure HCl (5 mL, 0.1 M) manufactured to good manufacturing practice (GMP) requirements (ABX, Germany). Gallium-67 was obtained from Guy's radiopharmacy as ^{67}Ga-citrate (5.5 mL, 600 MBq) manufactured for clinical use in patients.

5.1.2 Synthesis and characterisation of THP-Phospholipid

For the synthesis of the THP-phospholipid, the reaction was performed between the isothiocyanate derivative of the tris(hydroxypyridinone) and the amine derivative of DSPE-PEG (2000) phospholipid. THP-Bz-NCS (tris(hydroxypyridinone) isothiocyanate) (5 mg, 0.0052 mmol) was dissolved in DMSO (250 µL). DSPE-PEG (2000)-amine (1,2-distearoyl-sn-glycero-3-phosphoethanolamine-N-[amino(polyethylene glycol)-2000) (10 mg, 0.0035 mmol) was dissolved in DMSO (250 µL). The phospholipid solution was added to the THP solution along with 5 µL of DIPEA (Diisopropyl ethylamine). The reaction was continued at R.T. for 24 h. TLC on silica gel GF (75:36:6

chloroform/methanol/water) was used for monitoring the progress of the reaction, showing a new spot below the amino-PEG-DSPE spot due to the formation of the product. Both the reactant and product were confirmed by charred staining with primuline dye (lipid staining dye). The disappearance of amino-PEG-DSPE (R_f= 0.76) from the reaction mixture was also confirmed by ninhydrin spray. For purification, the DMSO concentration was diluted to 5 % using deionised water. The supernatant was dialyzed against deionised water (3 x 2000 mL) for over 24 hours. The dialysate containing only the product THP-PL (single spot by TLC, MW: 3733 g/mL), was collected and lyophilised. The purified THP-PL was dissolved in deuterated chloroform and ^{1}H were obtained (H NMR (400 MHz, $CDCl_3$) δ 1H NMR (400 MHz, DMSO) δ 7.45 (s, 1H), 7.27 (s, 1H), 7.19(s, $CHCl_3$), 6.93 (s, 1H), 6.72 (s, 2H), 5.71(s, 3H), 5.15 (s, 1H), 4.32-4.29 (m, 4H), 4.09 (s, 2H), 3.94 (s, 2H), 3.76 (m, 2H), 3.74 (s, 6H), 3.57- 3.55 (m, 180H), 3.42- 3.38 (m, 9H), 3.32(s, 2H), 2.38 (s, 9H), 2.25-2.19 (m, 2H), 2.05 (m, 6H), 1.98 (s, 4H) 1.94 (m, 4H)1.81 (s, 4H), 1.51 (s, 2H), 1.18 (s, 56H), 0.83- 0.76 (m, 6H)). THP-PL was also characterised by high-resolution mass spectrometry (z = 2 species in the range 1700-2000 m/z (peak found at 1866; calculated for THP-PL = 1866), the z = 3 species in the range 1200-1350 m/z (peak found at 1245; calculated for THP-PL = 1244), and the z = 4 species in the range 850-1000 m/z (peak found at 938; calculated for THP-PL = 933))(Figure 2.6 and 2.7).

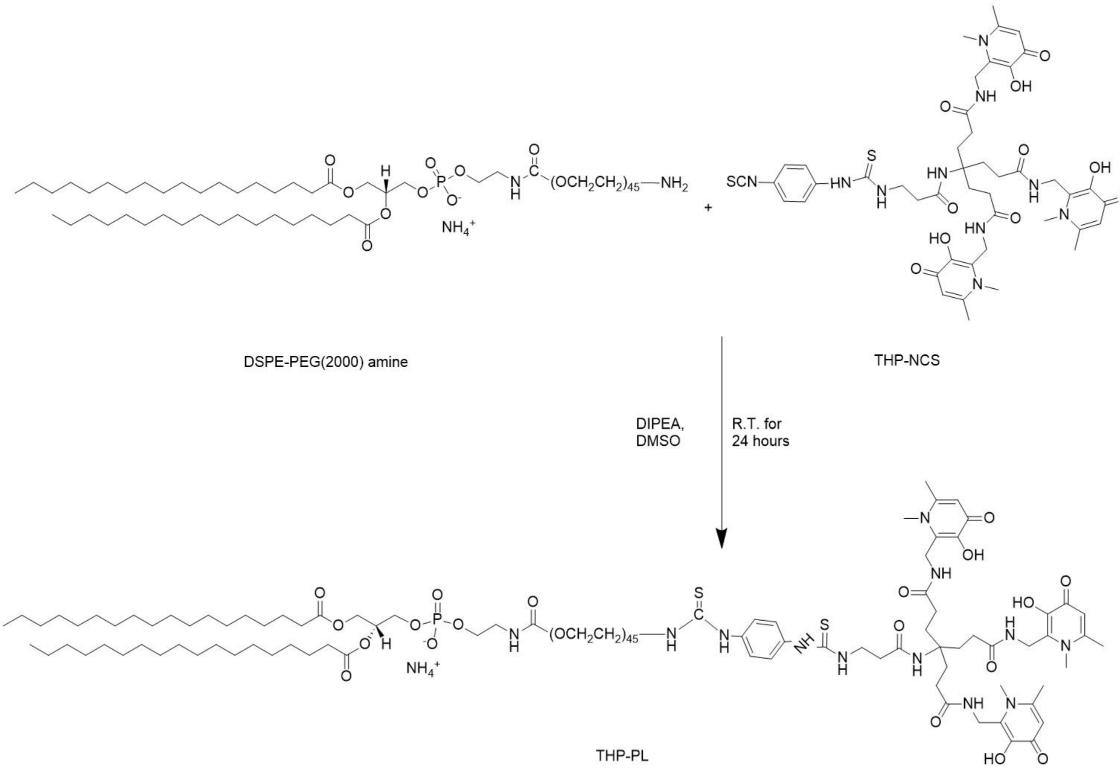

Figure 5.1. Synthesis of THP-PL: DSPE-PEG2000 amine was reacted with the isothiocyanate derivative of THP to give the THP-PEG-phospholipid (THP-PL)

5.1.3 Synthesis and characterisation of THP-PL-liposomes

THP-PL was incorporated into the bilayer of PEG(2k)-liposomes by equilibrating the Doxebo dispersion (100 µL, 24.4 mM) and the THP-PL dispersion (0.05 mg, 100 µL) at 50°C. The equilibrated dispersions were mixed and incubated under constant shaking for 30 minutes to give THP-PL-liposomes. The formed THP-PL-liposomes were purified using a PD minitrap G-25 size exclusion column (GE Healthcare) following the manufacturer's gravity protocol. Dynamic light scattering quantified the change in hydrodynamic size, zeta potential and PDIs of the PEG(2k)-liposomes pre- and post-insertion reaction. The formed THP-PL-liposomes were also characterised by radiolabelling with ^{68}Ga to examine the presence of THP on the surface.

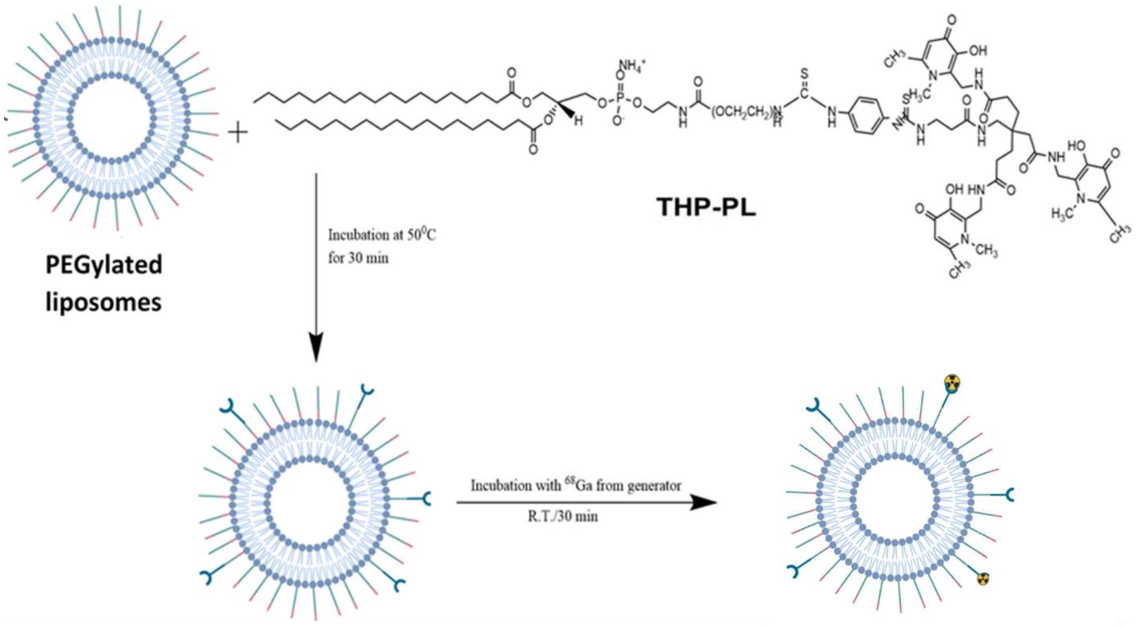

Figure 5.2. Synthesis of THP-PL-liposomes: THP containing PEGylated liposomes are synthesised by insertion of THP-PL in preformed liposomes at mild heating below the phase transition temperature. The purified liposomes are radiolabelled to confirm the incorporation of THP on the liposomal surface as shown above. Created with BioRender.com.

5.1.4 Nanoparticle Tracking Analysis (NTA)

The concentration and the hydrodynamic size of synthesised THP-PL-liposomes were measured by NTA using NanoSight LM10 and NTA software v3.2 (Malvern Panalytical). The stock sample was diluted to achieve ~100 particles/viewing frame. Measurements were made in triplicates for 60 s with a 488 nm laser, for up to three serial dilutions of the sample.

5.1.5 Cryo-Electron Microscopy

QUANTIFOIL R 2/2 carbon grids (mesh: Cu 300, #234901; Agar Scientific) were plasma discharged for 50 s at 30 SCCM gas flow in Nanoclean 1070 (Fischione instruments). Aliquots (5 µL) of THP-PL-liposomes or PEGylated liposomes were deposited on the carbon grids in Vitrobot Mark IV (FEI). The excess liquid was removed by blotting with filter paper (Agar Scientific); Parameters: blotting time = 2 s, wait time = 30 s, and blotting force = 2. The grids were instantly frozen in liquid ethane (−188 °C) and maintained in liquid N_2 (−196 °C) in a grid box and transferred into a cryo-transfer holder. CryoEM of these samples was recorded on TECNAI 12 G2 (FEI) system interfaced with a TemCam-F216 camera and operated using Temmenu v4 software (Tietz Video & Image Processing Systems GmbH, Germany). Parameters used to capture images are as follows: electron acceleration = 120 kV, magnification = 52,000×, acquisition time = 1 s, and spot size = 5. Paul Simpson from Imperial College London performed these measurements on the CryoEM.

5.1.6 Radiochemistry

5.1.6.1 Buffering of $^{68}GaCl_3$ used for labelling and purification.

^{68}Ga was eluted from ^{68}Ge/^{68}Ga generator with 0.1 N HCl. The peak radioactivity containing 1 mL elution was used for radiolabelling after buffering with 3.4 M Sodium acetate/1 M Sodium carbonate to pH 6. Buffered ^{68}Ga was used for all radiolabelling and i.v. injections after removal of colloids using saline pre-rinsed centrifugal filter MW cutoff 50 kDa.

5.1.6.2 Radiolabelling of THP-Phospholipid

THP-phospholipid conjugate was radiolabelled with ^{68}Ga. THP-Bz-SCN, DSPE PEG (2000)-amine and ^{68}Ga are used as controls. THP-phospholipid (50 µL, 1 mg/mL) was added to ^{68}Ga (< 1 MBq, 20 µL) and incubated at R.T. for 30 minutes. RadioTLC on ITLC silica gel GF was performed in mobile phase A (75:36:6 chloroform/methanol/water, Unbound ^{68}Ga $R_f = 0$; ^{68}Ga-THP $R_f = 0$; ^{68}Ga colloid $R_f=0$; ^{68}Ga-THP-PL $R_f = 0.5-0.7$) or mobile phase B (0.175 M citric acid and 0.325 M trisodium citrate in water, Unbound ^{68}Ga $R_f = 0.7–1$;

^{68}Ga-THP $R_f = 0$; ^{68}Ga colloid $R_f=0$; ^{68}Ga-THP-PL $R_f = 0\text{-}0.1$) enabled separation of different radioactive species for qualitative analysis. Quantification of radiochemical yield of ^{68}Ga radiolabelling was performed via PD minitrap G-25 size exclusion column (GE healthcare) following the manufacturer's gravity protocol.

5.1.6.3 Radiolabelling of THP-PL-PEG (2k)-liposomes

Further characterisation of the THP-PL-liposomes was performed *via* ^{68}Ga radiolabelling. THP-PL and unmodified PEG (2k)-liposomes were radiolabelled as controls. The radiolabelling was performed by adding 50 µL (2 MBq) of ^{68}Ga to the test samples. The radiolabelling reaction mixture was incubated for 30 minutes. The reaction was purified via PD minitrap G-25 size exclusion column (GE Healthcare) following the manufacturer's gravity protocol.

5.1.6.4 Synthesis of ^{67}Ga-THP-PL-liposomes

^{67}Ga-citrate (2 mL, 518 MBq, 5mL, Guy's radiopharmacy) was aliquoted in a vial and volume was made up to 5 mL with chelex-treated H_2O. The whole volume was loaded on the SEP-PAK silica light cartridge multiple times via a syringe until >80% radioactivity was loaded on the column (3 times optimum). Post loading, the loaded column was washed with 5 mL chelex H_2O @ 1mL min^{-1} thrice. $^{67}GaCl_3$ is eluted with metal-free HCl (0.1 M, 50 µL). The hottest fractions were buffered to pH 6 and used to radiolabel THP-PL-liposomes as mentioned above in section 5.1.6.3.

5.1.7 *In vitro* stability

^{68}Ga-THP-PL-liposomes (750 µL, 10 MBq, 6 mmol) were incubated at 37°C in human serum. Aliquots of the test sample were taken at different time points for stability study and applied to SEC HPLC at 0, 90 and 180 minutes. 1 mL fractions were eluted in PBS and UV, radioactivity signal is recorded.

The serum stability of ^{67}Ga-THP-PL-liposomes was also determined using the serum stability protocol mentioned above.

5.1.8 *In vitro* pretargeting methods

5.1.8.1 *In vitro* ^{68}Ga complexation tests -1

THP-PL-liposomes (200 µL, 4 mM) were added to commercially available human serum obtained from Sigma Aldrich (containing citrate as an anti-coagulant) (200 µL) and kept under incubation at 37°C for 60 minutes. Buffered ^{68}Ga was added to serum incubated THP-PL-liposomes and incubated at 37°C. Aliquots of the incubated reaction were collected at 15, 30 and 45 minutes, applied to SEC HPLC, eluted with PBS in 30 fractions of 1 mL, and measured for UV signal and radioactivity.

5.1.8.2 *In vitro* ^{68}Ga complexation tests -2

THP-PL-liposomes (200 µL, 4 mM) were added to metal-free human serum (200 µL) obtained from human blood samples post-filtration through BD Gold SST vacutainer® tubes and kept under incubation at 37°C for 60 minutes. Buffered ^{68}Ga was added to serum incubated THP-PL-liposomes and incubated at 37°C. Aliquots of the incubated reaction were collected at 15, 30 and 45 minutes, applied to SEC HPLC, eluted with PBS in 30 fractions of 1 mL, and measured for UV signal and radioactivity.

5.1.9 *In vivo* PET imaging

5.1.9.1 Animals

Animal imaging studies were carried out in accordance with British Home Office regulations governing animal experimentation (licenses: PBBA9A243 and P9C94E8A4). All *in vivo* experiments were conducted on healthy, female Balb/c mice (8-9 weeks old) obtained from Charles River UK Ltd.

5.1.9.2 Preclinical PET/CT and SPECT/CT scanners

Each mouse (n=3-5, BALB/c, female, aged 6–8 weeks, 17–20 g body weight) was anaesthetised by inhalation of isoflurane (2–3% in oxygen). The tracer/molecule of interest was injected via tail vein intravenous injection. The mouse was scanned in either nanoscan *in vivo* preclinical PET/CT imaging system (1:5 coincidence mode; 5-ns coincidence time window) and SPECT/CT imaging system (start frame: 3 mm; end frame: 107 mm; frame time:83 s, scan time: ~1 h) (Mediso medical imaging systems, Budapest, Hungary) depending on the tracer injected. PET/CT images were reconstructed using Tera-Tomo 3D reconstruction (400–600 keV energy window, 1–3 coincidence mode, 4 iterations and subsets) at a voxel size of (0.4 × 0.4 × 0.4) mm^3 and corrected for attenuation, scatter, and decay. The data were binned into 17 frames (1 × 1, 10 × 3, 5 × 5 and 1 × 4 min) for dynamic analysis. SPECT images were reconstructed using HiSPECT standard method.

5.1.9.3 Pretargeting of THP-PL-liposomes in healthy animals

For negative control group 1, the mice (n=3) were anaesthetised and injected i.v. with ^{68}Ga (10 MBq, 100 µL). The mice were kept anaesthetised for 2 hours post-injection and then imaged via *in vivo* preclinical PET/CT imaging system.

For pretargeting test group 2, the mice (n=4) were anaesthetised and injected i.v. with THP-PL-liposomes (50µM/mL lipid concentration, 100 µL) at t = -3 h. At t = 0 h, mice were anaesthetised and injected i.v. with ^{68}Ga (10 MBq, 100 µL). The mice were kept anaesthetised for 2 hours post-injection and then imaged via *in vivo* preclinical PET/CT imaging system. At t=22 h, mice were anaesthetised and injected i.v. with ^{68}Ga (10 MBq, 100 µL). The mice were kept anaesthetised for 2 hours post-injection and then imaged via *in vivo* preclinical PET/CT imaging system.

For positive control group 3, the mice (n=6) were anaesthetised and injected i.v. with ^{67}Ga-THP-PL-liposomes (3 MBq, 50µM/mL lipid concentration, 100 µL) and imaged at t=2h, 24 h via a preclinical SPECT-CT imaging system.

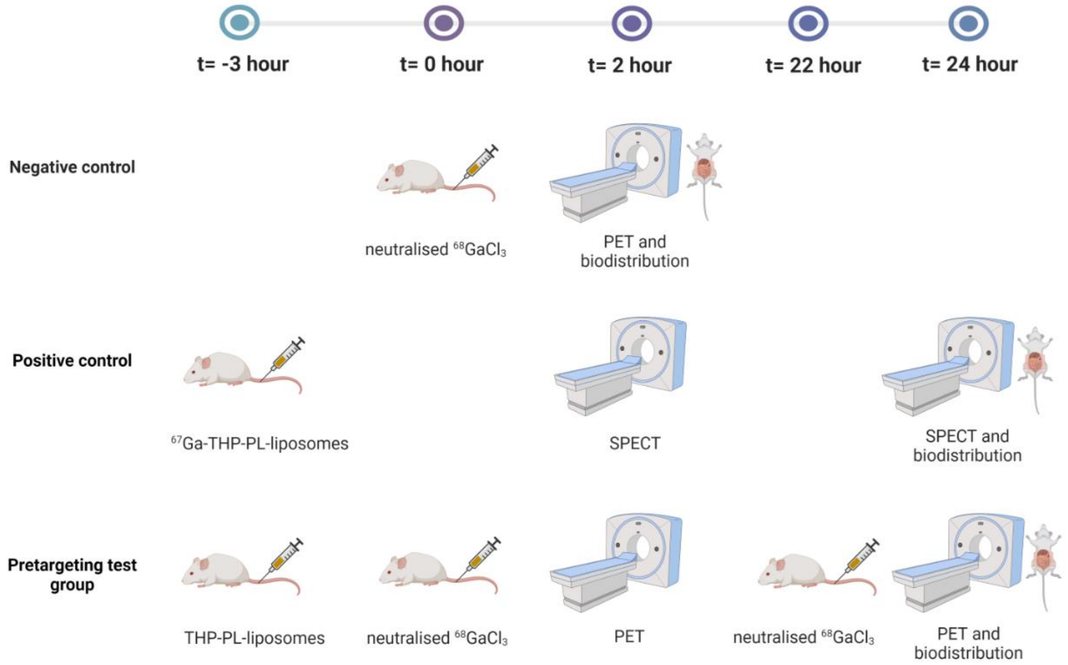

Figure 5.3. Scheme of *in vivo* pretargeting experiment using metal chelation approach: Negative control: Group 1: ^{68}GaCl$_3$; Pretargeting: Group 2: THP-PL-liposomes followed by introduction of ^{68}GaCl$_3$; Positive control: Group 3: ^{67}Ga-THP-PL-liposomes. Created with BioRender.com.

For the blood kinetic study, blood was withdrawn from a puncture made on the tail vein using 20 µl capillary tubes at 3, 6, 9, 22 and 25 h p.i. The collected blood was measured and counted for radioactivity and %ID/g was determined at each time point.

The mice were culled post-scan by cervical dislocation and required organs were collected, weighed, and measured for radioactivity along with the standards and *ex vivo* biodistributions were determined.

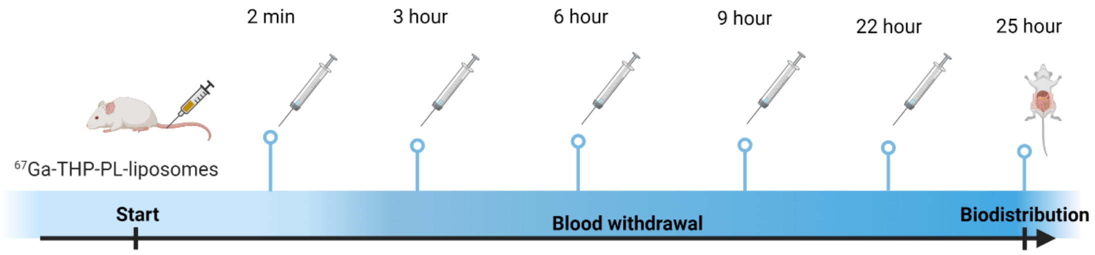

Figure 5.4. Scheme of blood kinetic study to determine the blood half-life of THP-PEG-PL liposomes. Created with BioRender.com.

5.1.9.4 Pretargeting of bone targeting THP-Pam in healthy animals

THP-Pam was synthesised in our laboratory by George Keeling. The synthesis and radiolabelling of THP-Pam are described in detail in this paper.[265]

For THP-Pam *in vivo* labelling group, the mice (n=4) were anaesthetised and injected i.v. with THP-Palmidronate (50 ug in 100 µL saline) at t=-3 h. At t=0 h, mice were anaesthetised and injected i.v. with ^{68}Ga (10 MBq, 100 µL). The mice were kept anaesthetised for 2 hours post-injection and then imaged via *in vivo* preclinical PET/CT imaging system. At t=24 h, mice were anaesthetised and injected i.v. with ^{68}Ga (10 MBq, 100 µL). The mice were kept anaesthetised for 2 hours post-injection and then imaged via *in vivo* preclinical PET/CT imaging system. The mice were culled post-scan by cervical dislocation and required organs were collected, weighed, and measured for radioactivity in a gamma counter.

For THP-Pam positive control group, the mice (n=4) were anaesthetised and injected with radiolabelled ^{68}Ga-THP-Pam (22 MBq, 100 µL) which was imaged at 1 h p.i. The mice were culled post-scan by cervical dislocation and required organs were collected, weighed, and measured for radioactivity in a gamma counter. Serial standard dilution of the injected radiotracer was measured alongside the collected organs to calculate the percentage injected dose per organ (%ID/g).

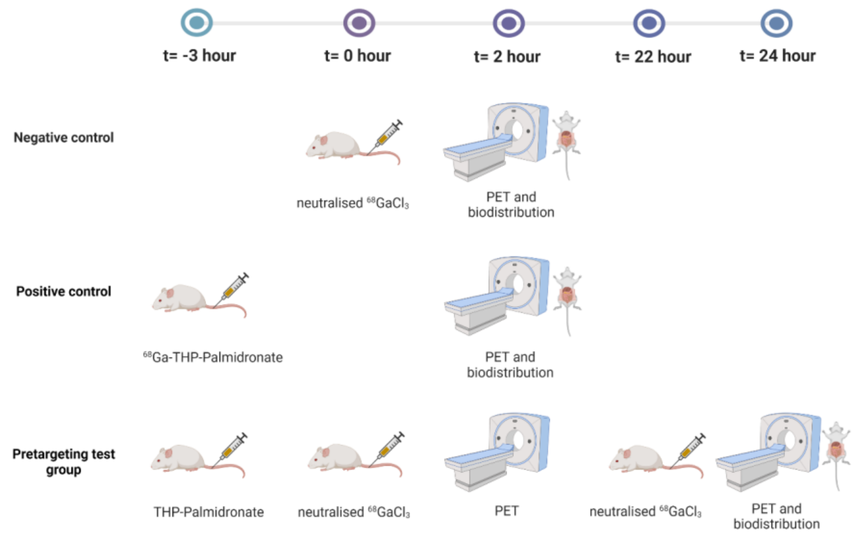

Figure 5.5. Scheme of pretargeting experiment of bone tracer THP-Pam using metal chelation approach: Negative control: Group 1: ^{68}GaCl$_3$; Pretargeting: Group 2: THP-Pamidronate followed by introduction of ^{68}GaCl$_3$; Positive control: Group 3: ^{67}Ga-Palmidronate. Created with BioRender.com.

5.1.10 Analysis

The analysis of the reconstructed *in vivo* images is performed using the VivoQuant 3.5 (Invicro Inc.). For image quantification, regions of interest were drawn over the knees for bones, heart as a measure of the blood pool, kidneys, lungs, bladder, spleen, liver, muscles, and brain. All numerical data were analysed on either GraphPad Prism 8 or advanced versions. Data are presented as mean ± standard deviation (SD) unless stated otherwise.

5.2 Chapter 3

5.2.1 Materials

5.2.1.1 Equipment and Instrumentation

Nuclear magnetic resonance (NMR) data were acquired on a Bruker 400 MHz and analysed using MestReNova software. High-resolution mass spectrometry was performed on Autoflex, Bruker Daltonics at Mass spectrometry facility at Waterloo campus, King’s College London or National Mass Spectrometry facility at Swansea on Bruker ultrafleXtreme MALDI-TOF/TOF. RadioHPLC experiments were performed on an Agilent 1260 Infinity instrument with ultraviolet (UV) detector at wavelength 254 nm and radioactivity detector at Lablogic Flow-Count detector with Bioscan Inc. B-FC-3200 photomultiplier tube detector. The data was analysed using Laura software. Liquid chromatography/mass spectrometry (LC/MS) data were acquired on an Agilent 1200 Series Liquid Chromatograph with UV detector at 254 nm, interfaced with an Advion Expression CMS mass spectrometer with electrospray ionisation (ESI) source. Preparative HPLC was performed on Agilent Technologies Prostar instrument interfaced with 410 Autosampler and 440-LC fraction collector. Silica gel aluminium TLC plates coated with fluorescent indicator F254 were purchased from Merck millipore. Slide-A-Lyzer^{TM} Dialysis Cassettes 3.5 K MWCO, 3 mL were used for purification were obtained from Sigma. All cartridge purifications were performed on Sep-Pak Light, Plus Light tC18, C18, or Silica Cartridges. Radio ITLC was developed on Agilent Technologies glass microfibre chromatography paper impregnated with silicic acid. Radio instant thin-layer chromatography (ITLC) samples were recorded using a Lablogic Flow-count TLC scanner and a BioScan B-FC-3200 PMT detector and analysed using Laura software. Size exclusion chromatography (SEC) was performed on a Superose 10/30 column (GE Healthcare Life Sciences) run at 0.5 mL/min in PBS. UV detection was performed at 214 and 280nm on a GE Purifier ÄKTA™ HPLC. Manual SEC purification was PD MiniTrap™ G-25 Medium size exclusion column containing 2.1 mL Sephadex resin (GE healthcare). Radioactivity for all samples was measured in a gamma counter (LKB Wallac 1282 Compugamma S) using EdenTerm software or dose calibrator (Capintec. Inc.). The centrifuge used was a Hettich MIKRO 20. Lyophilisation of purified samples was performed using an Edwards Freeze Dryer Modulyo. Hydrodynamic size and zeta potential were measured on Zetasizer NanoZS from Malvern Panalytical using specialised plastic cuvettes. The electron microscopy facility at Imperial College London was used to screen the liposome samples under CryoEM.

5.2.1.2 Reagents

All inorganic and organic chemicals were of the highest purity grade available and used as received. 1,2-distearoyl-sn-glycero-3-phosphoethanolamine-N-[amino(polyethylene glycol)-2000] ammonium salt powder (DSPE-PEG(2000) Amine) was obtained from Avanti Polar Lipids, Inc. (Alabaster, AL) via Merck. Isothiocyanate derivative of tris(Hydroxypyridinone) was obtained from CheMatech (Dijon, France) as a white solid. TCO-PEG4-NHS ester (trans-Cyclooctene-PEG4-NHS ester) and 6-Methyl-Tetrazine-Amine (HCl salt) were obtained from Jena Biosciences via Stratech Scientific as an oily, clear liquid and pinkish solid respectively. Plain HSPC/Choline/mPEG2000-DSPE-liposomes were obtained from FormuMax Scientific Inc., USA as a translucent whitish liquid in a clear glass vial. Primuline dye, Dimethyl sulphoxide, Chloroform, Diisopropylethylamine were obtained from Sigma (St. Louis, MO). Deionised water of resistivity more than 18 MΩ (MilliQ) was used for all aqueous preparations. Deionised water treated with Chelex-50 resin was used for all metal free chelation reactions. Gallium-68 was eluted as $^{68}GaCl_3$ from an Eckert & Ziegler $^{68}Ge/^{68}Ga$ generator in ultra-pure HCl (5 mL, 0.1 M) manufactured to good manufacturing practice (GMP) requirements (ABX, Germany). Gallium-67 was obtained from Guy's radiopharmacy as ^{67}Ga-citrate (5.5 mL, 600 MBq) manufactured for clinical use in patients.

5.2.2 Purification methods

5.2.2.1 HPLC methods

The following HPLC/FPLC methods were used in this chapter

Method 1. Analytical HPLC method for LC/MS

Solvent A= Water (0.1% Trifluoroacetic acid v/v), Solvent B= Acetonitrile (0.1% Trifluoroacetic acid v/v)

TIME (MIN)	FLOW RATE (ML MIN-1)	% A	% B
0	1	95	5
2	1	95	5
11	1	5	95
12	1	5	95
12.1	1	95	5
15	1	95	5

Column: Agilent Eclipse XDB-C18 column (4.6 x 150 mm, 5 µm)

Method 2. Semi-prep HPLC method

Solvent A= Acetonitrile (0.1% Trifluoroacetic acid v/v), Solvent B= Water (0.1% Trifluoroacetic acid v/v)

TIME (MIN)	FLOW RATE (ML MIN-1)	% A	% B
0	4	5	95
2	4	5	95
52	4	50	50
62	4	5	95

Column: Agilent Zorbax XDB C18 (21.2 x 150 mm, 5 µm)

Method 3. Analytical radioHPLC method

Solvent A= Water (0.1% Trifluoroacetic acid v/v), Solvent B= Acetonitrile (0.1% Trifluoroacetic acid v/v)

Time (min)	Flow rate (mL min-1)	% A	% B
0	1	95	5
2	1	95	5
11	1	5	95
12	1	5	95
12.1	1	95	5
15	1	95	5
Column: Agilent Eclipse XDB-C18 column (4.6 x 150 mm, 5 µm)			

Method 4. Serum stability HPLC method

Solvent A = phosphate buffered saline

Time (min)	Flow rate (ml min^{-1})	Solvent A (%)
0	1	100
40	1	100
Column: Phenomenex BioSep SEC-s2000 column (300 x 7.8 mm, 5 µm)		

Method 5. FPLC method

Solvent A = phosphate buffered saline

Time (min)	Flow rate (ml min^{-1})	Solvent A (%)
0	0.5	100
30	0.5	100
60	0.5	100
Column: Superose 6 increase 10/300 GL column (bed volume:24 ml)		

5.2.2.2 Size exclusion purification method

A G-25 size exclusion column pre-equilibrated with 15 column volumes of 0.9% filtered saline was used. The test sample for purification is applied to the column in 500 µL Volume, followed by 750 µL fractions which are collected in separate vials. Liposomes elute in the first 750 µL fraction as seen in figure below.

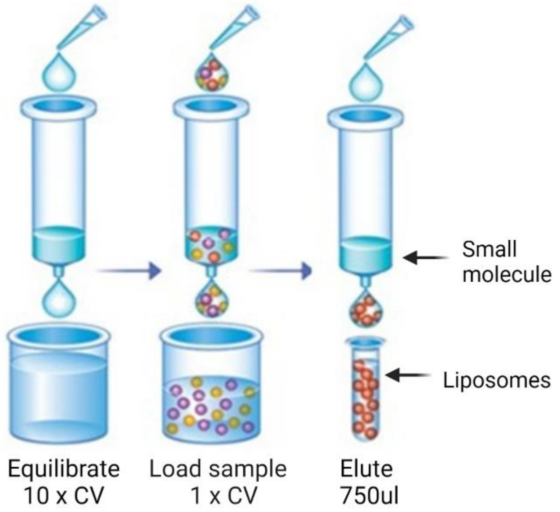

Figure 5.6. Procedure for purification of liposomes using size exclusion chromatography column. Created with BioRender.com.

5.2.3 Synthesis and characterisation of TCO-phospholipid

TCO-PEG$_4$-NHS ester (trans-Cyclooctene-PEG4-NHS ester) (8.2 mg, 0.0159 mmol, 3 equivalents) was dissolved in DMSO (1 mL) followed by addition of DSPE-PEG (2000)-amine (1,2-distearoyl-sn-glycero-3-phosphoethanolamine-N-[amino(polyethylene glycol)-2000) (15 mg, 0.0053 mmol, 1 equivalent). 20 µl of DIPEA (Diisopropyl ethylamine) was added to the reaction mixture to initiate the reaction. The reaction was stirred at 40 ^{0}C, and the progress of the reaction was checked periodically using TLC on silica gel GF developed in solvent system (75:36:6 chloroform/methanol/water) and stained with either ninhydrin solution or primuline dye. The reaction was stirred overnight and the disappearance of DSPE-PEG (2000)-amine spot on the TLC confirmed the completion of the reaction. The reaction was diluted to 5% DMSO/water and dialyzed against PBS for 4 hours followed by deionised water (3 x 2000 mL) for over 24 h. The purified dialysate TCO-Phospholipid was lyophilised, weighed (reaction yield: 96%) and stored at -20^{o}C until further use. The purified TCO-PL was dissolved in $CDCl_3$ and ^{1}H, ^{12}C was obtained (^{1}H NMR (400 MHz, CDCl3) δ 6.66 (s, 1H), 5.57-5.53 (m, 2H)

5.17-5.14 (m, 1H), 4.67 (s, 1H), 4.23-4.06 (m, 6H), 4.18 (s, 2H), 3.76-3.47 (m, 196H), 3.40-3.37 (s, 2H), 3.28 (s, 2H), 2.69-2.66 (t, 2H), 2.55-2.52 (t, 2H), 2.42 (s, 1H), 2.27-2.21 (m, 4H), 2.10-2.01 (m, 4H), 1.891.84 (m, 6H), 1.74 (m, 2H), 1.70 (m, 2H), 1.19 (s, 56H), 0.81 (t, 6H)) (Figure 3.8).

TCO-PL was further characterised by High-resolution mass spectrometry at NMSF Swansea facility (TCO-PL: m/z=2700-3700 (z=1); DSPE-PEG2000 amine m/z=2400-3200 (z=1), Figure 3.9). The analysed samples were embedded in aprotic matrix DCTB and dissolved in Methanol and THF.

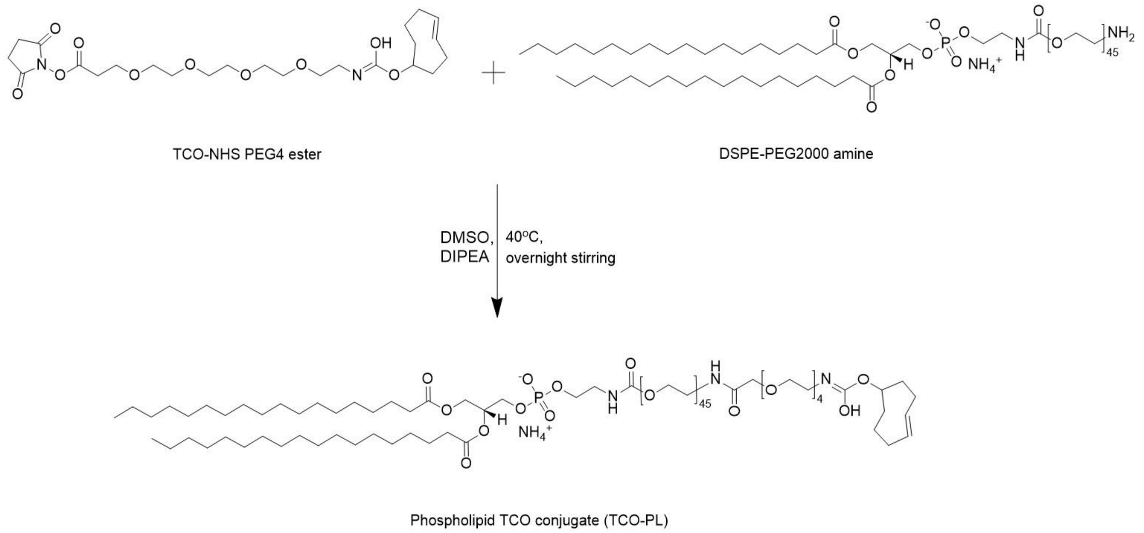

Figure 5.7. Synthesis of TCO-PL: DSPE-PEG2000 amine was reacted with NHS ester derivative of TCO to give the Phospholipid-TCO conjugate (TCO-PL)

5.2.4 Synthesis and characterisation of THP-tetrazines

6-Methyl Tetrazine amine (4.5 mg, 0.021 mmol, 2 equivalents) was dissolved in DMSO (1 mL) followed by addition of THP-Bz-NCS (tris(hydroxypyridinone) isothiocyanate) (10 mg, 0.01 mmol, 1 equivalent). 20 µl of DIPEA (Diisopropyl ethylamine) was added to the reaction mixture to initiate the reaction. The reaction was stirred at RT for 3 hours, and the progress of the reaction was stirred using LCMS. The LCMS showed a clear peak formation at ~1161 showing the formation of the product. The reaction was left overnight to completion. To remove the excess tetrazine, DIPEA and DMSO, the reaction mixture was purified using HPLC method 1 in ACN/Water in 0.1%TFA. The purification was performed using a prep column with ~3 mg sample injected in each run. The multiple UV active fractions were collected and examined for mass using LCMS. The samples showing the mass of 1161 MW were collected, combined, and freeze-dried to give a pink fluffy solid (6.2 mg, 52 % yield). ^{1}H NMR was performed in d-ACN/d-H_2O to characterize the THP-tetrazine (^{1}H NMR (400 MHz) δ 8.43-8.41 (d, (*J* = 8.3 Hz), 2H Ar-H from tetrazine), 7.57 (d, (*J* = 8.2 Hz), 2H), 7.25-7.36 (4H from N-H), 6.96 (m, 6H from Ar-H from tetrazine), 4.89(s, 3H from Ar-H from THP), 4.54 (s, 2H), 3.79-3.82 (m, 9H from CH_3-N, 8H from CH_2-N), 3.01 (s, 2H) 2.48 (s, 3H), 2-42-2.44 (m, 2H), 2.11-2.15 (m, 4H), 1.95 (m, 9H), 1.85 (s, 2H), 1.25 (m, 4H), Figure 3.11) and was supplemented by characterisation via Mass spectrometry (THP-tetrazine (m/z $[M + 2H]^{2+}$ = 581.52) and (m/z $[M+H]^{+}$ = 1162.5), Figure 3.12).

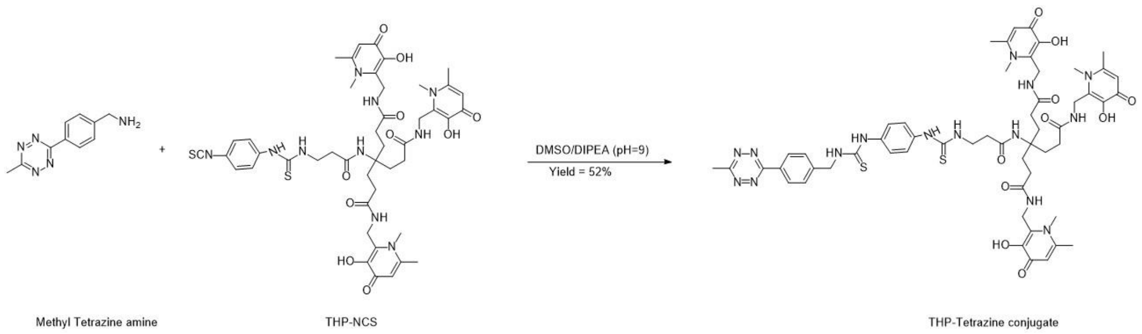

Figure 5.8. Synthesis of THP-tetrazine

5.2.5 Synthesis of TCO-PL-liposomes

The synthesised TCO-phospholipid was transferred from the micellar phase in solution to phospholipid bilayers of PEGylated liposomes. The insertion was performed by equilibrating the PEGylated liposomes (400 µL, 60 mM lipid concentration) and the TCO-Phospholipid dispersion (0.2 mg, 100 µL 10% ethanol/water) at 50^{o}C. The equilibrated dispersions were mixed and incubated under constant shaking for 40 minutes to give

TCO-PL-liposomes. The formed TCO-PL-liposomes are purified using PD minitrap G-25 size exclusion column (GE Healthcare) following the size exclusion chromatography method mentioned above in section 5.2.2.2. Dynamic light scattering quantified the change in hydrodynamic size, zeta potential and PDIs of the PEGylated liposomes pre- and post-insertion reaction.

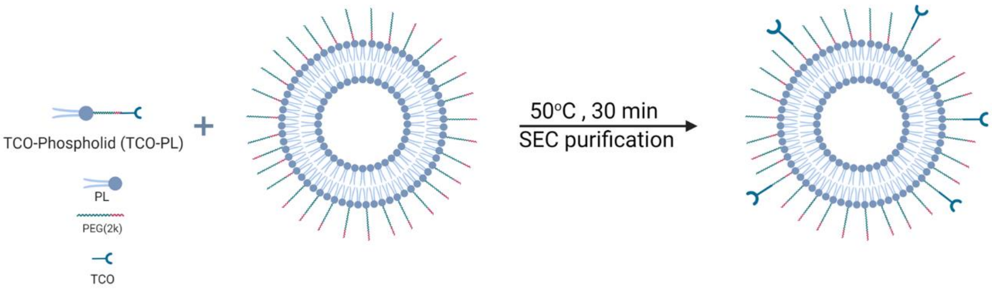

Figure 5.9. Synthesis of TCO-PL-liposomes: Insertion of TCO-PL conjugate into the lipid bilayer of preformed PEGylated liposomes at mild heating below phase transition temperature. Created with BioRender.com.

5.2.6 Nanoparticle Tracking Analysis

The concentration and the hydrodynamic of synthesised TCO-PL-liposomes were measured by NTA using NanoSight LM10 and NTA software v3.2 (Malvern Panalytical). The stock sample was diluted to achieve ~100 particles/viewing frame. Measurements were made in triplicates for 60 s with a 488 nm laser, for up to three serial dilutions of the sample.

5.2.7 Cryo-Electron Microscopy

QUANTIFOIL R 2/2 carbon grids (mesh: Cu 300, #234901; Agar Scientific) were plasma discharged for 50 s at 30 SCCM gas flow in Nanoclean 1070 (Fischione instruments). Aliquots (5 µL) of TCO-PL-liposomes or PEGylated liposomes were deposited on the carbon grids in Vitrobot Mark IV (FEI). The excess liquid was removed by blotting with filter paper (Agar Scientific); Parameters: blotting time = 2 s, wait time = 30 s, and blotting force = 2. The grids were instantly frozen in liquid ethane (−188 °C) and maintained in liquid N_2 (−196 °C) in a grid box and transferred into a cryo-transfer holder. CryoEM of these samples was recorded on TECNAI 12 G2 (FEI) system interfaced with a TemCam-F216 camera and operated using Temmenu v4 software (Tietz Video & Image Processing Systems GmbH, Germany). Parameters used to capture images are as follows: electron acceleration = 120 kV, magnification = 52,000×, acquisition time = 1 s, and spot size = 5.

5.2.8 Radiochemistry

^{68}Ga was eluted from ^{68}Ge/^{68}Ga generator with 0.1 N HCl. The peak radioactivity containing 1 mL elution was used for radiolabelling after buffering with 1 M Sodium carbonate to pH 6. Buffered ^{68}Ga was used for all radiolabelling.

^{68}Ga was also processed for high specific activity labelling. Gallum-68 (140−200 MBq) eluted from a generator was passed through a Phenomenex Strata-X-C 33 µm SPE cartridge. The cartridge was washed with acetone/0.1 M hydrochloric acid (80:20 v/v, 5 mL) to remove trace metal impurities. The gallium-68 was recovered from the cartridge by washing slowly with acetone/ 0.05 M hydrochloric acid (98/2 v/v, 700 µL). The recovered gallium-68 was dried under nitrogen and resuspended for use in radiolabelling.

^{67}Ga-citrate is obtained from Guy's radiopharmacy in the form of citrate salt which cannot be used for radiolabelling. 2 mL of ^{67}Ga-citrate (stock: 518 MBq, 5mL) was aliquoted in a vial and volume was made up to 5 mL with chelex H_2O. The whole volume was loaded on the SEP-PAK silica light cartridge multiple times via a syringe until >80% radioactivity was loaded on the column (3 times optimum). Post loading, the loaded column was washed with 5 mL chelex H_2O @ 1mL min^{-1} thrice. The $^{67}GaCl_3$ is eluted with metal-free HCl (0.1 M, 50 µL). The hottest fractions were buffered to pH 6 and used for radiolabelling.

THP-tetrazine stock (1 mg/mL) was prepared in 10% DMSO/water and used for radiolabelling. THP-tetrazine (5µl, 10 µl or 50 µl) was added to neutralised ^{68}Ga (200 µl, ~25 MBq) and incubated at R.T. for 15 minutes in either a glass vial or plastic vial. The pH of the reaction was measured at 6-6.5. The reaction mixture was spotted on an ITLC developed in either citrate buffer (0.175 M citric acid and 0.325 M trisodium citrate in water, Unbound ^{68}Ga R_f = 0.7–1; ^{68}Ga-THP-tetrazine R_f = 0; ^{68}Ga colloid R_f=0), Ammonium acetate: Methanol (1M, methanol concentration 80% v/v, Unbound ^{68}Ga R_f = 0; ^{68}Ga-THP-tetrazine R_f = 0.7-1; ^{68}Ga-THP-tetrazine colloid/impurity R_f=0), or Ammonium acetate: THF (50% v/v).

Purification of the reaction mixture was initially performed using a centrifugal filter. The reaction mixture was loaded on a centrifugal filter 10k MWCO and then centrifuged at 13000 for 5 minutes. The filtrate was collected and analysed using ITLC and gamma counter. The radiolabelled compound was retained in the filter and therefore could not be purified.

The reaction mixture was diluted with deionised water and loaded on a pre-equilibrated column SEP-PAK plus light C18 cartridge (equilibrated with 10 mL x ethanol and 10 x mL water). The loaded cartridge was washed with 15 mL of water and the compound of interest was eluted with 700 µl of either ethanol or methanol. The collected sample was dried under nitrogen and resuspended in 5% DMSO/water. The purified ^{68}Ga-THP-tetrazine was characterised using ITLC and used for further experiments. The radiolabelling method described above was also utilised for radiolabelling of THP-tetrazine with $^{67}GaCl_3$ obtained after conversion from ^{67}Ga-citrate.

$^{68/67}$Ga-THP-tetrazine purified post radiolabelling of THP-tetrazine was utilised for radiolabelling of TCO-PL-liposomes. $^{68/67}$Ga-THP-tetrazine (100 µl, 5-20 MBq, 5%

DMSO/water) was added to TCO-PL-liposomes (100µl, 50 mM lipid concentration) and incubated at R.T. for 60 minutes. The radiolabelled TCO-PL-liposomes were purified using PD minitrap G-25 size exclusion column (GE Healthcare) following the size exclusion chromatography method mentioned above (b(ii)) and collected in 750 µl fraction.

5.2.9 Log P and Log D measurements

For log P measurement, ^{68}Ga-THP-tetrazine (50 µL, 1 MBq) were added to vials containing a mixture of water saturated octanol (500 µL) and octanol saturated water (500 µL). The tubes were shaken for 3 min and the mixture was centrifuged for 5 min to separate the octanol and PBS phases. Aliquots (50 µL) of each phase were taken and transferred to separate vials for counting of radioactivity. For log $D_{7.4}$ measurement, the same procedure was performed by replacing water with PBS.

5.2.10 Serum stability

The serum stability ^{68}Ga-THP-tetrazine was performed in 50% (v/v) aqueous pooled serum from human male AB plasma. Samples (250 µl, 2-5 MBq) were added to serum (250 µl, filtered through a 0.22 um filter) at a final volume (500 µL), and subsequently incubated at 37 ^{o}C. Aliquots were taken after 0, 90, and 180 min and were analysed by HPLC using HPLC serum stability method mentioned above as method 4.

^{67}Ga-TCO-liposomes were incubated at 37 ^{o}C in human serum in a 1:1 ratio. Aliquots of the test sample were taken at different time points for stability study and applied to SEC HPLC at 0, 24 h and 48 h. Using FPLC method number 5, 1 mL fractions were eluted in PBS and UV, radioactivity signal is recorded.

5.2.11 *In vitro* pretargeting methods

TCO-PL-liposomes (200 µL, 4 mM) was added to either commercially available human serum obtained from Sigma Aldrich (500 µL) or PBS (500 µl) and kept under incubation at 37°C for 60 minutes. ^{68}Ga-THP-tetrazine (100 µl, 1-4 MBq) was added to serum or PBS incubated TCO-PL-liposomes and incubated at 37°C. The incubated samples were purified using the size exclusion chromatography method (section b(ii)) and radiolabelled ^{68}Ga-TCO-PL-liposomes were collected in 750 µl fraction. The liposome associated radioactivity and size exclusion column retained radioactivity was measured using a gamma counter and the percentage yield of bioorthogonal reaction was calculated.

5.2.12 *In vivo* pretargeting methods

5.2.12.1 Animals

Animal imaging studies were carried out in accordance with British Home Office regulations governing animal experimentation. All *in vivo* experiments were conducted on healthy, female Balb/c mice (8-9 weeks old) obtained from Charles River UK Ltd. The cancer model experiments were also performed on BalB/c mice (8-9 weeks old) which were subcutaneously inoculated with mouse fibrosarcoma tumour cells.

For the subcutaneous tumour cell implantation, fibrosarcoma cell line (WEHI 164) syngenic to BALB/c mice was obtained from ATCC (batch number: CRL-1751TM). WEHI-164 tumour cells were subcultured in RPMI-1640 medium supplemented with 10% fetal bovine serum, 2 mM L-Glutamine, penicillin (100 U/mL) and streptomycin (100 µg/mL). Cells were incubated at 37°C with 5% CO2 and passaged periodically (~thrice a week) before reaching confluence (90%).

On the day of the inoculation, the cells were dissociated into a suspension using TrypLE™ Express, washed with PBS and resuspended at a concentration of 2-2.5 million cells per 100-200 µl of PBS.

The mice (n=15) were anaesthetised and using electric clippers, the fur off the animal around the shoulder was shaved. The tumour cells were subcutaneously implanted over the shoulder in the following concentration: WEHI-164 (2.5×10^6 cells/mL in 0.1-0.2mL PBS). The mice were monitored regularly and logged observations (including tumour size and mouse weight) in the monitoring forms. The mice were ready for imaging 8-10 days post tumour implantation (10 % of mice had small tumours or a slow growth rate). The mice chosen for imaging experiments had tumour sizes in the range of 70 mm^3-100 mm^3.

5.2.12.2 Preclinical PET/CT and SPECT/CT scanners

Each mouse (n=3-5, normal BALB/c, female, aged 6–8 weeks, 17–20 g body weight) was anaesthetised by inhalation of isoflurane (2–3% in oxygen). The tracer/molecule of interest was injected via tail vein intravenous injection. The mouse was scanned in either nanoscan *in vivo* preclinical PET/CT imaging system (1:5 coincidence mode; 5-ns coincidence time window) and SPECT/CT imaging system (start frame: 3 mm; end frame: 107 mm; frame time:83 s, scan time~1 h) (Mediso medical imaging systems, Budapest, Hungary) depending on the tracer injected. PET/CT images were reconstructed using Tera-Tomo 3D reconstruction (400–600 keV energy window, 1–3 coincidence mode, 4 iterations and subsets) at a voxel size of (0.4 × 0.4 × 0.4) mm^3 and corrected for attenuation, scatter, and decay. The data were binned into 17 frames (1 × 1, 10 × 3, 5 × 5 and 1 × 4 min) for dynamic analysis. SPECT images were reconstructed using HiSPECT standard method. Regions of interest were drawn over the knees as an area of growing bone, and the heart as an indication of blood, kidneys, bladder and liver.

5.2.12.3 Pretargeting of TCO-PL-liposomes in healthy animals

The mice were divided into three experimental groups as shown in figure 5.10: Positive control: ^{67}Ga-TCO-PL-liposomes, Negative control: ^{68}Ga-THP-tetrazine, and Test group: *In vivo* pretargeting groups for TCO-PL-liposomes.

For negative control group 1, the mice (n=4) were anaesthetised and injected i.v. with ^{68}Ga-THP-tetrazine (2-5 MBq, 100 µL). The mice were kept anaesthetised for 1-hour post-injection and then imaged via *in vivo* preclinical PET/CT imaging system.

For the test group, the mice (n=4) were anaesthetised and injected i.v. with TCO-PL-liposomes (50µM/mL lipid concentration, 100 µL) at t=-3 h. At t=0 h, mice were anaesthetised and injected i.v. with ^{68}Ga-THP-tetrazine (2-5 MBq, 100 µL). The mice were kept anaesthetised for 1-hour post-injection and then imaged via *in vivo* preclinical PET/CT imaging system. The scanned mice were revived and used for imaging on the following day. At t=23 h, mice were anaesthetised and injected i.v. with ^{68}Ga-THP-tetrazine (2-5 MBq, 100 µL). The mice were kept anaesthetised for 1-hour post-injection and then imaged via *in vivo* preclinical PET/CT imaging system.

For positive control group 3, the mice (n=4) were anaesthetised and injected i.v. with ^{67}Ga-THP-PL PEG (2k)-liposomes (3 MBq, 50µM/mL lipid concentration, 100 µL) and imaged at t=2h, 24 h via a preclinical SPECT-CT imaging system.

The mice were culled post-scan by cervical dislocation and required organs were collected, weighed and measured for radioactivity along with the standards and ex vivo biodistributions were determined.

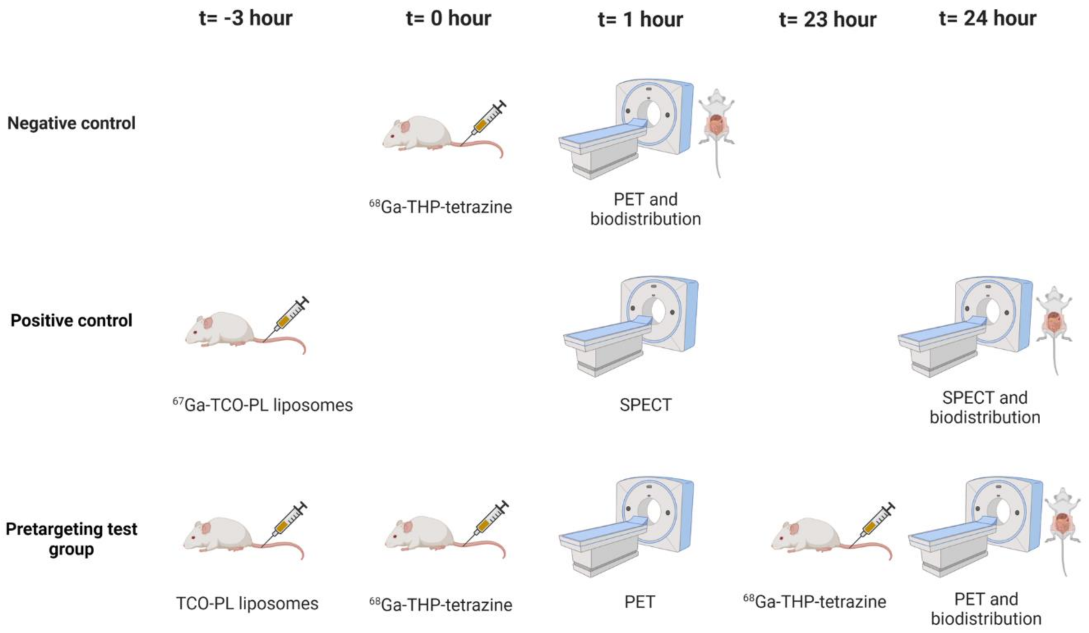

Figure 5.10. Scheme of *in vivo* pretargeting experiment of TCO liposomes using biorthogonal chemistry in healthy animal. Created with BioRender.com.

5.2.12.4 Pretargeting of TCO-PL-liposomes in tumoured animals

The mice with subcutaneously implanted sarcoma tumours were selected for experiments when tumour size>75mm^3. The mice were divided randomly into three experimental groups as shown in figure 5.11: Positive control: ^{67}Ga-TCO-PL-liposomes, Negative control: ^{68}Ga-THP-tetrazine, and Test group: *In vivo* pretargeting groups for TCO-PL-liposomes.

For negative control group 1, the mice (n=5, 3 were imaged and 2 were used for biodistribution only) were anaesthetised and injected i.v. with ^{68}Ga-THP-tetrazine (2-5 MBq, 100 µL). The mice were kept anaesthetised for 1-hour post-injection and then imaged via *in vivo* preclinical PET/CT imaging system.

For the test group, the mice (n=5, 3 were imaged and 2 were used for biodistribution only) were anaesthetised and injected i.v. with TCO-PL-liposomes

(50µM/mL lipid concentration, 100 µL) at t=-3 h. At t=0 h, mice were anaesthetised and injected i.v. with ^{68}Ga-THP-tetrazine (2-5 MBq, 100 µL). The mice were kept anaesthetised for 1-hour post-injection and then imaged via *in vivo* preclinical PET/CT imaging system. The scanned mice were revived and used for imaging on the following day. At t=23 h, mice were anaesthetised and injected i.v. with ^{68}Ga-THP-tetrazine (2-5 MBq, 100 µL). The mice were kept anaesthetised for 1-hour post-injection and then imaged via *in vivo* preclinical PET/CT imaging system.

For group 3, the mice (n=5, 3 were imaged and 2 were used for biodistribution only) were anaesthetised and injected i.v. with ^{67}Ga-TCO-PL-liposomes (8 MBq, 50µM/mL lipid concentration, 100 µL) and imaged at t=4 h, 24 h, 48 h post liposomal injection via a preclinical SPECT-CT imaging system.

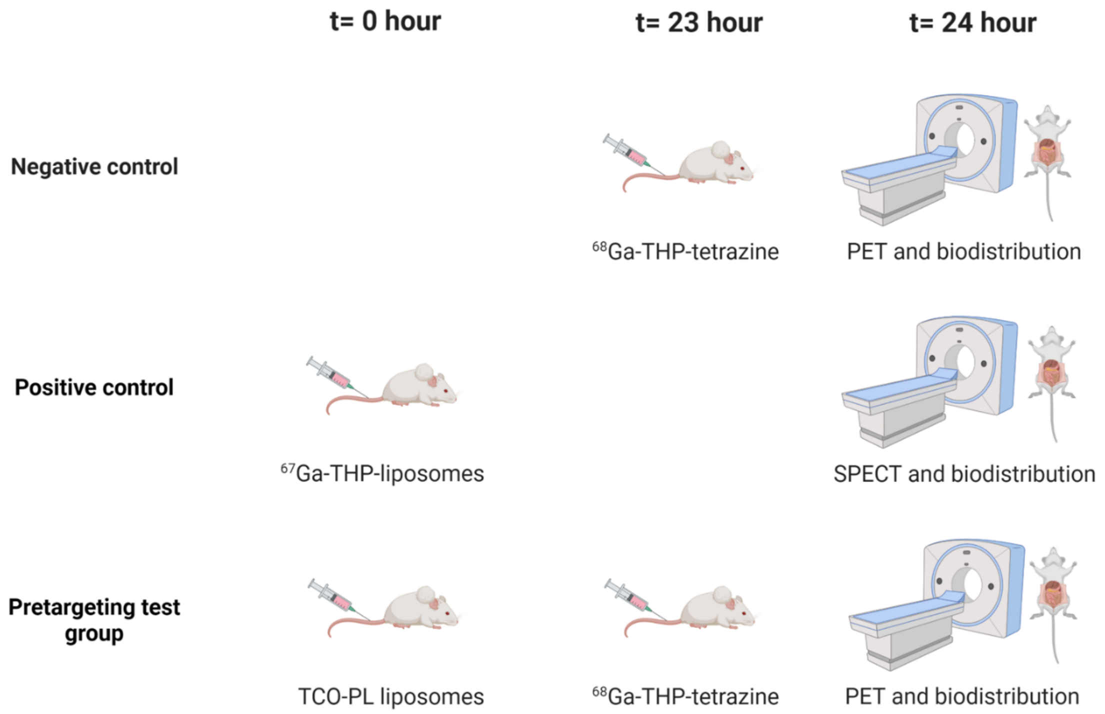

Figure 5.11. Scheme of *in vivo* pretargeting experiment of TCO liposomes using biorthogonal chemistry in tumoured animal. Created with BioRender.com.

The mice were culled post-scan by cervical dislocation and required organs were collected, weighed, and measured for radioactivity along with the standards and ex vivo biodistributions were determined. Serial standard dilution of the injected radiotracer was measured alongside the collected organs to calculate the percentage injected dose (%ID/g).

The tumours obtained from the positive control and test group were either cold-fixed or submerged in 10% neutral-buffered formalin and stored at 4°C for 24 h. The organs were then transferred into a solution of 70% absolute ethanol/water (v/v). The fixed tumours were submerged in OCT under liquid nitrogen and then cryosectioning was performed on these slices and developed on a phosphor screen for autoradiography. The obtained phosphor images were analysed using the free license software ImageJ.

5.2.13 Analysis

The analysis of the reconstructed *in vivo* images is performed using the VivoQuant 3.5 (Invicro Inc.). For image quantification, regions of interest were drawn over the knees for bones, heart as a measure of the blood pool, kidneys, lungs, bladder, spleen, liver, muscles, and brain. All numerical data were analysed on either GraphPad Prism 8 or advanced versions. Data are presented as mean ± standard deviation (SD) unless stated otherwise.

5.3 Chapter 4

This method section describes the experiments carried out to evaluate the delivery of liposomal nanomedicines to the brain using focused ultrasound. The efficacy and safety of liposome delivery was evaluated under ultrasound in a RaSP sequence and compared alongside the long pulse sequence. The brain of mice was treated at 0.4 or 0.6 MPa with either followed by waiting either 0 h or 2 h after the ultrasound treatment. The amount and distribution of the delivered liposomes was detected in brain tissue collected post culling through fluorescence microscopy. Immunohistological staining and image processing was performed to determine which cells were uptaking the liposomes, including glial cells. Tissue damage was assessed by staining to determine whether delivery could be performed safely to the brain by emitting RaSP at a higher ultrasound pressure (0.6 MPa). This section has been taken from the published work in Morse, Mishra et al and modified where necessary.

5.3.1 Materials

For the synthesis of the liposomes, the following materials and instruments were used. Plain PEGylated liposomes (HSPC/Choline/ mPEG2000-DSPE-liposomes (50:45:5 mol/mol, 100 nm) (Doxebo) were obtained from FormuMax Scientific Inc., USA as a translucent white liquid in a clear glass vial. A long alkyl chain dialkylcarbocyanine fluorescent dye DiD (DiIC18(5)) (1,1′ -Dioctadecyl-3,3,3′ ,3′ -Tetramethylindodicarbocyanine, 4-Chlorobenzenesulfonate Salt) was obtained from Invitrogen™ as a blue solid. Size exclusion chromatography (SEC) was performed on a Superose 10/30 column (GE Healthcare Life Sciences) run at 0.5 mL/min in PBS on a GE Purifier AKTÄ FPLC (Fast Protein Liquid Chromatography). Centrifugal filtration was performed using Merck Millipore Amicon™ Ultra 100 KDa Centrifugal Filter Units in a high speed Hettich MIKRO 20 centrifuge. UV detection was performed at 214 and 280 nm. The fluorescence measurements were performed on Promega GLomax® discover system using the red excitation source at a wavelength of 644 nm with emission detected at 660–720 nm.

5.3.2 Synthesis and characterisation of fluorescent PEGylated liposomes (DPLs)

In our design we used a DiD fluorophore to fluorescently label the PEGylated liposomes. To this end, DiD solid (2.5 mg, 2.3 µM) was dissolved in pure ethanol (1 mL) using sonication. The dye solution (3 µL) obtained was added to a Doxebo dispersion (500 µL, 60 mM lipid concentration) yielding a final DiD concentration of 15 µg/mL in the DiD/ Doxebo dispersion. The DiD/Doxebo dispersion was incubated under constant rotation for 2 h at 37 ◦C to give DiD-PEGylated liposomes (DPLs). Free DiD solid and ethanol was removed from formed DiD-PEGylated liposomes using a PD10 minitrap G-25 size exclusion column (GE healthcare) following the manufacturer’s gravity protocol. DiD-PEGylated liposomes were further purified using a 100 kDa size exclusion centrifugal filter at maximum speed. Any unattached dye that precipitated during centrifugation was separated. Dynamic light scattering (DLS) was used to study the hydrodynamic size, zeta potential and polydispersity index of the DiD-PEGylated liposomes pre- and post-

DiD labelling. The incorporated dye concentration in the DPL sample was assessed by measuring fluorescence of samples at excitation wavelength of 644 nm and emission at 664 nm and compared with standard curves for the free dye signal measured in ethanol.

5.3.3 *In vitro* serum stability of fluorescent DiD-PEGylated liposomes (DPLs)

The stability of the DiD-PEGylated liposomes in the presence of blood biomolecules was assessed to monitor dye leakage *in vitro*. The DiD-PEGylated liposomes were incubated at 37 ◦C in human serum (n = 3). At 0, 3, 12, 18, 24 and 48 h, we obtained aliquots of the serum incubated liposomes and passed them through size exclusion column of the Fast protein liquid chromatography system. 1 mL fractions from the size exclusion column were collected in PBS and UV signal was recorded. DiD-PEGylated liposomes eluted as a single peak between fractions 8 and 11, and serum proteins eluted between 18 and 25 as shown by UV signal. The fluorescence of all collected fractions was measured, and stability of the dye-labelled liposomes (DiD-PEGylated liposomes) was calculated as shown below:

$$\%dye\ labelled\ liposomes(stability) = \left[\frac{LF}{LF + SF}\right] * 100$$

With LF being the liposome fractions FL signal and SF being the serum protein fractions FL signal. FL is the fluorescence signal due to DiD dye associated to respective molecules at excitation wavelength of 644 nm and emission at 664 nm.

5.3.4 Ultrasound setup

Therapeutic ultrasound pulses were emitted from a single element spherical-segment focused ultrasound transducer (Figure 5.12; centre frequency: 1 MHz; active diameter: 90 mm; focal depth: 60.5 mm; part number: H-198; Sonic Concepts, Bothell, WA, USA) driven by one or two function generators (33500B Series; Agilent Technologies, Santa

Clara, CA, USA) through a 50-dB power amplifier (2100L Electronics and Innovation, Rochester, NY) and an impedance matching box (Sonic Concepts, WA, USA). When ultrasound was emitted with a RaSP sequence, two function generators were used, one to define the pulse shape and the other to define the pulse sequence. For the long pulse sequence only one function generator was needed. The elevational, lateral and axial full width at half maximum (FWHM) at the ultrasound focus were 1 mm, 2 mm and 20 mm respectively. The acoustic pressures reported here are de-rated using an 11% attenuation, which was measured experimentally by placing the top layer of the mouse skull (post-mortem, n = 4) between the transducer and the focal point, where a hydrophone was positioned. The transducer, surrounded by a transparent casing, was mounted onto a three-dimensional positioning system (Velmex, Bloomfield, NY, USA) to move to the desired targeted location.

Acoustic emissions from microbubbles were passively captured during the ultrasound treatment using a passive cavitation detector (PCD; centre frequency: 7.5 MHz; diameter: 12.7 mm, focal length: 76.2 mm; Olympus Industrial, Essex, UK). The PCD was coaxially aligned through the rectangular central opening of the therapeutic transducer. The emissions were captured by the PCD, filtered by a 3-30 MHz band-pass filter, amplified by a 28-dB pre-amplifier and recorded by an 8-bit oscilloscope (PicoScope 3205A). Time domain traces were displayed in real-time and were used to determine whether microbubble activity was occurring during the ultrasound treatment. Further processing of these signals was not carried out here, however, the data was saved for future off-line processing.

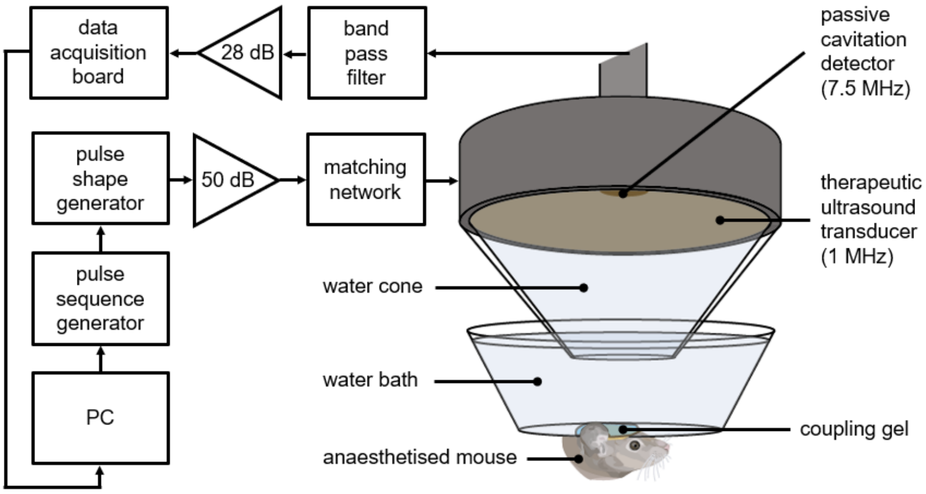

Figure 5.12. Ultrasound experimental setup: Ultrasound was focused through the intact scalp and skull onto the left hippocampus of the mouse's brain while the right hippocampus was used as a control (no ultrasound). Ultrasound pulses were emitted from the therapeutic transducer (1 MHz) driven by one or two function generators through a 50-dB amplifier and an impedance matching network. A 7.5 MHz passive cavitation detector captured the acoustic emissions from the microbubbles, which were filtered by a band pass filter, amplified by a 28-dB pre-amplifier and recorded by an 8-bit oscilloscope.

5.3.5 Animals

Thirty-six female C57bl/6 wild-type mice (8-12 weeks old, 19-20g; Envigo, Huntingdon, UK) were used in this study (Table 5.1). All animal experiments were performed in approval with the UK Home Office and Imperial College London's animal facility committee.

Twenty-four mice were used to compare the dose and distribution of liposomes in brains treated with both sequence types (RaSP or long pulses), with two acoustic pressures (0.4 or 0.6 MPa) with either a 0 h or 2 h recovery period. Staining was performed on these brains to determine which cells were uptaking the liposomes once delivered into the brain.

To assess damage, twelve mice were sonicated with both sequence types (RaSP and long pulses) at both acoustic pressures (0.4 and 0.6 MPa; n = 3 for each parameter group) with no recovery time following ultrasound treatment (0 h). These additional twelve mice were needed as haematoxylin and eosin (H&E) staining, used to assess damage, requires the brains to be processed with a paraffin-embedding technique rather than cryofreezing which was used to assess the dose and distribution of the liposomes. In all mice, the left hippocampus was treated with ultrasound while the right hippocampus was used as a no-ultrasound control. Variabilities caused by physiological differences between animals were reduced by using each animal as its control.

Table 5.1. Summary of mice used in each study: Twenty-four mice were used to compare the delivery and distribution of liposomes with RaSP or long pulse sequences at 0.4 or 0.6 MPa either immediately or 2 h after the ultrasound treatment. Twelve mice were used to assess tissue damage with haematoxylin and eosin (H&E) staining at the two acoustic pressures and with the two sequence types at 0 h.

Study	Sequence type	Pressure	Recovery time	Number of mice
Delivery Comparison	RaSP	0.4 MPa	0 h	3
			2 h	3
		0.6 MPa	0 h	3
			2 h	3
	Long	0.4 MPa	0 h	3
			2 h	3
		0.6 MPa	0 h	3
			2 h	3
Tissue Damage Assessment	RaSP	0.4 MPa	0 h	3
		0.6 MPa		3
	Long	0.4 MPa		3
		0.6 MPa		3
Total				36

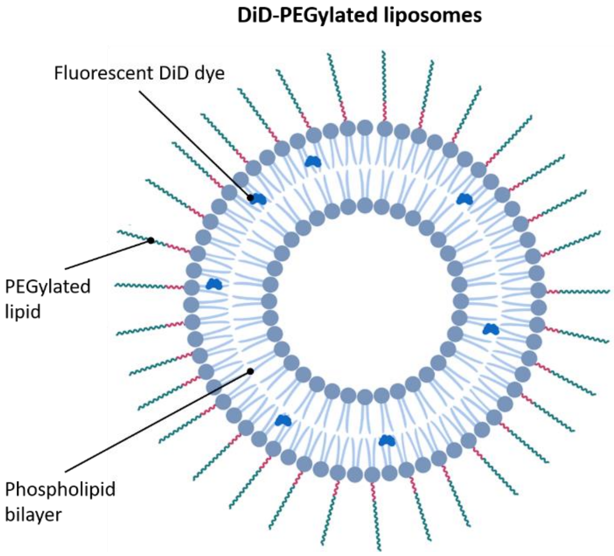

Figure 5.13. DiD-PEGylated liposome structure. The liposomes consist of a phospholipid bilayer with PEG brushes attached to the surface for biocompatibility and the DiD fluorophore embedded within the lipid bilayer to enable ex vivo fluorescence detection of the liposomes. Created with BioRender.com.

5.3.6 Microbubbles

SonoVue (Bracco, Milan, Italy) microbubbles were used to deliver the above liposomes into the brain (concentration: 5 µl/g of body mass, volume: 100 µL, mean diameter: 2.5 µm, vial concentration: 3x10^{8}/mL). A fresh vial of microbubbles was activated on each day of experiments and used within six hours from activation, following the manufacturer's instructions.

5.3.7 Sonication experimental workflow

The experimental workflow was similar to that described in paper.[424] The mice were anesthetised, and the fur was shaved from the mouse's head. The mouse's head was then fixed within a stereotaxic frame and ultrasound gel was applied to the head. The water bath was lowered onto the gel so that a metal cross could be positioned in alignment with the skull sutures. Based on the position of this metal cross, the transducer was moved to target the left hippocampus. Once the tail vein injection was in place, the liposomes were injected, and the ultrasound treatment (RaSP or long pulse sequence) was started. Ten seconds into the treatment, the microbubbles were injected, allowing the initial ultrasound pulses to be used as control pulses for future acoustic emissions analysis. The microbubbles were injected over the course of 30 seconds through a 30-gauge home-made catheter.

At the end of the treatment, either immediately or after two hours of recovery, an overdose of pentobarbital was administered intraperitoneally and the mice were transcardially perfused with 20 mL ice cold phosphate-buffered saline with added heparin (20 units/mL; Sigma Aldrich, St Louis, MO, USA) and 10% formalin solution (Sigma Aldrich) to clear the vessels and fix the tissue. The brains were extracted and placed in 10 mL 10% formalin overnight, 15% sucrose for 6 h and then 30% sucrose overnight until the brains sunk to the bottom of the solution for cryoprotection. Brains used for H&E staining were instead kept in formalin and prepared by IQPath laboratory at University College London for paraffin-embedding and microtome sectioning.

5.3.7 Brain sectioning

Brains used to observe the detected dose and distribution of the liposomes and cellular uptake were cryosectioned. Samples were snap-frozen by embedding the brains in optimal cutting temperature and placing them in a bath of isopentane and dry ice for five minutes. They were then sectioned into 30 µm horizontal slices using a cryostat (CryoStar NX70; Thermo Fisher, Waltham, MA, USA) at -12 to -14 °C. Initially, 1.5 mm of the embedded brain was trimmed from the bottom and then sixty 30 µm slices were cut to cover the entire hippocampus. Brain slices were collected on positively charged slides (Superfrost^{TM} Ultra Plus Adhesion Slides, Thermo Fisher) and stored in the dark at 4 °C until imaged.

5.3.8 Histological staining

Brains used to observe the detected dose and distribution of the liposomes and cellular uptake were cryosectioned. Samples were snap-frozen by embedding the brains in optimal cutting temperature and placing them in a bath of isopentane and dry ice for five minutes. They were then sectioned into 30 µm horizontal slices using a cryostat (CryoStar NX70; Thermo Fisher, Waltham, MA, USA) at -12 to -14 °C. Initially, 1.5 mm of the embedded brain was trimmed from the bottom and then sixty 30 µm slices were cut to cover the entire hippocampus. Brain slices were collected on positively charged slides (Superfrost^{TM} Ultra Plus Adhesion Slides, Thermo Fisher) and stored in the dark at 4 °C until imaged.

Immunostaining was performed on these brain slices to detect whether the liposomes were being uptaken by neurons, microglia or astrocytes. Only slices where cellular uptake was observed were stained for these cells and the antibodies used for each stain are shown in Table 5.2. A DAPI mounting medium was applied before coverslipping the slides to stain the cell nuclei.

Table 5.2. Primary and secondary antibodies used to stain for neurons, microglia and astrocytes

Stain	Primary Antibody	Secondary Antibody
Neurons	Recombinant anti-NeuN antibody [EPR12763] (ab177487) - 1:500	Goat anti-rabbit IgG H&L (Alexa Fluor® 488) (ab150077) - 1:500
Microglia	Anti-Iba1 antibody (ab5076) - 1:500	Donkey anti-goat IgG H&L (Alexa Fluor® 488) (ab150129) - 1:500
Astrocytes	GFAP monoclonal antibody (2.2B10) (13-0300) - 1:100	Mouse anti-rat IgG2a (FITC) (11-4817-82) - 1:500

5.3.9 Microscopy

Images were acquired using either a widefield microscope (10x; Zeiss Axio Observer, Oberkochen, Germany) or a confocal microscope (20x; Zeiss LSM-510 inverted, Oberkochen, Germany). Images were taken using both brightfield and fluorescent channels. The DiD fluorophore on the liposomes was imaged with the Cy5 channel, the Alexa 488 or FITC fluorophores on the antibodies to stain for cell uptake were imaged with the GFP (green fluorescent protein) channel and the nuclei with the DAPI channel (Table 5.3). All imaging parameters, such as laser power and exposure time were kept constant to allow more accurate quantitative measurements.

Table 5.3. Excitation and emission filters for the fluorophores: Excitation and emission filters are given as the centre wavelength and the bandwidth.

Fluorophore	Excitation (nm)	Emission (nm)
DAPI	390/40	450/40
Alexa 488, FITC	470/40	525/50
Texas Red	562/40	624/40

5.3.10 Analysis

Analysis on the acquired images was performed to determine the detected dose, distribution and areas of liposome delivery as well as tissue damage.

To compare the detected dose of liposomes delivered to the brain with the different parameters used, the normalised optical density (NOD) was calculated. Regions of interest (ROIs) were selected around the left and right hippocampus by using MATLAB R2019b (Mathworks, Natick, MA, USA). If present, artefacts, such as folds and air bubbles, were removed from these regions. The NOD is a normalised measurement of the detected dose of the liposomes. Pixels with intensities above twice the standard deviation added to the mean of the control pixel intensities were summed in both ROIs. The sum in the targeted ROI was subtracted by that of the control ROI to obtain the NOD. Delivery was considered successful if the NOD was at least two standard deviations above the mean of the control region. The NOD was calculated on six slices for each quantified brain.

To quantify any differences in distribution between parameter sets, the coefficient of variation (COV) was calculated. The COV is defined as the ratio of the standard deviation over the mean fluorescence pixel intensity in the targeted region. The COV quantification was performed on six sections for each brain and was not performed on brains that displayed no liposomal delivery.

To determine the number of spot-like areas where liposomes were delivered, the number of areas above 100 μm^2 was quantified. Larger areas of delivery were expected if the liposomes diffused further away from the blood vessels. Regions of interest were selected around all spots of liposome delivery in six sections per brain. An automatic threshold was applied equally to all images in ImageJ (dark triangle) to only select regions of liposome delivery. The area of each region was determined by using the automated 'Analyse Particles' tool in ImageJ.

To assess tissue damage, seven H&E stained slices were analysed per brain. First, adjacent unstained sections were imaged under a fluorescence microscope to identify the location of dextran delivery and therefore the ultrasound targeted brain region. Second, in the H&E stained slices, three histological measures were evaluated: number of sites with more than five extravasated red blood cells, number of microvacuolations and the number of dark neurons. The different values were plotted for RaSP and long-pulse-treated brains. Histological evaluation of the targeted and control hippocampi was performed without knowledge of which side was targeted with ultrasound.

5.3.11 Statistical analysis

A one-way analysis of variance (ANOVA) test was conducted to assess whether differences were present between the parameter sets in the NOD, COV and areas above 100 µm^2 results. *Post hoc* Bonferroni analysis was performed to estimate any significant differences in a pairwise manner ($P < 0.05$). A Wilcoxon rank sum test was performed to test whether differences between the H&E results were significant. All analysis was carried out in MATLAB R2019b.

5.3.12 Autoradiography via ^{68}Ga based pretargeting

The delivery of radioisotope tagged liposomes to the brain to quantify non-invasively was the next step to combine the two aspects of my research. However, due to the absence of radiation-controlled area in focussed ultrasound labs, this study was planned to deliver the THP-liposomes synthesised in chapter 2 to the brain using the RaSP sequence at 0.6 MPa followed by 2 h wait before sacrifice and collection of brain tissues.

Using the above focussed ultrasound protocol, THP-PL-liposomes (Chapter 2) were injected in n=3 mice each under RaSP FUS at 0.6 MPa and followed by 2 h recovery. The mice were sacrificed, and the brains were extracted and placed in 10 mL 10% formalin overnight, 15% sucrose for 6 h and then 30% sucrose overnight until the brains sunk to the bottom of the solution for cryoprotection.

The cryoprotected brains were flash frozen and 30 uM horizontal slices were made using a cryostat (CryoStar NX70; Thermo Fisher, Waltham, MA, USA) to cover the whole campus. The tissue was fixed on positively charged slides. The tissues were stained with buffered ^{68}Ga (as prepared in chapter 2) followed by wash with either H_2O, EDTA (1 M), citrate (1 M) for varying durations to wash off non-specific bound ^{68}Ga. These stained slices were then developed on phosphor imaging plates for autoradiography with varying exposure times for highest resolution. These developed phosphor imaging plates were then recorded using a cyclone phosphor imaging Typhoon system. The images obtained were analysed and quantified using ImageJ.

6 CONCLUSIONS AND FUTURE OUTLOOK

In this thesis, we have aimed to address the gap between the preclinical development and application of liposomal nanomedicines and their successful clinical application using imaging and drug delivery techniques. PEGylated liposomal nanomedicines have shown variable clinical efficacy in different tumour types, stages and patients due to the EPR heterogeneity. Nuclear imaging provides a method to determine the potential efficacy of these liposomal nanomedicines at an early stage and understand the reasons behind their variability. However, due to the long $T_{1/2}$ nature of these PEGylated nanomedicines, long-lived radioisotopes are required for their imaging leading to significant radiation doses and low contrast. To overcome these drawbacks, we have hypothesised and developed two different pretargeted nuclear imaging methods based on the gallium-68 chelator THP, which can radiolabel quickly and efficiently at room temperature and pH 7, and in the presence of competing biomolecules.

The first pretargeting system was based on the metal chelation strategy, where the high affinity of THP towards ^{68}Ga was exploited. To this end, as mentioned in Chapter 2, a THP-phospholipid conjugate was developed, characterised, and radiolabelled, followed by embedding this conjugate to provide THP-PL-liposomes. The synthesised THP-PL-liposomes were characterised by dynamic light scattering, nanoparticle tracking analysis, cryo-electron microscopy, and radiolabelling, showing no modifications to properties of PEGylated liposomes while exhibiting ^{68}Ga/^{67}Ga chelating properties. To validate metal chelation-based pretargeting, *in vitro* studies were performed. Experiments showed high radiolabelling of serum-incubated THP-PL-liposomes when incubated with neutralised ^{68}Ga (for as low as 15 minutes), suggesting efficient tracking of PEGylated liposomes in serum with high efficiency. For conventional imaging with long-lived radioisotopes, the THP-PL-liposomes were radiolabelled with ^{67}Ga with ^{67}Ga-

THP-PL-liposomes. *In vivo* SPECT imaging was performed to track PEGylated liposomes up to 24 hours and determine the blood half-life of PEGylated liposomes. *In vivo* PET pretargeting of THP-PL-liposomes was conducted to track them with short-lived isotopes at different time points. *In vivo* PET pretargeting with neutralised ^{68}Ga at an earlier time (*i.e.,* 5 h post administration of THP-PL-liposomes) showed radiolabelled liposomes circulating in the blood, liver and spleen. The observed biodistribution in the PET images at the earlier time point resembled the biodistribution observed in the SPECT images for ^{67}Ga-THP-PL-liposomes, suggesting a successful pretargeting at this time point. However, *in vivo* PET pretargeting with neutralised ^{68}Ga at the later time point (*i.e.,* 27 h post administration of THP-PL-liposomes), when the liposomes are expected to be concentrated in liver and spleen, showed minimal biodistribution in these organs, suggesting low pretargeting at this time point. This observation resembled the biodistribution in PET images of mice administered with neutralised ^{68}Ga only. These findings suggest that we can use this strategy to effectively pretarget the circulating THP-PL-liposomes with neutralised ^{68}Ga in blood. However, the ability to pretarget within the liver and spleen is limited. The possible reason behind this observation could be the inability of ^{68}Ga to access the THP-PL-liposomes accumulated in the liver (*e.g.,* inside macrophages) and spleen tissue (*e.g.,* liposomes are already inside macrophages) or saturation of THP chelator on the liposomal surface by sequestering of Fe within the body.

In chapter 2, we also evaluated this metal chelation PET pretargeting strategy for a bone-targeting tracer THP-Pamidronate (THP-Pam) to test its capabilities further. The pretargeting of THP-Pam with ^{68}Ga was successfully observed at both time points (5 h and 27 h) post-administration. However, the bone uptake values observed for pretargeting groups were lower than those observed for the prelabelled ^{68}Ga-THP-Pam group. Likewise, the uptake observed in the bones in the pretargeting group could be partially due to the inherent affinity and accumulation of neutralised ^{68}Ga to bone tissue.

Future work on the metal chelation strategy will explore the reasons behind the limited pretargeting of THP-PL liposomes in the liver and spleen, which is observed at later times and explore ways to overcome it. These will include the determination of the number of THP chelators incorporated on the liposomal surface and using a weakly lipophilic chelator of ^{68}Ga as a secondary imaging agent instead of neutralised ^{68}Ga, as the latter might be unable to cross cell membranes within tissues to reach the liposomes. Also, future work will aim to find applications for the efficient pretargeting of liposomes observed circulating in the blood.

In Chapter 3, we explored another pretargeting strategy – IEDDA-based biorthogonal chemistry – which has been shown to perform successfully in the nuclear imaging of non-internalising antibodies as a direct comparison to the metal chelation pretargeting performed in Chapter 2. To incorporate the biorthogonal system for imaging PEGylated liposomes with conventional or pretargeting methods, we synthesised two novel molecules, THP-tetrazine (a small molecule with Ga binding properties) and TCO-PL (transcyclooctene PEG2000 phospholipid conjugate). These molecules were purified and characterised successfully using NMR and mass spectroscopy. TCO-PL was successfully incorporated in the bilayer of the PEGylated liposomes to give TCO-PL-liposomes no impact on liposomal properties while providing the liposomes affinity towards tetrazine. These TCO-PL-liposomes formed the primary targeting component of our pretargeting system. THP-tetrazine, on the other hand, was radiolabelled with both ^{68}Ga/^{67}Ga, characterised and purified to give ^{68}Ga-THP-tetrazine/^{67}Ga-THP-tetrazine where ^{68}Ga-THP-tetrazine formed the secondary imaging agent of our pretargeting system, and ^{67}Ga-THP-tetrazine was utilised to label the TCO-PL-liposomes to give 67Ga-TCO-PL-liposomes directly.

The pretargeting pair of TCO-PL-liposomes and ^{68}Ga-THP-tetrazine on evaluation *in vitro* in high dilution conditions in either PBS or serum at physiological pH showed a successful biorthogonal reaction in as low as 15 minutes to ^{68}Ga-TCO-PL-liposomes. This pretargeting pair was then evaluated *in vivo* and compared against PET images and biodistribution of ^{68}Ga-THP-tetrazine and SPECT images and biodistribution of directly labelled ^{67}Ga-TCO-PL-liposomes. The pretargeting experiments in healthy mice showed successful pretargeting with higher uptake observed in the liver and spleen (the target organs for long-circulating liposomes) compared to uptake observed in these organs in mice injected with just ^{68}Ga-THP-tetrazine. The observed biodistribution and images in the pretargeting group corresponded to the observed biodistribution and images for mice injected with directly labelled ^{67}Ga-TCO-PL-liposomes, thereby confirming the pretargeting.

Further *in vivo* pretargeted imaging evaluation of TCO-PL-liposomes was performed in a fibrosarcoma tumour model in mice showing successful pretargeting in the liver and spleen. However, unexpectedly minimal pretargeting happened in the tumours and the observed uptake in tumours was very low compared to tumour uptake observed in directly labelled ^{67}Ga-TCO-PL-liposomes. The possible reasons behind this observation could be an internalisation of the TCO-PL-liposomes at the site of tumours, low relative concentration of TCO/tetrazine molecules or low reactivity of the THP-tetrazine towards the TCO. Also, due to the highly lipophilic nature of the secondary imaging agent ^{68}Ga-THP-tetrazine, the observed clearance routes in PET images are through both renal (uptake in kidney and urinary bladder) and hepatobiliary excretion (uptake in gall bladder, liver, intestines) pathways. This characteristic lipophilic nature of the ^{68}Ga-THP-tetrazine leads to variable uptake in organs such as the liver, spleen and even lungs in both negative control and pretargeting group.

Future work on the biorthogonal pretargeting includes optimisation of the pretargeting system components to achieve higher uptake in the tumours. This will consist of work on higher TCO loading on liposomes, developing a library of THP-tetrazine derivatives with high reactivity towards TCO and low lipophilicity with PEG incorporation, determination of the optimal relative concentration of TCO-liposomes/THP-tetrazine required to obtain the most increased reactivity *in vivo*, and use of therapeutic radionuclides for pretargeted radionanotherapy.

Imaging provides an excellent method to track drug delivery and we aimed to utilise the imaging to assess the extent of delivery of liposomal nanomedicines to the brain. The size of liposomal nanomedicines (~100 nm) limits their delivery to the brain and therefore, we hypothesised that the novel RaSP sequence could be used to deliver the PEGylated liposomes efficiently and safely. We aimed to use nuclear imaging methods developed in previous chapters to quantify the delivery of the PEGylated liposomes to the brain. However, due to logistical limitations on the designation of the focussed ultrasound as a radiation use area, we used optical imaging to quantify the delivery of liposomal nanomedicines using FUS and microbubble as proof of concept.

In Chapter 4, the assessment of the delivery of fluorescent PEGylated liposomes into the brain using the RaSP sequence of focussed ultrasound was investigated. The PEGylated liposomes were fluorescently labelled using a lipophilic dye, DiD, to give fluorescent DPL liposomes, which showed minimum dye leaching even after 48 hours and no impact on liposomal properties. The efficacy of delivery of DPLs using RaSP was compared to long pulses and was found to be lower for RaSP. However, delivery using RaSP showed an improved safety profile compared to conventional long pulses of focussed ultrasound. Delivery of the DPLs with RaSP required higher pressures showing lowered delivery regions and detected dose compared to long pulses. The tissue damage was observed in all long-pulse-treated brains compared to just one red blood cell observed in a single slice in RaSP-treated brains. Moreover, the observations from the study included uptake of DPLs in neurons using RaSP but at a lower level compared to long pulse. Microglial uptake was only observed at a higher pressure and after a two-hour recovery period, but no astrocyte uptake was observed within this time period. These cellular level uptakes showed that the delivered DPLs localised within the cells' cytoplasm. The reduced delivery of DPLs and safer profile of RaSP alongside the observed lower involvement of glial cells into the brain indicates a gentler stimulation of the vasculature using RaSP. We also attempted to deliver THP-PL-liposomes developed in Chapter 2 to the brain using RaSP sequence of focussed ultrasound followed by *ex vivo* pretargeting of these brain-delivered liposomes with ^{68}Ga. However, the pretargeting could not be quantified as ^{68}Ga showed high levels of non-specific uptake to the whole brain slices.

Future work will focus on optimising the RaSP sequence to improve the efficacy of delivery of the liposomal nanomedicines into the brain. The therapeutic effects of different liposomal nanomedicine formulations delivered into the brain with focused ultrasound will be explored in disease models. Finally, the delivery of radiolabelled liposomal nanomedicines to the brain using focussed ultrasound will be explored to allow us to monitor the opening of BBB and drug delivery in real-time and non-invasively.

In conclusion to this thesis, we have contributed towards improving the currently available imaging and brain delivery methods for clinically approved PEGylated liposomal nanomedicines, intending to overcome the issues faced in their clinical applications and support the move towards personalised nanomedicine. The pretargeted imaging methods and focused ultrasound-mediated delivery methods described here have provided important information on their capabilities and will contribute to the future development of these techniques in both the preclinical and clinical settings. A particular area that we believe should be the focus of future investigations using these techniques is the delivery of therapeutic radionuclides such as alpha and beta particle emitters *via* liposomal nanomedicines to required targets, with minimal doses to non-target organs and the brain, respectively.

7 APPENDIX

Table 7.1. Biodistribution data from the THP-PL-liposomes pretargeting experiment on healthy animals

	Positive control-24 h			Pretargeting group-24 h			Negative control-2 h		
	Mean	Standard dev	4	Mean	Standard dev	4	Mean	Standard dev	3
Blood	18.684815	2.85830311	4	14.6229093	0.44974944	4	11.924969	1.42559801	3
Heart	4.98534294	0.31169122	4	7.57643651	1.54511222	4	4.7594512	0.94350402	3
Lungs	8.23078667	3.63594849	4	10.006928	0.5792361	4	7.50390306	1.08977254	3
Stomach	1.7970355	0.99987349	4	2.08831584	0.30488751	4	2.09214997	0.41427861	3
Pancreas	2.00678029	0.63356415	4	4.98010363	2.99185828	4	4.83365191	1.32850175	3
Spleen	186.749174	20.6322369	4	6.3978485	0.6226168	4	3.90800848	0.21197821	3
Small intestine	4.10763012	0.49679057	4	9.46423108	2.17713435	4	9.62279268	0.87195302	3
Large intestine	1.66668659	0.38039854	4	2.98446093	0.23863823	4	2.54758598	0.71822231	3
Liver	41.1713259	3.19164368	4	4.56266727	0.48256863	4	4.12097125	0.58710029	3
Bone	5.08079405	0.77691535	4	16.3036907	6.24136568	4	12.534295	2.54618991	3
Muscle	0.85628106	0.1680016	4	2.19512946	0.15859963	4	2.02654886	0.35082095	3
Skin and Fur	1.59182171	0.25577248	4	5.26397628	0.60974227	4	4.51445908	0.58123766	3
Tail	11.3567979	9.70922273	4	7.47570157	1.29710382	4	6.74980414	0.80734757	3
Brain	0.79563845	0.39602108	4	0.45969326	0.25603728	4	0.60885293	0.37032288	3
Kidney	9.055389	0.57610042	4	8.95333213	0.67289646	4	5.45528236	1.19959875	3

Table 7.2. Biodistribution data from the THP-PL-Pam pretargeting experiment on healthy animals

	Positive control-2 h			Pretargeting group-24 hr			Negative control-2 hr		
	Mean	Standard dev	4	Mean	Standard dev	4	Mean	Standard dev	3
Tail	1.944128	0.387633	5	4.390262	0.645368	4	6.749804	0.807348	3
Tibia	22.55777	9.286342	5	14.01481	1.338307	4	12.5343	2.54619	3
Skin & Fur	0.244854	0.079671	5	4.012535	0.351982	4	4.514459	0.581238	3
Muscle	1.009902	1.014949	5	1.353754	0.337167	4	2.026549	0.350821	3
Small Intestines	1.436041	0.370178	5	8.08313	0.571976	4	9.622793	0.871953	3
Large intestines	0.104214	0.043307	5	2.27807	0.112884	4	2.547586	0.718222	3
Stomach	0.114589	0.037271	5	1.339165	0.107256	4	2.09215	0.414279	3
Spleen	0.215741	0.046595	5	2.211043	0.39373	4	3.908008	0.211978	3
Kidneys	2.477382	0.510541	5	4.483694	0.679695	4	5.455282	1.199599	3
Liver	0.262791	0.055487	5	2.663134	0.632946	4	4.120971	0.5871	3
Heart	0.274888	0.245772	5	2.926157	0.508296	4	4.759451	0.943504	3
Lungs	0.311444	0.065706	5	7.327005	1.307299	4	7.503903	1.089773	3
Brain	0.425424	0.561038	5	0.286825	0.061072	4	0.608853	0.370323	3
Blood	0.291129	0.266816	5	7.255046	1.163609	4	11.92497	1.425598	3

Table 7.3. Biodistribution data from the TCO-PL-liposomes pretargeting experiment on healthy animals

	^{68}Ga-THP-tetrazine (Negative control)			Pretargeting group-24 h			^{67}Ga-TCO-liposomes (Positive control)- 24 h		
	Mean	Standard dev	4	Mean	Standard dev	4	Mean	Standard dev	3
Blood	5.626807911	2.45921956	4	4.674034751	1.43091048	4	16.98061324	2.757014718	4
Heart	2.534111445	1.310687271	4	2.020845332	0.651391938	4	4.334614519	0.388103858	4
Lungs	28.03630434	7.66594347	4	18.12860383	14.70351432	4	5.780277022	0.8651312	4
Stomach	0.970225656	0.503065361	4	0.65832653	0.115264928	4	1.066092208	0.352535389	4
Pancreas	0.885373628	0.473348616	4	3.391809463	4.041000404	4	1.75344565	0.520053016	4
Spleen	11.87526429	6.027187305	4	32.82954566	16.3309688	4	48.8433591	2.629610051	4
Small intestine	21.30868063	6.874148889	4	11.8192986	5.424517069	4	2.220519374	0.184252849	4
Large intestine	2.033573358	1.585917596	4	3.411370967	3.577939566	4	1.298217835	0.084173876	4
Liver	22.37020567	11.44575327	4	31.30443392	21.54211264	4	44.45899745	4.784803357	4
Bone	1.327226797	0.465553275	4	2.676462914	1.569143175	4	3.489126499	2.145516357	4
Muscle	0.62218617	0.296595309	4	0.665588529	0.091346205	4	0.525962398	0.102649409	4
Skin and Fur	3.858789788	1.851406863	4	2.934304287	0.483974034	4	1.414591504	0.218278802	4
Tail	3.58191388	1.965527666	4	3.195798508	0.779530681	4	1.625103345	0.746248968	4
Brain	0.268754083	0.125391133	4	0.171779431	0.042736477	4	0.986483798	0.266561575	4
Kidney	6.752648032	5.079592266	4	4.886517577	0.730655011	4	5.831151214	0.749681987	4

Table 7.4. Biodistribution data from the TCO-PL-liposomes pretargeting experiment on tumour animals

	^{67}Ga-TCO-liposomes-48 h (Positive control)			^{68}Ga-THP-tetrazine (Negative control)			Pretargeting group- 24 h		
	Mean	Standard dev	4	Mean	Standard dev	4	Mean	Standard dev	3
Blood	3.745671	1.575558	4	4.210877	0.947796	3	4.168174	5.257386	5
Heart	1.553543	0.497039	4	1.553129	0.449273	3	2.450205	1.886517	5
Lungs	1.733273	0.330726	4	8.829553	7.099763	3	18.43101	13.22112	5
Stomach	0.738245	0.169509	4	0.652772	0.089637	3	1.122039	1.126008	5
Pancreas	1.55159	1.294178	4	0.753637	0.208766	3	1.052	1.418785	5
Spleen	51.02272	20.41804	4	6.502822	0.58481	3	19.99855	8.000653	5
Small Intestine	1.317335	0.151532	4	3.141064	1.383721	3	8.659665	1.267427	5
Large instestine	0.885356	0.204259	4	5.846163	3.318049	3	1.807485	1.571937	5
Liver	40.6665	4.389445	4	9.446526	2.739664	3	34.83466	22.79337	5
Bone	2.493422	0.739933	4	1.029953	0.472213	3	2.012306	2.351149	5
Muscle	0.278623	0.091204	4	0.440502	0.091305	3	0.711072	0.599797	5
Skin and Fur	1.516088	0.273866	4	1.497613	0.349109	3	2.08836	1.028997	5
Tail	1.175871	0.343965	4	2.091081	0.650515	3	2.623479	1.321404	5
Brain	0.15547	0.139344	4	0.145119	0.043302	3	0.282092	0.291367	5
Kidney	3.803221	0.696908	4	6.264872	4.499794	3	4.423072	2.285061	5
Urine	4.169576	0.508672	4	461.0004	366.8738	3	234.6064	169.7733	5
Bladder	0.547079	0.113357	4	1.879929	1.882884	3	10.82124	11.87311	5
Salivary glands	0.907305	0.60242	4	0.764007	0.346333	3	1.409566	1.042137	5
Ovaries	0.940056	0.653437	4	0.694487	0.465829	3	1.117211	1.065748	5
Uterus	2.701091	1.255419	4	1.609073	0.785208	3	2.448279	3.01738	5
Thymus	1.507303	0.547012	4	1.010553	0.090178	3	1.701703	1.744682	5
Tumour	10.83139	1.93873	4	1.135511	0.149272	3	1.8213	1.113882	5
Bile	0.346731	0.261945	3	22.38266	4.51	3	29.10507	22.56379	5

8 REFERENCES

1. EHRLICH, P. Experimental Researches on Specific Therapy: On Immunity with special Reference to the Relationship between Distribution and Action of Antigens: FIRST HARBEN LECTURE. *The Collected Papers of Paul Ehrlich* 106–117 (1960) doi:10.1016/B978-0-08-009056-6.50015-4.

2. Strebhardt, K. & Ullrich, A. Paul Ehrlich's magic bullet concept: 100 years of progress. *Nature Reviews Cancer 2008 8:6* **8**, 473–480 (2008).

3. Shi, J., Kantoff, P. W., Wooster, R. & Farokhzad, O. C. Cancer nanomedicine: progress, challenges and opportunities. *Nature Reviews Cancer 2016 17:1* **17**, 20–37 (2016).

4. Fornaguera, C. & García-Celma, M. J. Personalized Nanomedicine: A Revolution at the Nanoscale. *J Pers Med* **7**, (2017).

5. Lammers, T., Aime, S., Hennink, W. E., Storm, G. & Kiessling, F. Theranostic nanomedicine. *Acc Chem Res* **44**, 1029–1038 (2011).

6. Duncan, R. & Gaspar, R. Nanomedicine(s) under the microscope. *Mol Pharm* **8**, 2101–2141 (2011).

7. Bobo, D., Robinson, K. J., Islam, J., Thurecht, K. J. & Corrie, S. R. Nanoparticle-Based Medicines: A Review of FDA-Approved Materials and Clinical Trials to Date. *Pharm Res* **33**, 2373–2387 (2016).

8. Weissig, V. & Guzman-Villanueva, D. Nanopharmaceuticals (part 2): products in the pipeline. *Int J Nanomedicine* **10**, 1245–1257 (2015).

9. Nanomedicine. (2014) doi:10.1007/978-1-4614-2140-5.

10. Shi, J., Kantoff, P. W., Wooster, R. & Farokhzad, O. C. Cancer nanomedicine: progress, challenges and opportunities. *Nature Reviews Cancer 2016 17:1* **17**, 20–37 (2016).

11. Etheridge, M. L. *et al.* THE BIG PICTURE ON SMALL MEDICINE: THE STATE OF NANOMEDICINE PRODUCTS APPROVED FOR USE OR IN CLINICAL TRIALS. *Nanomedicine* **9**, 1 (2013).

12. Howard, K., Dannpeer, T.-J. & Nanomedicine, E. Advances in Delivery Science and Technology.

13. Liu, D., Yang, F., Xiong, F. & Gu, N. The smart drug delivery system and its clinical potential. *Theranostics* **6**, 1306–1323 (2016).

14. Bregoli, L. *et al.* Nanomedicine applied to translational oncology: A future perspective on cancer treatment. *Nanomedicine* **12**, 81–103 (2016).

15. Ehmann, F. *et al.* Next-generation nanomedicines and nanosimilars: EU regulators' initiatives relating to the development and evaluation of nanomedicines. *https://doi.org/10.2217/nnm.13.68* **8**, 849–856 (2013).

16. Ramanathan, R. K. *et al.* Correlation between ferumoxytol uptake in tumour lesions by MRI and response to nanoliposomal irinotecan in patients with advanced solid tumours: A pilot study. *Clinical Cancer Research* (2017) doi:10.1158/1078-0432.CCR-16-1990.

17. Dawidczyk, C. M. *et al.* State-of-the-art in design rules for drug delivery platforms: Lessons learned from FDA-approved nanomedicines. *Journal of Controlled Release* (2014) doi:10.1016/j.jconrel.2014.05.036.

18. Gabizon, A., Shmeeda, H., Horowitz, A. T. & Zalipsky, S. Tumour cell targeting of liposome-entrapped drugs with phospholipid-anchored folic acid–PEG conjugates. *Adv Drug Deliv Rev* **56**, 1177–1192 (2004).

19. Ayala-Orozco, C. *et al.* Au nanomatryoshkas as efficient near-infrared photothermal transducers for cancer treatment: Benchmarking against nanoshells. *ACS Nano* (2014) doi:10.1021/nn501871d.

20. Jørgensen, J. T. *et al.* Single Particle and PET-based Platform for Identifying Optimal Plasmonic Nano-Heaters for Photothermal Cancer Therapy. *Sci Rep* (2016) doi:10.1038/srep30076.

21. Barenholz, Y. Doxil® — The first FDA-approved nano-drug: Lessons learned. *Journal of Controlled Release* **160**, 117–134 (2012).

22. FDA approves DaunoXome as first-line therapy for Kaposi's sarcoma. Food and Drug Administration. *J Int Assoc Physicians AIDS Care* **2**, 50–51 (1996).

23. Bulbake, U., Doppalapudi, S., Kommineni, N. & Khan, W. Liposomal Formulations in Clinical Use: An Updated Review. *Pharmaceutics* **9**, (2017).

24. Chaudhuri, T. R. *et al.* Tumour-Priming Smoothened Inhibitor Enhances Deposition and Efficacy of Cytotoxic Nanoparticles in a Pancreatic Cancer Model. *Mol Cancer Ther* **15**, 84–93 (2016).

25. Gonda, A. *et al.* Engineering Tumour-Targeting Nanoparticles as Vehicles for Precision Nanomedicine. *Med One* **4**, (2019).

26. Düzgüneş, N. & Gregoriadis, G. Introduction: The origins of liposomes: Alec Bangham at Babraham. *Methods Enzymol* **391**, 1–3 (2005).

27. Bangham, A. D. ; H. M. W. ; M. N. G. A., Hill, M. W. & Miller, N. G. A. Preparation and Use of Liposomes as Models of Biological Membranes. *Methods in Membrane Biology* 1–68 (1974) doi:10.1007/978-1-4615-7422-4_1.

28. Allen, T. M. & Cullis, P. R. Liposomal drug delivery systems: From concept to clinical applications. *Adv Drug Deliv Rev* **65**, 36–48 (2013).

29. Bozzuto, G. & Molinari, A. Liposomes as nanomedical devices. *Int J Nanomedicine* **10**, 975–999 (2015).

30. Schoenmaker, L. *et al.* mRNA-lipid nanoparticle COVID-19 vaccines: Structure and stability. *Int J Pharm* **601**, 120586 (2021).

31. Gao, Y., Wijewardhana, C. & Mann, J. F. S. Virus-like particle, liposome, and polymeric particle-based vaccines against HIV-1. *Front Immunol* **9**, 345 (2018).

32. Chonn, A. & Cullis, P. R. Recent advances in liposomal drug-delivery systems. *Curr Opin Biotechnol* **6**, 698–708 (1995).

33. Pinot, M. *et al.* Polyunsaturated phospholipids facilitate membrane deformation and fission by endocytic proteins. *Science (1979)* **345**, 693–697 (2014).

34. Monteiro, N., Martins, A., Reis, R. L. & Neves, N. M. Liposomes in tissue engineering and regenerative medicine. *J R Soc Interface* **11**, (2014).

35. Rothfield, L. *Structure and function of biological membranes*. (2014).

36. Priev, A., Zalipsky, S., Cohen, R. & Barenholz, Y. Determination of Critical Micelle Concentration of Lipopolymers and Other Amphiphiles: Comparison of Sound Velocity and Fluorescent Measurements. *Langmuir* **18**, 612–617 (2002).

37. Zamani, P., Momtazi-Borojeni, A. A., Nik, M. E., Oskuee, R. K. & Sahebkar, A. Nanoliposomes as the adjuvant delivery systems in cancer immunotherapy. *J Cell Physiol* **233**, 5189–5199 (2018).

38. Li, J. *et al.* A review on phospholipids and their main applications in drug delivery systems. *Asian J Pharm Sci* **10**, 81–98 (2015).

39. Lin, X. & Gu, N. Surface properties of encapsulating hydrophobic nanoparticles regulate the main phase transition temperature of lipid bilayers: A simulation study. *Nano Research 2014 7:8* **7**, 1195–1204 (2014).

40. Hussain, A. *et al.* Elastic liposomes as novel carriers: recent advances in drug delivery. *Int J Nanomedicine* **12**, 5087–5108 (2017).

41. Murthy, A. V. R., Guyomarc’h, F. & Lopez, C. The temperature-dependent physical state of polar lipids and their miscibility impact the topography and mechanical properties of bilayer models of the milk fat globule membrane. *Biochimica et Biophysica Acta (BBA) - Biomembranes* **1858**, 2181–2190 (2016).

42. Rühling, A. *et al.* Influence of the Headgroup of Azolium-Based Lipids on Their Biophysical Properties and Cytotoxicity. *Chemistry – A European Journal* **23**, 5920–5924 (2017).

43. Vallejo, A. A., Velázquez, J. B. & Fernández, M. S. Lateral organization of mixed, two-phosphatidylcholine liposomes as investigated by GPS, the slope of Laurdan generalized polarization spectra. *Arch Biochem Biophys* **466**, 145–154 (2007).

44. Agassandian, M. & Mallampalli, R. K. Surfactant phospholipid metabolism. *Biochimica et Biophysica Acta (BBA) - Molecular and Cell Biology of Lipids* **1831**, 612–625 (2013).

45. Hernández-Caselles, T., Villalaín, J. & Gómez-Fernández, J. C. Influence of liposome charge and composition on their interaction with human blood serum proteins. *Molecular and Cellular Biochemistry 1993 120:2* **120**, 119–126 (1993).

46. Sugiyama, H., Osaki, T., Takeuchi, S. & Toyota, T. Role of Negatively Charged Lipids Achieving Rapid Accumulation of Water-Soluble Molecules and Macromolecules into Cell-Sized Liposomes against a Concentration Gradient. *Langmuir* **38**, 112–121 (2022).

47. Merino, M., Zalba, S. & Garrido, M. J. Immunoliposomes in clinical oncology: State of the art and future perspectives. *Journal of Controlled Release* **275**, 162–176 (2018).

48. Bourquin, J. *et al.* Biodistribution, Clearance, and Long-Term Fate of Clinically Relevant Nanomaterials. *Advanced Materials* **30**, 1704307 (2018).

49. Kraft, J. C., Freeling, J. P., Wang, Z. & Ho, R. J. Y. Emerging Research and Clinical Development Trends of Liposome and Lipid Nanoparticle Drug Delivery Systems. *J Pharm Sci* **103**, 29–52 (2014).

50. Briuglia, M. L., Rotella, C., McFarlane, A. & Lamprou, D. A. Influence of cholesterol on liposome stability and on in vitro drug release. *Drug Deliv Transl Res* **5**, 231–242 (2015).

51. Sercombe, L. *et al.* Advances and challenges of liposome assisted drug delivery. *Front Pharmacol* **6**, 286 (2015).

52. Danaei, M. *et al.* Impact of Particle Size and Polydispersity Index on the Clinical Applications of Lipidic Nanocarrier Systems. *Pharmaceutics* **10**, (2018).

53. Gabizon, A. & Papahadjopoulos, D. Liposome formulations with prolonged circulation time in blood and enhanced uptake by tumours (phospholipid vesicles/drug delivery systems/cancer therapy/glycolipids). *Proc. Natl. Acad. Sci. USA* **85**, 6949–6953 (1988).

54. Lasic, D. D., Martin, F. J., Gabizon, A., Huang, S. K. & Papahadjopoulos, D. Sterically stabilized liposomes: a hypothesis on the molecular origin of the extended circulation times. *Biochim Biophys Acta* **1070**, 187–192 (1991).

55. Gabizon, A., Shmeeda, H. & Barenholz, Y. Pharmacokinetics of pegylated liposomal doxorubicin: Review of animal and human studies. *Clin Pharmacokinet* **42**, 419–436 (2003).

56. Litzinger, D. C., Buiting, A. M. J., van Rooijen, N. & Huang, L. Effect of liposome size on the circulation time and intraorgan distribution of amphipathic poly(ethylene glycol)-containing liposomes. *Biochim Biophys Acta* **1190**, 99–107 (1994).

57. Allen, T. M. Long-circulating (sterically stabilized) liposomes for targeted drug delivery. *Trends Pharmacol Sci* **15**, 215–220 (1994).

58. Yingchoncharoen, P., Kalinowski, D. S. & Richardson, D. R. Lipid-Based Drug Delivery Systems in Cancer Therapy: What Is Available and What Is Yet to Come. *Pharmacol Rev* **68**, 701–787 (2016).

59. Barenholz, Y. (Chezy). Doxil® — The first FDA-approved nano-drug: Lessons learned. *Journal of Controlled Release* **160**, 117–134 (2012).

60. Maranhão, R. C., Vital, C. G., Tavoni, T. M. & Graziani, S. R. Clinical experience with drug delivery systems as tools to decrease the toxicity of anticancer

chemotherapeutic agents. *http://dx.doi.org/10.1080/17425247.2017.1276560* **14**, 1217–1226 (2017).

61. Meng, J. *et al.* Combination Therapy using Co-encapsulated Resveratrol and Paclitaxel in Liposomes for Drug Resistance Reversal in Breast Cancer Cells in vivo. *Scientific Reports 2016 6:1* **6**, 1–11 (2016).

62. Rose, S. J., Neville, M. E., Gupta, R. & Bermudez, L. E. Delivery of Aerosolized Liposomal Amikacin as a Novel Approach for the Treatment of Nontuberculous Mycobacteria in an Experimental Model of Pulmonary Infection. *PLoS One* **9**, e108703 (2014).

63. Xia, Y. *et al.* Liposome-based probes for molecular imaging: from basic research to the bedside. *Nanoscale* **11**, 5822–5838 (2019).

64. Lamichhane, N. *et al.* Liposomes: Clinical Applications and Potential for Image-Guided Drug Delivery. *Molecules* **23**, (2018).

65. Attia, M. F., Anton, N., Wallyn, J., Omran, Z. & Vandamme, T. F. An overview of active and passive targeting strategies to improve the nanocarriers efficiency to tumour sites. *Journal of Pharmacy and Pharmacology* **71**, 1185–1198 (2019).

66. Noble, G. T., Stefanick, J. F., Ashley, J. D., Kiziltepe, T. & Bilgicer, B. Ligand-targeted liposome design: challenges and fundamental considerations. *Trends Biotechnol* **32**, 32–45 (2014).

67. Riaz, M. K. *et al.* Surface Functionalization and Targeting Strategies of Liposomes in Solid Tumour Therapy: A Review. *International Journal of Molecular Sciences 2018, Vol. 19, Page 195* **19**, 195 (2018).

68. Matsumura, Y. & Maeda, H. A new concept for macromolecular therapeutics in cancer chemotherapy: mechanism of tumouritropic accumulation of proteins and the antitumour agent smancs. *Cancer Res* **46**, 6387–92 (1986).

69. Maeda, H., Wu, J., Sawa, T., Matsumura, Y. & Hori, K. Tumour vascular permeability and the EPR effect in macromolecular therapeutics: A review.

Journal of Controlled Release Preprint at https://doi.org/10.1016/S0168-3659(99)00248-5 (2000).

70. Kobayashi, H., Watanabe, R. & Choyke, P. L. Improving conventional enhanced permeability and retention (EPR) effects; What is the appropriate target? *Theranostics* **4**, 81–89 (2014).

71. Torchilin, V. Tumour delivery of macromolecular drugs based on the EPR effect. *Adv Drug Deliv Rev* **63**, 131–135 (2011).

72. Maeda, H. The enhanced permeability and retention (EPR) effect in tumour vasculature: the key role of tumor-selective macromolecular drug targeting. *Adv Enzyme Regul* **41**, 189–207 (2001).

73. Fang, J., Nakamura, H. & Maeda, H. The EPR effect: Unique features of tumor blood vessels for drug delivery, factors involved, and limitations and augmentation of the effect. *Adv Drug Deliv Rev* **63**, 136–151 (2011).

74. Arap, W., Pasqualini, R. & Ruoslahti, E. Cancer treatment by targeted drug delivery to tumor vasculature in a mouse model. *Science* **279**, 377–380 (1998).

75. Chono, S., Tanino, T., Seki, T. & Morimoto, K. Uptake characteristics of liposomes by rat alveolar macrophages: influence of particle size and surface mannose modification. *Journal of Pharmacy and Pharmacology* **59**, 75–80 (2007).

76. Osaki, F., Kanamori, T., Sando, S., Sera, T. & Aoyama, Y. A quantum dot conjugated sugar ball and its cellular uptake. On the size effects of endocytosis in the subviral region. *J Am Chem Soc* **126**, 6520–6521 (2004).

77. Yin Win, K. & Feng, S. S. Effects of particle size and surface coating on cellular uptake of polymeric nanoparticles for oral delivery of anticancer drugs. *Biomaterials* **26**, 2713–2722 (2005).

78. Foged, C., Brodin, B., Frokjaer, S. & Sundblad, A. Particle size and surface charge affect particle uptake by human dendritic cells in an in vitro model. *Int J Pharm* **298**, 315–322 (2005).

79. Chithrani, B. D., Ghazani, A. A. & Chan, W. C. W. Determining the size and shape dependence of gold nanoparticle uptake into mammalian cells. *Nano Lett* **6**, 662–668 (2006).

80. Lu, F., Wu, S. H., Hung, Y. & Mou, C. Y. Size effect on cell uptake in well-suspended, uniform mesoporous silica nanoparticles. *Small* **5**, 1408–1413 (2009).

81. Immordino, M. L., Dosio, F. & Cattel, L. Stealth liposomes: review of the basic science, rationale, and clinical applications, existing and potential. *Int J Nanomedicine* **1**, 297 (2006).

82. Huynh, E. & Zheng, G. Cancer nanomedicine: addressing the dark side of the enhanced permeability and retention effect. *Nanomedicine (Lond)* **10**, 1993–1995 (2015).

83. Man, F., Lammers, T. & T. M. de Rosales, R. Imaging Nanomedicine-Based Drug Delivery: a Review of Clinical Studies. *Mol Imaging Biol* **20**, 683–695 (2018).

84. Lammers, T., Kiessling, F., Hennink, W. E. & Storm, G. Drug targeting to tumors: Principles, pitfalls and (pre-) clinical progress. *Journal of Controlled Release* **161**, 175–187 (2012).

85. Lammers, T. *et al.* Polymeric nanomedicines for image-guided drug delivery and tumor-targeted combination therapy. *Nano Today* **5**, 197–212 (2010).

86. Danhier, F. To exploit the tumor microenvironment: Since the EPR effect fails in the clinic, what is the future of nanomedicine? *Journal of Controlled Release* **244**, 108–121 (2016).

87. James, M. L. & Gambhir, S. S. A molecular imaging primer: modalities, imaging agents, and applications. *Physiol Rev* **92**, 897–965 (2012).

88. Marie, H. *et al.* Superparamagnetic liposomes for MRI monitoring and external magnetic field-induced selective targeting of malignant brain tumors. *Adv Funct Mater* **25**, 1258–1269 (2015).

89. Béalle, G. *et al.* Ultra magnetic liposomes for MR imaging, targeting, and hyperthermia. *Langmuir* **28**, 11834–11842 (2012).

90. Kostevšek, N. *et al.* Magneto-Liposomes as MRI Contrast Agents: A Systematic Study of Different Liposomal Formulations. *Nanomaterials* **10**, (2020).

91. Jin, R., Lin, B., Li, D. & Ai, H. Superparamagnetic iron oxide nanoparticles for MR imaging and therapy: Design considerations and clinical applications. *Curr Opin Pharmacol* **18**, 18–27 (2014).

92. Rogosnitzky, M. & Branch, S. Gadolinium-based contrast agent toxicity: a review of known and proposed mechanisms. *Biometals* **29**, 365 (2016).

93. Russo, P. *Handbook of X-ray imaging : physics and technology*. *Handbook of X-ray Imaging: Physics and Technology* (2018).

94. Liu, Y., Ai, K. & Lu, L. Nanoparticulate X-ray computed tomography contrast agents: From design validation to in vivo applications. *Acc Chem Res* **45**, 1817–1827 (2012).

95. Elrod, D. B., Partha, R., Danila, D., Casscells, S. W. & Conyers, J. L. An iodinated liposomal computed tomographic contrast agent prepared from a diiodophosphatidylcholine lipid. *Nanomedicine* **5**, 42–45 (2009).

96. Ashton, J. R., West, J. L. & Badea, C. T. In vivo small animal micro-CT using nanoparticle contrast agents. *Front Pharmacol* **6**, 256 (2015).

97. Ghaghada, K. B., Sato, A. F., Starosolski, Z. A., Berg, J. & Vail, D. M. Computed Tomography Imaging of Solid Tumors Using a Liposomal-Iodine Contrast Agent in Companion Dogs with Naturally Occurring Cancer. *PLoS One* **11**, e0152718 (2016).

98. Lusic, H. & Grinstaff, M. W. X-ray-computed tomography contrast agents. *Chem Rev* **113**, 1641–1666 (2013).

99. Versluis, M., Stride, E., Lajoinie, G., Dollet, B. & Segers, T. Ultrasound Contrast Agent Modeling: A Review. *Ultrasound Med Biol* **46**, 2117–2144 (2020).

100. Gessner, R. & Dayton, P. a. Advances in molecular imaging with ultrasound. *Molecular imaging : official journal of the Society for Molecular Imaging* **9**, 117–127 (2010).

101. Kheirolomoom, A. *et al.* Acoustically-Active Microbubbles Conjugated to Liposomes: Characterization of a Proposed Drug Delivery Vehicle. *J Control Release* **118**, 275 (2007).

102. de Matos, M. B. C. *et al.* Ultrasound-sensitive liposomes for triggered macromolecular drug delivery: Formulation and in vitro characterization. *Front Pharmacol* **10**, (2019).

103. Kunjachan, S. *et al.* Noninvasive optical imaging of nanomedicine biodistribution. *ACS Nano* **7**, 252–262 (2013).

104. Morse, S. v., Mishra, A., Chan, T. G., T. M. de Rosales, R. & Choi, J. J. Liposome delivery to the brain with rapid short-pulses of focused ultrasound and microbubbles. *J Control Release* **341**, 605–615 (2022).

105. May, J. N. *et al.* Multimodal and multiscale optical imaging of nanomedicine delivery across the blood-brain barrier upon sonopermeation. *Theranostics* **10**, 1948 (2020).

106. Al-Jamal, W. T. & Kostarelos, K. Liposomes: From a clinically established drug delivery system to a nanoparticle platform for theranostic nanomedicine. *Acc Chem Res* **44**, 1094–1104 (2011).

107. Yoon, Y. I. l. *et al.* Ultrasound-mediated gene and drug delivery using a microbubble-liposome particle system. *Theranostics* **4**, 1133–1144 (2014).

108. Karathanasis, E. *et al.* Tumor Vascular Permeability to a Nanoprobe Correlates to Tumor-Specific Expression Levels of Angiogenic Markers. *PLoS One* **4**, e5843 (2009).

109. Man, F. *et al.* In Vivo PET Tracking of 89 Zr-Labeled Vγ9Vδ2 T Cells to Mouse Xenograft Breast Tumors Activated with Liposomal Alendronate. *Molecular Therapy* **27**, 219–229 (2019).

110. Harrington, K. J. *et al.* Effective Targeting of Solid Tumors in Patients With Locally Advanced Cancers by Radiolabeled Pegylated Liposomes.

111. Lee, H. *et al.* ^{64} Cu-MM-302 Positron Emission Tomography Quantifies Variability of Enhanced Permeability and Retention of Nanoparticles in Relation to Treatment Response in Patients with Metastatic Breast Cancer. *Clinical Cancer Research* **23**, 4190–4202 (2017).

112. Pérez-Medina, C. *et al.* Nanoreporter PET predicts the efficacy of anti-cancer nanotherapy. *Nat Commun* **7**, 11838 (2016).

113. Sun, D. Nanotheranostics: Integration of Imaging and Targeted Drug Delivery. *Mol Pharm* **7**, 1879–1879 (2010).

114. van der Geest, T., Laverman, P., Metselaar, J. M., Storm, G. & Boerman, O. C. Radionuclide imaging of liposomal drug delivery. *Expert Opin Drug Deliv* **13**, 1231–1242 (2016).

115. Seymour, L. W. *et al.* Hepatic Drug Targeting: Phase I Evaluation of Polymer-Bound Doxorubicin. *Journal of Clinical Oncology* **20**, 1668–1676 (2002).

116. Engudar, G. *et al.* Remote loading of liposomes with a 124I-radioiodinated compound and their in vivo evaluation by PET/CT in a murine tumor model. *Theranostics* **8**, 5828–5841 (2018).

117. Yu, B. *et al.* Efficient Uptake of 177Lu-Porphyrin-PEG Nanocomplexes by Tumor Mitochondria for Multimodal-Imaging-Guided Combination Therapy. *Angewandte Chemie International Edition* **57**, 218–222 (2018).

118. Yang, X. *et al.* cRGD-functionalized, DOX-conjugated, and 64Cu-labeled superparamagnetic iron oxide nanoparticles for targeted anticancer drug delivery and PET/MR imaging. *Biomaterials* **32**, 4151–4160 (2011).

119. Pérez-Medina, C. *et al.* Nanoreporter PET predicts the efficacy of anti-cancer nanotherapy. *Nature Communications 2016 7:1* **7**, 1–8 (2016).

120. Pérez-Medina, C., Teunissen, A. J. P., Kluza, E., Mulder, W. J. M. & van der Meel, R. Nuclear imaging approaches facilitating nanomedicine translation. *Adv Drug Deliv Rev* **154–155**, 123–141 (2020).

121. Beyer, T., Townsend, D. W., Czernin, J. & Freudenberg, L. S. The future of hybrid imaging—part 2: PET/CT. *Insights into Imaging 2011 2:3* **2**, 225–234 (2011).

122. Phelps, M. E. PET: the merging of biology and imaging into molecular imaging. *J Nucl Med* **41**, 661–81 (2000).

123. Cherry, S. R. *et al.* Total-Body PET: Maximizing Sensitivity to Create New Opportunities for Clinical Research and Patient Care. *J Nucl Med* **59**, 3–12 (2018).

124. Madsen, M. T. Recent Advances in SPECT Imaging. *J Nucl Med* **48**, 661–673 (2007).

125. Rahmim, A. & Zaidi, H. PET versus SPECT: strengths, limitations and challenges. *Nucl Med Commun* **29**, 193–207 (2008).

126. Khalil, M. M., Tremoleda, J. L., Bayomy, T. B. & Gsell, W. Molecular SPECT Imaging: An Overview. *Int J Mol Imaging* **2011**, 15 (2011).

127. Heinzmann, K., Carter, L. M., Lewis, J. S. & Aboagye, E. O. Multiplexed imaging for diagnosis and therapy. *Nature Biomedical Engineering 2017 1:9* **1**, 697–713 (2017).

128. Poley, M. *et al.* Nanoparticles Accumulate in the Female Reproductive System during Ovulation Affecting Cancer Treatment and Fertility. *ACS Nano* (2022) doi:10.1021/ACSNANO.1C07237.

129. Judenhofer, M. S. *et al.* Simultaneous PET-MRI: a new approach for functional and morphological imaging. *Nature Medicine 2008 14:4* **14**, 459–465 (2008).

130. Kunjachan, S., Ehling, J., Storm, G., Kiessling, F. & Lammers, T. Noninvasive Imaging of Nanomedicines and Nanotheranostics: Principles, Progress, and Prospects. *Chem Rev* **115**, 10907–10937 (2015).

131. Ni, D., Ehlerding, E. B. & Cai, W. Multimodality Imaging Agents with PET as the Fundamental Pillar. *Angewandte Chemie International Edition* **58**, 2570–2579 (2019).

132. Beyer, T., Freudenberg, L. S., Townsend, D. W. & Czernin, J. The future of hybrid imaging—part 1: hybrid imaging technologies and SPECT/CT. *Insights into Imaging 2011 2:2* **2**, 161–169 (2011).

133. Martí-Bonmatí, L., Sopena, R., Bartumeus, P. & Sopena, P. Multimodality imaging techniques. *Contrast Media Mol Imaging* **5**, 180–189 (2010).

134. Beyer, T., Freudenberg, L. S., Czernin, J. & Townsend, D. W. The future of hybrid imaging—part 3: PET/MR, small-animal imaging and beyond. *Insights into Imaging 2011 2:3* **2**, 235–246 (2011).

135. Nahrendorf, M. *et al.* Hybrid PET-optical imaging using targeted probes. *Proc Natl Acad Sci U S A* **107**, 7910–7915 (2010).

136. Majmudar, M. D. *et al.* Polymeric nanoparticle PET/MR imaging allows macrophage detection in atherosclerotic plaques. *Circ Res* **112**, 755–761 (2013).

137. Liu, F., Jang, H., Kijowski, R., Bradshaw, T. & McMillan, A. B. Deep learning MR imaging-based attenuation correction for PET/MR imaging. *Radiology* **286**, 676–684 (2018).

138. Belcari, N. ; B. R. ; M. M., Boellaard, R. & Morrocchi, M. PET/CT and PET/MR Tomographs: Image Acquisition and Processing. *Nuclear Medicine Textbook* 199–217 (2019) doi:10.1007/978-3-319-95564-3_9.

139. Silindir-Gunay, M., Karpuz, M. & Ozer, A. Y. Targeted Alpha Therapy and Nanocarrier Approach. *Cancer Biother Radiopharm* **35**, 446–458 (2020).

140. Jeon, J. Review of Therapeutic Applications of Radiolabeled Functional Nanomaterials. *International Journal of Molecular Sciences 2019, Vol. 20, Page 2323* **20**, 2323 (2019).

141. Poty, S., Francesconi, L. C., McDevitt, M. R., Morris, M. J. & Lewis, J. S. α-Emitters for Radiotherapy: From Basic Radiochemistry to Clinical Studies-Part 1. *J Nucl Med* **59**, 878–884 (2018).

142. Baidoo, K. E., Yong, K. & Brechbiel, M. W. Molecular Pathways: Targeted α-Particle Radiation Therapy. *Clin Cancer Res* **19**, 530 (2013).

143. Aghevlian, S., Boyle, A. J. & Reilly, R. M. Radioimmunotherapy of cancer with high linear energy transfer (LET) radiation delivered by radionuclides emitting α-particles or Auger electrons. *Adv Drug Deliv Rev* **109**, 102–118 (2017).

144. Ku, A., Facca, V. J., Cai, Z. & Reilly, R. M. Auger electrons for cancer therapy – a review. *EJNMMI Radiopharmacy and Chemistry 2019 4:1* **4**, 1–36 (2019).

145. Qaim, S. M., Scholten, B. & Neumaier, B. New developments in the production of theranostic pairs of radionuclides. *J Radioanal Nucl Chem* **318**, 1493–1509 (2018).

146. Chang, Y. J. *et al.* Therapeutic efficacy and microSPECT/CT imaging of 188Re-DXR-liposome in a C26 murine colon carcinoma solid tumor model. *Nucl Med Biol* **37**, 95–104 (2010).

147. Chen, L. C. *et al.* Biodistribution, pharmacokinetics and imaging of 188Re-BMEDA-labeled pegylated liposomes after intraperitoneal injection in a C26 colon carcinoma ascites mouse model. *Nucl Med Biol* **34**, 415–423 (2007).

148. Chen, L. C. *et al.* Pharmacokinetics, micro-SPECT/CT imaging and therapeutic efficacy of 188Re-DXR-liposome in C26 colon carcinoma ascites mice model. *Nucl Med Biol* **35**, 883–893 (2008).

149. Petersen, A. L. *et al.* In vivo evaluation of PEGylated 64Cu-liposomes with theranostic and radiotherapeutic potential using micro PET/CT. *Eur J Nucl Med Mol Imaging* **43**, 941–952 (2016).

150. Yu, B. *et al.* Efficient Uptake of 177Lu-Porphyrin-PEG Nanocomplexes by Tumor Mitochondria for Multimodal-Imaging-Guided Combination Therapy. *Angewandte Chemie International Edition* **57**, 218–222 (2018).

151. Buckway, B., Frazier, N., Gormley, A. J., Ray, A. & Ghandehari, H. Gold nanorod-mediated hyperthermia enhances the efficacy of HPMA copolymer-90Y conjugates in treatment of prostate tumors. *Nucl Med Biol* **41**, 282–289 (2014).

152. Shi, W. *et al.* The influence of linker length on the properties of cathepsin S cleavable 177Lu-labeled HPMA copolymers for pancreatic cancer imaging. *Biomaterials* **35**, 5760–5770 (2014).

153. Zhu, W. *et al.* 131I-Labeled Multifunctional Polyphosphazene Nanospheres for SPECT Imaging-Guided Radiotherapy of Tumors. *Adv Healthc Mater* **8**, 1901299 (2019).

154. Cheng, Y. *et al.* 131I-labeled multifunctional dendrimers modified with BmK CT for targeted SPECT imaging and radiotherapy of gliomas. *https://doi.org/10.2217/nnm-2016-0001* **11**, 1253–1266 (2016).

155. Moeendarbari, S. *et al.* Theranostic Nanoseeds for Efficacious Internal Radiation Therapy of Unresectable Solid Tumors. *Scientific Reports 2016 6:1* **6**, 1–9 (2016).

156. Yook, S. *et al.* Intratumorally Injected 177Lu-Labeled Gold Nanoparticles: Gold Nanoseed Brachytherapy with Application for Neoadjuvant Treatment of Locally Advanced Breast Cancer. *Journal of Nuclear Medicine* **57**, 936–942 (2016).

157. Li, Z. & Conti, P. S. Radiopharmaceutical chemistry for positron emission tomography. *Adv Drug Deliv Rev* **62**, 1031–1051 (2010).

158. Adak, S. *et al.* Radiotracers for SPECT imaging: Current scenario and future prospects. *Radiochim Acta* **100**, 95–107 (2012).

159. Brandt, M., Cardinale, J., Aulsebrook, M. L., Gasser, G. & Mindt, T. L. An Overview of PET Radiochemistry, Part 2: Radiometals. *Journal of Nuclear Medicine* **59**, 1500–1506 (2018).

160. Price, E. W. & Orvig, C. Matching chelators to radiometals for radiopharmaceuticals. *Chem Soc Rev* **43**, 260–290 (2013).

161. Southworth, R. *et al.* Opportunities and Challenges for Metal Chemistry in Molecular Imaging: From Gamma Camera Imaging to PET and Multimodality Imaging. *Adv Inorg Chem* **68**, 1–41 (2016).

162. Abou, D. S., Ku, T. & Smith-Jones, P. M. In vivo biodistribution and accumulation of 89Zr in mice. *Nucl Med Biol* **38**, 675–681 (2011).

163. Ródenas, J. & Jabaloyas, E. Analysis of radionuclide production in cyclotrons for application in positron emission tomography (PET). *J Radioanal Nucl Chem* **322**, 1691–1695 (2019).

164. Tressaud, Alain. & Haufe, G. Fluorine and health : molecular imaging, biomedical materials and pharmaceuticals. 792 (2008).

165. Alauddin, M. M. Positron emission tomography (PET) imaging with 18F-based radiotracers. *Am J Nucl Med Mol Imaging* **2**, 55 (2012).

166. Emmetiere, F. *et al.* F-Labeled-Bioorthogonal Liposomes for In Vivo Targeting. (2013) doi:10.1021/bc400322h.

167. Helbok, A. *et al.* Radiolabeling of lipid-based nanoparticles for diagnostics and therapeutic applications: a comparison using different radiometals. *http://dx.doi.org/10.3109/08982100903311812* **20**, 219–227 (2010).

168. Zhang-Yin, J. *et al.* A comparative study of peptide-based imaging agents [68Ga]Ga-PSMA-11, [68Ga]Ga-AMBA, [68Ga]Ga-NODAGA-RGD and [68Ga]Ga-DOTA-NT-20.3 in preclinical prostate tumour models. *Nucl Med Biol* **84–85**, 88–95 (2020).

169. Verel, I. *et al.* 89Zr Immuno-PET: Comprehensive Procedures for the Production of 89Zr-Labeled Monoclonal Antibodies. *Journal of Nuclear Medicine* **44**, (2003).

170. Blower, P. J., Lewis, J. S. & Zweit, J. Copper radionuclides and radiopharmaceuticals in nuclear medicine. *Nucl Med Biol* **23**, 957–80 (1996).

171. Locke, L. W., Mayo, M. W., Yoo, A. D., Williams, M. B. & Berr, S. S. PET imaging of tumor associated macrophages using mannose coated 64Cu liposomes. *Biomaterials* **33**, 7785–7793 (2012).

172. Petersen, A. L. *et al.* 64Cu loaded liposomes as positron emission tomography imaging agents. *Biomaterials* **32**, 2334–2341 (2011).

173. Petersen, A. L. *et al.* In vivo evaluation of PEGylated ^{64}Cu-liposomes with theranostic and radiotherapeutic potential using micro PET/CT. *Eur J Nucl Med Mol Imaging* **43**, 941–952 (2016).

174. Abou, D. S. *et al.* 89Zr-labeled paramagnetic octreotide-liposomes for PET-MR imaging of cancer. *Pharm Res* **30**, 878–888 (2013).

175. Radioactivity Radionuclides Radiation. *Radioactivity Radionuclides Radiation* (2005) doi:10.1007/B138236.

176. Eckerman, K. F., Endo, A. & Wong, F. C. MIRD: Radionuclide Data and Decay Schemes. *Journal of Nuclear Medicine* **50**, 2091–2091 (2009).

177. Boerman, O. C., Laverman, P., Oyen, W. J. G., Corstens, F. H. M. & Storm, G. Radiolabeled liposomes for scintigraphic imaging. *Prog Lipid Res* **39**, 461–475 (2000).

178. Ogawa, M., Uchino, R., Kawai, A., Kosugi, M. & Magata, Y. PEG modification on (111)In-labeled phosphatidyl serine liposomes for imaging of atherosclerotic plaques. *Nucl Med Biol* **42**, 299–304 (2015).

179. Boschi, A., Uccelli, L. & Martini, P. A Picture of Modern Tc-99m Radiopharmaceuticals: Production, Chemistry, and Applications in Molecular Imaging. *Applied Sciences 2019, Vol. 9, Page 2526* **9**, 2526 (2019).

180. Pimlott, S. L. & Sutherland, A. Molecular tracers for the PET and SPECT imaging of disease. *Chem Soc Rev* **40**, 149–162 (2010).

181. Lin, Y. Y. *et al.* Tumor burden talks in cancer treatment with PEGylated liposomal drugs. *PLoS One* **8**, (2013).

182. Moghimi, S. M. & Szebeni, J. Stealth liposomes and long circulating nanoparticles: critical issues in pharmacokinetics, opsonization and protein-binding properties. *Prog Lipid Res* **42**, 463–478 (2003).

183. Ogawa, M. *et al.* Development of 111In-labeled liposomes for vulnerable atherosclerotic plaque imaging. *J Nucl Med* **55**, 115–120 (2014).

184. Allen, D. R. Radiopharmaceutical chemistry. *Appl Radiol* **4**, (1975).

185. Richardson, V. J., Ryman, B. E., Jewkes, R. F., Tattersall, M. H. N. & Newlands, E. S. 99mTc-labelled liposomes preparation of radiopharmaceutical and its distribution in a hepatoma patient. *Int J Nucl Med Biol* **5**, 118–122 (1978).

186. Richardson, V. J., Jeyasingh, K. & Jewkes, R. F. Properties of [99mTc] technetium-labelled liposomes in normal and tumour-bearing rats. *Biochem Soc Trans* **5**, 290–291 (1977).

187. Hnatowich, D. J., Friedman, B., Clancy, B. & Novak, M. Labeling of Preformed Liposomes with Ga-67 and Tc-99m by Chelation. *Journal of Nuclear Medicine* **22**, (1981).

188. Laverman, P. *et al.* A Novel Method to Label Liposomes with 99mTc by the Hydrazino Nicotinyl Derivative. *Journal of Nuclear Medicine* **40**, (1999).

189. Hwang, H. *et al.* PEGylated nanoliposomes encapsulating angiogenic peptides improve perfusion defects: Radionuclide imaging-based study. *Nucl Med Biol* **43**, 552–558 (2016).

190. Monteiro, L. O. F. *et al.* Paclitaxel-loaded folate-coated long circulating and pH-sensitive liposomes as a potential drug delivery system: A biodistribution study. *Biomedicine & Pharmacotherapy* **97**, 489–495 (2018).

191. e Silva, A. T. M. *et al.* Synthesis of cholesterol-based neoglycoconjugates and their use in the preparation of liposomes for active liver targeting. *Carbohydr Res* **465**, 52–57 (2018).

192. Helbok, A. *et al.* Radiolabeling of lipid-based nanoparticles for diagnostics and therapeutic applications: a comparison using different radiometals. *http://dx.doi.org/10.3109/08982100903311812* **20**, 219–227 (2010).

193. Malinge, J. *et al.* Liposomes for PET and MR imaging and for dual targeting (magnetic field/glucose moiety): Synthesis, properties, and in vivo studies. *Mol Pharm* **14**, 406–414 (2017).

194. Jai, W. S., Zhang, H., Kukis, D. L., Meares, C. F. & Ferrara, K. W. A Novel Method to Label Preformed Liposomes with 64Cu for Positron Emission Tomography (PET) Imaging. *Bioconjug Chem* **19**, 2577–2584 (2008).

195. Pérez-Medina, C. *et al.* A Modular Labeling Strategy for In Vivo PET and Near-Infrared Fluorescence Imaging of Nanoparticle Tumor Targeting. *Journal of Nuclear Medicine* **55**, 1706–1711 (2014).

196. Hood, E. D. *et al.* Vascular Targeting of Radiolabeled Liposomes with Bio-Orthogonally Conjugated Ligands: Single Chain Fragments Provide Higher Specificity than Antibodies. *Bioconjug Chem* **29**, 3626–3637 (2018).

197. Emmetiere, F. *et al.* 18F-labeled-bioorthogonal liposomes for in vivo targeting. *Bioconjug Chem* **24**, 1784–1789 (2013).

198. Marik, J. *et al.* Long-circulating liposomes radiolabeled with [18F]fluorodipalmitin ([18F]FDP). *Nucl Med Biol* **34**, 165–171 (2007).

199. Pérez-Campaña, C. *et al.* Tracing nanoparticles in vivo: a new general synthesis of positron emitting metal oxide nanoparticles by proton beam activation. *Analyst* **137**, 4902–4906 (2012).

200. Wong, R. M., Gilbert, D. A., Liu, K. & Louie, A. Y. Rapid Size-Controlled Synthesis of Dextran-Coated, ^{64} Cu-Doped Iron Oxide Nanoparticles. *ACS Nano* **6**, 3461–3467 (2012).

201. Gawne, P. J. *et al.* Manganese-52: Applications in Cell Radiolabelling and Liposomal Nanomedicine PET Imaging using Oxine (8-hydroxyquinoline) as an Ionophore. *Dalton Transactions* **47**, 9283 (2018).

202. Mauk, M. R. & Gamble, R. C. Preparation of lipid vesicles containing high levels of entrapped radioactive cations. *Anal Biochem* **94**, 302–307 (1979).

203. Proffitt, R. T. *et al.* Tumor-Imaging Potential of Liposomes Loaded with In-111-NTA: Biodistribution in Mice. *Journal of Nuclear Medicine* **24**, (1983).

204. Utkhede, D., Yeh, V., Szucs, M. & Tilcock, C. Uptake of yttrium-90 into lipid vesicles. *http://dx.doi.org/10.3109/08982109409018621* **4**, 1049–1061 (2008).

205. Essien, H. & Hwang, K. J. Preparation of liposomes entrapping a high specific activity of 111In3+-bound inulin. *Biochim Biophys Acta* **944**, 329–336 (1988).

206. Beaumier, P. L. & Hwang, K. J. An Efficient Method for Loading Indium-111 into Liposomes Using Acetylacetone. *Journal of Nuclear Medicine* **23**, (1982).

207. Hwang, K. J. Modes of Interaction of (In3+)-8-Hydroxyquinoline with Membrane Bilayer. *Journal of Nuclear Medicine* **19**, (1978).

208. Beaumier, P. L. & Hwang, K. J. Effects of liposome size on the degradation of bovine brain sphingomyelin/cholesterol liposomes in the mouse liver. *Biochim Biophys Acta* **731**, 23–30 (1983).

209. Gabizon, A., Hliberty, J., Straubinger, R. M., Price, D. C. & Papahadjopoulos, D. An Improved Method for in Vivo Tracing and Imaging of Liposomes Using a Gallium 67-Deferoxamine Complex. *http://dx.doi.org/10.3109/08982108809035986* **1**, 123–135 (2008).

210. Boerman, O. C. *et al.* Sterically Stabilized Liposomes Labeled with Indium-111 to Image Focal Infection. *Journal of Nuclear Medicine* **36**, (1995).

211. Postma, N. S., Boerman, O. C., Oyen, W. J. G., Zuidema, J. & Storm, G. Absorption and biodistribution of 111indium-labelled desferrioxamine (111In-

DFO) after subcutaneous injection of 111In-DFO liposomes. *Journal of Controlled Release* **58**, 51–60 (1999).

212. Metselaar, J. M., Wauben, M. H. M., Wagenaar-Hilbers, J. P. A., Boerman, O. C. & Storm, G. Complete remission of experimental arthritis by joint targeting of glucocorticoids with long-circulating liposomes. *Arthritis Rheum* **48**, 2059–2066 (2003).

213. Corvo, M. L. *et al.* Intravenous administration of superoxide dismutase entrapped in long circulating liposomes: II. In vivo fate in a rat model of adjuvant arthritis. *Biochimica et Biophysica Acta (BBA) - Biomembranes* **1419**, 325–334 (1999).

214. Petersen, A. L. *et al.* 64Cu loaded liposomes as positron emission tomography imaging agents. *Biomaterials* **32**, 2334–2341 (2011).

215. Petersen, A. L. *et al.* Positron emission tomography evaluation of somatostatin receptor targeted 64Cu-TATE-liposomes in a human neuroendocrine carcinoma mouse model. *Journal of Controlled Release* **160**, 254–263 (2012).

216. Locke, L. W., Mayo, M. W., Yoo, A. D., Williams, M. B. & Berr, S. S. PET imaging of tumor associated macrophages using mannose coated 64Cu liposomes. *Biomaterials* **33**, 7785–7793 (2012).

217. Jensen, A. I. *et al.* Remote-loading of liposomes with manganese-52 and in vivo evaluation of the stabilities of 52Mn-DOTA and 64Cu-DOTA using radiolabelled liposomes and PET imaging. *Journal of Controlled Release* **269**, 100–109 (2018).

218. Li, N., Yu, Z., Pham, T. T., Blower, P. J. & Yan, R. A generic 89 Zr labeling method to quantify the in vivo pharmacokinetics of liposomal nanoparticles with positron emission tomography. *Int J Nanomedicine* **12**, 3281–3294 (2017).

219. Edmonds, S. *et al.* Exploiting the Metal-Chelating Properties of the Drug Cargo for in Vivo Positron Emission Tomography Imaging of Liposomal Nanomedicines. *ACS Nano* **10**, 10294–10307 (2016).

220. Gawne, P. J. *et al.* PET imaging of liposomal glucocorticoids using 89Zr-oxine: Theranostic applications in inflammatory arthritis. *Theranostics* **10**, 3867–3879 (2020).

221. Rudolph, A. S., Klipper, R. W., Goins, B. & Phillips, W. T. In vivo biodistribution of a radiolabeled blood substitute:99mTc-labeled liposome-encapsulated hemoglobin in an anesthetized rabbit. *Proc Natl Acad Sci U S A* **88**, 10976–10980 (1991).

222. Phillips, W. T. *et al.* A simple method for producing a technetium-99m-labeled liposome which is stable In Vivo. *Int J Rad Appl Instrum B* **19**, 539–547 (1992).

223. A Simple And Efficient Method For Radiolabeling Of Preformed Liposomes. https://sites.ualberta.ca/~csps/JPPS1(1)/M.Suresh/liposomeresearch.htm.

224. Bao, A. *et al.* A Novel Liposome Radiolabeling Method Using 99mTc-“SNS/S” Complexes: In Vitro and In Vivo Evaluation. *J Pharm Sci* **92**, 1893–1904 (2003).

225. Li, S., Goins, B., Phillips, W. T. & Bao, A. Remote-loading labeling of liposomes with 99mTc-BMEDA and its stability evaluation: effects of lipid formulation and pH/chemical gradient. *https://doi.org/10.3109/08982101003699036* **21**, 17–27 (2011).

226. Bao, A., Goins, B., Klipper, R., Negrete, G. & Phillips, W. T. Direct 99mTc Labeling of Pegylated Liposomal Doxorubicin (Doxil) for Pharmacokinetic and Non-Invasive Imaging Studies. *Journal of Pharmacology and Experimental Therapeutics* **308**, 419–425 (2004).

227. Soundararajan, A., Bao, A., Phillips, W. T., McManus, L. M. & Goins, B. A. Chemoradionuclide Therapy with 186Re-Labeled Liposomal Doxorubicin: Toxicity, Dosimetry, and Therapeutic Response. *https://home.liebertpub.com/cbr* **26**, 603–614 (2011).

228. Chen, L. C. *et al.* Pharmacokinetics, dosimetry and comparative efficacy of 188Re-liposome and 5-FU in a CT26-luc lung-metastatic mice model. *Nucl Med Biol* **39**, 35–43 (2012).

229. Engudar, G. *et al.* Remote loading of liposomes with a 124I-radioiodinated compound and their in vivo evaluation by PET/CT in a murine tumor model. *Theranostics* **8**, 5828–5841 (2018).

230. Lamichhane, N., Dewkar, G. K., Sundaresan, G., Mahon, R. N. & Zweit, J. [18F]-Fluorinated Carboplatin and [111In]-Liposome for Image-Guided Drug Delivery. *International Journal of Molecular Sciences 2017, Vol. 18, Page 1079* **18**, 1079 (2017).

231. Henriksen, J. R. *et al.* Remote Loading of 64Cu2+ into Liposomes without the Use of Ion Transport Enhancers. *ACS Appl Mater Interfaces* **7**, 22796–22806 (2015).

232. Förster, G. J. *et al.* Preliminary data on biodistribution and dosimetry for therapy planning of somatostatin receptor positive tumours: comparison of 86Y-DOTATOC and 111In-DTPA-octreotide. *Eur J Nucl Med* **28**, 1743–1750 (2001).

233. Conti, M. & Eriksson, L. Physics of pure and non-pure positron emitters for PET: a review and a discussion. *EJNMMI Phys* **3**, 8 (2016).

234. Mettler, F. A., Huda, W., Yoshizumi, T. T. & Mahesh, M. Effective Doses in Radiology and Diagnostic Nuclear Medicine: A Catalog1. *https://doi.org/10.1148/radiol.2481071451* **248**, 254–263 (2008).

235. Sarrett, S. M. *et al.* Inverse electron demand Diels–Alder click chemistry for pretargeted PET imaging and radioimmunotherapy. *Nature Protocols 2021 16:7* **16**, 3348–3381 (2021).

236. Zeglis, B. M. *et al.* A Pretargeted PET Imaging Strategy Based on Bioorthogonal Diels–Alder Click Chemistry. *J Nucl Med* **54**, 1389 (2013).

237. Reardan, D. T. *et al.* Antibodies against metal chelates. *Nature* **316**, 265–268 (1985).

238. van de Watering, F. C. J., Rijpkema, M., Robillard, M., Oyen, W. J. G. & Boerman, O. C. Pretargeted Imaging and Radioimmunotherapy of Cancer Using Antibodies and Bioorthogonal Chemistry. *Front Med (Lausanne)* **1**, 1–11 (2014).

239. Altai, M., Membreno, R., Cook, B., Tolmachev, V. & Zeglis, B. M. Pretargeted Imaging and Therapy. *Journal of Nuclear Medicine* **58**, 1553 (2017).

240. Goldenberg, D. M., Rossi, E. A., Sharkey, R. M., McBride, W. J. & Chang, C.-H. Multifunctional antibodies by the Dock-and-Lock method for improved cancer imaging and therapy by pretargeting. *J Nucl Med* **49**, 158–63 (2008).

241. Sharkey, R. M., Karacay, H. & Goldenberg, D. M. Improving the treatment of non-Hodgkin lymphoma with antibody-targeted radionuclides. *Cancer* **116**, 1134–45 (2010).

242. Rauscher, A. *et al.* Improvement of the Targeting of Radiolabeled and Functionalized Liposomes with a Two-Step System Using a Bispecific Monoclonal Antibody (Anti-CEA × Anti-DTPA-In). *Front Med (Lausanne)* **2**, 83 (2015).

243. Hnatowich, D. J., Virzi, F. & Rusckowski, M. Investigations of avidin and biotin for imaging applications. *J Nucl Med* **28**, 1294–302 (1987).

244. Förster, G. J., Santos, E. B., Smith-Jones, P. M., Zanzonico, P. & Larson, S. M. Pretargeted radioimmunotherapy with a single-chain antibody/streptavidin construct and radiolabeled DOTA-biotin: strategies for reduction of the renal dose. *J Nucl Med* **47**, 140–9 (2006).

245. Mohsin, H. *et al.* Comparison of Pretargeted and Conventional CC49 Radioimmunotherapy Using ^{149} Pm, ^{166} Ho, and ^{177} Lu. *Bioconjug Chem* **22**, 2444–2452 (2011).

246. Liu, G. *et al.* ^{90} Y labeled Phosphorodiamidate Morpholino Oligomer for Pretargeting Radiotherapy. *Bioconjug Chem* **22**, 2539–2545 (2011).

247. Saxon, E. & Bertozzi, C. R. Cell surface engineering by a modified Staudinger reaction. *Science* **287**, 2007–10 (2000).

248. Chang, P. v *et al.* Copper-free click chemistry in living animals. *Proc Natl Acad Sci U S A* **107**, 1821–6 (2010).

249. Prescher, J. A., Dube, D. H. & Bertozzi, C. R. Chemical remodelling of cell surfaces in living animals. *Nature* **430**, 873–877 (2004).

250. Laughlin, S. T., Baskin, J. M., Amacher, S. L. & Bertozzi, C. R. In vivo imaging of membrane-associated glycans in developing zebrafish. *Science* **320**, 664–7 (2008).

251. Devaraj, N. K., Thurber, G. M., Keliher, E. J., Marinelli, B. & Weissleder, R. Reactive polymer enables efficient in vivo bioorthogonal chemistry. *Proceedings of the National Academy of Sciences* **109**, 4762–4767 (2012).

252. Rossin, R., Lappchen, T., van den Bosch, S. M., Laforest, R. & Robillard, M. S. Diels-Alder Reaction for Tumor Pretargeting: In Vivo Chemistry Can Boost Tumor Radiation Dose Compared with Directly Labeled Antibody. *Journal of Nuclear Medicine* **54**, 1989–1995 (2013).

253. Zeglis, B. M. *et al.* A pretargeted PET imaging strategy based on bioorthogonal Diels-Alder click chemistry. *J Nucl Med* **54**, 1389–96 (2013).

254. Evans, H. L. *et al.* Copper-free click—a promising tool for pre-targeted PET imaging. *Chem. Commun.* **48**, 991–993 (2012).

255. Nichols, B., Qin, Z., Yang, J., Vera, D. R. & Devaraj, N. K. ^{68}Ga chelating bioorthogonal tetrazine polymers for the multistep labeling of cancer biomarkers. *Chem. Commun.* **50**, 5215–5217 (2014).

256. Denk, C. *et al.* Design, Synthesis, and Evaluation of a Low-Molecular-Weight11C-Labeled Tetrazine for Pretargeted PET Imaging Applying Bioorthogonal in Vivo Click Chemistry. *Bioconjug Chem* **27**, 1707–1712 (2016).

257. Rossin, R., Läppchen, T., van den Bosch, S. M., Laforest, R. & Robillard, M. S. Diels-Alder reaction for tumor pretargeting: in vivo chemistry can boost tumor radiation dose compared with directly labeled antibody. *J Nucl Med* **54**, 1989–1995 (2013).

258. Patra, M., Zarschler, K., Pietzsch, H. J., Stephan, H. & Gasser, G. New insights into the pretargeting approach to image and treat tumours. *Chem Soc Rev* **45**, 6415–6431 (2016).

259. Haun, J. B., Devaraj, N. K., Hilderbrand, S. A., Lee, H. & Weissleder, R. Bioorthogonal chemistry amplifies nanoparticle binding and enhances the sensitivity of cell detection. *Nat Nanotechnol* **5**, 660–665 (2010).

260. Steen, E. J. L. *et al.* Pretargeting in nuclear imaging and radionuclide therapy: improving efficacy of theranostics and nanomedicines. *Biomaterials* (2018) doi:10.1016/j.biomaterials.2018.06.021.

261. Liu, G. *et al.* Adding a Clearing Agent to Pretargeting Does Not Lower the Tumor Accumulation of the Effector as Predicted. *Cancer Biother Radiopharm* **25**, 757 (2010).

262. Berry, D. J. *et al.* Efficient bifunctional gallium-68 chelators for positron emission tomography: tris(hydroxypyridinone) ligands. *Chem Commun (Camb)* **47**, 7068–70 (2011).

263. Imberti, C. *et al. Tuning the properties of tris(hydroxypyridinone) ligands: efficient 68 Ga chelators for PET imaging*.

264. Floresta, G. *et al.* NHS-Functionalized THP Derivative for Efficient Synthesis of Kit-Based Precursors for 68Ga Labeled PET Probes. *Biomedicines 2021, Vol. 9, Page 367* **9**, 367 (2021).

265. Keeling, G. P. *et al.* Ga-THP-Pam: A Bisphosphonate PET Tracer with Facile Radiolabeling and Broad Calcium Mineral Affinity. *Bioconjug Chem* **32**, 1276–1289 (2021).

266. Young, J. D. *et al.* 68 Ga-THP-PSMA: A PET Imaging Agent for Prostate Cancer Offering Rapid, Room-Temperature, 1-Step Kit-Based Radiolabeling. *J Nucl Med* **58**, 1270–1277 (2017).

267. Hofman, M. S. *et al.* Cold Kit for Prostate-Specific Membrane Antigen (PSMA) PET Imaging: Phase 1 Study of 68 Ga-Tris(Hydroxypyridinone)-PSMA PET/CT in Patients with Prostate Cancer. *J Nucl Med* **59**, 625–631 (2018).

268. Nawaz, S. *et al.* Simple, mild, one-step labelling of proteins with gallium-68 using a tris(hydroxypyridinone) bifunctional chelator: a 68 Ga-THP-scFv targeting the prostate-specific membrane antigen. *EJNMMI Res* **7**, (2017).

269. Mishra, A., Kim, J. & T. M. de Rosales, R. In vivo 68Ga Radiolabelling of Liposomal Nanomedicines: Exploiting the Fast Complexation Kinetics and Selectivity of Tris(hydroxypyridinone) Ligands Towards Gallium(III). in *Controlled Release Society Annual Meeting* (2021).

270. Saha, G. B. Fundamentals of nuclear pharmacy. *Fundamentals of Nuclear Pharmacy* 1–409 (2010) doi:10.1007/978-1-4419-5860-0/COVER.

271. Weiner, R. E. & Thakur, M. L. Chemistry of Gallium and Indium Radiopharmaceuticals. *Handbook of Radiopharmaceuticals* 363–399 (2005) doi:10.1002/0470846380.CH11.

272. Othman, M. F. bin, Mitry, N. R., Lewington, V. J., Blower, P. J. & Terry, S. Y. A. Re-assessing gallium-67 as a therapeutic radionuclide. *Nucl Med Biol* **46**, 12–18 (2017).

273. Othman, M. F. bin *et al.* In vitro cytotoxicity of Auger electron-emitting [67 Ga]Ga-trastuzumab. *Nucl Med Biol* **80–81**, 57–64 (2020).

274. Even-Sapir, E. & Israel, O. Gallium-67 scintigraphy: a cornerstone in functional imaging of lymphoma. *Eur J Nucl Med Mol Imaging* **30 Suppl 1**, (2003).

275. Front, D. *et al.* Early Detection of Lymphoma Recurrence with Gallium-67 Scintigraphy. *Journal of Nuclear Medicine* **34**, (1993).

276. Ando, A. *et al.* Mechanism of gallium 67 accumulation in inflammatory tissue. *Eur J Nucl Med* **17**, 21–27 (1990).

277. Ioppolo, J. A. *et al.* 67Ga-labeled deferoxamine derivatives for imaging bacterial infection: Preparation and screening of functionalized siderophore complexes. *Nucl Med Biol* **52**, 32–41 (2017).

278. Ali, L., Khalil, M. & Hadi, N. Revisiting gallium-67 imaging: investigation of the energy photopeaks. *Nucl Med Commun* **31**, 1068–1074 (2010).

279. Velikyan, I. Prospective of 68Ga-Radiopharmaceutical Development. *Theranostics* **4**, 47 (2014).

280. Velikyan, I. 68Ga-based radiopharmaceuticals: Production and application relationship. *Molecules* **20**, 12913–12943 (2015).

281. He, P. *et al.* Monolith-based 68Ga processing: a new strategy for purification to facilitate direct radiolabelling methods. *React Chem Eng* **1**, 361–365 (2016).

282. Bartholomä, M. D., Louie, A. S., Valliant, J. F. & Zubieta, J. Technetium and gallium derived radiopharmaceuticals: Comparing and contrasting the chemistry of two important radiometals for the molecular imaging era. *Chem Rev* **110**, 2903–2920 (2010).

283. Green, M. A. & Welch, M. J. Gallium radiopharmaceutical chemistry. *Int J Rad Appl Instrum B* **16**, (1989).

284. Harris, W. R. & Pecoraro, V. L. Thermodynamic Binding Constants for Gallium Transferrin. *Biochemistry* **22**, 292–299 (1983).

285. Theobald, A. E. & Sampson, C. B. Design and Operation of radiopharmacy facilities. *Sampson's Texbook of Radiopharmacy* 465–482 (2011).

286. Shannon, R. D. & IUCr. Revised effective ionic radii and systematic studies of interatomic distances in halides and chalcogenides. *urn:issn:0567-7394* **32**, 751–767 (1976).

287. Harris, W. R. Thermodynamics of Gallium Complexation by Human Lactoferrin. *Biochemistry* **25**, 803–808 (1986).

288. Tsan, M. F. & Scheffel, U. Mechanism of gallium-67 accumulation in tumors. *Journal of nuclear medicine : official publication, Society of Nuclear Medicine* vol. 27 1215–1219 Preprint at (1986).

289. K-Y Tzen, Z. O. H. W. M.-F. T. Role of iron-binding proteins and enhanced capillary permeability on the accumulation of gallium-67. *J Nucl Med* **21**, 31–35 (1980).

290. Petrik, M. *et al.* Selected ^{68}Ga-siderophores versus ^{68}Ga-colloid and ^{68}Ga-citrate: biodistribution and small animal imaging in mice. *Biomed Pap Med Fac Univ Palacky Olomouc Czech Repub* **159**, 60–6 (2015).

291. Petrik, M. *et al.* 68Ga-triacetylfusarinine C and 68Ga-ferrioxamine e for aspergillus infection imaging: Uptake specificity in various microorganisms. *Mol Imaging Biol* **16**, 102–108 (2014).

292. Petrik, M. *et al.* 68Ga-siderophores for PET imaging of invasive pulmonary aspergillosis: Proof of principle. *Journal of Nuclear Medicine* **51**, 639–645 (2010).

293. Mota, F. *et al.* Radiotracer Development for Bacterial Imaging. *J Med Chem* **63**, 1964–1977 (2020).

294. Pandey, A., Śmiłowicz, D. & Boros, E. Galbofloxacin: a xenometal-antibiotic with potent in vitro and in vivo efficacy against S. aureus. *Chem Sci* **12**, 14546 (2021).

295. Pandey, A. *et al.* Theranostic Gallium Siderophore Ciprofloxacin Conjugate with Broad Spectrum Antibiotic Potency. *J Med Chem* **62**, 9947–9960 (2019).

296. Tsionou, M. I. *et al.* Comparison of macrocyclic and acyclic chelators for gallium-68 radiolabelling. *RSC Adv* **7**, 49586 (2017).

297. Spang, P., Herrmann, C. & Roesch, F. Bifunctional Gallium-68 Chelators: Past, Present, and Future. *Semin Nucl Med* **46**, 373–394 (2016).

298. Burke, B. P., Clemente, G. S. & Archibald, S. J. Recent advances in chelator design and labelling methodology for (68) Ga radiopharmaceuticals. *J Labelled Comp Radiopharm* **57**, 239–243 (2014).

299. Price, E. W. & Orvig, C. Matching chelators to radiometals for radiopharmaceuticals. *Chem Soc Rev* **43**, 260–290 (2013).

300. Imberti, C. *et al.* Enhancing PET Signal at Target Tissue in Vivo: Dendritic and Multimeric Tris(hydroxypyridinone) Conjugates for Molecular Imaging of αvβ3 Integrin Expression with Gallium-68. *Bioconjug Chem* **28**, 481–495 (2017).

301. McInnes, L. E., Rudd, S. E. & Donnelly, P. S. Copper, gallium and zirconium positron emission tomography imaging agents: The importance of metal ion speciation. *Coord Chem Rev* **352**, 499–516 (2017).

302. Bartholomä, M. D. Review. *Inorganica Chim Acta* **Complete**, 36–51 (2012).

303. Zhou, T. *et al.* Iron binding dendrimers: a novel approach for the treatment of haemochromatosis. *J Med Chem* **49**, 4171–4182 (2006).

304. Young, J. D. *et al.* 68 Ga-THP-PSMA: A PET Imaging Agent for Prostate Cancer Offering Rapid, Room-Temperature, 1-Step Kit-Based Radiolabeling. *J Nucl Med* **58**, 1270–1277 (2017).

305. Imberti, C. *et al.* Manipulating the In Vivo Behaviour of 68 Ga with Tris(Hydroxypyridinone) Chelators: Pretargeting and Blood Clearance. *Int J Mol Sci* **21**, (2020).

306. Landel, A. M. Stability studies on fluorescein isothiocyanate--bovine serum albumin conjugate. *Anal Biochem* **73**, 280–289 (1976).

307. Banks, P. R. & Paquette, D. M. Comparison of Three Common Amine Reactive Fluorescent Probes Used for Conjugation to Biomolecules by Capillary Zone Electrophoresis. *Bioconjug Chem* **6**, 447–458 (1995).

308. Hermanson, G. T. The Reactions of Bioconjugation. in *Bioconjugate Techniques* 229–258 (Elsevier, 2013). doi:10.1016/b978-0-12-382239-0.00003-0.

309. Gabizon, A. *et al.* Targeting Folate Receptor with Folate Linked to Extremities of Poly(ethylene glycol)-Grafted Liposomes: In Vitro Studies. doi:10.1021/bc9801124.

310. Uster, P. S. *et al.* Insertion of poly(ethylene glycol) derivatized phospholipid into pre-formed liposomes results in prolonged in vivo circulation time. *FEBS Lett* **386**, 243–246 (1996).

311. Gawne, P. *et al.* Manganese-52: applications in cell radiolabelling and liposomal nanomedicine PET imaging using oxine (8-hydroxyquinoline) as an ionophore. *Dalton Transactions* **47**, 9283–9293 (2018).

312. Bhagavan, N. V. & Ha, C.-E. Metabolism of Iron and Heme. *Essentials of Medical Biochemistry* 511–529 (2015) doi:10.1016/B978-0-12-416687-5.00027-0.

313. Gabizon, A., Shmeeda, H. & Barenholz, Y. Pharmacokinetics of pegylated liposomal doxorubicin: Review of animal and human studies. *Clinical Pharmacokinetics* vol. 42 419–436 Preprint at https://doi.org/10.2165/00003088-200342050-00002 (2003).

314. Gabizon, A., Shmeeda, H. & Barenholz, Y. Pharmacokinetics of pegylated liposomal doxorubicin: Review of animal and human studies. *Clin Pharmacokinet* **42**, 419–436 (2003).

315. Kumar, V., K. Boddeti, D., G. Evans, S. & Angelides, S. (68)Ga-Citrate-PET for diagnostic imaging of infection in rats and for intra-abdominal infection in a patient. *Curr Radiopharm* **5**, 71–75 (2012).

316. Silvola, J. M. U. *et al.* Uptake of 68gallium in atherosclerotic plaques in LDLR-/-ApoB100/100 mice. *EJNMMI Res* **1**, 14 (2011).

317. Yazdani, A. *et al.* A Bone-Seeking Trans-Cyclooctene for Pretargeting and Bioorthogonal Chemistry: A Proof of Concept Study Using 99mTc- and 177Lu-Labeled Tetrazines. *J Med Chem* **59**, 9381 (2016).

318. BM, Z. *et al.* A pretargeted PET imaging strategy based on bioorthogonal Diels-Alder click chemistry. *J Nucl Med* **54**, 1389–1396 (2013).

319. O, K. *et al.* Pretargeting of internalizing trastuzumab and cetuximab with a 18 F-tetrazine tracer in xenograft models. *EJNMMI Res* **7**, (2017).

320. JP, M. *et al.* (18)F-Based Pretargeted PET Imaging Based on Bioorthogonal Diels-Alder Click Chemistry. *Bioconjug Chem* **27**, 298–301 (2016).

321. Dube, D. H. & Bertozzi, C. R. Metabolic oligosaccharide engineering as a tool for glycobiology. *Curr Opin Chem Biol* **7**, 616–625 (2003).

322. Saxon, E., Armstrong, J. I. & Bertozzi, C. R. A ‘traceless’ Staudinger ligation for the chemoselective synthesis of amide bonds. *Org Lett* **2**, 2141–2143 (2000).

323. Nilsson, B. L., Kiessling, L. L. & Raines, R. T. Staudinger ligation: A peptide from a thioester and azide. *Org Lett* **2**, 1939–1941 (2000).

324. van Berkel, S. S., van Eldijk, M. B. & van Hest, J. C. M. Staudinger Ligation as a Method for Bioconjugation. *Angewandte Chemie International Edition* **50**, 8806–8827 (2011).

325. Kolb, H. C., Finn, M. G. & Sharpless, K. B. Click Chemistry: Diverse Chemical Function from a Few Good Reactions. *Angewandte Chemie International Edition* **40**, 2004–2021 (2001).

326. Tornøe, C. W., Christensen, C. & Meldal, M. Peptidotriazoles on solid phase: [1,2,3]-Triazoles by regiospecific copper(I)-catalyzed 1,3-dipolar cycloadditions of terminal alkynes to azides. *Journal of Organic Chemistry* **67**, 3057–3064 (2002).

327. Carroll, L., Evans, H. L., Aboagye, E. O. & Spivey, A. C. Bioorthogonal chemistry for pre-targeted molecular imaging – progress and prospects. *Org Biomol Chem* **11**, 5772–5781 (2013).

328. Agard, N. J., Prescher, J. A. & Bertozzi, C. R. A strain-promoted [3 + 2] azide-alkyne cycloaddition for covalent modification of biomolecules in living systems. *J Am Chem Soc* **126**, 15046–15047 (2004).

329. Baskin, J. M. *et al.* Copper-free click chemistry for dynamic in vivo imaging. *Proc Natl Acad Sci U S A* **104**, 16793–7 (2007).

330. Lee, D. E. *et al.* Facile method to radiolabel glycol chitosan nanoparticles with 64Cu via copper-free click chemistry for MicroPET imaging. *Mol Pharm* **10**, 2190–2198 (2013).

331. van den Bosch, S. M. *et al.* Evaluation of strained alkynes for Cu-free click reaction in live mice. *Nucl Med Biol* **40**, 415–423 (2013).

332. Lee, S. B. *et al.* Mesoporous silica nanoparticle pretargeting for PET imaging based on a rapid bioorthogonal reaction in a living body. *Angewandte Chemie - International Edition* **52**, 10549–10552 (2013).

333. Evans, H. L. *Bioorthogonal Chemistry for Pretargeted PET Imaging*.

334. Au, K. M. *et al.* Bespoke Pretargeted Nanoradioimmunotherapy for the Treatment of Non-Hodgkin Lymphoma. *ACS Nano* **12**, 1544–1563 (2018).

335. Li, M. *et al.* Red blood cell membrane-coated upconversion nanoparticles for pretargeted multimodality imaging of triple-negative breast cancer. *Biomater Sci* **8**, 1802–1814 (2020).

336. Blackman, M. L., Royzen, M. & Fox, J. M. Tetrazine ligation: Fast bioconjugation based on inverse-electron-demand Diels-Alder reactivity. *J Am Chem Soc* **130**, 13518–13519 (2008).

337. Devaraj, N. K., Weissleder, R. & Hilderbrand, S. A. Tetrazine-based cycloadditions: Application to pretargeted live cell imaging. *Bioconjug Chem* **19**, 2297–2299 (2008).

338. Rossin, R. *et al.* In Vivo Chemistry for Pretargeted Tumor Imaging in Live Mice. *Angewandte Chemie International Edition* **49**, 3375–3378 (2010).

339. BM, Z. *et al.* Optimization of a Pretargeted Strategy for the PET Imaging of Colorectal Carcinoma via the Modulation of Radioligand Pharmacokinetics. *Mol Pharm* **12**, 3575–3587 (2015).

340. Houghton, J. L. *et al.* Pretargeted Immuno-PET of Pancreatic Cancer: Overcoming Circulating Antigen and Internalized Antibody to Reduce Radiation Doses. *J Nucl Med* **57**, 453–9 (2016).

341. Fang, Y. *et al.* Photochemical syntheses, transformations, and bioorthogonal chemistry of trans-cycloheptene and sila trans-cycloheptene Ag(I) complexes. *Chem Sci* **9**, 1953–1963 (2018).

342. Darko, A. *et al.* Conformationally strained trans-cyclooctene with improved stability and excellent reactivity in tetrazine ligation. *Chem Sci* **5**, 3770–3776 (2014).

343. Meyer, J. P. *et al.* Exploring Structural Parameters for Pretargeting Radioligand Optimization. *J Med Chem* **60**, 8201–8217 (2017).

344. Boger, D. L., Schaum, R. P. & Garbaccio, R. M. Regioselective Inverse Electron Demand Diels-Alder Reactions of N-Acyl 6-Amino-3-(methylthio)-1,2,4,5-tetrazines. *Journal of Organic Chemistry* **63**, 6329–6337 (1998).

345. Sauer, J., Heldmann, D., … J. H.-E. J. of & 1998, undefined. 1, 2, 4, 5-Tetrazine: Synthesis and Reactivity in Cycloadditions. *Wiley Online Library*.

346. Sauer, J. & Sustmann, R. Mechanistic Aspects of Diels-Alder Reactions: A Critical Survey. *Angewandte Chemie International Edition in English* **19**, 779–807 (1980).

347. Stéen, E. J. L. *et al.* Lipophilicity and Click Reactivity Determine the Performance of Bioorthogonal Tetrazine Tools in Pretargeted in Vivo Chemistry. *ACS Pharmacol Transl Sci* **4**, 824–833 (2021).

348. Oliveira, B. L., Guo, Z. & Bernardes, G. J. L. Inverse electron demand Diels-Alder reactions in chemical biology. *Chem Soc Rev* **46**, 4895–4950 (2017).

349. Taylor, M. T., Blackman, M. L., Dmitrenko, O. & Fox, J. M. Design and synthesis of highly reactive dienophiles for the tetrazine-trans-cyclooctene ligation. *J Am Chem Soc* **133**, 9646–9649 (2011).

350. Denk, C. *et al.* Design, Synthesis, and Evaluation of a Low-Molecular-Weight 11C-Labeled Tetrazine for Pretargeted PET Imaging Applying Bioorthogonal in Vivo Click Chemistry. *Bioconjug Chem* **27**, 1707–1712 (2016).

351. Keinänen, O. *et al.* Pretargeted PET Imaging of trans-Cyclooctene-Modified Porous Silicon Nanoparticles. *ACS Omega* **2**, 62–69 (2017).

352. Hu, Y. *et al.* Enzyme-Mediated In Situ Self-Assembly Promotes In Vivo Bioorthogonal Reaction for Pretargeted Multimodality Imaging. *Angew Chem Int Ed Engl* **60**, 18082–18093 (2021).

353. Stéen, E. J. L. *et al.* Improved radiosynthesis and preliminary in vivo evaluation of the 11C-labeled tetrazine [11C]AE-1 for pretargeted PET imaging. *Bioorg Med Chem Lett* **29**, 986–990 (2019).

354. Hou, S. *et al.* Pretargeted positron emission tomography imaging that employs supramolecular nanoparticles with in vivo bioorthogonal chemistry. *ACS Nano* **10**, 1417–1424 (2016).

355. Stéen, E. J. L. *et al.* Trans-Cyclooctene-Functionalized PeptoBrushes with Improved Reaction Kinetics of the Tetrazine Ligation for Pretargeted Nuclear Imaging. *ACS Nano* **14**, 568–584 (2020).

356. Karver, M. R., Weissleder, R. & Hilderbrand, S. A. Synthesis and evaluation of a series of 1,2,4,5-tetrazines for bioorthogonal conjugation. *Bioconjug Chem* **22**, 2263–2270 (2011).

357. Young, J. D. *et al.* 68Ga-THP-PSMA: A PET imaging agent for prostate cancer offering rapid, room-temperature, 1-step kit-based raDiolabeling. *Journal of Nuclear Medicine* **58**, 1270–1277 (2017).

358. Zhou, Z., Meshaw, R., Zalutsky, M. R. & Vaidyanathan, G. Site-Specific and Residualizing Linker for 18F-Labeling with Enhanced Renal Clearance: Application to an Anti-HER2 Single Domain Antibody Fragment. *Journal of Nuclear Medicine* **62**, 1624–1630 (2021).

359. García, M. F. *et al.* Synthesis of hydrophilic HYNIC-[1,2,4,5]tetrazine conjugates and their use in antibody pretargeting with 99mTc. *Org Biomol Chem* **16**, 5275–5285 (2018).

360. *Worldwide: Dynamic light scattering, common terms defined. Inform White Paper. Malvern, UK: Malvern Instruments Limited* https://scholar.google.com/scholar_lookup?title=Dynamic+Light+Scattering,+Common+Terms+Defined&author=M.I.+Worldwide&publication_year=2011&#d=gs_cit&t=1664191567376&u=%2Fscholar%3Fq%3Dinfo%3Acu2lofDhMc4J%3Ascholar.google.com%2F%26output%3Dcite%26scirp%3D0%26hl%3Den (2011).

361. Guidelines for Dynamic Light Scattering Measurement and Analysis 1 NANOCOMPOSIX'S GUIDE TO DYNAMIC LIGHT SCATTERING MEASUREMENT AND ANALYSIS. (2015).

362. Poulie, C. B. M. *et al.* Evaluation of [64Cu]Cu-NOTA-PEG7-H-Tz for Pretargeted Imaging in LS174T Xenografts—Comparison to [111In]In-DOTA-PEG11-BisPy-Tz. *Molecules* **26**, (2021).

363. Pardridge, W. M. The blood-brain barrier: Bottleneck in brain drug development. *NeuroRX* **2**, 3–14 (2005).

364. Dong, X. Current Strategies for Brain Drug Delivery. *Theranostics* **8**, 1481 (2018).

365. Pardridge, W. M. Drug Transport across the Blood–Brain Barrier. *Journal of Cerebral Blood Flow & Metabolism* **32**, 1959–1972 (2012).

366. Vieira, D. B. & Gamarra, L. F. Getting into the brain: liposome-based strategies for effective drug delivery across the blood-brain barrier. *International Journal of Nanomedicine Dovepress* 11–5381 (2016) doi:10.2147/IJN.S117210.

367. Shazeeb, M. S., Feula, G. & Bogdanov, A. Liposome-encapsulated superoxide dismutase mimetic: theranostic potential of an MR detectable and neuroprotective agent. *Contrast Media Mol Imaging* **9**, 221 (2014).

368. Guo, H. *et al.* Theranostic magnetoliposomes coated by carboxymethyl dextran with controlled release by low-frequency alternating magnetic field. *Carbohydr Polym* **118**, 209–217 (2015).

369. WO2010025322 MAGNETIC NANODELIVERY OF THERAPEUTIC AGENTS ACROSS THE BLOOD BRAIN BARRIER. https://patentscope.wipo.int/search/en/detail.jsf?docId=WO2010025322.

370. Ding, H. *et al.* Enhanced blood-brain barrier transmigration using a novel transferrin embedded fluorescent magneto-liposome nanoformulation. *Nanotechnology* **25**, (2014).

371. McNeeley, K. M., Karathanasis, E., Annapragada, A. v. & Bellamkonda, R. v. Masking and triggered unmasking of targeting ligands on nanocarriers to improve drug delivery to brain tumors. *Biomaterials* **30**, 3986–3995 (2009).

372. McNeeley, K. M., Annapragada, A. & Bellamkonda, R. v. Decreased circulation time offsets increased efficacy of PEGylated nanocarriers targeting folate receptors of glioma. *Nanotechnology* **18**, (2007).

373. Huwyler, J., Wu, D. & Pardridge, W. M. Brain drug delivery of small molecules using immunoliposomes. *Proc Natl Acad Sci U S A* **93**, 14164 (1996).

374. Joshi, S. *et al.* Cationic surface charge enhances early regional deposition of liposomes after intracarotid injection. *J Neurooncol* **120**, 489 (2014).

375. Joshi, S. *et al.* Cerebral Hypoperfusion-assisted Intraarterial Deposition of Liposomes in Normal and Glioma-bearing Rats. *Neurosurgery* **76**, 92 (2015).

376. Dass, C. R. & Choong, P. F. M. Targeting of small molecule anticancer drugs to the tumour and its vasculature using cationic liposomes: Lessons from gene therapy. *Cancer Cell Int* **6**, 1–9 (2006).

377. Karmali, P. P. & Chaudhuri, A. Cationic liposomes as non-viral carriers of gene medicines: resolved issues, open questions, and future promises. *Med Res Rev* **27**, 696–722 (2007).

378. Lipinski, C. A., Lombardo, F., Dominy, B. W. & Feeney, P. J. Experimental and computational approaches to estimate solubility and permeability in drug discovery and development settings. *Adv Drug Deliv Rev* **23**, 3–25 (1997).

379. Rutecki, P. Ions in the Brain: Normal Function, Seizures, and Stroke. *Neurology* **66**, 618–618 (2006).

380. Abbott, N. J., Rönnbäck, L. & Hansson, E. Astrocyte–endothelial interactions at the blood–brain barrier. *Nat Rev Neurosci* **7**, 41–53 (2006).

381. Gingrich, M. B. & Traynelis, S. F. Serine proteases and brain damage – is there a link? *Trends Neurosci* **23**, 399–407 (2000).

382. Gabathuler, R. Approaches to transport therapeutic drugs across the blood-brain barrier to treat brain diseases. *Neurobiol Dis* **37**, 48–57 (2010).

383. S. Hersh, D. *et al.* Evolving Drug Delivery Strategies to Overcome the Blood Brain Barrier. *Curr Pharm Des* **22**, 1177–1193 (2016).

384. Neuwelt, E. A. *et al.* Osmotic blood-brain barrier disruption: a new means of increasing chemotherapeutic agent delivery. *Trans Am Neurol Assoc* **104**, 256–60 (1979).

385. RAPOPORT, S. I. & ROBINSON, P. J. Tight-Junctional Modification as the Basis of Osmotic Opening of the Blood-Brain Barrier. *Ann N Y Acad Sci* **481**, 250–267 (1986).

386. Neuwelt, E. A. *et al.* Osmotic blood-brain barrier disruption: pharmacodynamic studies in dogs and a clinical phase I trial in patients with malignant brain tumors. *Cancer Treat Rep* **65 Suppl 2**, 39–43 (1981).

387. Fredericks, W. R. & Rapoport, S. I. Reversible osmotic opening of the blood-brain barrier in mice. *Stroke* **19**, 266–8 (1988).

388. Rapoport, S. I. & Thompson, H. K. Osmotic Opening of the Blood-Brain Barrier in the Monkey without Associated Neurological Deficits. *Science (1979)* **180**, 971–971 (1973).

389. Rapoport, S. I., Fredericks, W. R., Ohno, K. & Pettigrew, K. D. Quantitative aspects of reversible osmotic opening of the blood-brain barrier. *American Journal of Physiology-Regulatory, Integrative and Comparative Physiology* **238**, R421–R431 (1980).

390. Nadal, A., Fuentes, E., Pastor, J. & McNaughton, P. A. Plasma albumin is a potent trigger of calcium signals and DNA synthesis in astrocytes. *Proceedings of the National Academy of Sciences* **92**, 1426–1430 (1995).

391. Dean, R. L., Emerich, D. F., Hasler, B. P. & Bartus, R. T. Cereport® (RMP-7) increases carboplatin levels in brain tumors after pretreatment with dexamethasone. *Neuro Oncol* **1**, 268–274 (1999).

392. Mackic, J. B. *et al.* Cereport (RMP-7) increases the permeability of human brain microvascular endothelial cell monolayers. *Pharm Res* **16**, 1360–5 (1999).

393. Yin, Y. *et al.* L-Borneol induces transient opening of the blood-brain barrier and enhances the therapeutic effect of cisplatin. *Neuroreport* **28**, 506–513 (2017).

394. Zhang, Q. *et al.* Improved blood-brain barrier distribution: effect of borneol on the brain pharmacokinetics of kaempferol in rats by in vivo microdialysis sampling. *J Ethnopharmacol* **162**, 270–277 (2015).

395. Zhang, Q. *et al.* Improved blood–brain barrier distribution: Effect of borneol on the brain pharmacokinetics of kaempferol in rats by in vivo microdialysis sampling. *J Ethnopharmacol* **162**, 270–277 (2015).

396. Hunt Bobo, R. *et al.* Convection-enhanced delivery of macromolecules in the brain. *Proc Natl Acad Sci U S A* **91**, 2076–2080 (1994).

397. Raghavan, R. *et al.* Convection-enhanced delivery of therapeutics for brain disease, and its optimization. *Neurosurg Focus* **20**, (2006).

398. Lonser, R. R., Sarntinoranont, M., Morrison, P. F. & Oldfield, E. H. Convection-enhanced delivery to the central nervous system. *J Neurosurg* **122**, 697–706 (2015).

399. Ksendzovsky, A. *et al.* Convection-enhanced delivery of M13 bacteriophage to the brain. *J Neurosurg* **117**, 197 (2012).

400. Dickinson, P. J. *et al.* Canine model of convection-enhanced delivery of liposomes containing CPT-11 monitored with real-time magnetic resonance imaging: Laboratory investigation. *J Neurosurg* **108**, 989–998 (2008).

401. Szerlip, N. J. *et al.* Real-time imaging of convection-enhanced delivery of viruses and virus-sized particles. *J Neurosurg* **107**, 560–567 (2007).

402. Huynh, N. T. *et al.* Administration-dependent efficacy of ferrociphenol lipid nanocapsules for the treatment of intracranial 9L rat gliosarcoma. *Int J Pharm* **423**, 55–62 (2012).

403. Raghavan, R., Brady, M. L. & Sampson, J. H. Delivering therapy to target: improving the odds for successful drug development. *Ther Deliv* **7**, 457–481 (2016).

404. Healy, A. & Vogelbaum, M. Convection-enhanced drug delivery for gliomas. *Surg Neurol Int* **6**, S59 (2015).

405. Casanova, F., Carney, P. R. & Sarntinoranont, M. Effect of Needle Insertion Speed on Tissue Injury, Stress, and Backflow Distribution for Convection-Enhanced Delivery in the Rat Brain. *PLoS One* **9**, e94919 (2014).

406. Hynynen, K. Focused ultrasound for blood-brain disruption and delivery of therapeutic molecules into the brain. *Expert Opinion on Drug Delivery* vol. 4 27–35 Preprint at https://doi.org/10.1517/17425247.4.1.27 (2007).

407. Kinoshita, M., McDannold, N., Jolesz, F. A. & Hynynen, K. Noninvasive localized delivery of Herceptin to the mouse brain by MRI-guided focused ultrasound-induced blood-brain barrier disruption. *Proc Natl Acad Sci U S A* **103**, 11719–11723 (2006).

408. Kinoshita, M., McDannold, N., Jolesz, F. A. & Hynynen, K. Targeted delivery of antibodies through the blood-brain barrier by MRI-guided focused ultrasound. *Biochem Biophys Res Commun* **340**, 1085–1090 (2006).

409. McDannold, N., Vykhodtseva, N. & Hynynen, K. Targeted disruption of the blood-brain barrier with focused ultrasound: Association with inertial cavitation. in *Proceedings - IEEE Ultrasonics Symposium* vol. 2 1249–1252 (IEEE, 2005).

410. Carpentier, A. *et al.* Clinical trial of blood-brain barrier disruption by pulsed ultrasound. *Sci Transl Med* **8**, 343re2 (2016).

411. Aryal, M., Vykhodtseva, N., Zhang, Y. Z., Park, J. & McDannold, N. Multiple treatments with liposomal doxorubicin and ultrasound-induced disruption of blood-tumor and blood-brain barriers improve outcomes in a rat glioma model. *Journal of Controlled Release* **169**, 103–111 (2013).

412. Alonso, A. *et al.* Focal Delivery of AAV2/1-transgenes Into the Rat Brain by Localized Ultrasound-induced BBB Opening. *Mol Ther Nucleic Acids* **2**, e73 (2013).

413. Burgess, A. *et al.* Targeted Delivery of Neural Stem Cells to the Brain Using MRI-Guided Focused Ultrasound to Disrupt the Blood-Brain Barrier. *PLoS One* **6**, 27877 (2011).

414. Wang, S., Samiotaki, G., Olumolade, O., Feshitan, J. A. & Konofagou, E. E. Microbubble type and distribution dependence of focused ultrasound-induced blood-brain barrier opening. *Ultrasound Med Biol* **40**, 130–137 (2014).

415. Samiotaki, G., Vlachos, F., Tung, Y. S. & Konofagou, E. E. A quantitative pressure and microbubble-size dependence study of focused ultrasound-induced blood-brain barrier opening reversibility in vivo using MRI. *Magn Reson Med* **67**, 769–777 (2012).

416. Vlachos, F., Tung, Y. S. & Konofagou, E. Permeability dependence study of the focused ultrasound-induced blood-brain barrier opening at distinct pressures and microbubble diameters using DCE-MRI. *Magn Reson Med* **66**, 821–830 (2011).

417. Konofagou, E. E. Optimization of the ultrasound-induced blood-brain barrier opening. *Theranostics* **2**, 1223–1237 (2012).

418. Samiotaki, G. & Konofagou, E. E. Dependence of the reversibility of focused-ultrasound-induced blood-brain barrier opening on pressure and pulse length in vivo. *IEEE Trans Ultrason Ferroelectr Freq Control* **60**, 2257–2265 (2013).

419. Hynynen, K., McDannold, N., Sheikov, N. A., Jolesz, F. A. & Vykhodtseva, N. Local and reversible blood-brain barrier disruption by noninvasive focused ultrasound at frequencies suitable for trans-skull sonications. *Neuroimage* **24**, 12–20 (2005).

420. Choi, J. J., Selert, K., Vlachos, F., Wong, A. & Konofagou, E. E. Noninvasive and localized neuronal delivery using short ultrasonic pulses and microbubbles. *Proc Natl Acad Sci U S A* **108**, 16539–16544 (2011).

421. Choi, J. J. *et al.* Noninvasive and localized blood-brain barrier disruption using focused ultrasound can be achieved at short pulse lengths and low pulse repetition frequencies. *Journal of Cerebral Blood Flow and Metabolism* **31**, 725–737 (2011).

422. Lipsman, N. *et al.* Blood–brain barrier opening in Alzheimer’s disease using MR-guided focused ultrasound. *Nat Commun* **9**, 2336 (2018).

423. Shamout, F. E. *et al.* Enhancement of Non-Invasive Trans-Membrane Drug Delivery Using Ultrasound and Microbubbles During Physiologically Relevant Flow. *Ultrasound Med Biol* **41**, 2435–2448 (2015).

424. Morse, S. v. *et al.* Rapid Short-pulse Ultrasound Delivers Drugs Uniformly across the Murine Blood-Brain Barrier with Negligible Disruption. *Radiology* (2019) doi:10.1148/radiol.2019181625.

425. Chen, W.-S., Brayman, A. A., Matula, T. J., Crum, L. A. & Miller, M. W. The pulse length-dependence of inertial cavitation dose and hemolysis. *Ultrasound Med Biol* **29**, 739–48 (2003).

426. Dayton, P. A. *et al.* A preliminary evaluation of the effects of primary and secondary radiation forces on acoustic contrast agents. *IEEE Trans Ultrason Ferroelectr Freq Control* **44**, 1264–1277 (1997).

427. Wasielewska, J. M. & White, A. R. "Focused Ultrasound-mediated Drug Delivery in Humans – a Path Towards Translation in Neurodegenerative Diseases". *Pharm Res* **39**, 427–439 (2022).

428. Chan, T. G., Morse, S. v., Copping, M. J., Choi, J. J. & Vilar, R. Targeted Delivery of DNA-Au Nanoparticles across the Blood–Brain Barrier Using Focused Ultrasound. *ChemMedChem* **13**, 1311–1314 (2018).

429. Yang, F. Y. *et al.* Pharmacokinetic Analysis of 111In-Labeled Liposomal Doxorubicin in Murine Glioblastoma after Blood-Brain Barrier Disruption by Focused Ultrasound. *PLoS One* (2012) doi:10.1371/journal.pone.0045468.

430. Treat, L. H., McDannold, N., Zhang, Y., Vykhodtseva, N. & Hynynen, K. Improved Anti-Tumor Effect of Liposomal Doxorubicin After Targeted Blood-Brain Barrier Disruption by MRI-Guided Focused Ultrasound in Rat Glioma. *Ultrasound Med Biol* **38**, 1716–1725 (2012).

431. Treat, L. H. *et al.* Targeted delivery of doxorubicin to the rat brain at therapeutic levels using MRI-guided focused ultrasound. *Int J Cancer* **121**, 901–907 (2007).

432. Shen, Y. *et al.* Enhanced delivery of paclitaxel liposomes using focused ultrasound with microbubbles for treating nude mice bearing intracranial glioblastoma xenografts. *Int J Nanomedicine* **12**, 5613–5629 (2017).

433. Shen, Y. *et al.* Delivery of liposomes with different sizes to mice brain after sonication by focused ultrasound in the presence of microbubbles. *Ultrasound Med Biol* **42**, 1499–1511 (2016).

434. Papachristodoulou, A. *et al.* Chemotherapy sensitization of glioblastoma by focused ultrasound-mediated delivery of therapeutic liposomes. *Journal of Controlled Release* **295**, 130–139 (2019).

435. May, J. N. *et al.* Multimodal and multiscale optical imaging of nanomedicine delivery across the blood-brain barrier upon sonopermeation. *Theranostics* **10**, 1948–1959 (2020).

436. Lin, Q. *et al.* Brain tumor-targeted delivery and therapy by focused ultrasound introduced doxorubicin-loaded cationic liposomes. *Cancer Chemother Pharmacol* **77**, 269–280 (2016).

437. Lin, C. Y. *et al.* Focused ultrasound-induced blood brain-barrier opening enhanced vascular permeability for GDNF delivery in Huntington's disease mouse model. *Brain Stimul* **12**, 1143–1150 (2019).

438. Lin, C. Y. *et al.* Focused ultrasound-induced blood-brain barrier opening for non-viral, non-invasive, and targeted gene delivery. *Journal of Controlled Release* **212**, 1–9 (2015).

439. Guo, J. *et al.* Passive delivery of liposomes to mouse brain after blood-brain barrier opening induced by focused ultrasound with microbubbles. in *2015 IEEE International Ultrasonics Symposium, IUS 2015* (Institute of Electrical and Electronics Engineers Inc., 2015). doi:10.1109/ULTSYM.2015.0405.

440. Aryal, M., Vykhodtseva, N., Zhang, Y. Z. & McDannold, N. Multiple sessions of liposomal doxorubicin delivery via focused ultrasound mediated blood-brain barrier disruption: A safety study. *Journal of Controlled Release* **204**, 60–69 (2015).

441. Aryal, M. *et al.* MRI Monitoring and Quantification of Ultrasound-Mediated Delivery of Liposomes Dually Labeled with Gadolinium and Fluorophore through the Blood-Brain Barrier. *Ultrasound Med Biol* **45**, 1733–1742 (2019).

442. Kovacs, Z. *et al.* Blood-brain barrier opening-based local delivery of 80 nm-sized liposomes in mice using pulsed focused ultrasound. *J Ther Ultrasound* **3**, (2015).

443. Liu, H. L. *et al.* Blood-brain barrier disruption with focused ultrasound enhances delivery of chemotherapeutic drugs for glioblastoma treatment. *Radiology* (2010) doi:10.1148/radiol.10090699.

444. Mei, J. *et al.* Experimental study on targeted methotrexate delivery to the rabbit brain via magnetic resonance imaging-guided focused ultrasound. *Journal of Ultrasound in Medicine* (2009) doi:10.7863/jum.2009.28.7.871.

445. Park, E. J., Zhang, Y. Z., Vykhodtseva, N. & McDannold, N. Ultrasound-mediated blood-brain/blood-tumor barrier disruption improves outcomes with trastuzumab in a breast cancer brain metastasis model. *Journal of Controlled Release* (2012) doi:10.1016/j.jconrel.2012.09.007.

446. Arvanitis, C. D., Ferraro, G. B. & Jain, R. K. The blood–brain barrier and blood–tumour barrier in brain tumours and metastases. *Nat Rev Cancer* **20**, 26 (2020).

447. Chen, H. & Konofagou, E. E. The size of blood-brain barrier opening induced by focused ultrasound is dictated by the acoustic pressure. *Journal of Cerebral Blood Flow and Metabolism* **34**, 1197–1204 (2014).

448. Marty, B. *et al.* Dynamic study of blood-brain barrier closure after its disruption using ultrasound: A quantitative analysis. *Journal of Cerebral Blood Flow and Metabolism* **32**, 1948–1958 (2012).

449. Arvanitis, C. D., Ferraro, G. B. & Jain, R. K. The blood–brain barrier and blood–tumour barrier in brain tumours and metastases. *Nature Reviews Cancer* Preprint at https://doi.org/10.1038/s41568-019-0205-x (2020).

450. Choi, J. J., Selert, K., Vlachos, F., Wong, A. & Konofagou, E. E. Noninvasive and localized neuronal delivery using short ultrasonic pulses and microbubbles. *Proc Natl Acad Sci U S A* **108**, 16539–44 (2011).

451. Choi, J. J., Wang, S., Tung, Y. S., Morrison, B. & Konofagou, E. E. Molecules of Various Pharmacologically-Relevant Sizes Can Cross the Ultrasound-Induced Blood-Brain Barrier Opening in vivo. *Ultrasound Med Biol* (2010) doi:10.1016/j.ultrasmedbio.2009.08.006.

452. Chan, T. Synthesis, in vitro and in vivo evaluation of nanoparticles and metal complexes for the treatment of brain diseases. (2020).

453. Pouliopoulos, A. N., Bonaccorsi, S. & Choi, J. J. Exploiting flow to control the in vitro spatiotemporal distribution of microbubble-seeded acoustic cavitation activity in ultrasound therapy. *Phys Med Biol* **59**, 6941–6957 (2014).

454. Pouliopoulos, A. N. *et al.* Rapid short-pulse sequences enhance the spatiotemporal uniformity of acoustically driven microbubble activity during flow conditions. *J Acoust Soc Am* **140**, 2469–2480 (2016).

455. Honig, M. G. & Hume, R. I. *Fluorescent Carbocyanine Dyes Allow Living Neurons of Identified Origin to Be Studied in Long-Term Cultures*. http://rupress.org/jcb/article-pdf/103/1/171/1053242/171.pdf.

456. Münter, R. *et al.* Dissociation of fluorescently labeled lipids from liposomes in biological environments challenges the interpretation of uptake studies. *Nanoscale* **10**, 22720–22724 (2018).

457. Bagci, H., Kohen, F., Kuscuoglu, U., Bayer, E. A. & Wilchek, M. Monoclonal anti-biotin antibodies simulate avidin m the recognition of biotin. *FEBS Lett* (1993) doi:10.1016/0014-5793(93)81108-C.

458. Tan, Y. H. *et al.* A nanoengineering approach for investigation and regulation of protein immobilization. *ACS Nano* (2008) doi:10.1021/nn800508f.

459. Choi, J. J., Wang, S., Tung, Y. S., Morrison, B. & Konofagou, E. E. Molecules of Various Pharmacologically-Relevant Sizes Can Cross the Ultrasound-Induced Blood-Brain Barrier Opening in vivo. *Ultrasound Med Biol* (2010) doi:10.1016/j.ultrasmedbio.2009.08.006.

460. Sheikov, N., McDannold, N., Sharma, S. & Hynynen, K. Effect of Focused Ultrasound Applied With an Ultrasound Contrast Agent on the Tight Junctional Integrity of the Brain Microvascular Endothelium. *Ultrasound Med Biol* **34**, 1093–1104 (2008).

461. Samiotaki, G. & Konofagou, E. E. Dependence of the reversibility of focused-ultrasound-induced blood-brain barrier opening on pressure and pulse length in vivo. *IEEE Trans Ultrason Ferroelectr Freq Control* **60**, 2257–2265 (2013).

462. Zhao, B. *et al.* Blood-brain barrier disruption induced by diagnostic ultrasound combined with microbubbles in mice. *Oncotarget* **9**, 4897–4914 (2018).

463. Arvanitis, C. D., Ferraro, G. B. & Jain, R. K. The blood–brain barrier and blood–tumour barrier in brain tumours and metastases. *Nature Reviews Cancer* Preprint at https://doi.org/10.1038/s41568-019-0205-x (2020).

464. Bilalis, P., Tziveleka, L. A., Varlas, S. & Iatrou, H. pH-Sensitive nanogates based on poly(l-histidine) for controlled drug release from mesoporous silica nanoparticles. *Polym Chem* **7**, 1475–1485 (2016).

465. Thorne, R. G. & Nicholson, C. In vivo diffusion analysis with quantum dots and dextrans predicts the width of brain extracellular space. *Proc Natl Acad Sci U S A* **103**, 5567–5572 (2006).

466. Netti, P. A. *et al.* Enhancement of fluid filtration across tumor vessels: Implication for delivery of macromolecules. *Proc Natl Acad Sci U S A* (1999) doi:10.1073/pnas.96.6.3137.

467. Azzazy, H. M. E., Hong, K., Wu, M. C. & Gross, G. W. Interaction of cationic liposomes with cells of electrically active neuronal networks in culture. *Brain Res* **695**, 231–236 (1995).

468. Lakkaraju, A., Rahman, Y. E. & Dubinsky, J. M. Low-density lipoprotein receptor-related protein mediates the endocytosis of anionic liposomes in neurons. *Journal of Biological Chemistry* **277**, 15085–15092 (2002).

469. Chu, Z., Sun, Y., Kuan, C. Y., Grabowski, G. A. & Qi, X. Saposin C: Neuronal effect and CNS delivery by liposomes. in *Annals of the New York Academy of Sciences* vol. 1053 237–246 (2005).

470. Lee, S., Ashizawa, A. T., Kim, K. S., Falk, D. J. & Notterpek, L. Liposomes to target peripheral neurons and Schwann cells. *PLoS One* **8**, (2013).

471. Thunnissen, I. E., Marani, E. & Rietveld, W. J. ‘Homing’ of Lucifer Yellow liposomes into hypothalamic neurons: a combined neuroanatomical Golgi and tracing technique. *J Neurosci Methods* **12**, 113–123 (1984).

472. Hashioka, S. *et al.* Phosphatidylserine and phosphatidylcholine-containing liposomes inhibit amyloid β and interferon-γ-induced microglial activation. *Free Radic Biol Med* **42**, 945–954 (2007).

473. Hashioka, S. *et al.* Phospholipids modulate superoxide and nitric oxide production by lipopolysaccharide and phorbol 12-myristate-13-acetate-activated microglia. *Neurochem Int* **50**, 499–506 (2007).

474. Wiley, N. J. *et al.* Lipopolysaccharide Modified Liposomes for Amyotropic Lateral Sclerosis Therapy: Efficacy in SOD1 Mouse Model. *Adv Nanopart* **01**, 44–53 (2012).

475. Pustylnikov, S., Sagar, D., Jain, P. & Khan, Z. K. Targeting the C-type Lectins-Mediated Host-Pathogen Interactions with Dextran. *Journal of Pharmacy & Pharmaceutical Sciences* **17**, 371–392 (2014).

476. Madhusudanan, P., Reade, S. & Shankarappa, S. A. Neuroglia as targets for drug delivery systems: A review. *Nanomedicine: Nanotechnology, Biology, and Medicine* vol. 13 667–679 Preprint at https://doi.org/10.1016/j.nano.2016.08.013 (2017).

477. Zhang, F., Lin, Y. A., Kannan, S. & Kannan, R. M. Targeting specific cells in the brain with nanomedicines for CNS therapies. *Journal of Controlled Release* **240**, 212–226 (2016).

478. Liddelow, S. A. & Barres, B. A. Reactive Astrocytes: Production, Function, and Therapeutic Potential. *Immunity* vol. 46 957–967 Preprint at https://doi.org/10.1016/j.immuni.2017.06.006 (2017).

479. Schmidt-Kastner, R., Wietasch, K., Weigel, H. & Eysel, U. T. Immunohistochemical staining for glial fibrillary acidic protein (GFAP) after deafferentation or ischemic infarction in rat visual system: Features of reactive and

damaged astrocytes. *International Journal of Developmental Neuroscience* **11**, 157–174 (1993).

480. Chopra, R., Vykhodtseva, N. & Hynynen, K. Influence of exposure time and pressure amplitude on blood-brain-barrier opening using transcranial ultrasound exposures. *ACS Chem Neurosci* **1**, 391–398 (2010).

481. McDannold, N., Vykhodtseva, N. & Hynynen, K. Blood-Brain Barrier Disruption Induced by Focused Ultrasound and Circulating Preformed Microbubbles Appears to Be Characterized by the Mechanical Index. *Ultrasound Med Biol* **34**, 834–840 (2008).

482. McDannold, N., Vykhodtseva, N. & Hynynen, K. Targeted disruption of the blood-brain barrier with focused ultrasound: Association with cavitation activity. *Phys Med Biol* **51**, 793–807 (2006).

483. McDannold, N., Vykhodtseva, N., Raymond, S., Jolesz, F. A. & Hynynen, K. MRI-guided targeted blood-brain barrier disruption with focused ultrasound: Histological findings in rabbits. *Ultrasound Med Biol* **31**, 1527–1537 (2005).

484. Aryal, M., Arvanitis, C. D., Alexander, P. M. & McDannold, N. Ultrasound-mediated blood-brain barrier disruption for targeted drug delivery in the central nervous system. *Advanced Drug Delivery Reviews* vol. 72 94–109 Preprint at https://doi.org/10.1016/j.addr.2014.01.008 (2014).

485. Cho, E. E., Drazic, J., Ganguly, M., Stefanovic, B. & Hynynen, K. Two-photon fluorescence microscopy study of cerebrovascular dynamics in ultrasound-induced blood-brain barrier opening. *Journal of Cerebral Blood Flow and Metabolism* **31**, 1852–1862 (2011).

486. Tung, Y.-S., Vlachos, F., Feshitan, J. A., Borden, M. A. & Konofagou, E. E. The mechanism of interaction between focused ultrasound and microbubbles in blood-brain barrier opening in mice. *J Acoust Soc Am* **130**, 3059–3067 (2011).

487. Baban, D. F. & Seymour, L. W. Control of tumour vascular permeability. *Advanced Drug Delivery Reviews* vol. 34 109–119 Preprint at https://doi.org/10.1016/S0169-409X(98)00003-9 (1998).

488. Boucher, Y., Salehi, H., Witwer, B., Harsh, G. & Jain, R. Interstitial fluid pressure in intracranial tumours in patients and in rodents. *Br J Cancer* **75**, 829–836 (1997).

489. Bhowmik, B. B., Basu, S. & Ray, D. Photophysical studies of 3,3′ dioctadecyloxacarbocyanine dye in model biological membranes and different solvents. *Chem Phys Lipids* **109**, 175–183 (2001).

490. Packard, B. S. & Wolf, D. E. Fluorescence Lifetimes of Carbocyanine Lipid Analogues in Phospholipid Bilayers. *Biochemistry* **24**, 5176–5181 (1985).

491. Yu, F. T. H., Chen, X., Wang, J., Qin, B. & Villanueva, F. S. Low Intensity Ultrasound Mediated Liposomal Doxorubicin Delivery Using Polymer Microbubbles. *Mol Pharm* **13**, 55–64 (2016).

492. Schroeder, A., Kost, J. & Barenholz, Y. Ultrasound, liposomes, and drug delivery: principles for using ultrasound to control the release of drugs from liposomes. *Chemistry and Physics of Lipids* vol. 162 1–16 Preprint at https://doi.org/10.1016/j.chemphyslip.2009.08.003 (2009).

493. Dromi, S. *et al.* Pulsed-high intensity focused ultrasound and low temperature - Sensitive liposomes for enhanced targeted drug delivery and antitumor effect. *Clinical Cancer Research* **13**, 2722–2727 (2007).

494. Burgess, A. & Hynynen, K. H. Drug delivery across the blood-brain barrier using focused ultrasound. doi:10.1517/17425247.2014.897693.